Mathematical liver modeling : hemodynamics and function in hepatectomy

Chloé Audebert

Mathematical liver modeling: hemodynamics and function in hepatectomy.

THÈSE DE DOCTORAT

Présentée par

Chloe Audebert

pour obtenir le grade de

DOCTEUR DE
L' UNIVERSITÉ PIERRE ET MARIE CURIE - Paris VI

Spécialité : Mathématiques Appliquées

Soutenue publiquement le 24 février 2017 devant le jury composé de :

Jordi Alastruey	Rapporteur
Astrid Decoene	Examinatrice
Jean-Frédéric Gerbeau	Directeur de thèse
Pierre-Yves Lagrée	Président
Philippe Moireau	Rapporteur
Irene Vignon-Clementel	Directrice de thèse

Après avis favorables des rapporteurs: Jordi Alastruey et Philippe Moireau

Thèse préparée au sein de l'équipe-projet REO
Laboratoire Jacques-Louis Lions
Université Pierre et Marie Curie - Paris 6
et **Centre de Recherche Inria de Paris**
2 rue Simone Iff
75589 Paris Cedex 12

Remerciements

Je remercie mes rapporteurs, Philippe Moireau et Jordi Alastruey d'avoir accepté de rapporter cette thèse. Merci à Astrid Decoene et Pierre-Yves Lagrée d'avoir fait partie de mon jury de thèse.

Je souhaite remercier mes directeurs de thèse, Jean-Frédéric Gerbeau et Irène Vignon-Clementel, de m'avoir proposé ce sujet et de m'avoir accompagnée tout au long de cette thèse. Vous m'avez transmis votre goût pour la recherche, je vous en remercie. Merci à Jean-Frédéric pour les nombreuses discussions scientifiques ainsi que sa disponibilité et son enthousiasme. Irène, je te remercie pour ta grande disponibilité, pour tous nos échanges ainsi que pour ta confiance et tes conseils tout au long de ce projet. J'ai énormément appris lors de ces années grâce à vous.

Je souhaite également remercier tous les partenaires du projet iFLOW, avec qui j'ai pu échanger au cours de ma thèse. Je souhaite particulièrement remercier Eric Vibert pour son enthousiasme débordant qui m'a motivé tout au long mon travail. Merci à Antony Daubres pour sa disponibilité et toutes les discussions ainsi que les nombreuses quantifications des données de fluorescence. Petru Bucur, je suis très heureuse d'avoir travaillé avec toi, j'ai beaucoup appris de nos conversations scientifiques et parfois philosophiques. Je suis contente d'avoir participé aux chirurgies et j'espère que nous aurons de nouveau l'occasion de travailler ensemble. Mohamed Bekheit, thanks a lot for your time and all the explanations about liver and liver surgery. I also thank you for letting me assist you in one surgery, or more precisely for letting me hold the surgical aspirator, it was a unique experience. Je souhaite remercier Mylène Wartenberg de m'avoir aidé pour la prise de mesures lors des chirurgies ainsi que pour son travail pour la base de donnée. J'ai également eu la chance de discuter et de travailler avec Marc-Antoine Allard, Rodrigo Figueroa et Nicolas Golse, je vous remercie pour votre temps et pour les conversations sur les enjeux de la chirurgie hépatique.

Je souhaite également remercier Jacques Sainte-Marie pour toutes ses explications sur les schémas cinétiques, j'ai beaucoup apprécié nos échanges. Merci à Damiano Lombardi pour les nombreuses discussions sur divers sujets scientifiques mais également sportifs. I express a special thank to Sanjay Pant, for your warm welcome when I arrived. I also thank you a lot for all your explanations on Kalman Filter and the debug of IDA, and your UKF code in python. I learned a lot working with you.

Je remercie mes collègues de Inria, les équipes ANGE et MAMBA, merci à l'ancien bâtiment 16 et au nouveau 3^{me} étage. Merci à Maryse Desnous de m'avoir accompagné avec mes (trop) nombreuses questions. Merci à Marina pour sa bonne humeur matinale et merci Céline pour les pauses thé animées. Merci à tous pour les nombreuses conversations autour du café du matin. Merci à Eliott d'avoir enrichie ma culture, grazie mille Matteo per le lezioni di italiano, ainsi que les nombreux debug C/C++ et les retours sur le metro 6 avec multiples conversations. Nicolas, merci d'avoir partagé le bureau de Paris avec moi et merci de m'avoir écouté râler. Fabien, merci pour ta bonne humeur toujours au rendez vous. Léa, merci pour les organisations toujours au top (cinéma, repas, ...). Nora, merci pour tous les

conseils à la fin qui m'ont beaucoup aidé. Noémie, merci pour tout! Tu es une collègue en or mais aussi une amie exceptionnelle. Merci pour les discussions sur notre travail et notre vie, merci d'avoir relu une partie de cette thèse et pour toutes tes relectures en général et tes nombreux commentaires. Je te remercie de m'avoir encouragée et épaulée pendant cette thèse. Thank you Faisal for all the discussions about America, thank you Jessica for the talks about science and life and thank you Stephanie for all the fun and I will remember for a long time the thanksgiving diner we organized. Je remercie aussi 'les anciens': Benoit, merci pour ton aide avec les classes, les debugs, et de m'avoir fait découvrir gdb et Valgrind, je ne suis presque plus une noob. Mikel, je suis contente d'avoir partagé le bureau avec toi. Elisa, je te remercie beaucoup pour toutes nos conversations et les nombreuses pauses thé que nous avons partagées. Je remercie également toutes les personnes que j'ai croisé pendant mes études à Orsay: Bastian, Cyril, Xavier, Lola, Joséphine, Ketlyne, Marie-Noelle, Lucie, Lucille, Maxime, Sebastien, Malek, Erwann, et les autres, merci pour les conversations, les échanges et les soirées. Merci les filles, Charlotte, Christèle, Céline, Aurora, pour les soirées et les weekends qui permettent de se changer les idées. Je souhaite remercier Thierry Ramond pour les nombreux cours depuis la L1 jusqu'au master. Merci à Bertrand Maury de m'avoir donné l'envie de faire des mathématiques appliquées à la médecine. Je remercie aussi Christophe Giraud pour ces nombreux conseils. Ramla, je te remercie beaucoup, tu m'as toujours encouragée et aidée, je pense que c'est en partie grâce à toi que j'en suis là, encore merci.

Je remercie également mes amis, internes de médecine, Louis, Ségolène, Arthur, merci de répondre à mes questions farfelues et merci pour les discussions autour des questions médicales ainsi que pour les soirées ensemble. Chloé je te remercie d'être toujours là pour moi depuis toutes ces années. Merci Romuald et Patricia pour les sorties et merci de penser que "c'est vraiment trop cool" ce que je fais. Je remercie aussi ma famille de m'avoir soutenue, merci à mes soeurs et mes parents de m'avoir supportée et encouragée. Merci papa pour les conseils, et merci maman pour toutes les relectures en partie celles pour ce manuscrit de thèse. Enfin, merci Adrien, d'être là, de me soutenir et de croire en moi.

Modèles mathématiques de l'hémodynamique et de la fonction du foie lors d'une hepatectomie

Résumé: L'ablation partielle du foie (hépatectomie partielle) est une chirurgie qui intervient dans le traitement des lésions du foie ainsi que lors d'une transplantation partielle de foie (donneur vivant). Grâce à la capacité de régénération du foie, quelques mois après la chirurgie il retrouve sa masse initiale. Les complications de cette chirurgie sont l'insuffisance hépatique et après une transplantation le syndrome du trop petit foie (small-for-size syndrome). Ces deux complications sont liées à une fonction hépatique post-opératoire faible. Les relations entre l'hémodynamique du foie, son volume et ses fonctions restent à élucider pour mieux comprendre les causes de ces complications. Lors de la chirurgie, l'hémodynamique du foie est altérée suite à l'augmentation de la résistance au flux sanguin de l'organe. Les conséquences de cette chirurgie sur l'hémodynamique sont difficiles à analyser du fait de la double perfusion sanguine du foie. En effet, le foie reçoit du sang oxygéné via l'artère hépatique et du sang riche en nutriment via la veine porte. De plus, la régénération du foie semble dépendante des changements de débit et de pression dans la veine porte. D'autre part, comme le foie reçoit 25% du débit cardiaque, l'ablation partielle du foie impacte surement la circulation sanguine globale.
Dans ce contexte, le premier objectif de cette thèse est de mieux comprendre, grâce à des modèles mathématiques, l'influence de l'hépatectomie sur l'hémodynamique. Le second objectif est l'analyse de la perfusion et de la fonction du foie. Un modèle de transport dans le sang d'un composé ainsi que la modélisation du traitement de ce composé par le foie sont développés.
Des mesures expérimentales sont nécessaires pour la construction et la validation de ces modèles. Des ablations du foie de différentes tailles sont effectuées sur des porcs et pendant ces chirurgies plusieurs pressions et débits sont mesurés. De plus, un colorant fluorescent (le vert d'indocyanine) est injecté avant ou après l'ablation partielle, et la fluorescence de ce composé est mesurée.

Dans une première partie, la procédure chirurgicale, les conditions expérimentales ainsi que les mesures obtenues sont détaillées.
Ensuite, les changements hémodynamiques, conséquence de l'ablation partielle du foie, sont analysés. Les valeurs moyennes mesurées lors de douze chirurgies sont reproduites par un modèle de circulation entière (circuit fermé), basé sur des équations différentielles ordinaires. Le modèle permet de prendre en compte les changements de volume sanguins qui peuvent se produire (saignements) lors de la chirurgie. Par conséquent, ce modèle propose une explication de la variabilité des mesures acquises lors de ces chirurgies.
Lors des différentes hépatectomies, des changements de forme de courbe de débit et de pression sont observés. Un modèle de circulation entière, basée sur des équations 1D et 0D est proposé pour analyser ces changements. Ce travail pourrait permettre une meilleure compréhension

des changements d'architecture du foie induits par l'hépatectomie.
Puis, le transport dans le sang d'un composé ainsi que son traitement par le foie sont modélisés. La dynamique d'un composé depuis l'injection intraveineuse jusqu'au moment où il atteint les vaisseaux du foie (artère hépatique et veine porte) est analysé avec des modèles 1D et 0D. Les résultats des simulations numériques sont comparés aux mesures de fluorescence de vert d'indocyanine. Afin d'analyser la dynamique du traitement du vert d'indocyanine par le foie, un modèle pharmacocinétique est développé. De plus, grâce aux mesures, les paramètres du modèle sont estimés dans le but de proposer une nouvelle méthode pour estimer la fonction du foie (pendant la chirurgie).

Le contrôle des changements de débit et de pression de la veine porte après une hepatectomie pourrait protèger le foie restant (ou le greffon) et améliorer sa régénération post-opératoire. Les deux sujets abordés dans cette thèse ont pour but d'améliorer l'efficacité d'un dispositif médical (anneau ajustable MID-AVR^{TM}) permettant ce contrôle. En effet, pour contrôler l'hémodynamique de la veine porte avec l'anneau, il faut tout d'abord connaitre l'impact de l'hépatectomie sur l'hémodynamique. De plus, l'efficacité de l'anneau pourrait être vérifiée grâce à l'estimation de la fonction hépatique pendant l'opération, en utilisant la mesure de fluorescence du vert d'indocyanine. Cette thèse propose des premières pistes de réflexion dans le but d'améliorer la chirurgie hépatique.

Mathematical liver modeling: hemodynamics and function in hepatectomy

Abstract: Major liver resection (partial hepatectomy) is being performed to treat liver lesions or for adult-to-adult living donor liver transplantation. Due to liver regeneration, during the post-operative period lasting a few months, the patient re-gains a normal liver mass. The major complications of these surgeries are post-operative liver failure (after partial hepatectomy) and small-for-size syndrome (after partial transplantation). Both complications are related to a poor liver function. The links between liver hemodynamics, liver volume and liver function remain unclear and are important to better understand these complications.
The surgery increases the resistance to blood flow in the organ, therefore it modifies liver hemodynamics. These changes are difficult to understand, partly because the liver receives arterial (through the hepatic artery) and venous blood (through the portal vein). Large modifications of the portal vein hemodynamics have been associated with poor liver regeneration. Moreover the liver receives 25% of the cardiac outflow, therefore liver surgery may impact the whole blood circulation.
In this context, the first goal of this thesis is to investigate with mathematical models the impact of liver surgery on liver hemodynamics. The second goal is to study the liver perfusion and function with mathematical models of the transport of a compound and its processing by the liver. Data is required to build and verify these mathematical models. Therefore, liver resections were performed on pigs, during which various pressures and flows were recorded. Moreover, indocyanine green, a dye exclusively eliminated by the liver into the bile, is intravenously injected before or after liver resection and its fluorescence is measured.

The first part of this thesis describes the experimental conditions and reports the measurements recorded.
Then, the second part focuses on the liver hemodynamics during partial hepatectomy. On one hand, the hemodynamics during several surgeries is quantitatively reproduced and explained by a closed-loop model based on ordinary differential equations. The closed-loop model has enabled to take into account blood volume changes occurring during liver surgeries. On the other hand, the change of waveforms observed after different levels of liver resection is reproduced with a model of the global circulation, including 0D and 1D equations. This may contribute to a better understanding of the change of liver architecture induced by hepatectomy.
Next, the transport in blood of a compound as well as the indocyanine green processing by the liver is studied. The dynamics of a compound from its intravenous injection to when it reaches the two liver vessels (hepatic artery and portal vein) is modeled by 0D and 1D equations. The results are compared to the indocyanine green fluorescence measurements. A new framework is established to quantitatively analyze indocyanine green fluorescence dynamics. It consists in the development of a specific pharmacokinetics model and its parameter identification. The aim is to provide a novel estimation of the liver function(s) peri-operatively using indocyanine

green fluorescence measurements.
The modulation of portal vein hemodynamics may protect the liver and improve the regeneration, as the regeneration is impacted by portal hemodynamics. The two topics of this thesis aim at improving the efficacy of a medical device controlling portal vein hemodynamics (vascular ring MID-AVR^{TM}). Knowing the hemodynamics evolution during liver surgery enable to know how to modulate this hemodynamics with the ring. Moreover, the ring efficacy could be controlled by the indocyanine green fluorescence measurements to quantify and thus evaluate the liver function intra-operatively. This thesis can be seen as first step to reach the final goals.

Contents

1 Thesis introduction **1**
- 1.1 Motivations . . . 3
- 1.2 Mathematical modeling of liver perfusion and function . . . 11
- 1.3 Contributions . . . 12
- 1.4 List of publications . . . 13

I Partial hepatectomy on pigs **15**

2 Liver resection on pigs: surgery and measurements **17**
- 2.1 Material and methods . . . 20
- 2.2 Results . . . 30
- 2.3 Conclusion . . . 50

II Partial hepatectomy hemodynamics modeling tools **57**

3 Introduction **59**

4 Experimental data explained by closed-loop lumped modeling **63**
- 4.1 Methods . . . 65
- 4.2 Results . . . 73
- 4.3 Discussion and conclusions . . . 77

5 Liver lumped model **81**
- 5.1 Methods . . . 83
- 5.2 Results . . . 85
- 5.3 Discussion and conclusions . . . 88

6 Kinetic scheme for arterial and venous blood flow **93**
- 6.1 Kinetic scheme for arterial and venous blood flow . . . 95
- 6.2 Application to hepatectomy . . . 115
- 6.3 Conclusions . . . 126

7 Perspectives **127**
- 7.1 Liver micro-architecture impact on macro hemodynamics . . . 127
- 7.2 Hepatic artery tree model . . . 129

III Indocyanine green fluorescence transport in blood and processing by the liver **133**

8 Introduction **135**

9 Compound transport from the heart to the liver **139**
9.1 Transport models . . . 141
9.2 Numerical resolution . . . 146
9.3 Results . . . 148
9.4 Discussion and conclusions . . . 159

10 Model and Methods to assess liver function from ICG fluorescence measurements **163**
10.1 Methods . . . 165
10.2 Results . . . 167
10.3 Discussion and conclusions . . . 179

11 Hepatic elimination of indocyanine green before/after partial hepatectomy in pigs **189**
11.1 Material and methods . . . 191
11.2 Results . . . 197
11.3 Discussion and conclusions . . . 204

12 Clinical application of indocyanine green measurements **213**
12.1 Material and methods . . . 215
12.2 Results . . . 221
12.3 Conclusions . . . 225

13 Conclusions and perspectives **227**

14 Thesis conclusions and perspectives **229**
14.1 Liver hemodynamics . . . 229
14.2 Liver function . . . 230

A Unscented Kalman Filter **233**
A.1 Parameter estimation: inverse problem . . . 233
A.2 Unscented Kalman Filter . . . 233

B Sensitivity Analysis **235**
B.1 Traditional sensitivity . . . 235
B.2 Generalized sensitivity . . . 236

C Kinetic scheme **237**
C.1 Kinetic approach . . . 237
C.2 Kinetic numerical scheme . . . 238

D Monolix: parameter estimation by population approach **241**
D.1 Population approach principle 241
D.2 Stochastic approximation of expectation-maximization (SAEM) algorithm . . 242
D.3 Parameter estimation with Monolix 243

E Model of bile duct delay with a series of compartments **245**

Bibliography **247**

List of Figures

1.1 The liver in the abdominal cavity, inferior to the diaphragm, image from [Ana] 4
1.2 Schematic representation of the splanchnic circulation from [Spl], redrawn from [GM04]. 5
1.3 Liver lobule schematic representation and H&E staining photos, from [TD08] 6
1.4 (a) Schematic representation of healthy and cirrhotic liver from [Liv]. (b) Trichrome stain showing characteristic pattern of advanced fibrosis from [Kri13] (magnification x100). 9

2.1 Reconstruction from arterial time CT-scan. The zoom on celiac and splanchnic circulations displays the vessels where flow or pressure are measured. 22
2.2 Hepatic artery and portal vein pressure catheters and flow probes placed. . . 23
2.3 The MID-AVR^{TM} vascular ring for portal vein hemodynamic modulation. The ring is shown in different shapes according to the degree of inflation: (a) the balloon is completely deflated and the ring is closed; (b) the balloon is inflated with a small amount of saline solution and the ring is closed with a reduced diameter; (c) the balloon is inflated with a large amount of saline solution and the ring is opened; (d) the MID-AVR^{TM} ring is placed around the portal vein, it is inflated with a small amount of saline and moderate constriction of the portal vein is shown. 24
2.4 Clamping procedure. A tape is placed around the planed liver resected part (left) and then it is pulled (right) to block the blood and reduce blood losses during resection. 25
2.5 Pig liver before liver resection (left), the left and median resected liver lobes (top right) and the remaining right lobe after 75% liver resection (bottom right). 26
2.6 Recording installation for pressures, Millar Instruments PCU-2000 and for flows, Transonic T403-PPP flowmeter. emka TECHNOLOGIES itf16USB usbAMP amplifier and the computer with iox2 software. 27
2.7 Fluorescence element of reference to normalize the measured intensities, in order to compare the measurements for different animals and different days. . 28
2.8 Domain of observation for fluorescence measurements, the four regions of interest are present, the liver tissue, the hepatic artery, the portal vein and the common bile duct. 29
2.9 Database website screen-shot. A typical animal form for data storage and analysis. 29
2.10 Database website screen-shot of an example of SQL request (for portal vein flow before and after liver resection and the pre-resection estimated liver volume). 30

2.11 Schematic representation of the blood circulation, with a zoom on splanchnic circulation. The vessels where the hemodynamics measurements are recorded are recalled. Images modified from [Spl] and [Sys]. 31
2.12 Central venous pressure average and standard deviation for the different surgeries (75% liver resection, 90% liver resection without and with MID-AVR^{TM} ring) histogram, before and after liver resection and at various post-operative days. 34
2.13 Carotid artery pressure average and standard deviation for the different surgeries (75% liver resection, 90% liver resection without and with MID-AVR^{TM} ring) histogram, before and after liver resection and at various post-operative days. 34
2.14 Celiac aorta flow average and standard deviation for the different surgeries (75% liver resection, 90% liver resection without and with MID-AVR^{TM} ring) histogram, before and after liver resection and at various post-operative days. 35
2.15 Aorta flow below mesenteric artery average and standard deviation for the different surgeries (75% liver resection, 90% liver resection without and with MID-AVR^{TM} ring) histogram, before and after liver resection and at various post-operative days. 35
2.16 Hepatic artery pressure average and standard deviation for the different surgeries (75% liver resection, 90% liver resection without and with MID-AVR^{TM} ring) histogram, before and after liver resection and at various post-operative days. 36
2.17 Hepatic artery flow average and standard deviation for the different surgeries (75% liver resection, 90% liver resection without and with MID-AVR^{TM} ring) histogram, before and after liver resection and at various post-operative days. 36
2.18 Portal vein pressure average and standard deviation for the different surgeries (75% liver resection, 90% liver resection without and with MID-AVR^{TM} ring) histogram, before and after liver resection and at various post-operative days. 37
2.19 Portal vein flow average and standard deviation for the different surgeries (75% liver resection, 90% liver resection without and with MID-AVR^{TM} ring) histogram, before and after liver resection and at various post-operative days. 37
2.20 Venous pressure difference across the liver average and standard deviation for the different surgeries (75% liver resection, 90% liver resection without and with MID-AVR^{TM} ring) histogram, before and after liver resection and at various post-operative days. 38
2.21 Pressures (a) in mmHg and flow rates (b) in L/min over a few respiration cycles at the beginning of the surgery, before the liver resection. 40
2.22 Central venous, carotid artery, hepatic artery and portal vein pressures and hepatic artery (HA), portal vein (PV) and celiac aorta (AoC) flows measured in one animal during the clamping for 75% liver resection over time. Black lines indicate approximately the clamping time. 41
2.23 Central venous, carotid artery, hepatic artery and portal vein pressures and hepatic artery (HA), portal vein (PV) and celiac aorta (AoC) flows measured in one animal during the clamping from 75% to 90% liver resection over time. Black lines indicate approximately the clamping time. 42

2.24 Portal vein and hepatic artery flow per liver weight before and after various liver resection (75% , 90% and 90% with MID-AVR^{TM} vascular ring). 45
2.25 Hepatic artery and portal vein ICG fluorescence measurements over time (normalized by the reference intensity), in five animals before liver resection. . 47
2.26 Hepatic artery and portal vein ICG fluorescence measurements over time (normalized by the reference intensity), in six animals after 75% (top line) and 90% (bottom line) liver resection. 47
2.27 Hepatic artery and portal vein ICG fluorescence measurements over time (normalized by the reference intensity), for the same animal, before liver resection, on first post-operative day and on third post-operative day. 48
2.28 Hepatic artery and portal vein ICG fluorescence measurements over time (normalized by the reference intensity), for the same animal, after liver resection, on first post-operative day and on third post-operative day. 48
2.29 The delay between the maximum ICG intensity in the hepatic artery and the portal vein, before and after liver resection (75% or 90%), on first, third and seventh post-operative day. 49
2.30 Liver tissue ICG fluorescence measurements over time (normalized by the reference intensity), in five animals before liver resection. 51
2.31 Common bile duct ICG fluorescence measurements over time (normalized by the reference intensity), in five animals before liver resection. 51
2.32 Liver tissue ICG fluorescence measurements over time (normalized by the reference intensity), in six animals after 75% (top line) and 90% (bottom line) liver resection. 52
2.33 Common bile duct ICG fluorescence measurements over time (normalized by the reference intensity), in six animals after 75% (top line) and 90% (bottom line) liver resection. 52
2.34 Liver tissue and common bile duct ICG fluorescence measurements over time (normalized by the reference intensity), in one animals before 75% liver resection, on post-operative day one and three. 53
2.35 Liver tissue and common bile duct ICG fluorescence measurements over time (normalized by the reference intensity), in one animals after 75% liver resection, on post-operative day one and three. 54

4.1 Schematic representation of planned resected and remaining parts of the liver, for 75% partial hepatectomy on pig. 66
4.2 Schematic representation of the 0D closed-loop cardiovascular and liver blood circulations. RCR block and liver lobe i parameters are shown. $Q_{i,b}$ is the infused or removed flow to account for blood volume changes. 67
4.3 Pre-resection measurements vs simulation values in log/log scale, for each variable (unique color) and for each animal (one dot). Pressures are in mmHg and flow rates are in L/min. 74
4.4 Measurements (full) and simulations (dash) at different states of the surgery: pre-resection, post-resection. Simulations with (dashed green) and without (dashed red) blood volume changes are represented for the A4 mass estimation. 76

5.1 Schematic representation of the CR and RCR Windkessel models. The model equations are recalled, where the resistance and capacitance are mass dependent parameters. 83
5.2 Hepatic artery pressure over time: measurements (dot) and approximation obtained with 30 coefficients Fourier series (solid line). 84
5.3 Unscented Kalman filter results for CR (green solid line) and RCR (blue solid line) models, for two animals. For each figure: top left: hepatic artery flow measured (grey dot) and simulated (solid line), with both models, for few cardiac cycles after parameters convergence; top right: R_p parameter estimation over time for the RCR model; bottom left: C parameter estimation over time for CR and RCR model; bottom right: R and R_d parameter estimations over time for CR and RCR model respectively. The grey zone is the geometric variance of the estimated parameter. 86
5.4 Unscented Kalman filter results for CR (green solid line) and RCR (blue solid line) models, for two animals. For each figure: top left: hepatic artery flow measured (grey dot) and simulated (solid line), with both models, for few cardiac cycles after parameters convergence; top right: R_p parameter estimation over time for the RCR model; bottom left: C parameter estimation over time for CR and RCR model; bottom right: R and R_d parameter estimations over time for CR and RCR model respectively. The grey zone is the geometric variance of the estimated parameter. 87
5.5 Schematic representation of pre-resection 3-lobes liver lumped model. 89
5.6 Hepatic artery pressure (mmHg) measurements over two cardiac cycles, before and after liver resection for four pigs. 89
5.7 Hepatic artery flow (l/min) over two cardiac cycles, 3-lobe model simulation results (solid line) and pre-resection measurements (dot) for four pigs. 90

6.1 Comparison between time and space first order kinetic scheme results with $\Delta x = 0.1$cm, and $\Delta t = 1.0\,10^{-4}$s (blue), with $\Delta x = 0.01$cm, and $\Delta t = 1.0\,10^{-5}$s (red) and numerical results from [BNB+15] (dash black) for the inviscid single pulse propagation test. The pressure over space is represented for different time instants: 0.1s, 0.3s, 0.5s, 0.7s, 0.9s, 1.1s, 1.3s, and 1.5s. 104
6.2 Comparison between first order in time and second order in space kinetic scheme results with $\Delta x = 0.1$ cm, and $\Delta t = 1.0\,10^{-5}$s and numerical results from [BNB+15] with inviscid (a) and viscous (b) blood for the single pulse propagation test. The pressure over space is represented for various times: 0.1s, 0.3s, 0.5s, 0.7s, 0.9s, 1.1s, 1.3s, and 1.5s. 105
6.3 Common carotid artery test simulation results with first order kinetic scheme with $\Delta t = 10^{-5}$s and $\Delta x = 0.1$cm over one cardiac cycle compare with STM and 3D simulation solutions from [BNB+15]. 108
6.4 Upper thoracic aorta test results obtained with first order kinetic scheme with $\Delta t = 10^{-4}$s and $\Delta x = 0.1$cm over one cardiac cycle compare with the STM and 3D simulation results from [BNB+15]. 110

6.5 Aorta bifurcation test case: kinetic first order scheme results with $\Delta t = 5.10^{-5}$ s and $\Delta x = 0.1$ cm, and 3D and STM scheme results from [BNB+15], over one cardiac cycle. . . . 111
6.6 Giraffe jugular vein test: (a) at time t = 5.7s (black) and t=50s (red), simulation results with kinetic scheme ($\Delta t = 10^{-4}$ s, $\Delta x = 1.0$ cm). $\alpha = \frac{A}{A_0}$ (top) and velocity in m/s (bottom) are plotted over the vessel length. (b) schematic representation including gravity. . . . 113
6.7 Uncollapse of portal vein simulation: $\alpha = \frac{A}{A_0}$ is plotted along the vessel at various time instants. . . . 114
6.8 Schematic representation of the 1D-0D closed-loop model. 1D blood flow is simulated in the thick lines arteries while thin lines represent the 0D model connections. All RCR units and the liver are linked (thin arrows) to the vena cava (VC). . . . 116
6.9 1D arteries node number and arteries id; see Table 6.9 for their parameter values. 117
6.10 Carotid pressure over two cardiac cycles: measurement curves for four pigs (dashed lines) and 1D-0D closed-loop model simulated curve (solid line). . . . 122
6.11 Experimental measurements of hepatic artery pressure and flow rate during 75% hepatectomy for four different pigs, the dark lines indicating the clamping time. . . . 123
6.12 Experimental measurements of hepatic artery pressure and flow rate during 75% to 90% hepatectomy for two different pigs, the dark lines indicating the clamping time. . . . 123
6.13 1D-0D closed-loop model results: hepatic artery pressure (mmHg) and flow rate (L/min) during 75% simulated hepatectomy and 75% to 90% simulated hepatectomy, the dark lines indicating the time of simulated clamping. . . . 124
6.14 Pressure GSF of hepatic arterial trees for the resistance and the capacitance . 125
6.15 Flow rate GSF of hepatic arterial trees for the resistance and the capacitance 125
6.16 Simulated pressure and flow in the hepatic artery, with reduced capacitance and increased resistance in each of the 3 lobes (blue) and with previous parameters after the simulated 75% hepatectomy (red). . . . 126

7.1 Average and standard deviation of liver volume estimation from CT-scan for the different time instants of the surgical protocol. . . . 129
7.2 Average and standard deviation of liver inflow (hepatic artery plus portal vein flow) for the different time instants of the surgical protocol. . . . 130
7.3 H&E stained histological pig slices showing differences in the micro-architecture seven days after 75% partial hepatectomy. (a) No dilatation after partial hepatectomy is observed; (b) dilatation of the sinusoids after partial hepatectomy is seen in the middle of the lobule. . . . 130

9.1 Schematic representation of the transport of compound through the organs vascular trees (arterial tree followed by venous tree). . . . 143

9.2 Schematic representation of the transport of compound through the large arteries (thick lines) and the organs vascular trees. All product exiting the organs (except the liver) is transported back to the heart and lungs compartment. 145
9.3 Transport in a single vessel, for different inlet flows. The imposed inlet flow over time is shown on the left side. The inlet concentration (C_{inlet}) as well as the concentration over time for three different locations in the vessel (right): the first node ($x/L = 0$); the middle of the vessel ($x/L \simeq 0.5$) and the outlet ($x/L = 1$). When a constant inlet flow is imposed, the analytic solution is also plotted. 150
9.4 Transport in a bifurcation, for two different inlet flows. The imposed inlet flow over time is shown on the left side. The inlet concentration (C_{inlet}) as well as the concentration over time for three different locations in the bifurcation (right): the first node ($x/L = 0$; v_0); the middle of the mother vessel ($x/L \simeq 0.5$; v_0) and the middle or end of the daughter vessels ($x/L \simeq 0.5$; $v_1; v_2$ or $x/L = 1$; $v_1; v_2$). When a constant inlet flow is imposed, the analytic solution is also potted. . . 151
9.5 Concentration over time for constant inlet flow (left) and for 1D-0D closed-loop model flow (right) at different locations of the 23 arteries system: the thoracic aorta and the abdominal aorta (top); the left and right common arteries (bottom). 152
9.6 ICG fluorescence measurements (normalized by the reference intensity) and simulated concentration over time in the hepatic artery. 154
9.7 ICG fluorescence measurements (normalized by the reference intensity) over time in the hepatic artery and the portal vein for two animals. 155
9.8 Simulated compound concentration over time in the hepatic artery and the portal vein without (full) and with (dashed) heart and lungs compartment. The simulations are obtained with the 1D-0D pig systemic circulation with constant inflow (open-loop model). 155
9.9 Simulated product concentration in the hepatic artery and the portal vein accounting or not for the product venous return over time. Simulations obtained with 1D-0D pig systemic circulation with constant inflow. 156
9.10 ICG fluorescence measurements over time in the hepatic artery and the portal vein for the same animal, before and after 75% liver resection. 157
9.11 Simulated compound concentration in the hepatic artery and the portal vein over time before and after 75% liver resection simulation. The simulations are obtained with 1D-0D pig systemic circulation with constant inflow. 158
9.12 Concentration over time in the right liver lobe without (solid line) and with outflow blockage (dash-dot line). Concentration over time exiting the hepatic artery (HA) (top left), the portal vein (PV) (top right) and the liver tissue concentration (bottom left) as well as the hepatic vein (HV) (bottom right) compartment. 159
9.13 Concentration over time in the left liver lobe without (solid line) and with outflow blockage (dash-dot line). Concentration over time exiting the hepatic artery (HA) (top left), the portal vein (PV) (top right) and the liver tissue concentration (bottom left) as well as the hepatic vein (HV) (bottom right) compartment. 160

9.14 Concentration over time in the median liver lobe without (solid line) and with outflow blockage (dash-dot line). Concentration over time exiting the hepatic artery (HA) (top left), the portal vein (PV) (top right) and the liver tissue concentration (bottom left) as well as the hepatic vein (HV) (bottom right) compartment. 161

10.1 Model schematic description. The parameters in blue are the ones fixed with literature or non-ICG measurements, in red the estimated parameters by the resolution of an inverse problem, and the state variables are framed in green. 167

10.2 **Case 1: Traditional sensitivity function** Left: ICG amount in the liver over time. Right: Traditional sensitivity functions for K_{sh}, K_{hb}, S and F_b parameters. 170

10.3 **Case 1: Generalized sensitivity functions** Generalized sensitivity functions for two parameters, with the two other parameters fixed, for all pairs of parameters K_{sh}, K_{hb}, S and F_b. A: F_b and S are fixed; B: K_{hb} and S are fixed; C: K_{hb} and F_b are fixed; D: K_{sh} and S are fixed; E: F_b and K_{sh} are fixed; F: K_{sh} and K_{hb} are fixed. 171

10.4 **Case 2: Traditional sensitivity function** Left: ICG amount in the liver over time. Right: Traditional sensitivity functions for K_{sh}, K_{hb}, S and F_b parameters. 172

10.5 **Case 2: Generalized sensitivity functions** Generalized sensitivity functions for two parameters, with the two other parameters fixed, for all pairs of parameters K_{sh}, K_{hb}, S and F_b. A : F_b and S are fixed; B : K_{hb} and S are fixed; C : K_{hb} and F_b are fixed; D : K_{sh} and S are fixed; E : F_b and K_{sh} are fixed; F : K_{sh} and K_{hb} are fixed. 173

10.6 Case 1 : All parameters are estimated. A : ICG amount in the liver over time, observations curve (grey) and results from UKF runs (solid line); B : ICG amount in the liver over time, observations curve (grey) and model direct solution with parameters from UKF estimation (black solid line). Geometric mean (solid line) of the estimated parameters evolution over time and +/- geometric standard deviation (grey zone) for: K_{sh} (C); K_{hb} (D); S (E) and F_b (F). 174

10.7 Case 1: F_b parameter is known. A: ICG amount in the liver over time, observations curve (grey) and results from UKF runs (solid line); B: ICG amount in the liver over time, observations curve (grey) and model direct solution with parameters from UKF estimation (black solid line). Geometric mean (solid line) of the estimated parameters evolution over time and +/- geometric standard deviation (grey zone) for: K_{sh} (C); K_{hb} (D) and S (E). . 175

10.8 Case 1: K_{sh} parameter is known. A: ICG amount in the liver over time, observations curve (grey) and results from UKF runs (solid line); B: ICG amount in the liver over time, observations curve (grey) and model direct solution with parameters from UKF estimation (black solid line). Geometric mean (solid line) of the estimated parameters evolution over time and +/- geometric standard deviation (grey zone) for: K_{hb}(D); S (E) and F_b (F). . . . 176

10.9 Case 2: all parameters are estimated. A: ICG amount in the liver over time, observations curve (grey) and results from UKF runs (solid line); B: ICG amount in the liver over time, observations curve (grey) and model direct solution with parameters from UKF estimation (black solid line). Geometric mean (solid line) of the estimated parameters evolution over time and +/- geometric standard deviation (grey zone) for: C: K_{sh} D: K_{hb} E: S and F: F_b . 177
10.10 Case 2: F_b parameter is known. A : ICG amount in the liver over time, observations curve (grey) and results from UKF runs (solid line); B : ICG amount in the liver over time, observations curve (grey) and model direct solution with parameters from UKF estimation (black solid line). Geometric mean (solid line) of the estimated parameters evolution over time and +/- geometric standard deviation (grey zone) for: K_{sh} (C); K_{hb} (D) and S (E). . 178
10.11 Case 2: K_{sh} parameter is known. A: ICG amount in the liver over time, observations curve (grey) and results from UKF runs (solid line); B: ICG amount in the liver over time, observations curve (grey) and model direct solution with parameters from UKF estimation (black solid line). Geometric mean (solid line) of the estimated parameters evolution over time and +/- geometric standard deviation (grey zone) for: K_{hb} (D); S (E) and F_b (F). . . 179
10.12 Model and observation liver ICG amount over time, for the bile ligation group. Bile ligation data curve from [EDSC+99] with added noise (grey line) and the forward problem solution, with the set of parameters found by theUKF algorithm (solid red line). 180
10.13 Model and observation liver ICG amount over time for control group. Control data curve from [EDSC+99] with added noise (grey line) and the forward problem solution, with the set of parameters found by UKF algorithm (solid red line). 181
10.14 Model and observations of liver ICG amount over time for different liver inflows. A: ICG amount over time obtained with the model for different inflows; B: Control group average measure (solid line red) +/- standard deviation (grey zone) and control simulation (solid line black); C: Hepatic artery occlusion (solid black line) group average measure +/- standard deviation (grey zone) and control group average measure (solid red line); D: Portal vein partial occlusion (solid black line) group average measure +/- standard deviation (grey zone) and control group average measure (solid red line). The measurements are from [EDSC+99]. 182
10.15 Hepatocytes - bile canaliculi exchange coefficient over time. $\frac{K_{hb}}{1+SC_h(t)}$ coefficient over time for control and bile ligation groups. 183
10.16 Model simulations of ICG amount over time in the different compartments of the liver: sinusoids, hepatocytes and bile canaliculi for the control simulation (solid lines) and the bile ligation simulation (dash lines). 185
10.17 Model simulations of % of ICG remaining in blood over 15 min. The simulation is performed for different groups: control group (solid red), bile ligation group (dash line black) and 70% inflow reduction group (dash line green) 186

11.1 Hepatic artery and portal vein indocyanine green fluorescence measurements over 2000s and the prolongation function curve. 192
11.2 Three different types of exchange for ICG between sinusoids and hepatocytes. 193
11.3 Schematic of the ICG phamaco-kinetic model. The dash blocks are the observations. The processes 1 2 and 3 are recalled in figure 11.2. 195
11.4 Liver ICG fluorescence measurements in two animals over time. 198
11.5 Liver ICG concentration simulation with the three different processes, with liver hepatocytes uptake larger (top) and lower (bottom) than liver inflow. . . 198
11.6 Model outputs and generalized sensitivity function for the model with process 1 when the hepatic uptake is larger than the liver inflow. 199
11.7 Model outputs and generalized sensitivity function for the model with process 1 when the hepatic uptake is lower than the liver inflow. 200
11.8 Model outputs and generalized sensitivity function for the model with process 2 when the hepatic uptake is larger than the liver inflow. 201
11.9 Model outputs and generalized sensitivity function for the model with process 2 when the hepatic uptake is lower than the liver inflow. 202
11.10Model outputs and generalized sensitivity function for the model with process 3 when the hepatic uptake is larger than the liver inflow. 203
11.11Model outputs and generalized sensitivity function for the model with process 3 when the hepatic uptake is lower than the liver inflow. 204
11.12Model outputs and measurements over time. The parameters are set to Monolix individual estimates. The animals are in the control group. 205
11.13Model outputs and measurements over time. The parameters are set to Monolix individual estimates. The two animals are in the 75% liver ablation group. . . 206
11.14Model outputs and measurements over time. The parameters are set to Monolix individual estimates. The three animals are in the 90% liver ablation group. . 206
11.15Hepatic artery and portal vein indocyanine green fluorescence measurements over 2000s and the prolongation curves for the three hypotheses: 1) concentration linearly decreases and no ICG remains after 1h; 2) concentration linearly decreases and no ICG remains after 1.5h; 3) concentration is extended with the formulas (11.1). 209
11.16Liver compartments ICG concentration over 3500s simulated with the three considered models (top: Model 1; middle: Model 2; bootom: Model 3) for the different assumptions to extend vessel measurements. 210
11.17Bile duct compartments ICG concentration over 3500s simulated with the three considered models (top: Model 1; middle: Model 2; bootom: Model 3) for the different assumptions to extend vessel measurements. 211

12.1 Schematic representation of mathematical model of liver ICG processing (for 2 minutes following injection). Three processes are considered to represent the exchange between sinusoids and hepatocytes. I_{ha} and I_{pv} are hepatic artery and portal vein fluorescence measurements respectively. The liver compartment ICG concentration is the observation (purple dash lines). 217

12.2 The three models and measurements liver ICG concentration over time, the parameters are set to individual estimates. The five animals are in the control group. 222
12.3 The three models and measurements liver ICG concentration over time, the parameters are set to individual estimates. The two animals are in the 75% liver ablation group. 223
12.4 The three models and measurements liver ICG concentration over time, the parameters are set to individual estimates. The three animals are in the 90% liver ablation group. 223
12.5 The models and measurements liver ICG concentration over time, the parameters are set to Monolix individual estimates. 225

List of Tables

4.1 The different mass estimations description of the total liver, left lobe, right lobe and median lobe. Their degree of certainty increases, and conversely their degree of predictability decreases from A1 to A4: preop calculation, peri-op calculation possible, post-op calculation. 66

4.2 Durations and times for contraction and relaxation of the different cardiac chambers. These parameters are the same for the left and right hearts. 71

4.3 0D closed-loop model parameter values for each animal as well as the average and standard deviation. The parameters common to all animals are: $Ea_{LA} = 200$ dyn/cm^5; $Eb_{LA} = 400$ dyn/cm^5; $V_{RA,0} = 4$ ml; $V_{RV,0} = 10$ ml; $V_{LA,0} = 4$ ml; $V_{LV,0} = 5$ ml; $C_{O0} = 7.36\,10^{-4}$ cm^5/dyn; $C_{D0} = 3\,10^{-4}$ cm^5/dyn. 72

4.4 Mass parameter values (using A4 estimation) for 0D closed-loop model for each animal as well as the average and standard deviation. 73

4.5 Mean and standard deviation (in parenthesis) of relative error $\mathcal{E}_{rel}$ for all the 12 simulations, $\mathcal{E}_{rel} = |X_{simu} - X_{mes}| \,/\, |X_{mes}|$ with X_{simu} the simulated and X_{mes} the measured post-resection variable. 75

4.6 p-values for TOST test between the 12 simulated post-resection variables and measurements. The simulations include or not the changes in blood volume. . 77

4.7 Simulation results (Sim) and measurements (Mes) for the 12 different pigs before resection (pre), after resection with constant blood volume (post constant vol) and after resection with constant blood volume (post vol change) for : arterial pressure P_a, portal vein pressure P_{pv}, venous pressure drop across the liver $P_{pv} - P_v$, hepatic artery flow Q_{ha} and portal vein flow Q_{pv}. The amount of volume added or removed for the simulation is given (vol change line). 80

5.1 Imposed boundary conditions and fixed parameters for forward and inverse problems. 90

6.1 Parameters for the single pulse propagation benchmark test case from [BNB+15]. 103

6.2 Normalized errors for the single pulse propagation test case; for cases 1,2,3 friction is neglected and case 4 is the viscous blood case. The normalized errors are defined by $\mathcal{E}_{l^2} = \|X_{kin} - X_{STM}\|_{l^2}/\|X_{STM}\|_{l^2}$ and $\mathcal{E}_\infty = \|X_{kin} - X_{STM}\|_\infty/\|X_{STM}\|_\infty$ where X_{STM} is the solution with the 1D STM scheme from [BNB+15] and X_{kin} is the solution obtained with the kinetic scheme. Case 1 presents the results of the first order kinetic scheme with $\Delta x = 0.1$cm, and $\Delta t = 1.0\,10^{-4}$s, case 2 of the first order kinetic scheme with $\Delta x = 0.01$cm, and $\Delta t = 1.0\,10^{-5}$s, case 3 of the first order in time and second order in space kinetic scheme with $\Delta x = 0.1$cm, and $\Delta t = 1.0\,10^{-5}$s, finally case 4 of the first order in time and second order in space kinetic scheme with $\Delta x = 0.1$cm and $\Delta t = 1.0\,10^{-5}$s with a non-zero friction term. 106

6.3 Parameters for common carotid artery benchmark test case from [BNB+15] . 107

6.4 Error with respect to 3D solution in percent as defined in [BNB+15] 109

6.5 Parameters for upper thoracic aorta benchmark test case from [BNB+15] . . . 109

6.6 Error for thoracic aorta test with respect to 3D solution in percent as defined in [BNB+15] 110

6.7 Parameters for the aortic bifurcation benchmark test case from [BNB+15]. . . 111

6.8 Errors for the aortic bifurcation test case with respect to the 3D solution in percent as defined in [BNB+15]. 112

6.9 Parameters for the 1D vessels of the pig cardiovascular model. The first column contains the id number of the artery (Figure 6.9), the second the name of the artery, the third l its length in cm, the fourth its cross-section area A_0 in cm^2 from CT-scan, the fifth is the vessel elasticity coefficient β (defined in equation (6.19)) divided by the fluid density ρ, and the last one the number of elements used to discretize the vessel. 118

6.10 Parameter for heart, lungs and vena cava 0D models. E_a is the contraction function amplitude, E_b the contraction function baseline, T_c is the duration of contraction, T_r is the duration of relaxation, t_c and t_r are the times when the atria begin to contract and relax, respectively and V_0 is the unstressed volume of the chamber. R_p and R_d are the proximal and distal resistances of the RCR model and C is the capacitance. 120

6.11 Parameters for the outlets RCR models. The first column contains the id of the artery, the second node id, the third R_p the proximal resistance, the fourth R_d the distal resistance, and the last one the capacitance. 120

6.12 1D-0D closed-loop simulation parameters, time and space discretization parameters, initial conditions for 1D part, P_0, friction parameter and fluid density values. 120

6.13 Liver 0D model parameters. First the different lobe masses are given and the ratio between proximal and total resistances in each lobe for the hepatic artery RCR model. Then, mass resistance and mass capacitance are given for hepatic artery tree, portal vein tree, tissue and hepatic vein tree, followed by the clamping parameters. r is the right lobe resected mass %. 121

7.1 Description of the proposed scenarios for micro-architecture changes after partial hepatectomy. 129

9.1 τ parameters for each organ compartment (Figure 9.2) 153

10.1 Notation and units. 166
10.2 Percentage of ICG retention in blood after 15 min simulation results. With the model the % of ICG remaining in blood compartment after 15 minutes is computed for control group, bile ligation group and 70% inflow reduction group. 187

11.1 Notation table with notation details and unit precision. 194
11.2 Average and standard deviation of the error $\mathcal{E}_2$ (eq. (11.3)) for each model. . . 204
11.3 Population parameter over control population parameter for each group estimated by Monolix for the first model (Figure 11.2). 207
11.4 Population parameters over control population parameters for each group estimated by Monolix for the second model (Figure 11.2). 207
11.5 Population parameters over control population parameters for each group estimated by Monolix for the third model (Figure 11.2). 207

12.1 Relative error of flow F and ratio $r = F_{ha}/F$ estimation average and standard deviation over all animals (error $= |X_e - X_m|/X_m$ with X being the flow F or the ratio r; e and m stand for estimation and measurements). In model 2, one animal flow estimation is very high, therefore the error average is computed with and without this animal. 221
12.2 Population parameters over control population parameters for each group estimated by Monolix with the third model (Eq. 12.3). 224
12.3 Model 3. parameter estimated with Monolix, using ICG concentration measured after liver transplantation. 226

Glossary

bile canaliculi The bile canaliculi are small ducts located between the hepatocytes in the liver tissue. 3, 137, 165, 191, 216, 227

central venous Central venous pressure is the blood pressure in the vena cava, near the right atrium of the heart. 21, 65, 83

cervicotomy A cervicotomy is a surgical incision of the neck. 21

common bile duct The common bile duct is the duct that carries bile from the liver (and the gallbladder) into the upper part of the small intestine. 3, 17, 137, 165, 189, 213, 227, 231

graft In transplantation surgery, the transplanted tissue or organ is called a graft. 10, 18, 60, 215

hepatectomy A partial hepatectomy is the surgical resection (removal of part) of the liver. 10, 17, 59, 63, 81, 93, 127, 135, 139, 215, 227, 233

hepatic arterial buffer response (HABR). Hepatic arterial blood flow changes so as to buffer the impact of portal flow alterations on total hepatic blood flow, thus tending to regulate total hepatic flow at a constant level. This response is called the "hepatic arterial buffer response". 7, 43, 78

hepatic artery (HA). The hepatic artery is the main blood vessel that supplies oxygenated blood to the liver. 3, 21, 59, 65, 81, 116, 127, 135, 139, 165, 189, 215, 227, 230

hepatocytes The hepatocytes are the main functional cells of the liver tissue. 3, 128, 137, 165, 191, 215, 227

indocyanine green (ICG). Indocyanine green is a cyanine dye used in medical diagnostics. It is used for determining cardiac output, hepatic function, and for ophthalmic angiography. 13, 17, 135, 139, 163, 189, 213, 227, 229

laparotomy A laparotomy is a surgical incision into the abdominal cavity, for diagnosis or in preparation for major surgery. 20

lobule The liver lobule is a unit of the liver, consisting of liver cells arranged around a central vein that is a terminal branch of one of the hepatic veins, and at whose periphery branches of the portal vein, hepatic artery, and bile duct are located. 3, 60, 128, 168

portal vein (PV). The portal vein is a vessel that supplies blood from the spleen and digestive organs to the liver. 3, 17, 59, 65, 83, 113, 127, 136, 139, 165, 189, 215, 227, 229

sinusoids The sinusoids are the small blood vessels (capillaries) of the liver tissue. 3, 127, 137, 165, 191, 215, 227, 229

NOMENCLATURE TABLE

Notation	Detail
R_{ha}	hepatic artery (HA) tree resistance
C_{ha}	hepatic artery tree capacitance
R_{pv}	portal vein (PV) tree resistance
R_l	liver tissue and hepatic venous tree resistance
C_l	the liver tissue capacitance per liver mass
ll	left lobe of the liver
ml	median lobe of the liver
rl	right lobe of the liver
M	liver mass
M_i	ith liver lobe mass
$T_{i/b}$	time of infusion/bleeding
$D_{i/b}$	duration of infusion/bleeding
$V_{i/b}$	added / removed volume
Ea_i	ith heart chamber contraction function amplitude
Eb_i	ith heart chamber contraction function baseline
V_{0_i}	unstressed volume of the ith heart chamber
R_p^i	ith RCR block proximal resistance
R_d^i	ith RCR block distal resistance
C^i	ith RCR block capacitance
T_{cc}	Cardiac cycle
T_{vc}	Ventricular contraction duration
T_{vr}	Ventricular relaxation duration
T_{ac}	Atrium contraction duration
T_{ar}	Atrium relaxation duration
t_{ac}	Time atrium begins to contract
t_{ar}	Time atrium begins to relax
τ	tree transit time
λ	length to radius ratio
blood	Rest of blood circulation
s	Sinusoids
h	Hepatocytes
bc	Bile Canaliculi
L	Liver
ha	Hepatic artery
pv	Portal vein
b	Bile
V_i	Volume of i^{th} compartment
C_i	Concentration of i^{th} compartment
F_i	i^{th} flow rate
K_{sh}	Exchange coefficient between sinusoids and hepatocytes
K_{hb}	Excretion coefficient from hepatocytes to bile canaliculi
S	Saturation parameter

Chapter 1

Thesis introduction

Contents

1.1 Motivations 3
1.1.1 Liver anatomy and function 3
1.1.2 Liver inflow regulatory processes 7
1.1.3 Liver regeneration 7
1.1.4 Liver diseases and treatments 8
1.2 Mathematical modeling of liver perfusion and function 11
1.3 Contributions 12
1.4 List of publications 13

1.1 Motivations

1.1.1 Liver anatomy and function

Liver is one of the largest organ of the body, weighting 1.5 kg for an average adult, corresponding to 2-2.5% of the total body weight [Lau07, GH06, TD08]. It is located in the abdominal cavity, below the diaphragm (Figure 1.1). The human liver is divided into two main lobes, a large right lobe and a left lobe.
Among the 25% of the cardiac output received by the liver, 25% is oxygenated blood, provided through the hepatic artery. The remaining 75%, is nutrient-rich blood, coming from the stomach, the intestine, the pancreas and the spleen, through the portal vein [Lau07] (Figure 1.2).

The liver tissue is composed of various cell types as detailed below. The major functional liver cells are the hepatocytes.
Metabolism and storage functions, drugs and hormones processing and bilirubin excretion among others, form the major roles of the liver [TD08]. Few functions are detailed below, and a complete review can be found in [TD08, GH06]. With its metabolism and storage functions, the liver controls the glucose level in blood. When the level is low, the hepatocytes metabolize glycogen into glucose and release it into the blood. On the contrary, when the blood glucose level is high (after a meal), the glucose is converted into glycogen and triglycerides, that are stored by the liver. The hepatocytes also metabolize some lipids and proteins. Therefore the blood composition is regulated by the liver. Moreover, the hepatocytes remove the toxins from the blood. Indeed, the liver detoxifies substances from the blood, such as alcohol, and excretes into bile drugs, such as penicillin. The bilirubin, coming from the dead red blood cells, is absorbed from the blood by the hepatocytes and secreted into the bile.
The bile, produced by hepatocytes, is collected by small ducts, located between the hepatocytes, called bile canaliculi (Figure 1.3 (a)). The bile flows from the bile canaliculi to the bile ductules and then it flows to the bile ducts. The bile ducts then merge to form the right and left hepatic ducts. The bile exits the liver through the common bile duct.
In the liver tissue, blood flows between rows of hepatocytes, in highly permeable capillaries called sinusoids. The sinusoids receive oxygenate blood from the hepatic artery branches, and nutriment-rich blood from the portal vein branches (Figures 1.2 and 1.3 (a)). Then, blood is delivered to the central vein. The central veins converge and form the hepatic veins, that empty into the inferior vena cava (Figure 1.2).
The liver tissue is organized in functional units, called lobules. Units have hexagonal shape, with the central vein in the middle (Figure 1.3). The hepatic artery and the portal vein branches with the bile duct form the portal triad, that are located on corners of the lobule. The hepatocytes are aligned between the portal triads and the central veins (Figure 1.3). In the liver lobule, the blood flows from the portal triads towards the central vein, while the bile flows in the opposite direction, to reach the bile ducts.

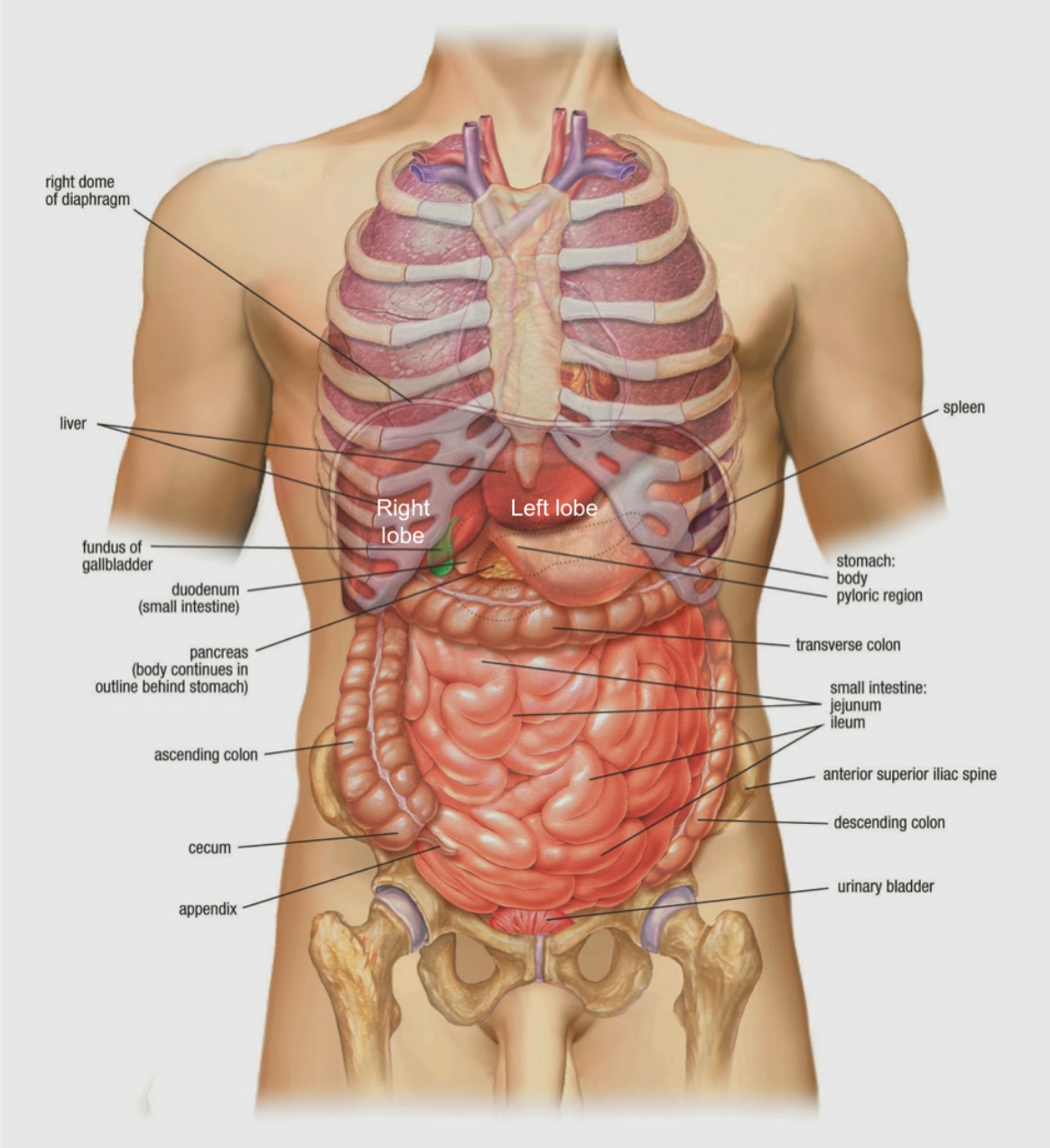

Figure 1.1: The liver in the abdominal cavity, inferior to the diaphragm, image from [Ana]

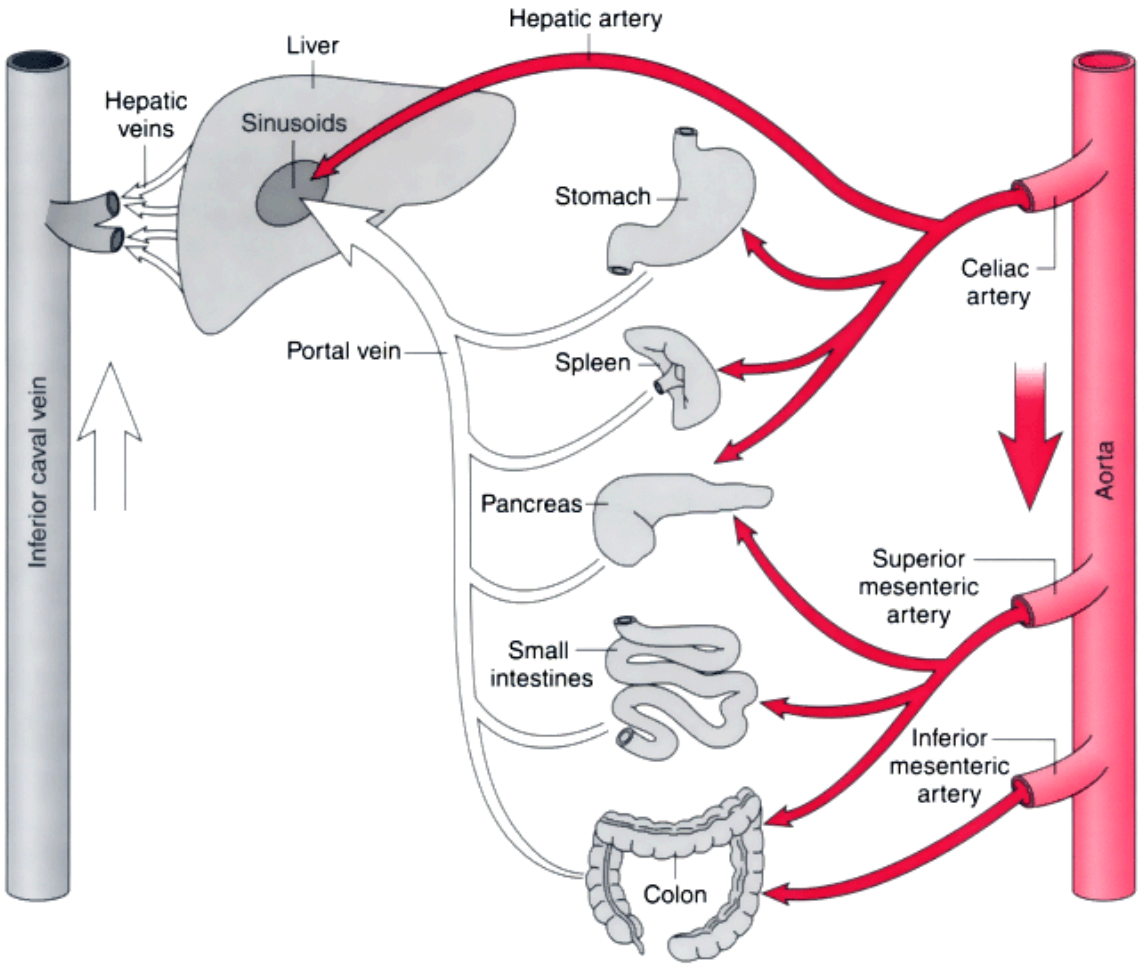

Figure 1.2: Schematic representation of the splanchnic circulation from [Spl], redrawn from [GM04].

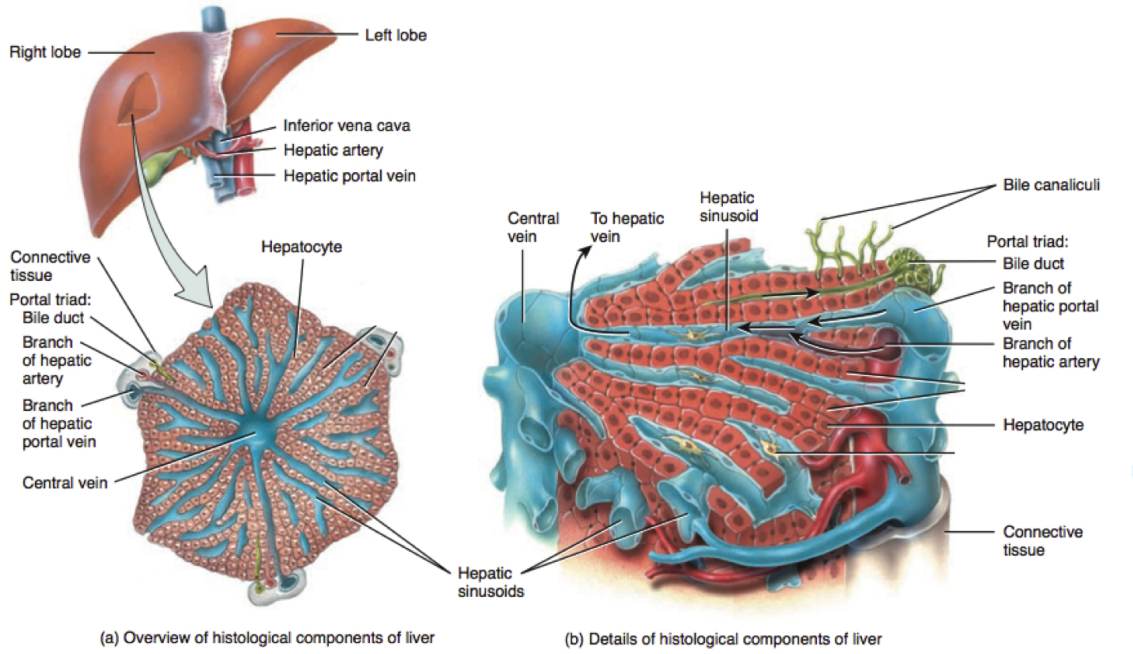

(a) Liver lobule organization

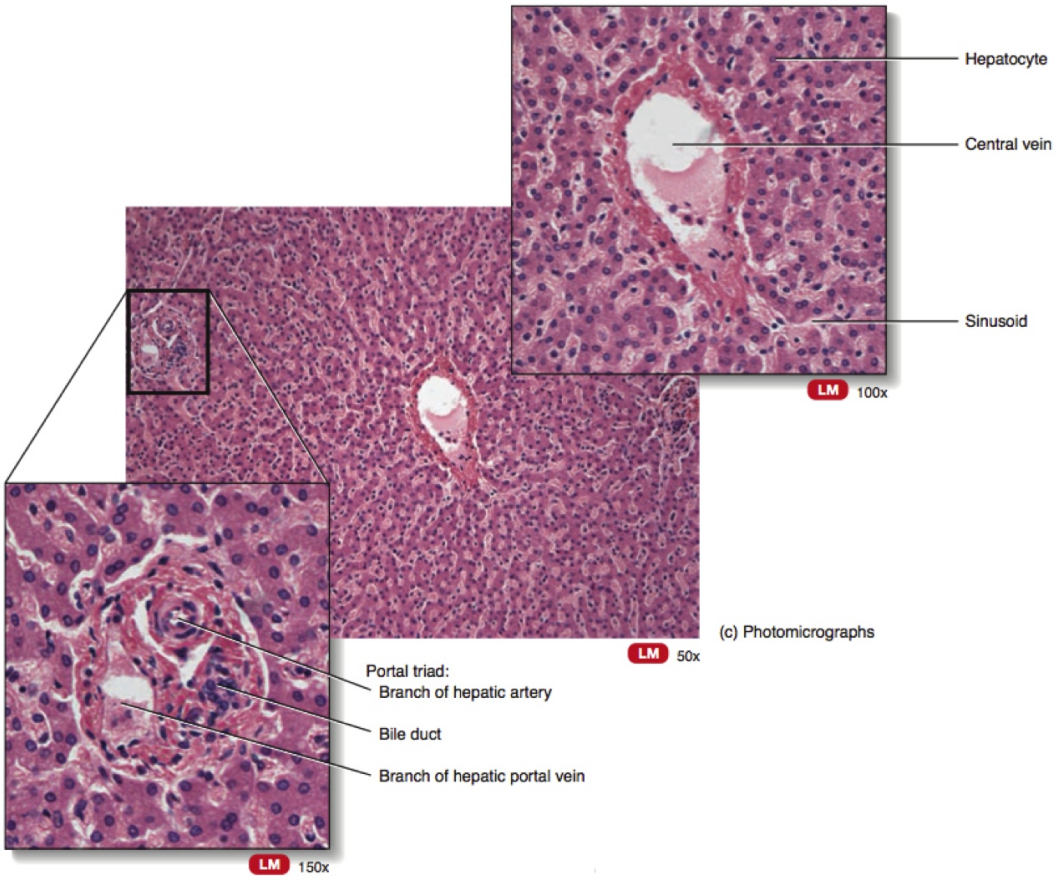

(b) Liver lobule staining

Figure 1.3: Liver lobule schematic representation and H&E staining photos, from [TD08]

1.1.2 Liver inflow regulatory processes

In addition to its other functions, the liver plays a role of blood volume reservoir, indeed 12% of the total blood volume is contained in the liver. Blood can rapidly be expelled from the liver to increase the venous return and thus the cardiac output, in response to an active or passive influence [Lau07].

As detailed previously, the liver has detoxification and metabolic functions, therefore the blood concentration in glucose, hormones etc, depends on the liver function and inflow. A relatively constant liver inflow is required for the hormone fluxes and the cardiovascular stability. Several interrelated mechanisms exist to maintain a constant flow per liver mass.

The portal flow depends on the digestive organs inflow, therefore, the liver has no direct control on the portal flow. However, indirect mechanisms exist. Two of them are detailed below, and more precision can be found in the review by Lautt [Lau07].
A decrease of portal vein flow leads to a decrease of the intrahepatic pressure. In response, the venous return is increased, with blood expulsion from the hepatic reservoir. The increase of venous return leads to cardiac output increase and therefore the blood flow of the digestive organ arteries increases, leading to the increase of portal vein flow. Therefore, the portal vein flow reduction is partially counterbalanced.
A second mechanism is the hepatic arterial buffer response (HABR). It consists of the counterbalance of portal flow changes by the arterial flow. Indeed, in the portal triads the level of vasodilator (called adenosine) is regulated with the portal vein flow. The vasodilator are assumed to be secreted at a constant rate. Therefore, a decreased flow in the portal vein leads to an accumulation of vasodilator, resulting in a dilation of the hepatic artery. The hepatic artery flow increases and compensates for the decrease of portal vein flow. On the contrary, an increase of portal vein flow, leads to the constriction of the hepatic artery and the decrease of arterial flow.

1.1.3 Liver regeneration

The liver possesses the ability to regenerate after a large loss of tissue. Liver regeneration is also a way to keep a constant inflow per liver mass. Hepatocytes replicate once or twice and grow, while the endothelial cells proliferation to restore the sinusoids network starts only after three days [Mic07]. After a short period the liver weight is restore (three to seven days in rats and pigs). The regeneration is "designed" to respect an optimal liver-to-body weight ratio for metabolism optimization [GH06]. Moreover, the liver functions are maintained during the liver regeneration.
The trigger and stopping mechanisms for liver regeneration are largely studied in the literature as detailed in the two reviews by Michalopoulos and De France [Mic10, MD05]. No single signal drives the liver regeneration, but multiple pathways exist [AEV12]. For example, hepatic growth factors play an important role in liver regeneration. Their level in blood, after a liver resection, is largely increased. Among other mechanisms, the portal vein hemodynamics is linked to liver regeneration [AEV12]. An increase of portal flow per liver mass is assumed to trigger the regeneration, as well as the increase of portal pressure [NMA+99]. However, a long and too severe hyperperfusion can lead to hepatic injuries and a damaged regeneration

[AEV12].

1.1.4 Liver diseases and treatments

Liver diseases. Early stage diagnosis of liver disease is difficult, because only few symptoms appear. Unfortunately, when major symptoms appear, the liver disease is usually in an advanced stage [LC10]. Therefore, the early diagnosis of liver diseases is important, and would improve the efficacy of treatments.

The two main causes of liver disease are the inflammation and necrosis of hepatocytes, leading to hepatocellular diseases, and the bile flow inhibition or obstruction, leading to cholestatic diseases. The most common diseases are hepatitis (A, B, C, D and E), diseases leading to steatosis, alcohol abuse, paracetamol overdose and a hereditary disease called hemochromatosis [ZLCK09]. The hepatitis are viral infection causing hepatocytes inflammation, the virus B and C can lead to chronic hepatitis.
The steatosis is related to a disfunction of fat metabolism by the liver, that is a risk factor for insulin resistance, type 2 diabetes and non-alcoholic fatty liver disease. Due to the dysfunction of the fat metabolism, an accumulation of lipid in the liver appears and disturbs the tissue architecture.
The metabolism of alcohol, by the hepatocyte, may result in the formation of metabolites, that are toxic for the liver. Therefore, a prolonged and repeated alcohol consumption leads to liver damage. Similarly, after a paracetamol overdose the ammonia detoxification is compromised, leading to high levels of ammonia in the blood, which cause neurological disorder.
The hemochromatosis is a hereditary disease altering the iron metabolism leading to iron accumulation in the liver [ZLCK09].

Chronic liver disease leads to fibrosis. The hepatic fibrosis is the accumulation of extracelullar matrix in the liver, and is associated to a healing process. The fibrosis is the consequence of a wound-healing response to the chronic liver injury (due to one of the previously mention diseases).
After 15 to 20 years, the fibrosis results in cirrhosis, the final stage of fibrosis [AWB+11]. The excessive amount of extracellular matrix degrades the exchange between blood and hepatocytes, leading to hepatocytes necrosis (Figure 1.4). Figure 1.4 (b) shows the micro-disorganization, due to fibrosis, compared with the healthy liver shown in Figure 1.3. To compensate for the injuries, the remaining hepatocytes regenerate, forming parenchymal nodules. Moreover, the hepatocytes in the nodule have lost the normal vascular and bilary connection. Therefore fibrosis, and then cirrhosis lead to a complete disorganization of the liver, and the liver function and vascularization are damaged (Figure 1.4).

A disorganized liver leads to the compression of central veins and hepatic veins, resulting in the increase of resistance to blood flow. Therefore the portal pressure tends to increase, leading to portal hypertension. The high resistance of the liver to blood flow results in the development of collateral circulation [PV05]. The fibrosis and cirrhosis lead to large vascular modification, inside and outside the liver. The cirrhosis is also a major risk factor for liver cancer (called hepatocellular carcinoma). Other liver cancers also exist, usually due to the

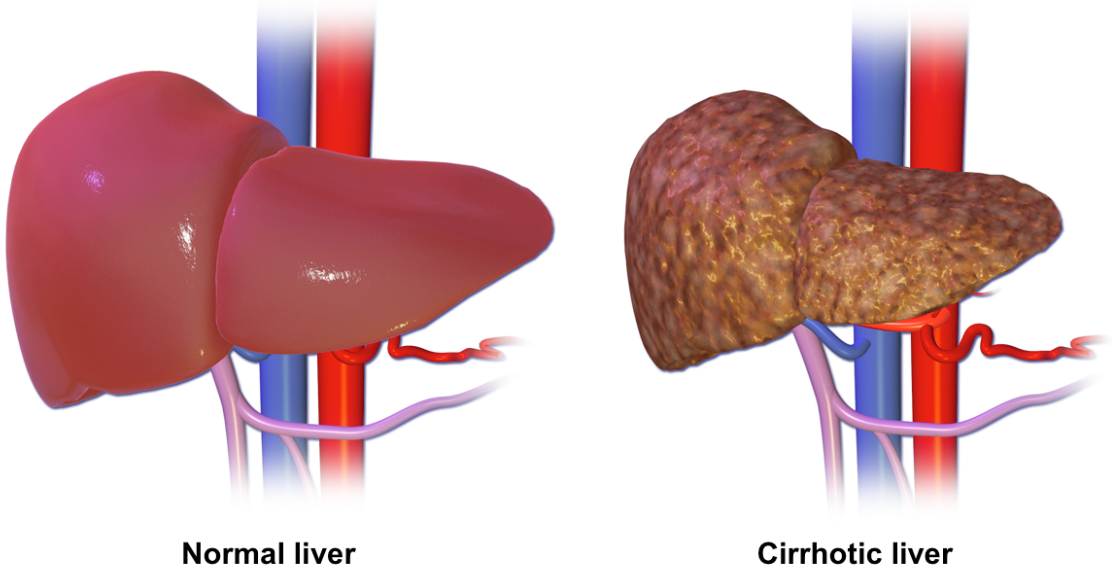

(a) Healthy and cirrhotic liver drawing

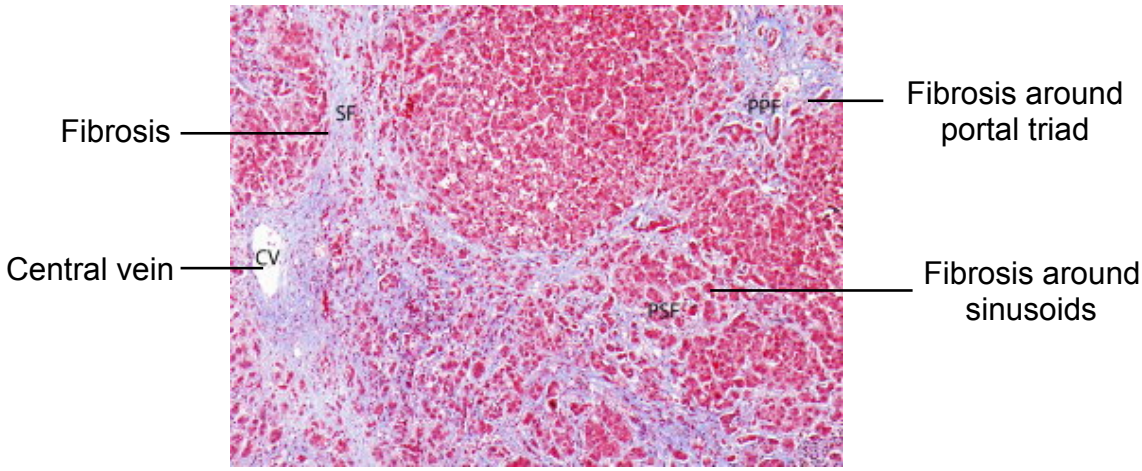

(b) Characteristic pattern of fibrosis

Figure 1.4: (a) Schematic representation of healthy and cirrhotic liver from [Liv]. (b) Trichrome stain showing characteristic pattern of advanced fibrosis from [Kri13] (magnification x100).

migration of metastases from other organs.

Treatments. The best treatment for fibrosis is to remove the cause of the liver injury (stop alcohol consumption, treat the hepatitis...). Moreover, some drug can reduce the formation of extracellular matrix [AWB+11]. The treatment for cirrhosis is the liver transplantation. Two types of transplantation exist, the total liver transplant (from a brain dead donor) or a split liver transplant (from a brain dead donor or a living donor). Liver transplantation is also the best treatment for liver cancer. However, if the transplantation is contraindicated, surgical resection (partial hepatectomy) of the tumor is proposed. The liver resection is considered for small cancer with early stage cirrhosis, and can be combined with chemotherapy to reduce the tumor size [CPDG07, ZLCK09].

After partial hepatectomy or liver transplantation, the remaining liver size needs to be sufficiently large to ensure metabolism, synthesis, storage and regeneration functions of the liver. If the post-operative liver size is too small, post-operative liver failure may occur. This complication is associated with high mortality, and may occur in large liver resection or in liver transplantation with a reduced liver graft. The liver failure due to a small graft, is referred as "small-for-size" syndrome, and after a major resection as "post-hepatectomy liver failure". Empirical threshold determines a "safe" post-operative liver size, it is based on remaining liver weight to body weight ratio [TOS+07, AVOS13].
Surgical strategies exist to increase the size of the future post-operative liver, before the resection. The most common one is the portal embolization, consisting in the partial occlusion of the portal vein. This leads to a reduction of the portal flow for the future resected liver and an increase of portal flow for the future remaining liver. The increased portal flow triggers the regeneration process, increasing the size of the future post-operative liver. However, portal embolization has also being associated with the stimulation of tumor growth [PLG+09, HvLV+13].

Major motivations for liver hemodynamics and function modeling. For liver surgery, the main problem is that for post-operative liver size considered "safe", some patients present a post-operative liver failure. And, on the contrary, absence of liver failure may occur with a small remaining liver size. Patients undergoing liver surgery have non-healthy livers, therefore their extra and intra liver hemodynamics is altered, e.g cirrhotic patients develop collateral circulation. The alteration of hepatic hemodynamics can explain the appearance of liver failure for liver sizes considered "safe" and the absence of post-operative liver failure for liver sizes considered "unsafe". Indeed, a drastic increase of portal flow per liver mass leads to intrahepatic pressure increase, and causes micro-architecture damages and hemorrhage. However, portal flow and pressure influence the regeneration. Therefore, strategies to control portal hemodynamics have been proposed after a major liver resection or a small graft transplantation, to prevent damages and keep the regeneration signal. Chemical modulation of portal hemodynamics has been proposed; the injection duration and the amount of product injected have been investigated [CPDG07, IHY+14]. These strategies have been successful in animal surgery. Clinical trials are needed to confirm their usefulness. Modulation of

portal flow has been studied with surgical deviation or reduction of the portal flow, such as portocaval shunt (adding a connection between portal vein and vena cava), ligation of the splenic artery or splenectomy (spleen resection) [AVOS13, GEN+06, PMPS07]. However, with these techniques, a precise modulation of the portal vein flow and pressure is difficult to obtain and some of them are permanent alterations.
Our surgeon collaborators (from the hospital Paul Brousse and the CHRU of Tours), have proposed to modulate the portal vein hemodynamics with an adjustable vascular ring. The vascular ring conception was performed by MID company in collaboration with the surgeons, resulting in the MID-AVR^{TM} device. This device enables a precise temporary modulation of the portal vein hemodynamics and can be percutaneously removed (more details about the device will be given in part I). 75% partial hepatectomy was performed on large pigs, with and without the vascular ring. The outcome of the surgery was improved when the portal vein hemodynamics was modulated (submitted paper, under review process). More investigations on the vascular ring efficacy are required to conclude. Moreover, a good understanding of the liver surgery impact on hemodynamics is necessary to enable a modulation of portal hemodynamics, preventing liver damages after a major liver resection (or a small graft transplantation). Testing various assumptions is simpler with mathematical modeling and numerical simulations than to perform many experiments. This motivates the development of mathematical modeling to improve knowledge on liver hemodynamics during liver surgery.

1.2 Mathematical modeling of liver perfusion and function

In literature, liver models exist for various scales, focusing on different topics and using various clinical data. Here, a brief review is proposed and more details can be found in the introduction of Charlotte Debbaut's thesis [Deb13].
The liver perfusion has been modeled with three-dimensional computational fluid dynamic (CFD) for a few main branches of liver vessel. The vascular geometry is idealized or based on imaging data (CT-scan, MRI, vascular cast). The boundary conditions are usually the inlet flow and the outlet flow split or pressure, and no-slip boundaries for the wall are assumed. In those studies, CFD simulations focus on the hemodynamics of few branches of portal vein [BVS+09], in case of hypertension, with thrombosis [PHNP03], for cirrhosis [LWC+15], or to study the wall shear stress in case of portal vein or bile duct ligation [VSTC+10]. Partial hepatectomy with one main portal vein branch removal is also simulated [HSBH12, HLT+10]. CFD has also been used to investigate the hemodynamics changes due to disease evolution and to find new parameters from MRI to evaluate disease progression [GEMG15].
3D simulation of the hepatic artery hemodynamics have been proposed to investigate microsphere transport and drug targeting [BKK+10, Bas10, KKBD10], comparing rigid and flexible walls [CK14].
More extensive vascular trees of the liver are modeled with reduced order models. Portal vein circulation, with and without shunt (porto-caval), has been simulated with one-dimensional model, based on CT images with pressure boundary conditions [HBH11]. In this work the collapsed status of veins is not taken into account. The hepatic circulation is included in a 1D-0D model of blood circulation in [MS15], with hepatic artery, portal vein and hepatic

veins one-dimensional model and electric analog, for the smaller vessels. The focus of this work is on wave dynamic, therefore the liver lobe structure is not modeled.
Liver hemodynamics is modeled with electric analog models, based on ordinary differential equations (also called lumped model or 0D models). The electric analog model can be based on imaging data (vascular cast [DMC+11, DDWC+12] or MRI [MKBW10]). Liver hemodynamics 0D model simulations have been performed to investigate hypothermic machine perfusion [DMS14, DMC+11, VDPtHV+04], to simulate partial hepatectomy and different surgery procedures (on rats) [DDWC+12], to study porto-caval shunt size impact on splanchnic circulation [RRS+87], or to model hepatic arterial buffer response with varying resistances [HSBH13].
Contrast fluid transport in liver tissue has been simulated and compared to CT-scans imaging. The blood flow in vascular trees has been modeled with Bernoulli equation and blood flow in tissue has been represented by Darcy model [LJJ+14]. 0D flow models are also used in multi-scales approach to transport a compound in the liver vascular trees. More precisely, the liver perfusion and function have been modeled with Physiologically Based PharmacoKinetic models (PBPK), for liver drug perfusion, coupled with a porous media model for liver tissue [SKN+14], investigating the liver heterogeneous pathophysiological changes [SSK+15], for better interpretation of clinical images, specially for hepatocellular carcinoma detection [MKBW10, KBWC07].
Liver lobule perfusion has been modeled with porous media and CFD simulation, for compound transport and metabolism [RWH+15], to investigate the impact of a vascular septum [DVS+14], or pressure variation [BLRS10], including cirrhosis [PDC+15]. The liver lobule regeneration has been modeled [HBB+10], as well as sinusoids remodeling [RDD10].

1.3 Contributions

As mentioned above, a strong link exists between liver hemodynamics, liver function and liver regeneration, that however remains to be fully explained. Mathematical modeling and numerical simulation may help to investigate liver surgery impact on hemodynamics, as well as this link between liver hemodynamics and function. In the literature, many models of the cardiovascular system exist, yet, none of them include a precise representation of the liver lobes and their vascular trees. Moreover, considering the data that will be available, the number of parameters in these models is too large. Some macro-scale models of liver hemodynamics exist but are not coupled with the whole body circulation, and none of them simulate dynamically liver partial ablation. In this work, we present a macro-scale model of liver hemodynamics (structured by lobes), coupled to the whole circulation, and in which liver surgeries are dynamically simulated.
The two main subjects addressed in this thesis are the followings:

1. The development of mathematical models to analyze the liver hemodynamics during liver surgery. In order to test the model, the simulation results are compared to hemodynamics measurements recorded during animals surgery.

2. The study of the transport and the processing of a compound, with mathematical models, to investigate the liver function. In order to compare data to numerical simulations, the intensity of a fluorescent dye, the indocyanine green, is measured during animals surgery.

This dissertation is organized in three parts. To build and validate the mathematical models, data is needed. The first part of this dissertation aims at describing the measurements, on which the mathematical models are based. After a short introduction, the surgery and the data acquisition procedures are described (section 2.1). Then, comments on measurements are made in section 2.2. Finally, section 2.3 concludes this part.
In the second part, the hemodynamics during liver surgery is studied with mathematical models. The part starts with an introduction (chapter 3). Then, chapter 4 proposes a closed-loop model of the entire blood circulation, based on ordinary differential equations. The hemodynamics changes observed during 75% liver resection are explained. Next, using the measurements, chapter 5 studies the hepatic artery model, based on ordinary differential equations. Then, chapter 6 presents a closed-loop model, based on partial differential equations, coupled with the models developed in chapters 4 and 5. With this model, the flow and pressure waveform changes observed during the liver surgery are captured. Chapter 7 ends this second part with some perspectives.
In the last part, the transport of a compound in blood is studied (chapter 9). For this model, the hemodynamics is described with the model presented in chapter 6. The hepatic artery and portal vein concentrations are qualitatively compared to the measurements of indocyanine green fluorescence. Next, the processing by the liver of a compound, the indocyanine green, is modeled in chapters 10, 11 and 12. Chapter 10 presents model output sensitivity to parameter and parameter estimation, with synthetic data and data from literature as observation. Chapter 11 proposes inverse problems for parameter estimation, with as observations the measurements recorded during the animals surgery described in part I. Finally, chapter 12 proposes to simplify the model developed in chapter 11 to match clinical requirements. Parameter estimation using indocyanine green measurements recorded during animal surgery are performed. Then, a feasibility study is performed on a few patient measurements after liver transplantation. The link between model parameters and liver function is investigated.

1.4 List of publications

First author papers.

- Chloe Audebert, Petru Bucur, Mohamed Bekheit, Eric Vibert, Irene Vignon-Clementel, and Jean-Frédéric Gerbeau. *Kinetic schemes for arterial and venous blood flow, and application to modeling of partial hepatectomy.* Computer Methods in Applied Mechanics and Engineering, 2017.

- Chloe Audebert, Mohamed Bekheit, Petru Bucur, Eric Vibert and Irene Vignon-Clementel. *Partial hepatectomy hemodynamics changes: experimental data explained by closed-loop lumped modeling.* Journal of Biomechanics, 2017.

Coauthor papers.

- Petru Bucur, Mohamed Bekheit, Chloe Audebert, Irene Vignon-Clementel and Eric Vibert. *Simplified technique for 75% and 90% hepatic resection with hemodynamic monitoring in a large white swine model.* Journal of Surgical Research, 2017.

- Petru Bucur, Mohamed Bekheit, Chloe Audebert, Amnah Othman, Seddik Hammad, Mylene Sebagh, Marc-Antoine Allard, Benoît Decante, Adrian Friebel, Dirk Drasdo, Elodie Miquelestorena-Standley, Jan G. Hengstler, Irene Vignon-Clementel and Eric Vibert. *Modulating portal hemodynamics with vascular ring allows efficient regeneration after partial hepatectomy in a porcine model.* Annals of Surgery (accepted).

Conference proceeding.

- Chloe Audebert, Petru Bucur, Eric Vibert, Jean-Frédéric Gerbeau, and Irene Vignon-Clementel. *Closed-loop cardiovascular system model and partial hepatectomy simulation.* In 4th International Conference on Computational and Mathematical Biomedical Engineering (CMBE2015), 2015.

Part I

Partial hepatectomy on pigs

Chapter 2

Liver resection on pigs: surgery and measurements

In this chapter the liver surgeries performed on pigs are described as well as the measurements recorded. The surgeries were performed by Petru Bucur (MD) and Mohamed Bekheit (MD) at the CIRE plateform, INRA Centre Val de Loire (Nouzilly, France). These surgeries are part of the project ANR iFLOW 13-TECS-0006. The readers with little interest in the experimental condition of these surgeries and in the details on the measurements can go directly to the conclusion of this chapter, where the required information for the next parts is summarized (section 2.3).

As mentioned in the introduction, the small-for-size syndrome and the post-operative liver failure are two conditions described in liver transplantation and in major hepatectomy (liver resection). These two types of liver failure are a consequence of a liver volume below a certain threshold. The liver metabolic, synthetic and detoxifying functions are then failing. The occurrence of liver failure depends on the liver hemodynamics, more especially on the portal vein hemodynamics [SBSC+11, AAB+13, AVOS13, VCZ14, XHW+16]. A modulation of portal vein hemodynamics is assumed to protect the liver cells and improve the regeneration process. To correctly modulate the portal vein hemodynamics during liver surgery, the impact of this surgery on the hemodynamics must be known. Our first goal is to investigate, with mathematical models, the impact of liver surgery on the hemodynamics. Data is required to build and validate the mathematical models. Therefore, liver resection is performed on pigs and various pressures and flows are recorded. The pig liver resembles to human in terms of anatomy and physiology [BDLB10, CWHM+03]. Moreover, its liver to body weight ratio is close to human's [Box80]. Our second goal is to study the liver perfusion and function using a dye exclusively eliminated by the liver into the bile, the indocyanine green [AKL+12, HdGN+13]. Indocyanine green is intravenously injected before or after liver resection, and its fluorescence is measured on the vessels, liver surface and common bile duct. With these measurements, mathematical models of the transport of a compound and its processing by the liver are set up.

Several groups studied liver resection and the associated hemodynamics on a porcine model. [XHW+16] have presented various sizes of liver resection on pigs. This work has concluded that the liver fails to regenerate, if the post-resection portal venous flow per liver mass is more than 5.6 times the pre-resection baseline. Liver regeneration can be disrupted by hemodynamics changes. Indeed, intraoperative ischemia, during 70% liver resection on pigs, has been shown to damage the sinusoidal endothelium and to cause post-operative liver failure [LXT+13]. In [IHY+14], a pharmacological approach has been proposed to control the post-resection liver hemodynamics on pigs. The pre-treatment with Oprinone has shown hepatoprotective effects, by modifying the portal vein pressure, for 70% liver resection in swine. The liver hemodynamics after liver resection may be controlled by a shunt linking the

mesenteric vein to the vena cava (using a vena cava graft from a pig donor). This technique has been studied in pigs in [PMPS07], showing that liver regeneration is preserved, despite a large reduction of liver venous inflow.

The presented surgeries, performed on pigs, consist in 75% and 90% liver resections, during which various pressures and flows are recorded. Moreover, indocyanine green intensities are measured in order to estimate the liver function. Temporary portal hemodynamics modulation, with an adjustable vascular ring (MID-AVR^{TM} developed by MID company [MID]), on 90% liver resection on pigs is also studied.
To our knowledge, no study has reported the continuous recording of the pressures and flows during liver resection, as well as ICG fluorescence of the liver larger vessels and tissue, and the common bile duct. These measurements lead to a better understanding of the liver hemodynamics and liver function during liver resection and regeneration.
This part is organized in the following manner. Chapter 2.1 presents the surgical and data acquisition protocols. The measurements are analyzed and discussed in chapter 2.2. Chapter 2.3 ends this first part with some conclusions.

Contents

2.1 Material and methods 20
2.1.1 Liver resection surgery 20
2.1.2 Data acquisition 23
2.2 Results 30
2.2.1 Hemodynamics measurements 30
2.2.2 Indocyanine green fluorescence 46
2.3 Conclusion 50

2.1 Material and methods

2.1.1 Liver resection surgery

Ethical approval This study was approved by the regional committee of ethics in animal research, by the ministry of higher education and scientific research and by the ministry of agriculture and fishing, according to European Union directives.

Protocols and studied population Two different percentages of liver resection are performed: 75% and 90%. For the 75% liver resection, two groups are considered. In the first group, the liver regeneration is studied during the seven post-operative days. In the second group (early sacrifice group), the early regeneration of the liver is studied, and pigs are sacrificed three days after surgery. For 90% liver resection, two groups are studied, a control group and a ring group, with the MID-AVR^{TM} vascular ring device.

Twenty-two pigs (all females except one) undergo 75% liver resection (34.5 $\pm$ 5 kg). In the 75% group, eight animals are in the early sacrificed group. The 90% liver resection group is composed of eight female pigs (37.1 $\pm$ 5 kg). The MID-AVR^{TM} vascular ring is placed on the portal vein of five animals.

For all animals, CT-scans are done before and after the surgery as well as on post-operative day one, three and seven (depending on the protocol). The CT-scan is performed with a Siemens Somatom AS definition 128 machine. Image acquisitions are done before, 15, 35, 55 and 75 seconds after injection of 75 ml of iohexol 350mg/ml (Omnipaque, GE Healthcare) with a rate of 5 ml per second. The liver volumes are estimated from the CT-scans. The pig liver anatomy with CT-scan has been presented in [BBWV17].

For all animals, during liver resection surgery (D0), pressures and flows are measured (as described in paragraph 2.1.1). Moreover, biopsy samples of the liver are taken before and after the liver resection. After the surgery, in all groups, the animal is kept in individual cage with daily care.

In the first group, the animals are kept until the seventh post operative day (D7). Then, a laparotomy is performed, a liver biopsy sample is taken and hemodynamics are measured before the animal is sacrificed. The regenerated liver and the spleen are weighted after sacrifice.

In the early sacrificed group, a laparotomy is performed the first post operative day (D1), to monitor the hemodynamics and take biopsy samples. Following the same protocol as in the first group, the animal is sacrificed on the third post-operative day (D3).

For 90% liver resection, in the ring group, a MID-AVR^{TM} vascular ring is positioned around the portal vein before liver resection. The ring is left around the portal vein for the first three post-operative days. In the control group, the same surgical protocol is followed, without the ring positioning. In practice, since all animals die before the fourth post-operative day, no sacrifice protocol is followed.

In both 75% and 90% partial hepatectomies, some animals receive an intravenous indocyanine green (ICG) injection. Indocyanine green is a dye exclusively eliminated by the liver [AKL$^+$12, HdGN$^+$13], thus it is used to assess liver function. The animals receive 1ml

of 0.1mg/ml ICG solution followed by 10ml of 5% glucose solution. The injection is done before or after liver resection and on post operative day one, three and seven (depending on the protocol). Paragraph 2.1.2 details the indocyanine green fluorescence measurements acquisition procedure.

Liver resection surgery Before the surgery each animal received anesthesia induction (2 ml Xylazine 2%, with 15 ml ketamine (Ketamin Panpharma 250mg/5ml)). A tracheal tube is then placed and secured, and the inhalational anesthesia is started (60% FiO2 inhalational oxygen mixed with 2% isoflurane (Isoflurane, Belamont, Centre des Spécialités Pharmaceutiques, France) at a rate of 2-3 ml mixed with 1.5-2 l/min oxygen in 1.5l of air). The surgery is conducted under sterile condition. During the surgery, the animals are covered with a heating blanket and oxygen saturation, as well as temperature is monitored.

The first stage of the surgery is a cervicotomy performed to reach the right internal jugular vein and the carotid artery, in order to measure central venous and systemic arterial pressures respectively. The pressure catheters are introduced in the jugular vein and in the carotid artery using respectively 8 Fr and 5 Fr vascular Desivalve (Vygon) cannula.

Then the laparotomy is performed. First, the aorta above the celiac trunk (Figure 2.1) is dissected to place a flow probe. Second, the dissection of the aorta between the mesenteric artery and the kidney arteries (Figure 2.1) is performed to position another flow probe. For some animals the aorta flows are not measured to shorten the surgical procedure.

When the two aorta flow probes are in place, the gastroduodenal artery is ligatured (Figure 2.1). The hepatic artery pressure catheter is introduced through the gastroduodenal artery in order to set the pressure catheter in the middle of the hepatic artery and obtain a precise pressure measurement. The hepatic artery and the portal vein are then dissected to place the flow probes. Finally, the portal vein pressure catheter is inserted in the vein. Figure 2.2 shows the hepatic artery and the portal vein with the pressure catheters and the flow probes set.

For the ring group, a MID-AVR^{TM} vascular ring is placed around the portal vein. The ring diameter is controlled by a regulated valve at the extremity of a long tube. Once around the portal vein, the two lips of the opened ring are sutured. The suture breaks when the ring is inflated such that it can easily be removed percutaneously on the third post-operative day (Figure 2.3). The MID-AVR^{TM} vascular ring diameter is reduced in order to aim for, after liver resection, a portal flow per liver mass between 2.5 and 4 times the initial measured value. Assuming the ratio of remaining liver mass over the initial liver mass is 0.1 (corresponding to 90% liver resection), the target portal flow is between 0.25 and 0.4 times the pre-resection measured flow. A moderate increase of the portal flow per liver mass is needed to trigger the regeneration process without damaging the liver tissue [AEV12, IYT^{+}07].

The pig liver is composed of three main lobes: left lobe, median lobe (subdivided in left and right medial lobes) and right lobe (composed of right lateral and caudate lobes) [CWHM^{+}03]. To reach 75% liver resection the left and median lobes are resected. Figure 2.5 displays the entire liver before the resection (left). The removed and remaining liver parts after 75% liver resection are shown in Figure 2.5 (right). The 90% liver resection is performed in two steps: first, the median and left lobes are removed, following the same surgical protocol than for the 75% liver resection. Then, the right lateral lobe is removed, leaving the caudate

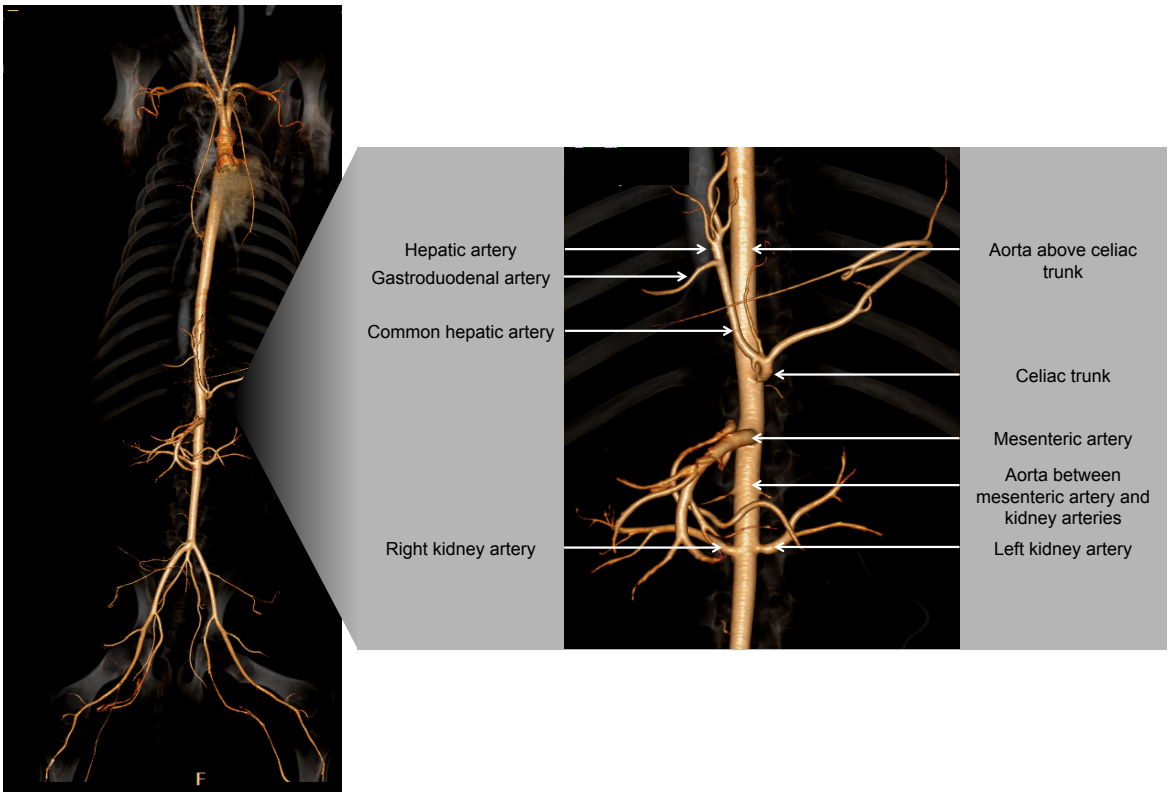

Figure 2.1: Reconstruction from arterial time CT-scan. The zoom on celiac and splanchnic circulations displays the vessels where flow or pressure are measured.

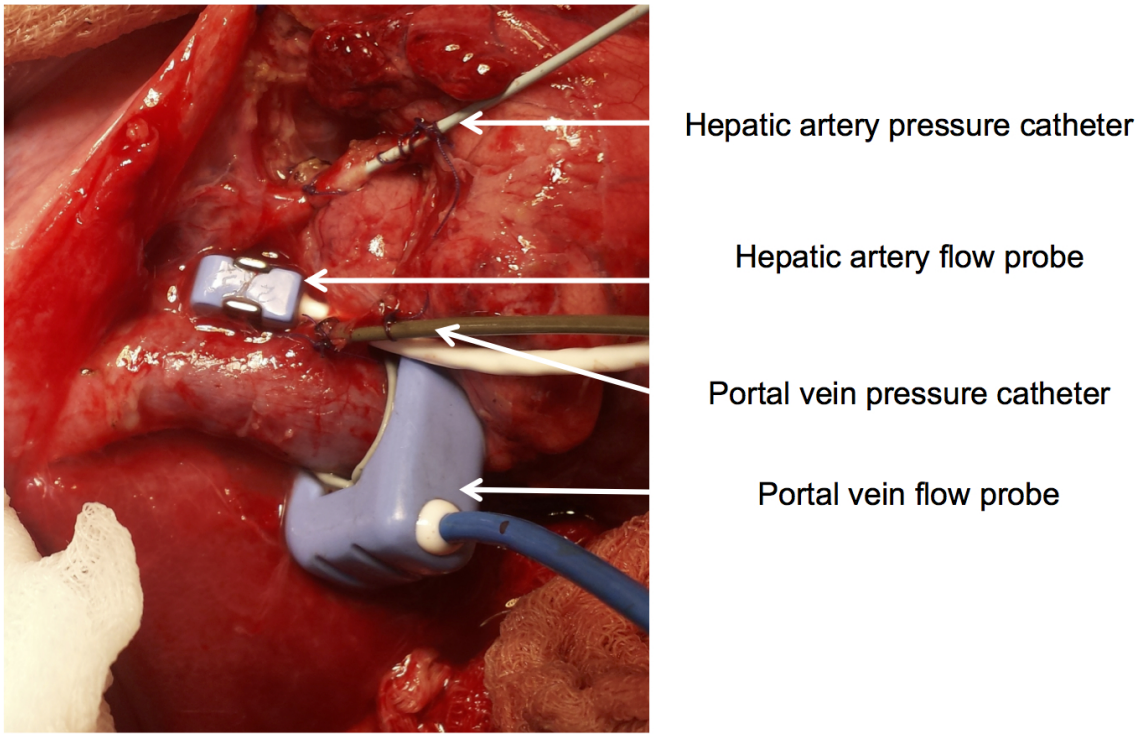

Figure 2.2: Hepatic artery and portal vein pressure catheters and flow probes placed.

lobe.

To perform the liver resection, the removed liver lobes are circled with a tape (a thin fabric strip). Then, the tape is pulled (clamping) to block the inflow of the corresponding liver tissue (Figure 2.4). Finally, the liver lobes are resected and sutures are done before removing the tape (declamping). Blood loss during the resection is reduced with this procedure.

After the resection, the removed liver parts are weighted. In the ring group, the ring diameter is adjusted if necessary according to the measured portal vein flow. Then, all the flow probes and pressure catheters are removed and the animal abdomen is sutured. The surgical technique has been detailed in [BBA+16].

2.1.2 Data acquisition

Hemodynamics measurements Millar Instruments pressure catheters are inserted to measure the pressures. 5Fr catheters are chosen for the central venous and the portal vein pressure measurements, while 4Fr and 3.5Fr are used for the carotid artery and the hepatic artery pressure measurements respectively. The four Millar Instruments catheters are connected to two Millar Instruments pressure control units PCU-2000 with two channels. A Transonic flowmeter (three channel perivascular flowmeter T403-PPP) measures the flow rates. The probe diameters used are: 10mm or 12mm for portal vein, 4mm or 6mm for hepatic artery, 10mm or 12mm for the aorta above the celiac trunk and 8mm for the aorta between the mesenteric artery and kidney arteries. The probe size is chosen according to the blood vessel diameter for each animal. Flows and pressures are recorded continuously during the surgery

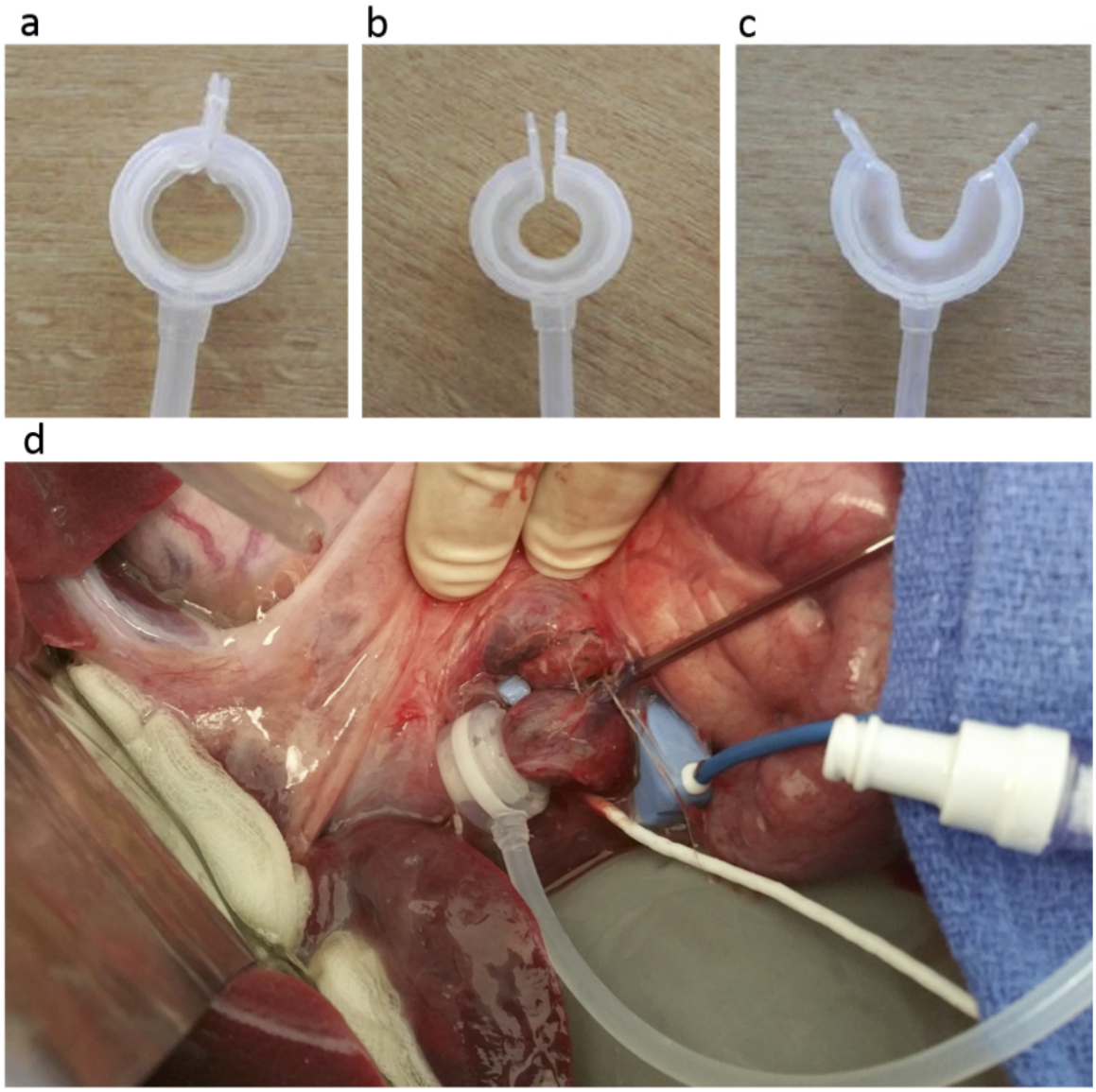

Figure 2.3: The MID-AVR^{TM} vascular ring for portal vein hemodynamic modulation. The ring is shown in different shapes according to the degree of inflation: (a) the balloon is completely deflated and the ring is closed; (b) the balloon is inflated with a small amount of saline solution and the ring is closed with a reduced diameter; (c) the balloon is inflated with a large amount of saline solution and the ring is opened; (d) the MID-AVR^{TM} ring is placed around the portal vein, it is inflated with a small amount of saline and moderate constriction of the portal vein is shown.

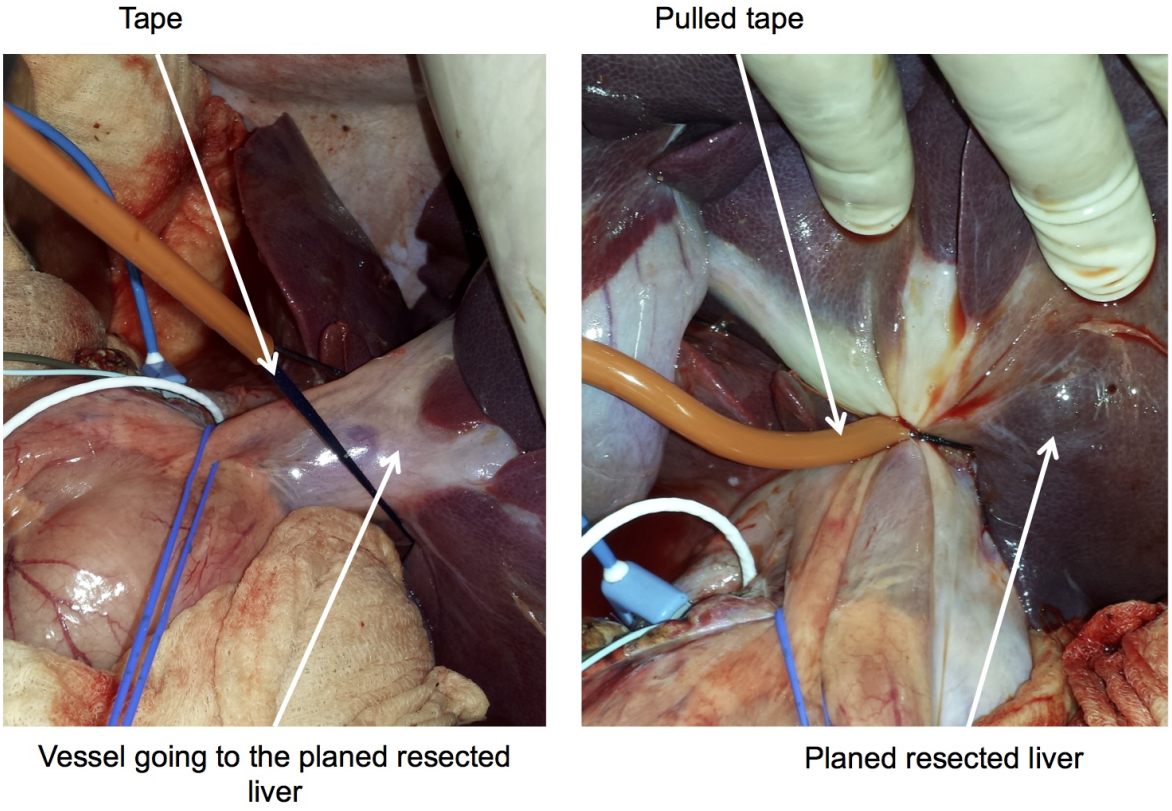

Figure 2.4: Clamping procedure. A tape is placed around the planed liver resected part (left) and then it is pulled (right) to block the blood and reduce blood losses during resection.

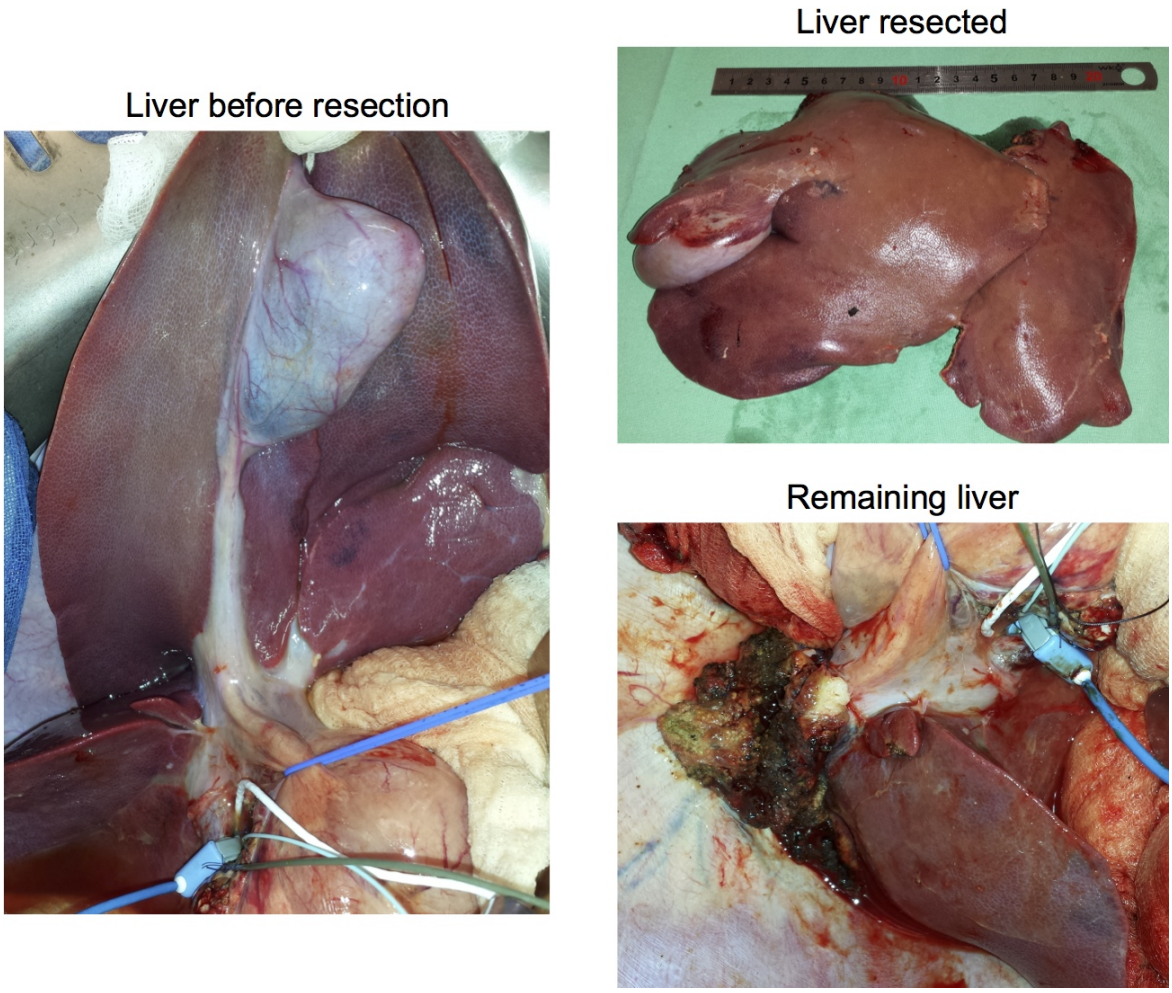

Figure 2.5: Pig liver before liver resection (left), the left and median resected liver lobes (top right) and the remaining right lobe after 75% liver resection (bottom right).

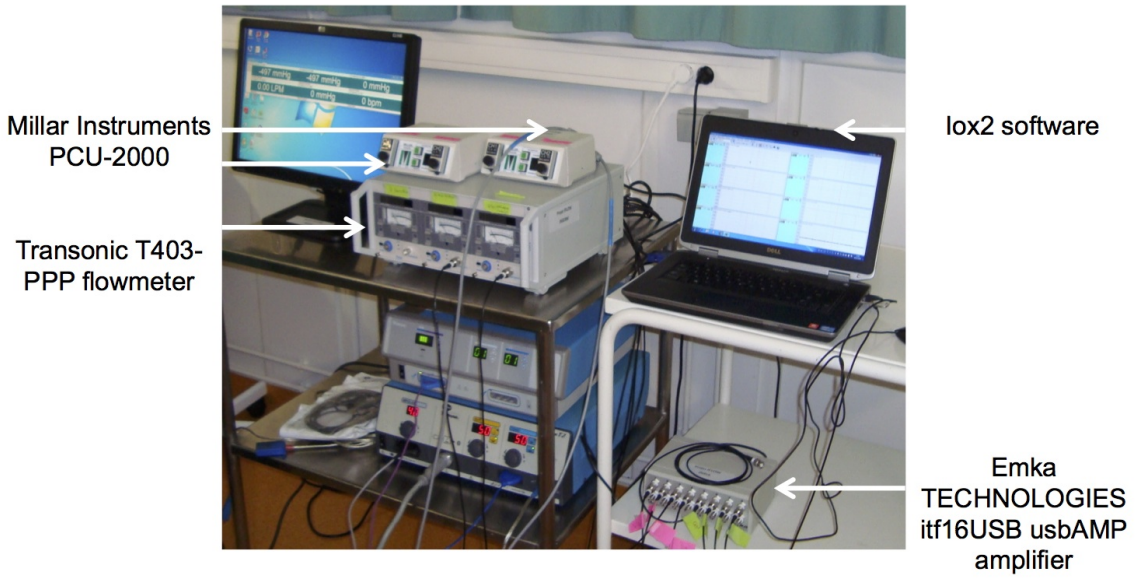

Figure 2.6: Recording installation for pressures, Millar Instruments PCU-2000 and for flows, Transonic T403-PPP flowmeter. emka TECHNOLOGIES itf16USB usbAMP amplifier and the computer with iox2 software.

with the Emka TECHNOLOGIES itf16USB usbAMP amplifier linked to a computer running the iox2 acquisition software (Figure 2.6). To have reliable pressure and flow measurements, a calibration in iox2 software is needed. The calibration consists in the comparison of the values measured by the device under test with a calibration standard. The calibration is performed at the beginning of each surgery, before the incision time. The flow calibrations are done with two points using electronic settings on the Transonic flowmeter T403-PPP. The pressure catheters are maintained in a saline solution for 5 minutes before calibration. The two point calibration procedure is done using the electronic calibration settings of the PCU-200 or with a manual inflation system controlled with a high precision digital manometer (Lex 1 manometer from KELLER AG).

Indocyanine green fluorescence measurements The principle of fluorescence imaging is to illuminate the region of interest with a light, at the excitation wavelength of the fluophores. Under excitement, the fluophores radiate a fluorescence signal (at emission wavelength). A fluorescence imaging device is used to capture the signal and to obtain an image with different intensity zones. The fluorescence imaging device used here is Fluobeam®, developed by the Fluoptics company [Flu]. The intensity of the signal received depends directly on the intensity of the source light but also on the distance to the tissues and the light in the room. The experimental conditions are as similar as possible between all animals: the lights are turned off and curtains are closed. A reference element, with stable intensity in time, is added inside the observation field to suppress by post-processing the dependency of measurements to the experimental conditions (Figure 2.7). The reference element is placed at the same distance to the camera than the regions of interest. The intensities measured are normalized by the

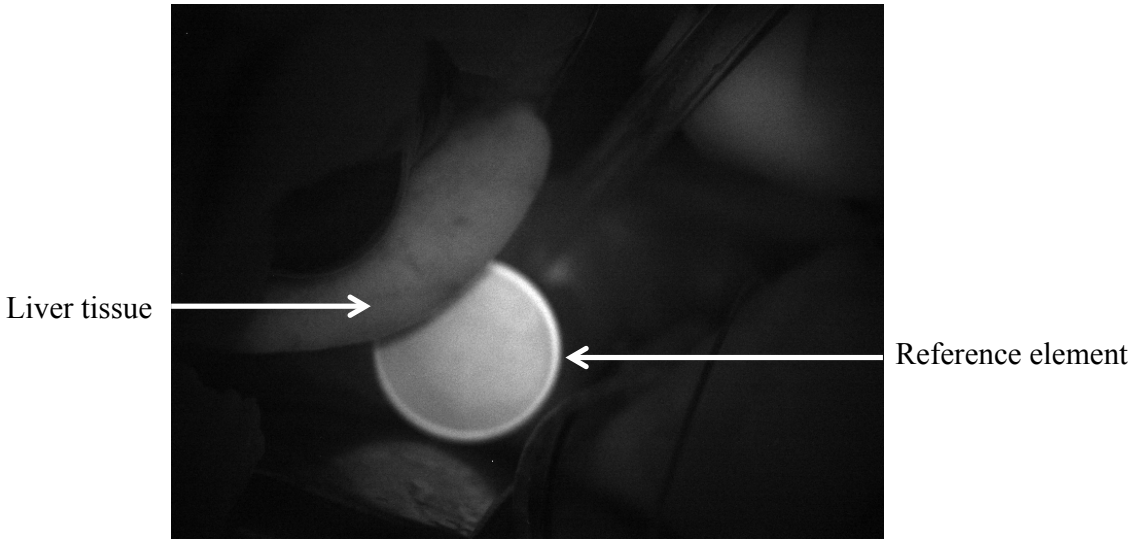

Figure 2.7: Fluorescence element of reference to normalize the measured intensities, in order to compare the measurements for different animals and different days.

measured intensity of this reference element. For each day and each animal the measured intensity is normalized by the same element of reference.

Fluorescence is measured in four regions of interest: liver tissue, hepatic artery, portal vein and common bile duct. The camera is placed such that all the regions of interest can be observed at the same time (Figure 2.8). The camera is fixed around 20 cm from the tissue surface, and when recording, the surgery is paused to avoid major perturbations on the signal.

Intensities are recorded for two minutes, with a frame approximately every 0.1 second, just after ICG injection. Then, with a 2 minute frequency, the intensity is recorded for 30 seconds, for a total recording of 20 to 50 minutes.
For each frame the average light intensity of the region of interest over time is assessed. The regions of interest are moving due to the animal breathing. An in-house algorithm is developed by Fluoptics to follow the same region of interest in all images. Curves of the intensity over time in each region of interest are thus obtained.

Database for the measurements storage In order to store, access and analyze the collected data, a relational database is implemented, with its web interface (written in php). The database is accessible via any web browser from any location (secured with log-in and password). An existing secure system for patients (from Hopital Paul Brousse, France) is re-used and adapted (https://hpbchir.u707.jussieu.fr/ehpbchir). Each animal has a form that gathers: the protocol notes, the hemodynamics measurements, the ICG curves over time and the blood sample analysis results (Figure 2.9). The volumes estimation from CT-scan as well as the vessel diameter are also stored in the database. SQL requests are available to select and analyze the collected data for all animals. Figure 2.10 shows the result of the request for pre-operative liver volume estimation and pre and post liver resection portal flows.

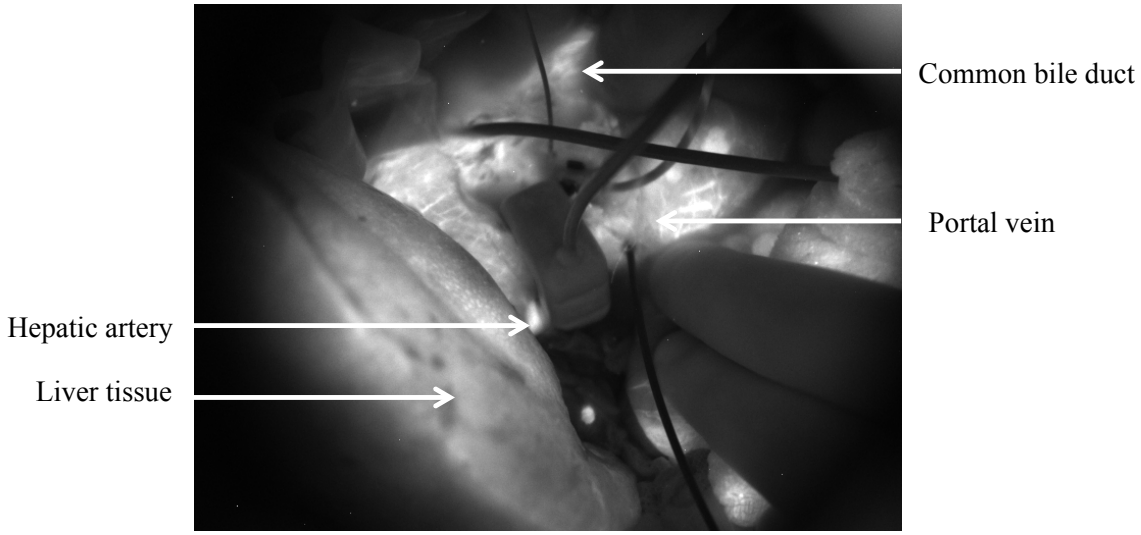

Figure 2.8: Domain of observation for fluorescence measurements, the four regions of interest are present, the liver tissue, the hepatic artery, the portal vein and the common bile duct.

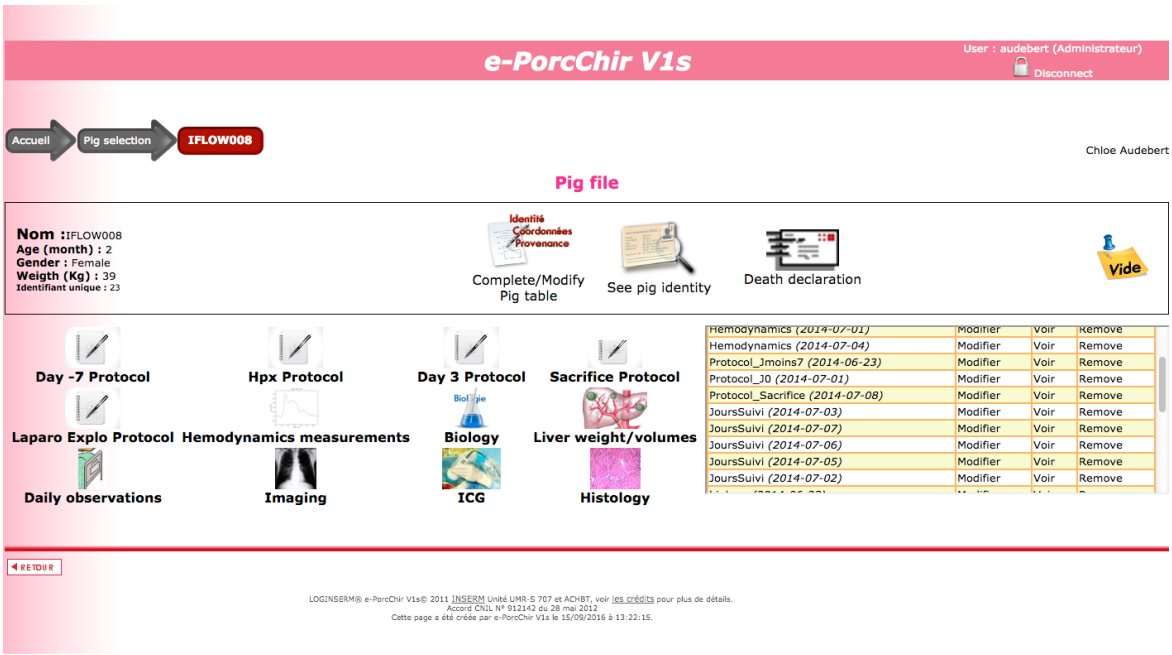

Figure 2.9: Database website screen-shot. A typical animal form for data storage and analysis.

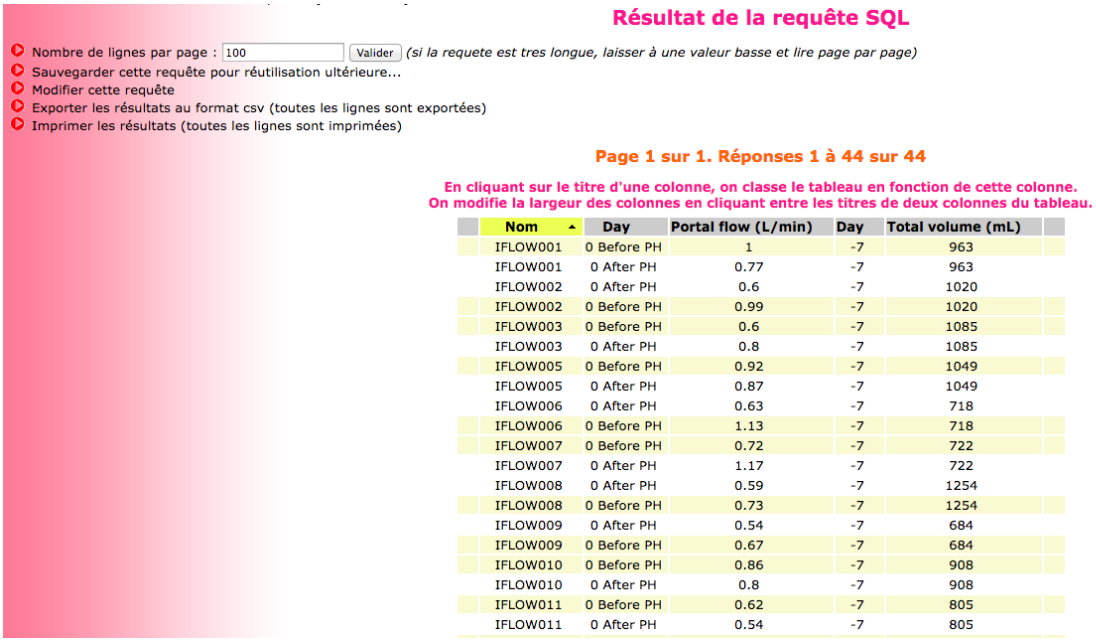

Résultat de la requête SQL

Nombre de lignes par page : 100 Valider *(si la requete est tres longue, laisser à une valeur basse et lire page par page)*
Sauvegarder cette requête pour réutilisation ultérieure...
Modifier cette requête
Exporter les résultats au format csv (toutes les lignes sont exportées)
Imprimer les résultats (toutes les lignes sont imprimées)

Page 1 sur 1. Réponses 1 à 44 sur 44

En cliquant sur le titre d'une colonne, on classe le tableau en fonction de cette colonne.
On modifie la largeur des colonnes en cliquant entre les titres de deux colonnes du tableau.

Nom	Day	Portal flow (L/min)	Day	Total volume (mL)
IFLOW001	0 Before PH	1	-7	963
IFLOW001	0 After PH	0.77	-7	963
IFLOW002	0 After PH	0.6	-7	1020
IFLOW002	0 Before PH	0.99	-7	1020
IFLOW003	0 Before PH	0.6	-7	1085
IFLOW003	0 After PH	0.8	-7	1085
IFLOW005	0 Before PH	0.92	-7	1049
IFLOW005	0 After PH	0.87	-7	1049
IFLOW006	0 After PH	0.63	-7	718
IFLOW006	0 Before PH	1.13	-7	718
IFLOW007	0 Before PH	0.72	-7	722
IFLOW007	0 After PH	1.17	-7	722
IFLOW008	0 After PH	0.59	-7	1254
IFLOW008	0 Before PH	0.73	-7	1254
IFLOW009	0 After PH	0.54	-7	684
IFLOW009	0 Before PH	0.67	-7	684
IFLOW010	0 Before PH	0.86	-7	908
IFLOW010	0 After PH	0.8	-7	908
IFLOW011	0 Before PH	0.62	-7	805
IFLOW011	0 After PH	0.54	-7	805

Figure 2.10: Database website screen-shot of an example of SQL request (for portal vein flow before and after liver resection and the pre-resection estimated liver volume).

2.2 Results

The reference values of blood analysis as well as oxygen consumption by the liver for pig has been presented in [BBV+16].

2.2.1 Hemodynamics measurements

2.2.1.1 Hemodynamics during liver resection

Evolution in average. Two key moments of the surgery are analyzed: the beginning of the surgery before liver resection and the end of the surgery after liver resection. During these moments, 20 seconds of stable signal (without surgeon interventions) are used to compute averaged pressure and flow values. The location in the blood circulation of each measurement is recalled in figure 2.11.

Figure 2.12 summarizes the central venous pressure measurements (Figure 2.11). The central venous pressure tends to decrease during liver resection surgeries. After 75% liver resection, a decrease of 58% at the end of the liver resection surgery is observed, in comparison with the pre-resection measurement. After 90% resection without MID-AVR^{TM} ring, the central venous pressure decreases by 6%. In the ring group, after liver resection, the measured central venous pressure becomes negative. Different experimental events could explain the negative pressure measurements: at certain time instant of the respiration cycle the pressure becomes negative, leading to a negative pressure in average, an error during the pressure catheter calibration occurred or the catheter used is deficient. However the evolution of central venous pressure is studied, a decrease of around 2 mmHg is measured after 90% liver resection

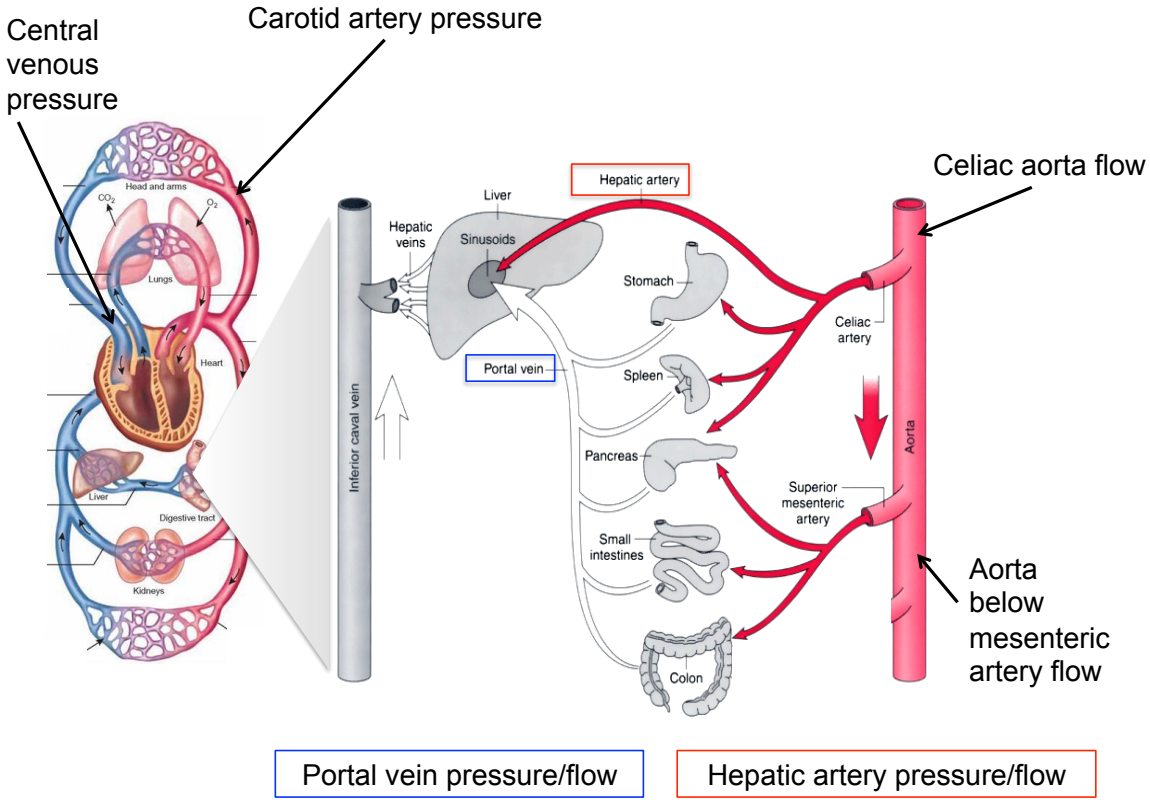

Figure 2.11: Schematic representation of the blood circulation, with a zoom on splanchnic circulation. The vessels where the hemodynamics measurements are recorded are recalled. Images modified from [Spl] and [Sys].

with MID-AVR^{TM} ring. The decrease of the venous pressure is linked to the blood losses occurring during the surgery. The blood losses are a consequence of bleeding, but also of the removal of liver tissues (filled with blood). The anesthesiologists compensate the blood losses with infusion of normal saline and 5% glucose solutions. The infusion tends to increase pressures. During the 90% liver resection, the infusion is greater because the blood losses are usually larger. The smaller decrease of the central venous pressure, after 90% liver resection surgery, can thus be explained.
The carotid pressure also decreases during the surgeries, Figure 2.13 sums up the measurements (Figure 2.11). 14%, 15% and 19% decreases are measured compared with pre-resection values, for resection of 75%, 90% and 90% with MID-AVR^{TM} ring, respectively. The reduction of arterial pressure is also linked to the blood losses and it is balanced with the infusion performed by the anesthesiologists.
The two flow rates measured in the aorta (Figure 2.11) are also impacted by the liver resection surgeries (Figures 2.14 and 2.15). The aorta flow above the celiac trunk decreases by 13% after 75% liver resection. A 16% and 23% decrease in celiac aorta flow is measured after 90% liver resection without and with the MID-AVR^{TM} ring respectively.
The aortic flow between mesenteric artery and kidney arteries increases after liver resection (3% after 75% liver resection and 13% after 90% liver resection without MID-AVR^{TM} ring). After liver resection, the arterial tree resistance of the liver is increased leading to a lower arterial flow. Moreover the celiac aorta flow and the portal vein flow are also decreased after liver resection. The aorta flow split is reorganized and the flow below the mesenteric artery is increased.

Locally, the hepatic hemodynamics is impacted by liver resection (Figure 2.11). The hepatic artery pressure is reduced by 12% after the 75% liver resection (Figure 2.16). After 90% resection, the pressure decreases by 26% and 17% without and with MID-AVR^{TM} ring respectively (Figure 2.16). The decrease of pressure is mainly due to the blood losses occurring during surgery, similarly to the pressure measured in the carotid artery.
The hepatic artery flow rate decreases drastically after liver resection. After 75% liver resection, a decrease of 72% is measured (Figure 2.17). The flow is reduced by 71% and 73% respectively after 90% liver resection without and with MID-AVR^{TM} ring (Figure 2.17). Just after the 75% liver resection clamping the hepatic artery flow is reduced by 74%. The flow decrease corresponds to the liver mass reduction. After the 90% liver resection without ring, a flow reduction of 78% is measured in the hepatic artery just after the clamping. The hepatic artery flow seems to decrease up to a certain value, even if the percentage of liver resection is larger. Then, due to the infusion, the flow increases at the end of the liver resection surgery.
For the venous side of the hepatic circulation, the portal vein flow tends to decrease after liver resection and the decrease seems strongly linked to the decrease of celiac aorta flow. Indeed, the portal vein flow (similarly to the celiac aorta flow) drops by 11% after the 75% liver resection. After 90% liver resection, the portal flow reduction is more significant, a decrease of 29% is measured. The decrease is greater than the one measured in celiac aorta. After the 90% liver resection with MID-AVR^{TM} ring, a decrease of 30% is measured for the portal vein flow. The change of portal flow with respect to the pre-resection value is similar with and without MID-AVR^{TM} ring, after 90% liver resection.
Finally, due to the liver resection, the portal pressure increases. After 75% resection, it is

increased by 9% at the end of the surgery. The portal vein pressure increases even more after 90% liver resection: a 93% increase is measured at the end of surgery without MID-AVR^{TM} ring (Figure 2.18). With MID-AVR^{TM} ring, only a 54% increase of portal vein pressure is measured. Therefore, with MID-AVR^{TM} ring the portal pressure does not increase too largely. Due to liver resection, the portal pressure increases and the central venous pressure decreases, leading to the drastic increase of venous pressure difference across the liver (Figure 2.20). In average and with respect to pre-resection value, the venous pressure difference increases by 41%, 241% and 155% at the end of liver resection of 75%, 90% without and with MID-AVR^{TM} ring respectively.
In comparison with the control group, with MID-AVR^{TM} ring, the liver cells experience smaller changes of portal vein pressure. Moreover, the venous pressure difference across the liver is reduced, for the liver resection with MID-AVR^{TM} ring.

Dynamics changes. The hemodynamics variations over the cardiac and respiratory cycles are evaluated with the continuous recording of pressures and flows. Moreover, the dynamics of pressures and flows during the clamping is assessed. All the curves presented in this section are for the same animal (curves with same features are measured in all animals). The surgery performed on this subject is a 90% liver resection, without MID-AVR^{TM} ring. First, 20 seconds of a stable signal are presented before the liver resection (Figure 2.21). As explained in section 2.1.1, the 90% liver resection is done in two steps. Figure 2.22 presents the clamping for the 75% resection. Figure 2.23 shows the 75% to 90% clamping.

Influence of respiration and heart beat on hemodynamics. Figure 2.21 presents the pressures and flows over time before the liver resection. The mechanical ventilation has a small impact on arterial pressures and flows, unlike the heart rate. To estimate the variation due to mechanical ventilation, for the arteries, the variation around the average at peak systole is computed for several animals. Similarly, for several animals, the variation due to heart beat is estimated computing the variation around the mean during two cardiac cycles ((mean-min)/mean and (max-mean)/mean). The mean values are reported in the next paragraph.
The variations around the average of pressures and flows, at peak systole, due to mechanical respiration are for hepatic artery flow: -7% and +9%, for the celiac aorta flow: -5% / +7% and for aorta between mesenteric artery and kidney arteries: -7% / +6% (average over several animals). Similarly, the sensitivity of the arterial pressures to ventilation is small, for carotid artery pressure: -4% / +5% and for the hepatic artery pressure: -5% / +6%. Over the several pressure measurements, a more significant impact of ventilation on arterial pressure, has been observed when the pressures are low. On the other hand, the variation around the averaged, due to the heart beat, is larger (in comparison with the impact of mechanical ventilation), for the carotid artery pressure: -23% / +29% and for hepatic artery pressure: -22% / +24%.
Aorta flow rate waveforms, in the celiac aorta and between mesenteric artery and kidney arteries are similar. The variation of the flow rates around the average during a cardiac cycle is for the celiac aorta: -74% / +133% and for the aorta beyond mesenteric artery: -94% / +197%.

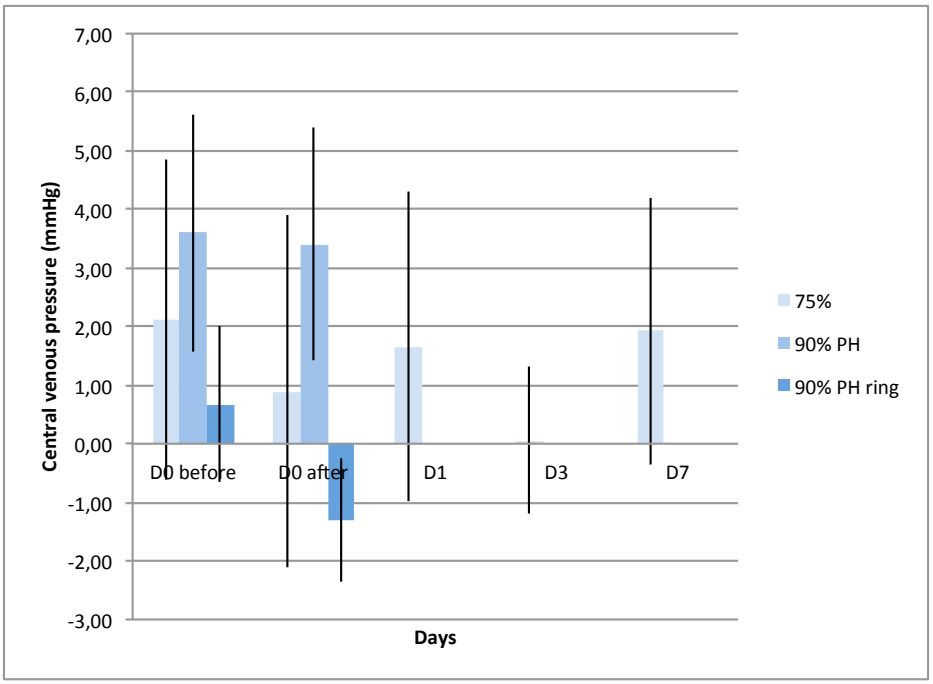

Figure 2.12: Central venous pressure average and standard deviation for the different surgeries (75% liver resection, 90% liver resection without and with MID-AVR^{TM} ring) histogram, before and after liver resection and at various post-operative days.

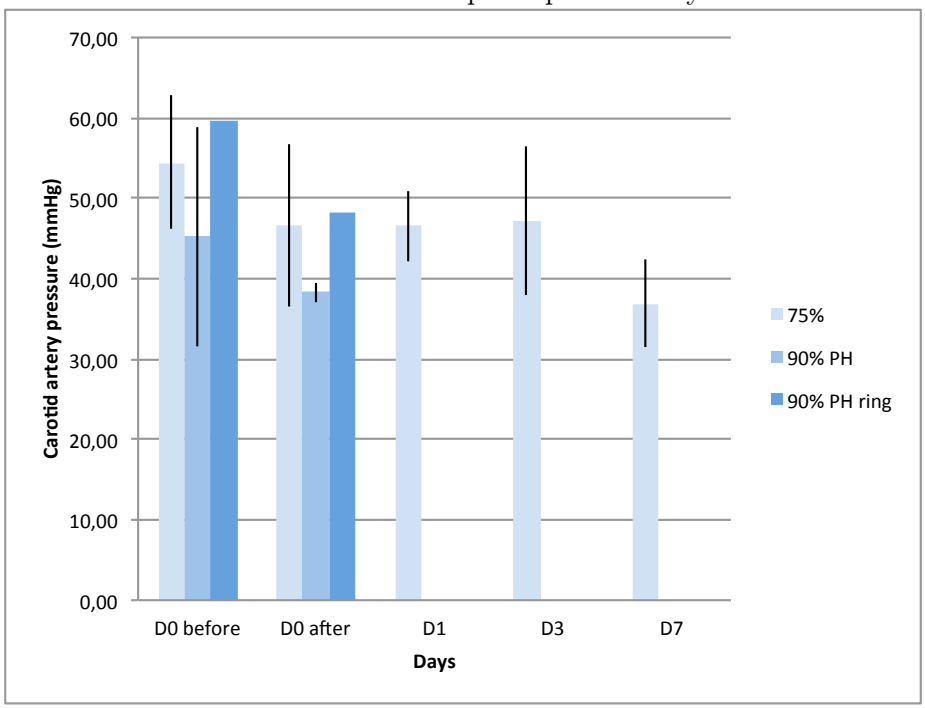

Figure 2.13: Carotid artery pressure average and standard deviation for the different surgeries (75% liver resection, 90% liver resection without and with MID-AVR^{TM} ring) histogram, before and after liver resection and at various post-operative days.

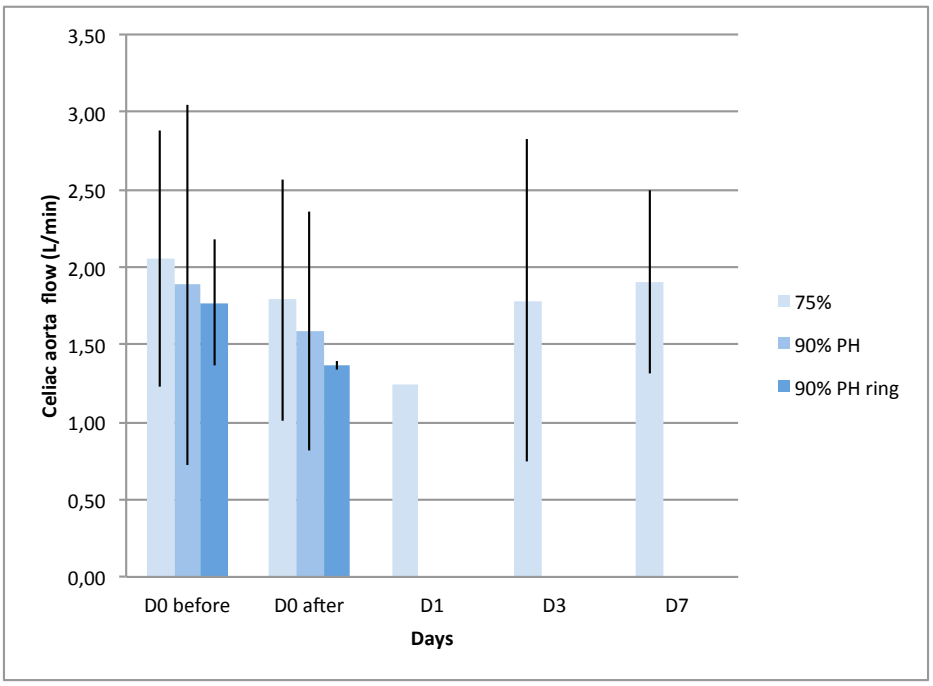

Figure 2.14: Celiac aorta flow average and standard deviation for the different surgeries (75% liver resection, 90% liver resection without and with MID-AVR^{TM} ring) histogram, before and after liver resection and at various post-operative days.

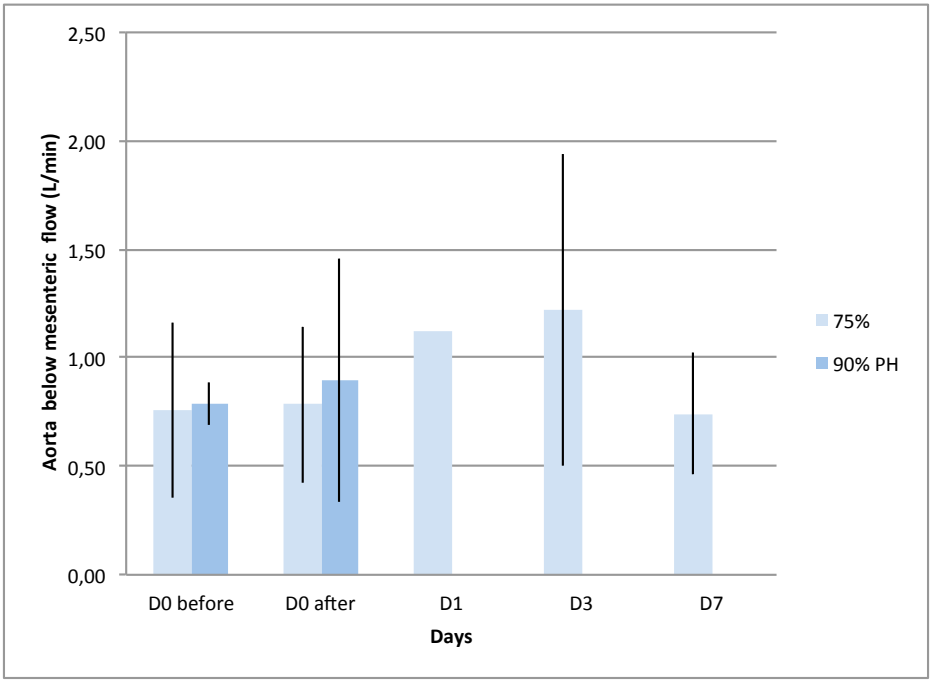

Figure 2.15: Aorta flow below mesenteric artery average and standard deviation for the different surgeries (75% liver resection, 90% liver resection without and with MID-AVR^{TM} ring) histogram, before and after liver resection and at various post-operative days.

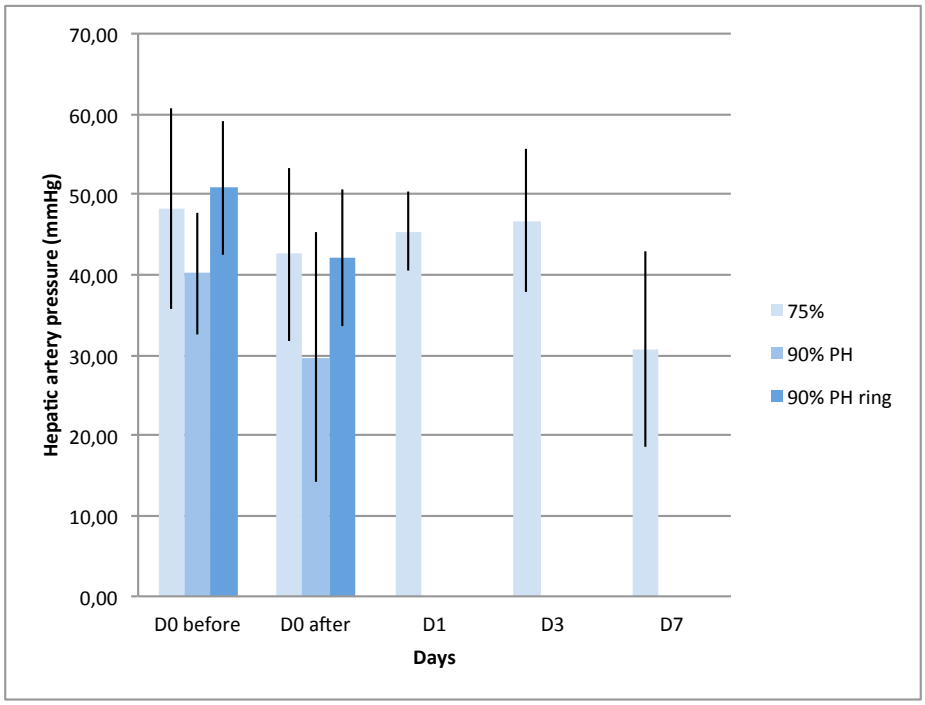

Figure 2.16: Hepatic artery pressure average and standard deviation for the different surgeries (75% liver resection, 90% liver resection without and with MID-AVR^{TM} ring) histogram, before and after liver resection and at various post-operative days.

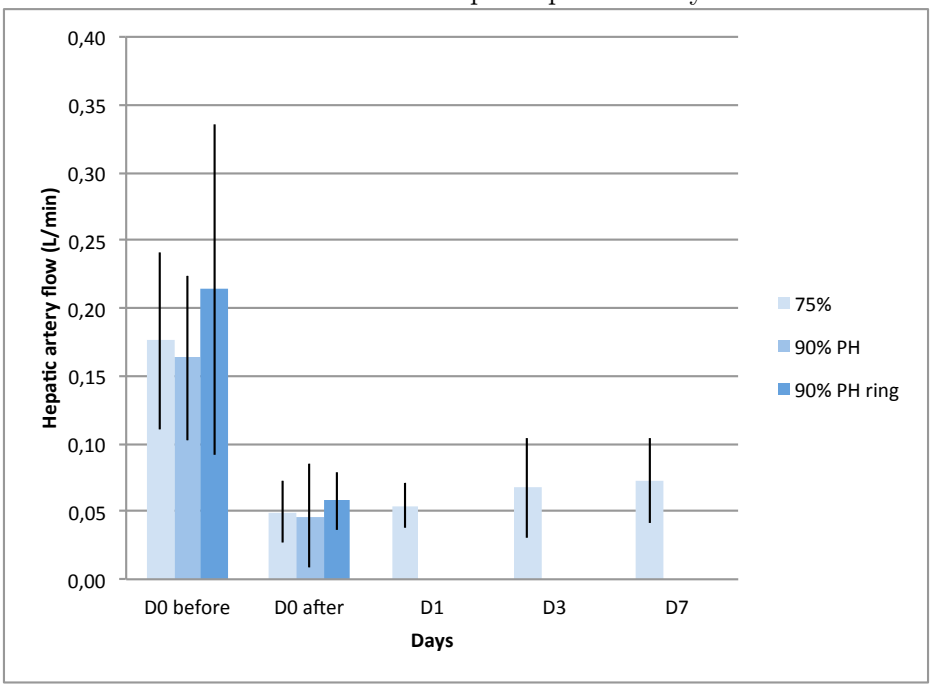

Figure 2.17: Hepatic artery flow average and standard deviation for the different surgeries (75% liver resection, 90% liver resection without and with MID-AVR^{TM} ring) histogram, before and after liver resection and at various post-operative days.

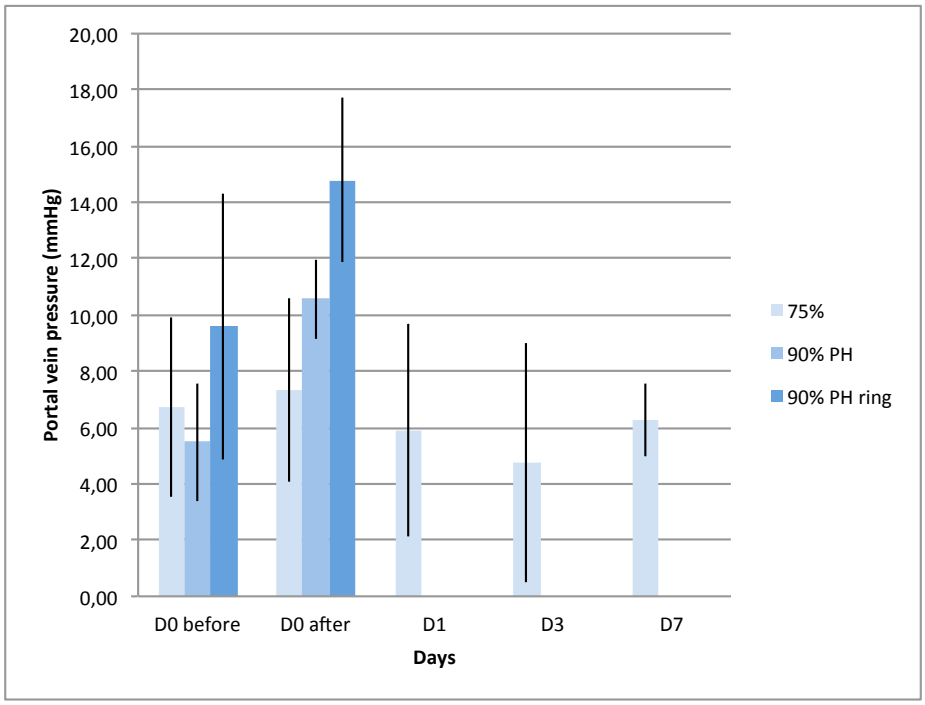

Figure 2.18: Portal vein pressure average and standard deviation for the different surgeries (75% liver resection, 90% liver resection without and with MID-AVR^{TM} ring) histogram, before and after liver resection and at various post-operative days.

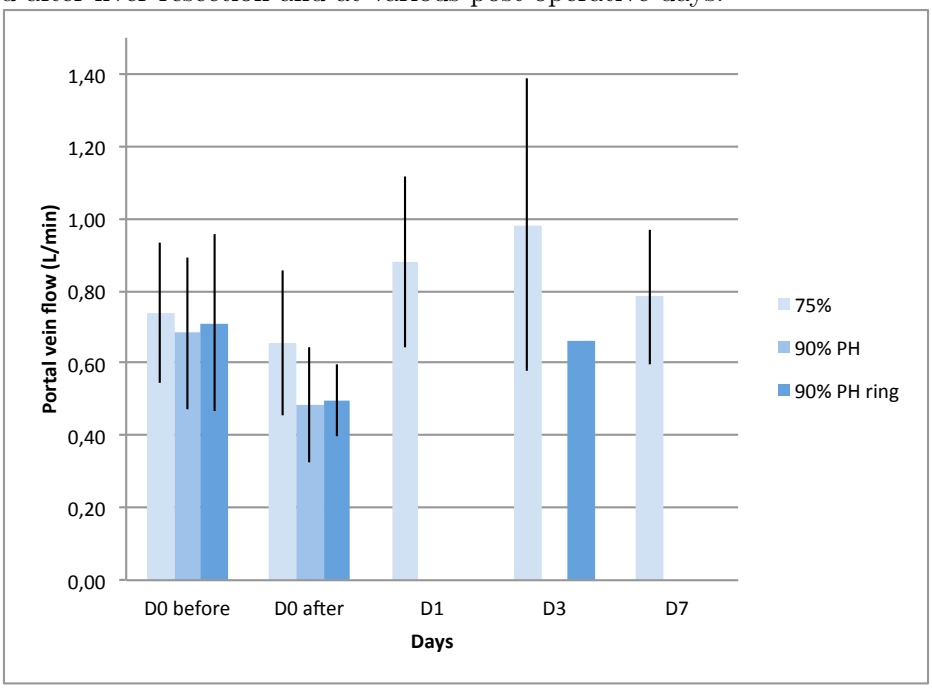

Figure 2.19: Portal vein flow average and standard deviation for the different surgeries (75% liver resection, 90% liver resection without and with MID-AVR^{TM} ring) histogram, before and after liver resection and at various post-operative days.

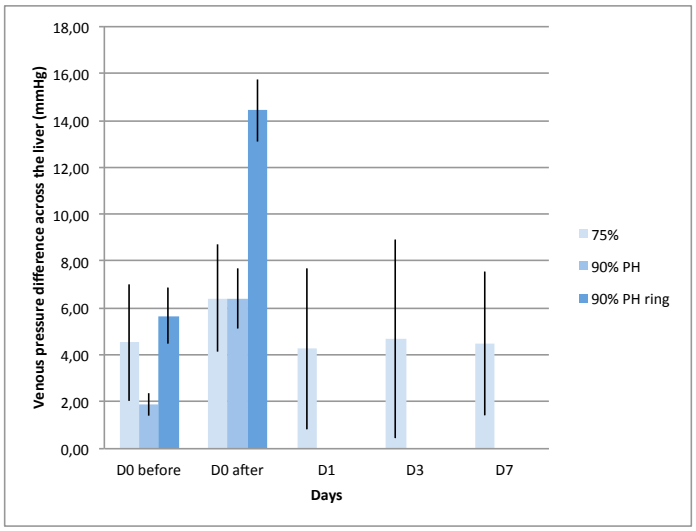

Figure 2.20: Venous pressure difference across the liver average and standard deviation for the different surgeries (75% liver resection, 90% liver resection without and with MID-AVR^{TM} ring) histogram, before and after liver resection and at various post-operative days.

The central venous pressure is sensitive to the ventilation, as well as to the heart beat. When the animal is under mechanical ventilation, the central venous pressure is maximal at the end of inspiration and minimal at the end of expiration. The variations around the average value (during 20s) due to respiration are -74% / + 117%.
The same observations are made for portal vein pressure. The heart beat impact on the portal vein pressure is smaller than on central venous pressure, probably due to the distance to the heart. The portal pressure is maximal at the end of inspiration and minimal at the end of expiration. The variations around the average value are: an increase of 26% and a decrease of 20%.
The mechanical ventilation also largely impacts the portal vein flow. Opposite to pressures, the portal flow is maximal at the end of the expiration cycle, and minimal at the end of the inspiration (for a mechanical ventilation). In comparison with the averaged value, the portal flow increases by 33% and decreases by 45% during the respiration cycle (in average over several animals). For the animal presented in Figure 2.21, the maximal variation of portal flow is around 0.6 L/min.

Hemodynamics changes due to clamping. In addition to average changes due to liver resection, the continuous recording enable to comment the evolution of the flow and pressure waveforms at the particular instant of vessel clamping. Figures 2.22 and 2.23 show the impact of the clamping on pressure and flow dynamics for 75% and from 75% to 90% without the MID ring liver resection respectively. The central venous pressures is not impacted by the two clampings (Figures 2.22 (a) and 2.23 (a)). The carotid artery pressure is varying at the 75% clamping instant, however it is because of the surgeon intervention. Once the surgeons intervention stops the carotid artery pressure returns to its pre-resection value and waveform. The carotid pressure is not impacted by the second clamping (Figure 2.23 (a)).

For 75% clamping and 75% to 90% clamping, the portal vein pressure seems to slowly increase (Figures 2.22 (a) and 2.23 (a)). The increase is larger for the second clamping. The increase of pressure occurs directly after the clamping.
The amplitude of the hepatic artery pressure increases after the 75% clamping (Figure 2.22 (a)) and no change is observed for 75% to 90% clamping (Figure 2.23 (a)).
The averaged hepatic artery flow decreases for the 75% clamping (Figure 2.22 (b)), as described above (Figure 2.17). Besides the mean value decrease, after the clamping two characteristic changes can be observed: the first peak is sharper, meaning the second peak is lower than before liver resection, and diastolic flow is at low values for longer. This change is typical and it is observed, in all animals, at 75% clamping time instant. By contrast, no major changes in waveform have been observed for 75% to 90% clamping (Figure 2.23 (b)). Apart from a small mean flow decrease, in some pigs, the flow rate minimum that follows systole becomes lower than the flow in diastole.

At clamping instant, the portal flow seems to decrease slowly as shown in Figures 2.22(b) and 2.23(b).
In the celiac aorta the flow waveform nor mean value is not impacted in the 10 seconds following the 75% clamping or 75% to 90% clamping (Figures 2.22 (b) and 2.23 (b)). The decrease observed of celiac aorta mean flow is therefore not instantaneously following the clamping.

2.2.1.2 Hemodynamics during liver regeneration

The hemodynamics measurements of post-operative day one and three are for the same pigs (second group: early sacrifice group), while the seventh post-operative day measurements are for different animals (first group).

Large variations of central venous pressure are measured for the different post-operative days (Figure 2.12). The central venous pressure is very sensitive to the fluid infusion and to the mechanical ventilation. The carotid artery and hepatic artery pressures remain in the same range, during liver regeneration. These pressures are decreased on post-operative day seven (Figures 2.13 and 2.16).
After liver resection and on post-operative day one, the celiac aorta flow is decreased in comparison with the pre-resection value. However, the celiac aorta flow is measured for only one animal on first post-operative day. On post-operative day three and seven, the aorta flow above celiac trunk is back to the pre-operative flow ranges (Figure 2.14). The celiac aorta flow seems to adapt to the liver size, during the regeneration. Indeed, according to liver volume estimation, the majority of liver growing happens in the first three post-operative days. Similarly, the aorta flow below the mesenteric artery increases until post-operative day three. On the seventh post-operative day the flow is close to the pre-resection value (Figure 2.15).
The hepatic artery flow increases during the liver regeneration, but remains lower than the pre-resection measurements (Figure 2.17).
The portal vein flow increases until post-operative day three. On seventh post-operative day the portal flow is similar to the pre-resection measurement. After 90% liver resection with MID-AVR^{TM} ring, the portal flow on third post-operative day is similar to the pre-resection

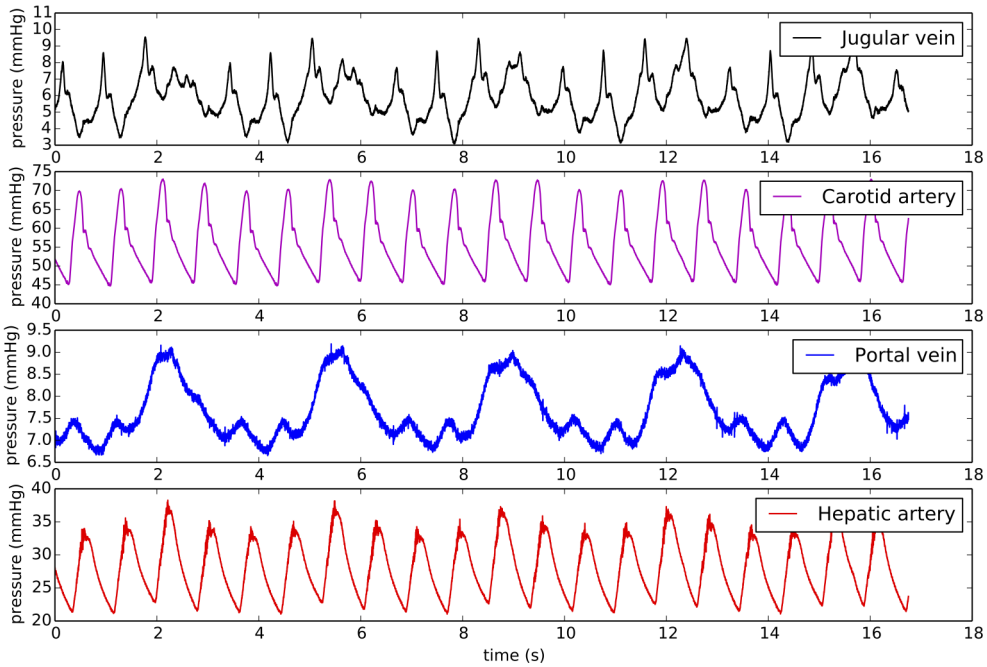

(a) Pressures

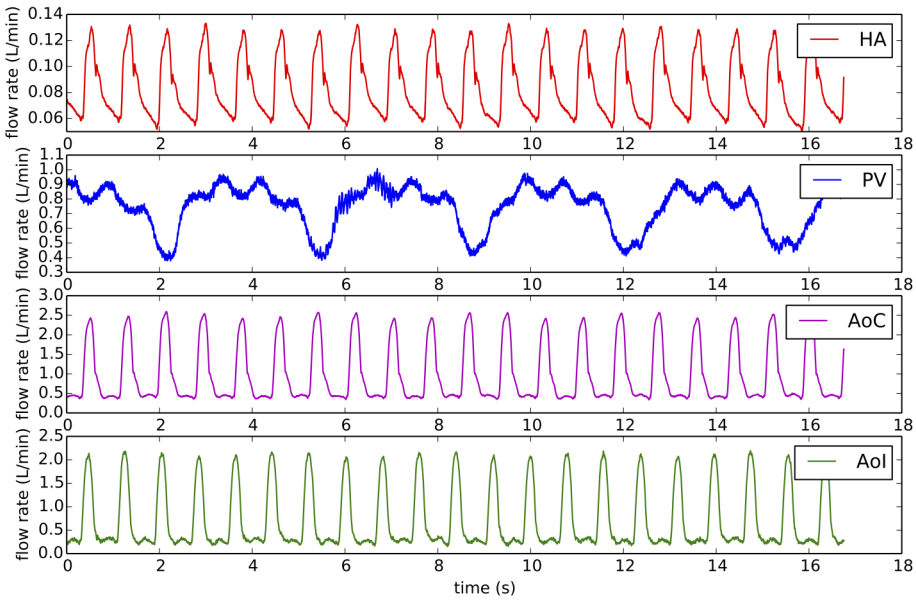

(b) Flow rates

Figure 2.21: Pressures (a) in mmHg and flow rates (b) in L/min over a few respiration cycles at the beginning of the surgery, before the liver resection.

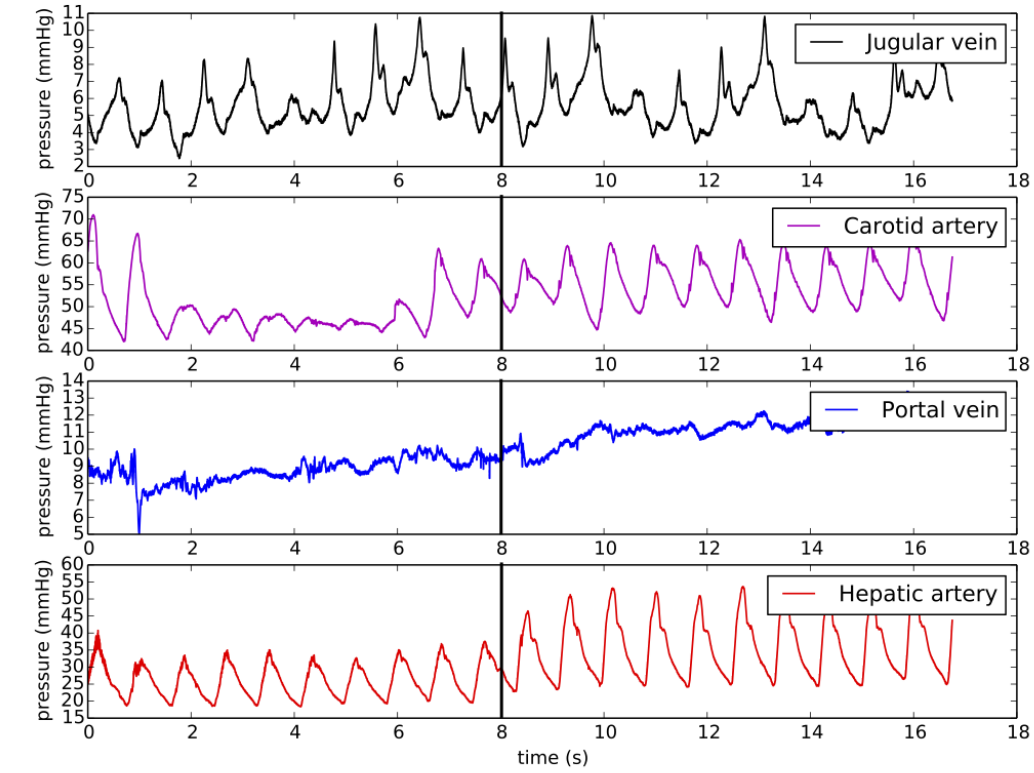

(a) Pressures

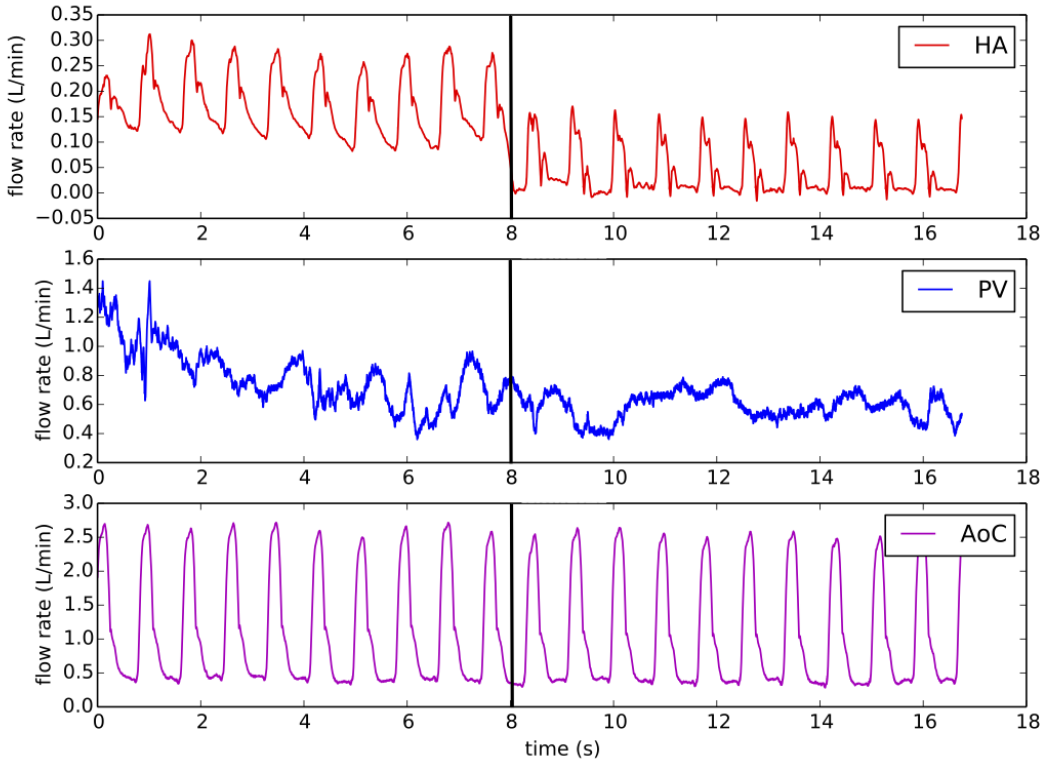

(b) Flow rates

Figure 2.22: Central venous, carotid artery, hepatic artery and portal vein pressures and hepatic artery (HA), portal vein (PV) and celiac aorta (AoC) flows measured in one animal during the clamping for 75% liver resection over time. Black lines indicate approximately the clamping time.

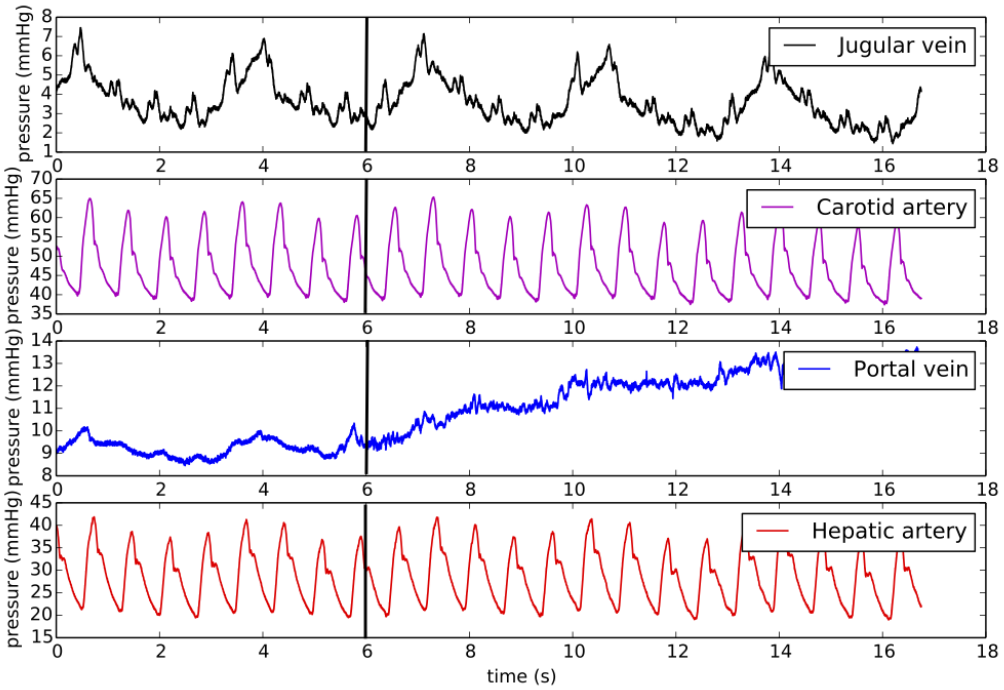

(a) Pressures

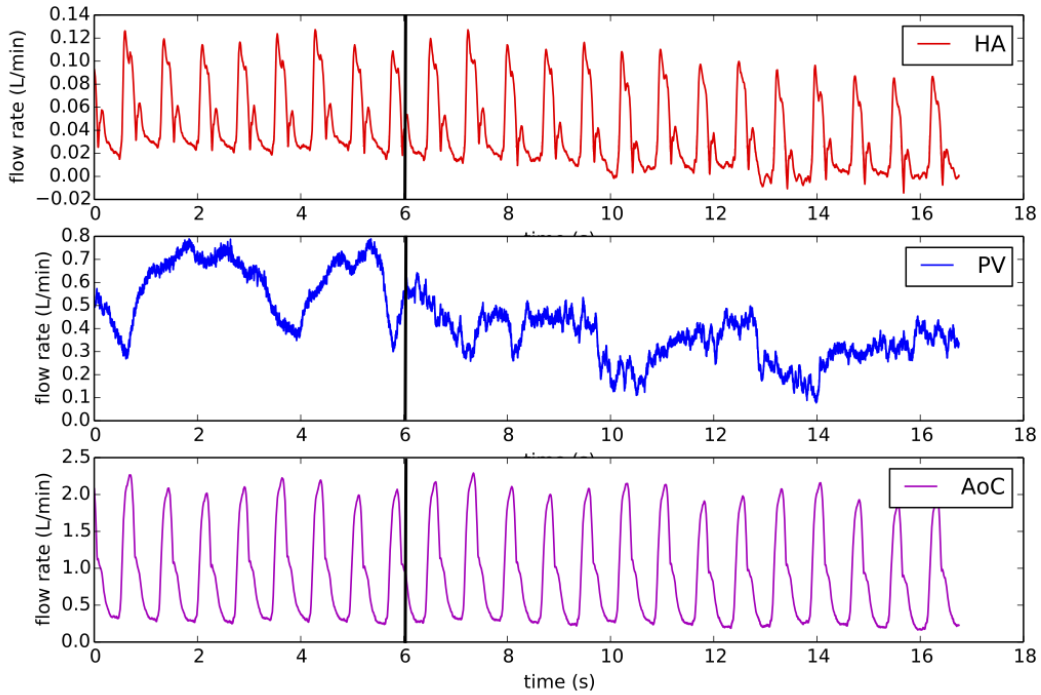

(b) Flow rates

Figure 2.23: Central venous, carotid artery, hepatic artery and portal vein pressures and hepatic artery (HA), portal vein (PV) and celiac aorta (AoC) flows measured in one animal during the clamping from 75% to 90% liver resection over time. Black lines indicate approximately the clamping time.

value (in one animal). The MID-AVR^{TM} ring seems to avoid the large increase of portal flow, observed after 75% liver resection, during the liver regeneration process (Figure 2.19). Data without the ring would confirm this hypothesis.
The portal vein pressure and the venous pressure difference during the regeneration, after 75% liver resection, remain around the pre-resection measurements (Figures 2.18 and 2.20). The large inter-subject variability of pressure measurements makes the analysis of the venous pressure evolution difficult. Moreover, these results are for a small amount of animals, more data are required to confirm these observations.

2.2.1.3 Discussion

Hemodynamics values before and after liver resection, in pig, are presented here. The hepatic artery flow has the smallest standard deviation, while the pressures have higher standard deviations. The calibration of the pressure catheters is harder than for flow probes. Therefore, the large standard deviation of the pressure may be due to the measurement technique. Furthermore, during the surgery we have observed that the pressures are more sensitive to fluid infusion and blood losses than the flows.

The liver hemodynamics is impacted by the two percentages of liver resection. Locally, the hepatic artery flow and the portal vein pressure are the two variables the most sensitive. For both surgeries the portal vein pressure increases. The increase of portal pressure is higher for a larger resection, as reported in [DHM^{+}06] for rats.

The hepatic artery flow decreases after both surgeries. Just after clamping, for 75% liver resection the hepatic artery flow decreases by 74%. The decrease is explained by the increase of the hepatic artery tree resistance, due to the liver resection. In chapter 4 this decrease is explained with a lumped model. The hepatic arterial buffer response (HABR) is a physiological mechanism in which the hepatic artery dilates or constricts to compensate for the changes in the portal vein flow (chapter 1). The mathematical model does not include the hepatic arterial buffer response. Therefore, this mechanism seems unnecessary to explain the decrease of hepatic artery flow after liver resection. After the 90% liver resection, the hepatic artery flow decreases too, but the decrease is not significantly larger than for the 75% liver resection.

The hepatic artery tree architecture after the 75% liver resection is changed (3 main liver lobes before resection and only one main liver lobe after resection). This change is assumed responsible for the typical change of waveform, observed in the hepatic artery pressure and flow. In chapter 6, a mathematical model is proposed to study these particular waveform changes.

With the continuous records, the impact of mechanical ventilation on the hemodynamics is assessed. As expected, the venous flow rates and pressures are sensitive to mechanical respiration. While arterial pressures and flow rates are mainly sensitive to the heart dynamics. The impact of the ventilation on venous pressure is large, larger for central venous pressure than for portal vein pressure. Thus, to estimate a venous pressure difference (across the liver for example), it is essential to take the venous pressures at the same instant in the respiration cycle or to use time averaged pressures. Venous pressures are also largely impacted by fluid infusion. However, all pressures are almost similarly impacted. The measurement of the

difference of two pressures (taken at the same instant in the respiration cycle) is then less sensitive to these changes. In order to evaluate the pressure changes due to liver resection it is recommended to measure a venous pressure difference and not just the portal vein pressure. The portal flow is also significantly impacted by the mechanical respiration. The average over 20 seconds of stable signal leads to a good estimation of the portal vein flow. Since the portal vein flow and the venous pressure difference are impacted by the respiratory cycle, what is sometimes called the liver resistance (venous pressure difference divided by portal vein flow) is also impacted. In the measurements, its variations around the mean are very large (-95% ; + 230 %).

The portal vein flow decreases, during 75% liver resection, similarly to celiac aorta flow, suggesting the decrease of portal vein flow is linked to a decrease of cardiac output. However, the first day after a 75% liver resection, the portal flow is higher than the pre-resection measurement. As a result, the portal flow decreases, during liver resection, may only be due to blood losses. This would explain the increase of portal flow on first and third post-operative days, when the blood volume is restored. However, with the mathematical model proposed in chapter 4, the simulations show that 75% liver resection tends to decrease portal flow by around 5%.

The portal vein flow per liver mass increases drastically. In the presented measurements, the liver weight is estimated with pre and post surgery CT-scans. The changes of portal vein and hepatic artery flow per liver mass, during the liver resection, are summarized in Figure 2.24. In [XHW+16] various liver resection are performed on pigs. In [XHW+16] the portal flow per liver mass is reported to be multiplied by around 4, 5.6 and 7.5 respectively, after 80%, 85% and 90% liver resection. In this work, after 75% liver resection the portal vein flow per liver mass is multiplied by around 3.8. The portal flow per liver mass, after 90% liver resection without and with the MID-AVR^{TM} ring, is multiplied by 13.5 and 5.2 respectively. The liver resection was in fact slightly larger in the non-ring group. In [SBSC+11] an increase of portal flow per liver mass superior to 4 times the baseline is associated with a risk of liver failure (after liver transplantation). In this study, the outcome of the 90% liver resection was not improved by the presence of the MID-AVR^{TM} ring. In both groups all animals died on the first post-operative day, exept one animal, in the ring group, that survived until third post-operative day. The proposed surgery with 90% liver resection and the large number of hemodynamics measurements (therefore many surgical acts) may be too severe [CLM+04].

The measured change of portal vein flow is not different after 90% liver resection in the control and in the ring group. However, on the third day after 90% liver resection with MID-AVR^{TM} ring, the portal flow measured in one animal is close to the pre-resection value. While, after 75% liver resection, the portal flow on post-operative day three is higher than the pre-resection measurement.

The modulation of portal hemodynamics with the MID-AVR^{TM} ring reduced the portal flow for the first post-operative days, after 90% liver resection. High portal flow may lead to post-operative liver failure [IYT+07, VCZ14], the MID-AVR^{TM} ring is likely to reduce this risk.

High portal pressure [AAB+13] and high hepatic venous pressure difference [SBSC+11] are associated with post-surgery liver failure. After 90% liver resection, the MID-AVR^{TM} ring limits the increase of portal vein pressure and venous pressure difference across the liver.

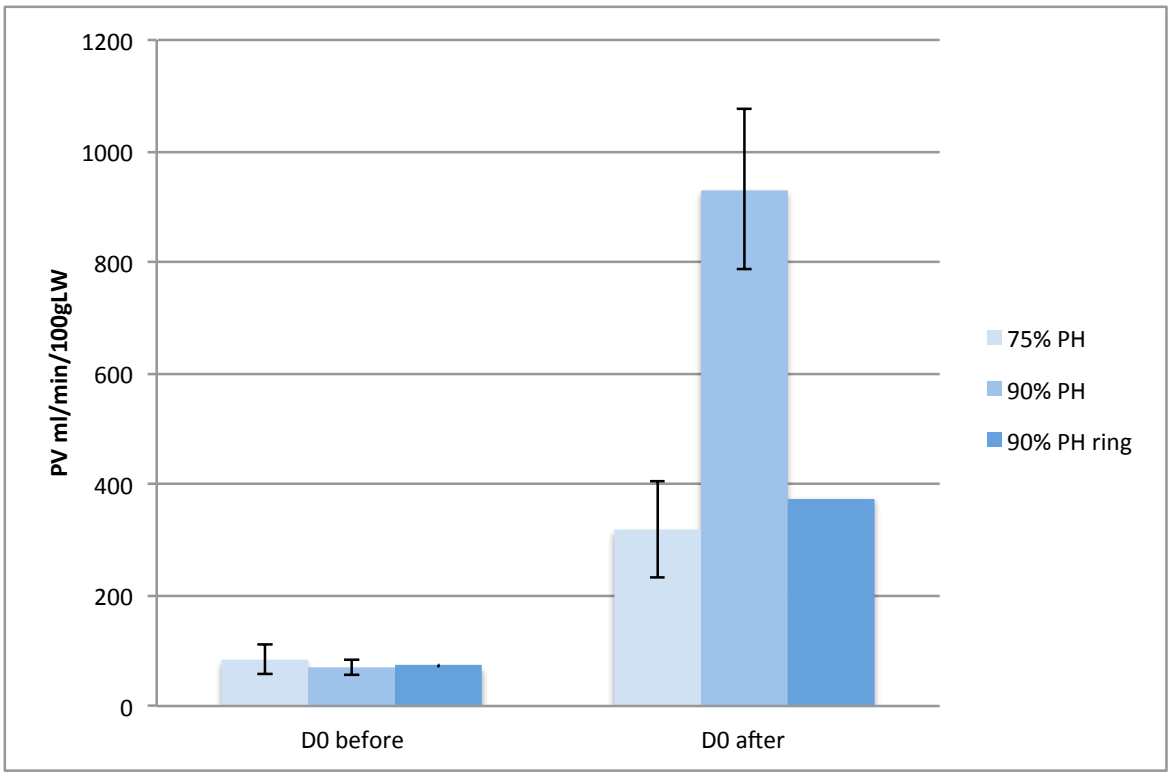

(a) Portal flow per liver weight (ml/min/100gLW)

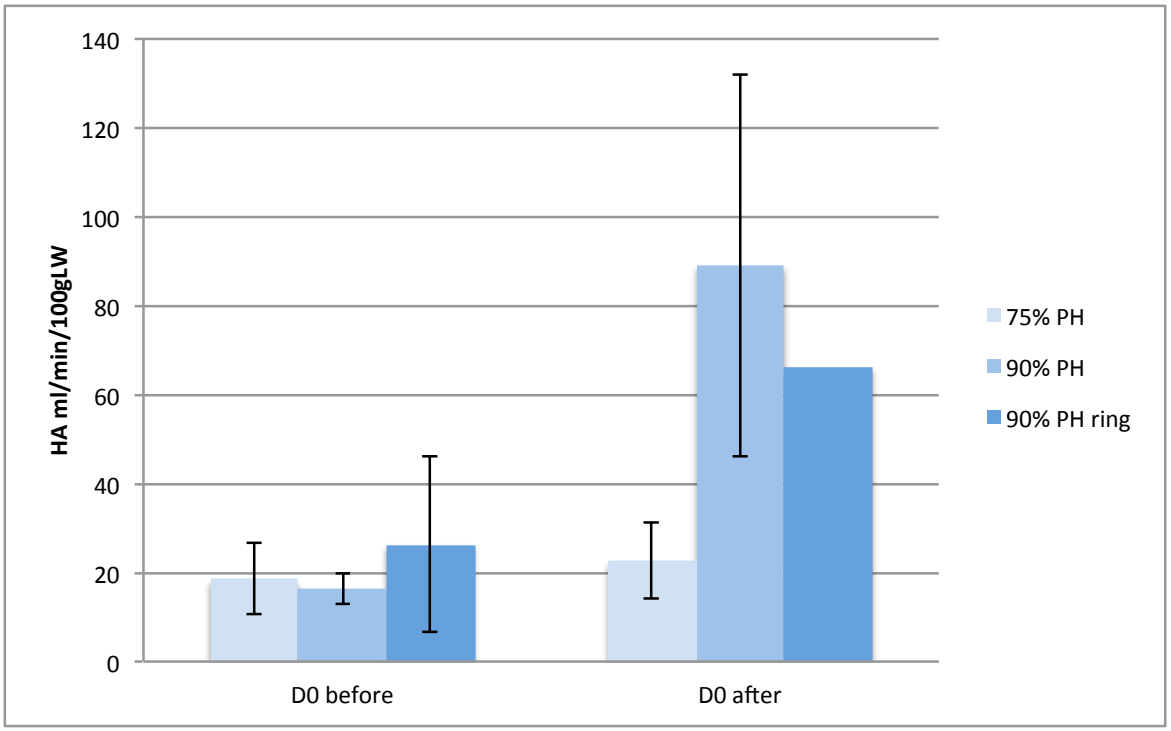

(b) Hepatic artery flow per liver weight (ml/min/100gLW)

Figure 2.24: Portal vein and hepatic artery flow per liver weight before and after various liver resection (75% , 90% and 90% with MID-AVR^{TM} vascular ring).

The fact that the MID-AVR^{TM} ring modulates the portal vein hemodynamics non-permanently is an advantage compared to other techniques, like splenectomy [GEN+06] or portal flow diversion with a porto-caval shunt [PMPS07] for example.
The hemodynamics during liver regeneration is not mathematically modeled in this work. Chapter 7 proposes some ideas to model the liver regeneration and to study the impact of the regeneration on the liver hemodynamics, and vice versa. The 90% liver resection with MID-AVR^{TM} ring group will not be studied in this thesis. In the future, a ring model could be added to the mathematical models proposed in the next chapters. With a ring model, simulations to optimize the ring diameter could be performed. However, before optimizing the ring diameter, a better understanding of the impact of liver resection on the liver hemodynamics is needed. The mathematical models and simulations proposed in part II focus on this topic.

2.2.2 Indocyanine green fluorescence

The indocyanine green could not be injected before and after liver resection on the same animal. Therefore, the curve presented are for different animals that received ICG injection before or after liver resection. Some animals also receive ICG injection on post-operative day one and three (early sacrificed group), while other animals receive the injection on seventh post-operative day (first group).

2.2.2.1 Hepatic artery and portal vein fluorescence measurements

The fluorescence is measured in the hepatic artery and in the portal vein for two minutes. Figures 2.25 and 2.26 show the measurements in the blood vessels in different animals before and after liver resection. No major differences are observed between before and after the liver resection. The portal vein intensity maximum is higher than in the hepatic artery for some animals. Before and after the liver resection the portal vein intensity curve is more diffused than the intensity curve measured in the hepatic artery. This phenomenon is due to the dispersion of the ICG in the digestive organ vascular trees, before reaching the portal vein.
For all animals, the curves intensity normalized by the reference value are in the same ranges. The curves between animals may then be compared.

In two animals, the vessel fluorescence measurements are plotted, before or after liver resection, on first and third post-operative days (see Figures 2.27 and 2.28). On the post-operative day, the portal vein intensity curve maximum is smaller. For the first animal (figure 2.27), on first post-operative day the curve is almost flat. On third post-operative day the maximum portal vein intensity remains small, in comparison with before liver resection curve. The two peaks observed in the hepatic artery fluorescence curve are probably due to a non-continuous injection (ICG injection in two times, explaining the two peaks). For the second animal (figure 2.28), no major changes are observed in the shape of the intensity curves during the liver regeneration. On third post-operative day, the maxima in portal vein and hepatic artery curves are almost the same. The shape of the intensity in the hepatic artery is different from the other days (more diffuse). Moreover, the delay between the two peaks is also very small (3.51 s).

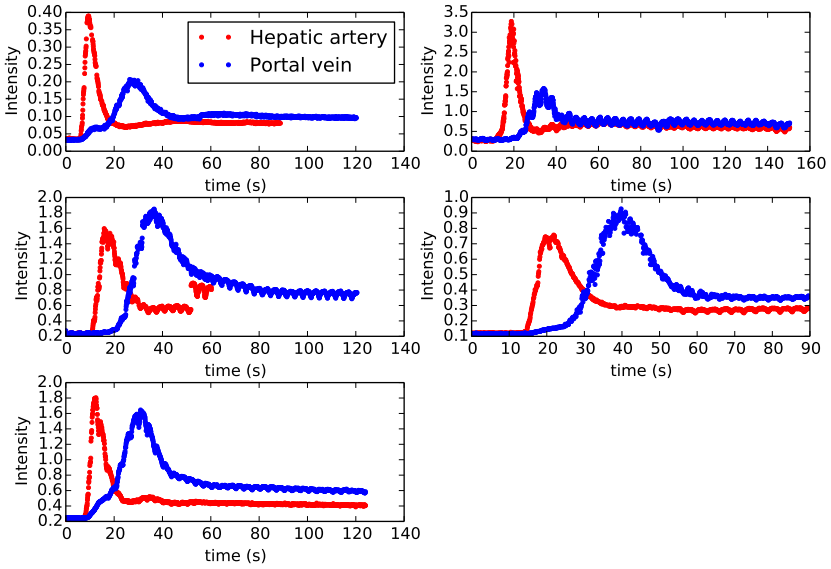

Figure 2.25: Hepatic artery and portal vein ICG fluorescence measurements over time (normalized by the reference intensity), in five animals before liver resection.

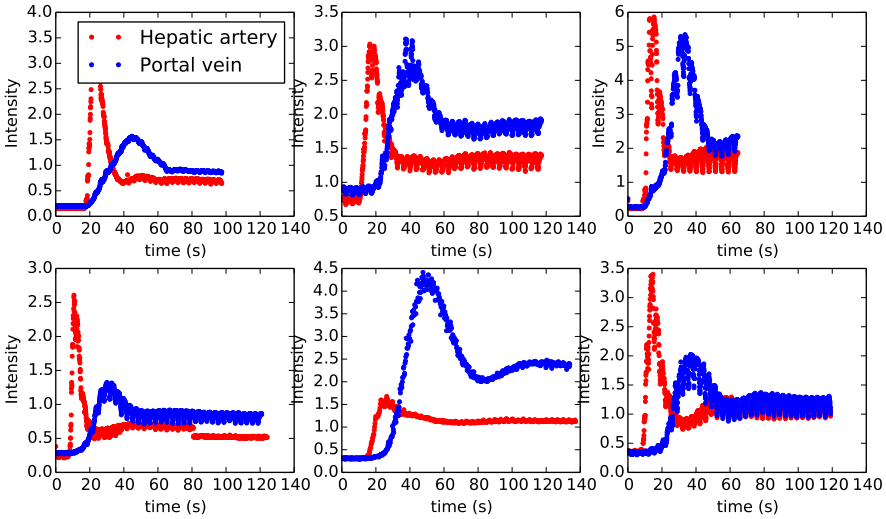

Figure 2.26: Hepatic artery and portal vein ICG fluorescence measurements over time (normalized by the reference intensity), in six animals after 75% (top line) and 90% (bottom line) liver resection.

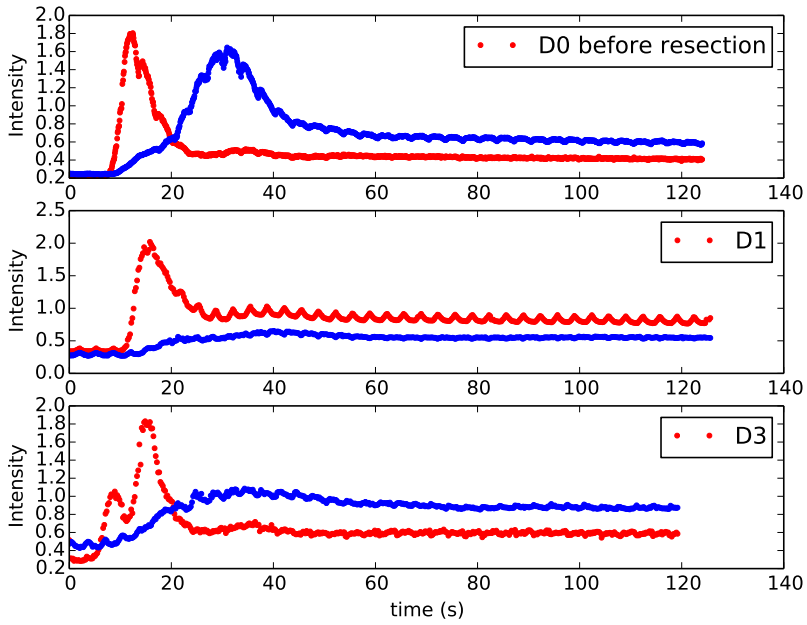

Figure 2.27: Hepatic artery and portal vein ICG fluorescence measurements over time (normalized by the reference intensity), for the same animal, before liver resection, on first post-operative day and on third post-operative day.

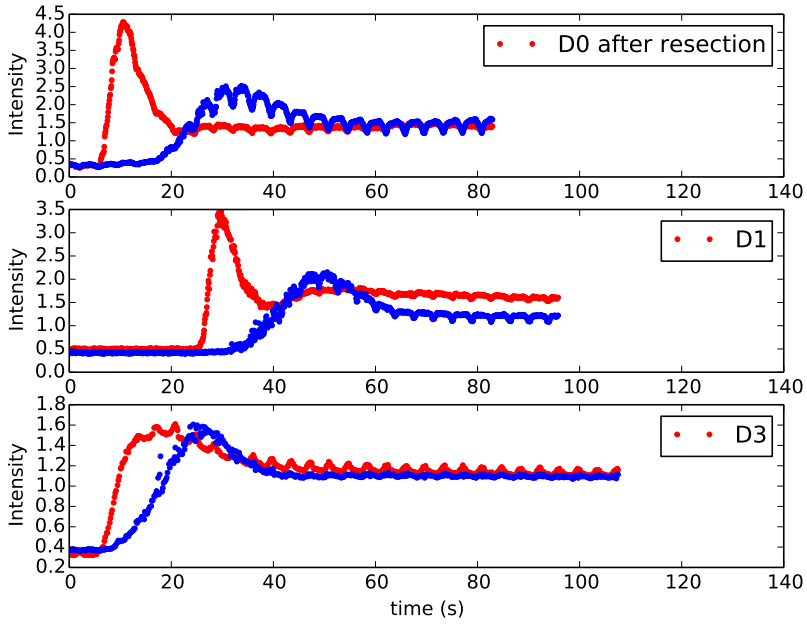

Figure 2.28: Hepatic artery and portal vein ICG fluorescence measurements over time (normalized by the reference intensity), for the same animal, after liver resection, on first post-operative day and on third post-operative day.

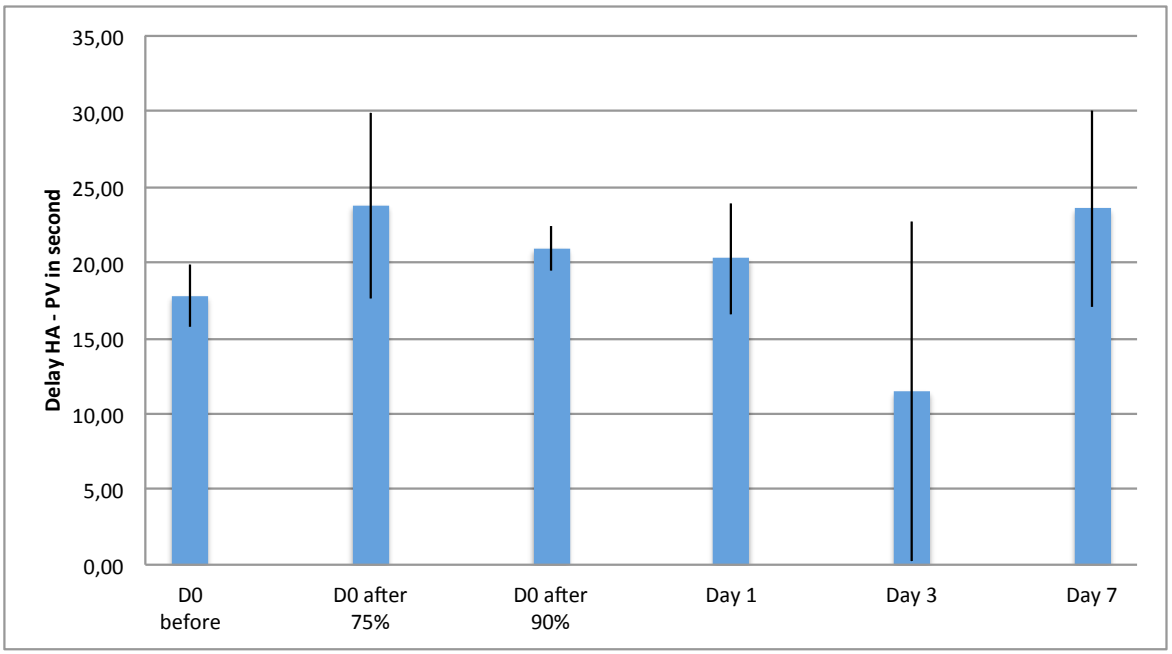

Figure 2.29: The delay between the maximum ICG intensity in the hepatic artery and the portal vein, before and after liver resection (75% or 90%), on first, third and seventh post-operative day.

The delay between the maximum intensity in the hepatic artery and in the portal vein is linked to the digestive organs vascular trees architecture and to the portal flow. A smaller portal flow or a vascular tree more resistive to flow should lead to a longer delay. Figure 2.29 shows the delay for the different stages of the surgery. The delay seems to increase a little after the liver resection, and to stay high on post-operative days. On third post-operative day the delay is lower, but only two measurements are available and for one on them the delay is really small (as shown in figure 2.28). The measured delay and the intensity curves maximum, shape and etc, in the hepatic artery and in the portal vein, are studied in chapter 9 with a mathematical model.

2.2.2.2 Liver tissue and bile duct fluorescence measurements

The ICG intensity over time is also measured in the liver tissue and in the common bile duct before (Figures 2.30 and 2.31) and after (Figures 2.32 and 2.33) liver resection. Before liver resection, the intensity in the liver tissue increases up to a certain value. Then, the intensity remains almost constant and, finally in some cases the curves start to decrease (curves B and C in Figure 2.30). After liver resection, no decrease is observed in the liver tissue. Moreover, for some animals, a first peak appears in the first part of the curve (curves A, C, E and F in Figure 2.32). The different shapes observed for the ICG intensity curves are studied and explained with a mathematical model in chapter 11.
The intensity in the common bile duct increases firstly because of the small arteries supplying blood to the common bile duct. Before and after liver resection, a delay of around 500

seconds is observed before the ICG appears in the common bile duct. Before liver resection, the ICG intensity increases and reaches a plateau. In one animal, the intensity starts to decrease (curve B Figure 2.30). After liver resection, a plateau is not reached after 30 minutes in all animals. In one animal (curve F Figure 2.33), after 90% liver resection, the intensity has not increased after 25 minutes (except for the first increase due to the small arteries).

The intensity in liver tissue and in the common bile duct is also measured during the regeneration. Figures 2.34 and 2.35 show the ICG intensity before or after liver resection and on post-operative day one and three for two animals. In the liver tissue, no major differences are observed between the different stages of liver regeneration. On post-operative days one and three the ICG intensity seems to increase in the liver tissue for a longer time than before liver resection (Figure 2.34). The ICG intensity measured in the common bile duct only reaches a plateau before liver resection. On post-operative days one and three, the increase of ICG in the common bile duct seems slower than before liver resection.
All the previous observations are qualitative. The ICG intensity of the liver vessel and tissue, as well as in the common bile duct, are linked to liver function and perfusion. The evaluation of liver function is not easy, and the quantification of the observed phenomena with ICG injection may give an evaluation of the liver function. Chapter 11 proposes a mathematical model to explain the intensity curves of the liver tissue and of the common bile duct, using the two vessel intensity curves. The model parameters are assumed to inform on the liver function or dysfunction. Therefore, inverse problems are studied to find the model parameters before and after liver resection. The combination of ICG measurements and mathematical modeling with parameter estimation, may lead to a quantification of the liver function.

2.3 Conclusion

The measurements taken during the liver resection surgery are used to build and validate the mathematical models proposed in the next parts. In turn, these mathematical models give possible hypotheses to explain the hemodynamics and functional changes observed through the hemodynamics and ICG intensity measurements. The continuous recordings of pressure and flow presented, enable to understand the sensitivity of hemodynamics to fluid infusion and mechanical ventilation. In addition, the dynamical changes due to liver resection, and more specifically at the time of liver vessel clamping are also assessed.

With the measurements, the main findings that are clinical relevant are the following:

1. The portal vein flow is decreasing after liver resection. This decrease seems principally due to a reduction of the total blood volume (caused by the blood losses and by the removal of the blood contained in the resected liver lobes). Therefore, the mathematical model, proposed in chapter 4, takes into account the changes of blood volume.

2. The portal and central venous pressures are largely impacted by the mechanical ventilation and the blood losses occurring during surgery. The measurements of pressure difference across the liver (often called in clinical papers 'pressure gradient') is thus sensitive to experimental conditions. In order to obtain a good estimation of this pressure

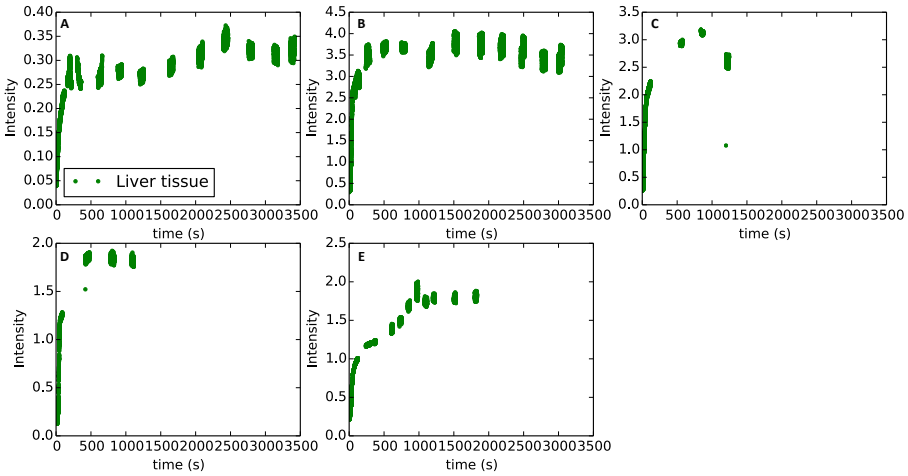

Figure 2.30: Liver tissue ICG fluorescence measurements over time (normalized by the reference intensity), in five animals before liver resection.

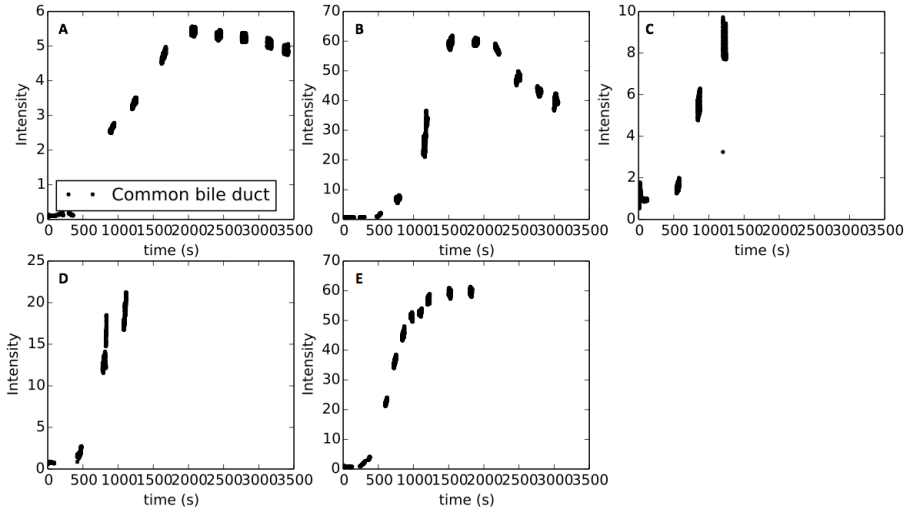

Figure 2.31: Common bile duct ICG fluorescence measurements over time (normalized by the reference intensity), in five animals before liver resection.

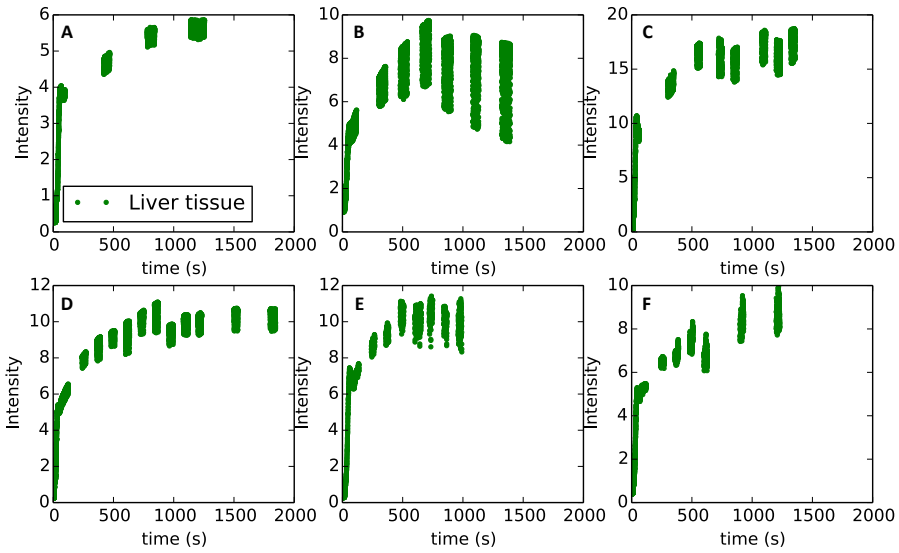

Figure 2.32: Liver tissue ICG fluorescence measurements over time (normalized by the reference intensity), in six animals after 75% (top line) and 90% (bottom line) liver resection.

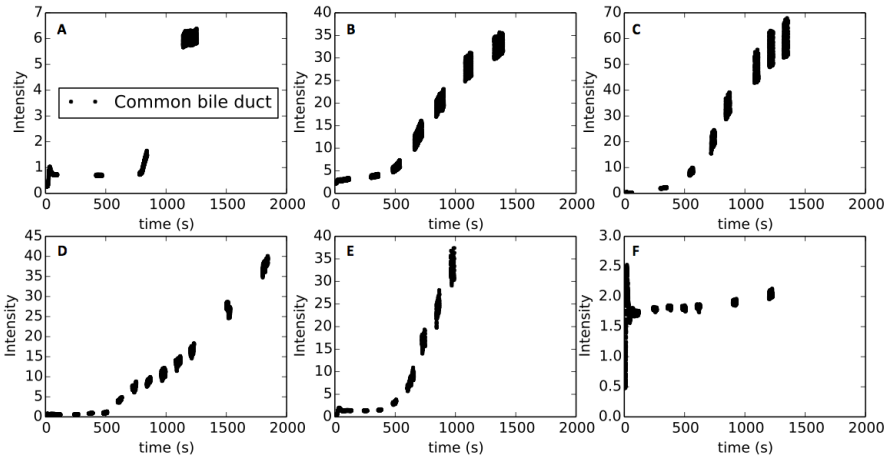

Figure 2.33: Common bile duct ICG fluorescence measurements over time (normalized by the reference intensity), in six animals after 75% (top line) and 90% (bottom line) liver resection.

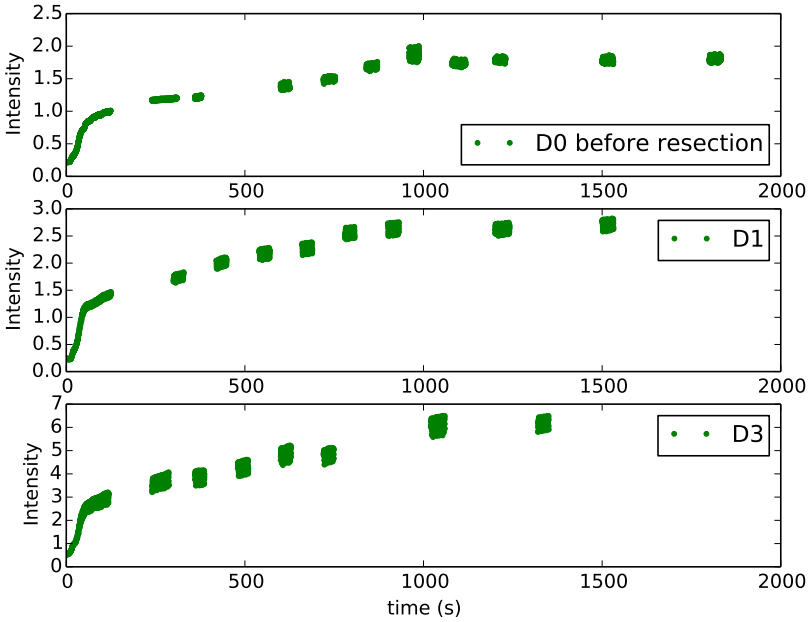

(a) Liver tissue

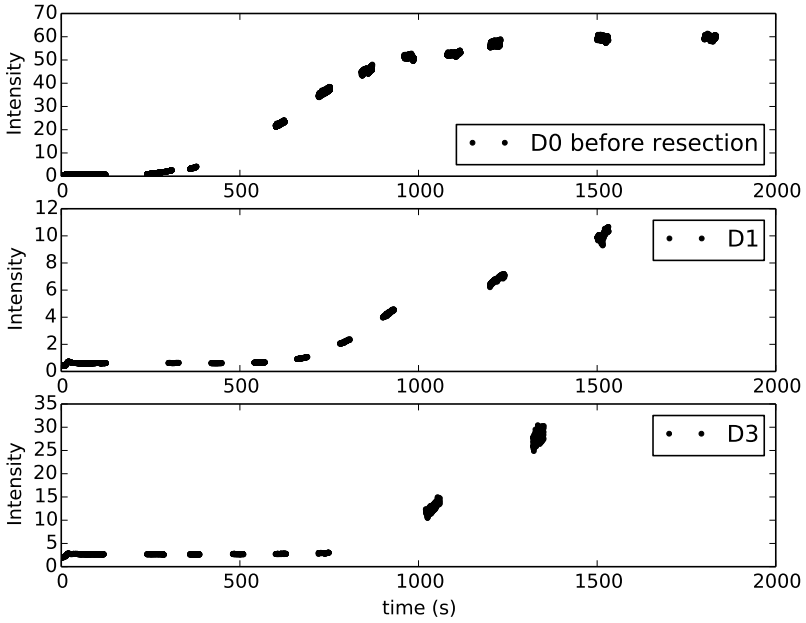

(b) Common bile duct

Figure 2.34: Liver tissue and common bile duct ICG fluorescence measurements over time (normalized by the reference intensity), in one animals before 75% liver resection, on post-operative day one and three.

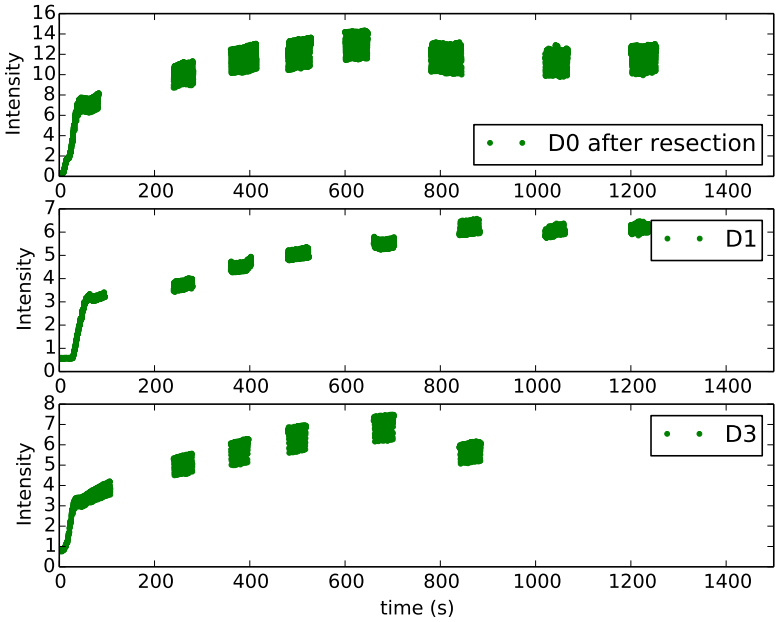

(a) Liver tissue

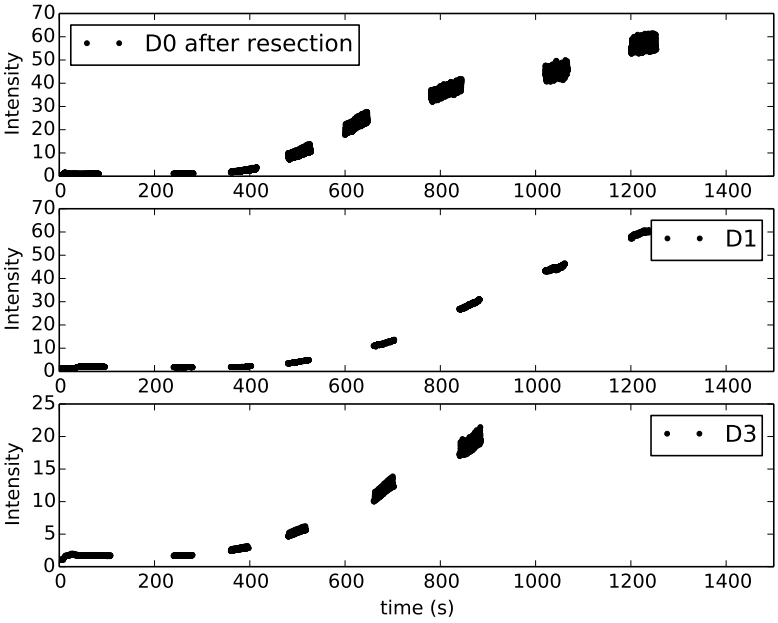

(b) Common bile duct

Figure 2.35: Liver tissue and common bile duct ICG fluorescence measurements over time (normalized by the reference intensity), in one animals after 75% liver resection, on post-operative day one and three.

difference, one-time measurements in both vessels should be taken at the same instant in the respiration cycle, e.g at the end of expiration. If continuous recording is possible, then average over few respiratory cycles may be used.

3. For 75% liver resection, the average decrease of hepatic artery flow is proportional to the liver mass resection. After the resection, the liver resistance to arterial flow is increased, leading to the reduction of arterial flow. This observation is reproduced with the mathematical model proposed in chapter 4. The hepatic arterial buffer response (see section 1.1.2) seems unnecessary to explain the decrease of liver arterial flow.

4. A typical change of waveform in the hepatic artery flow and pressure is observed during 75% liver resection. This change is assumed to be linked to the hepatic artery tree architecture. A mathematical model is proposed to explain the changes observed in the hepatic artery in part II.

Moreover, the indocyanine green intensity measurements in the portal vein and in the hepatic artery, inform on the perfusion of the liver tissue but also on the digestive organs blood supply. In order to explore more precisely these aspects, the transport of a compound through the large arteries and the organ vascular trees is studied with a mathematical model in chapter 9. The indocyanine green intensity measurements in the liver tissue and the common bile duct are connected to the liver perfusion, as well as the liver uptake and elimination function. The indocyanine green intensity curves are used, in chapters 10 and 11, to perform an inverse problem, in order to obtain model parameters. The model parameters are a manner to quantitatively estimate the liver function.
Some measurements were not used to develop mathematical models in this thesis. However, the analysis of this measurements lead to future work propositions:

1. The modulation of portal hemodynamics with the MID-AVR^{TM} ring reduces the portal flow on post-operative days. Moreover, the portal pressure and the venous pressure difference across the liver are also limited. Therefore, MID-AVR^{TM} ring may reduce the risk of post-operative liver failure. The ring group measurements are not used for mathematical modeling. A ring model can be added to the proposed models. In addition ring diameter optimization may be performed, to precisely control the portal vein hemodynamics during liver surgery.

2. The regeneration measurements inform on the link between liver regeneration and hemodynamics. These measurements are not used in this thesis. In the future, the liver regeneration and its impact on hemodynamics could be modeled. Some ideas are developed on this topic in chapter 7.

3. During these surgeries, in addition to hemodynamics and ICG fluorescence measurements, liver tissue and blood sample were taken. All these data should be analyzed to extract information and relations between liver hemodynamics and function.

Part II

Partial hepatectomy hemodynamics modeling tools

Chapter 3

Introduction

Major liver resection (partial hepatectomy) is being performed to treat liver lesions or for adult-to-adult living donor liver transplantation. Due to liver regeneration, during the post-operative period of a few months, the patient re-gains a normal liver mass. In order to get a functional regeneration of the liver, the weight ratio of the remaining liver to the body must be at least 0.5% for a healthy human [TOS+07]. However, the liver ablation percentage needs sometimes to be higher, in presence of large tumors for example. And occasionally liver function is poorly recovered, which can lead to post-operative liver failure.
Liver hemodynamics is modified by the surgery, which increases the resistance to flow of the organ. These changes are not easy to understand, partly because the liver is perfused by both arterial (through the hepatic artery) and venous blood (through the portal vein). Although high portal pressure [AAB+13], high portal flow [IYT+07, VCZ14], and high hepatic venous pressure gradient [SBSC+11] are associated with post-surgery liver failure, the link between resected volume and hemodynamics changes remains unclear. Since the liver receives around 25% of the cardiac output [Lau07], hepatectomy may impact the whole blood circulation. Thus the present work aims at developing mathematical models to explain the various hemodynamics changes observed during pig liver surgeries (see chapter 2.2). Pig is considered a good animal model for liver since its liver to body weight ratio is close to human's [Box80].

In chapter 4 a mathematical model is proposed to explain the measurements evolution observed in twelve pig liver surgery. The proposed model is built to satisfy the following requirements. First, the equations must be numerically fast to solve, to explore a diversity of hypotheses with all the pigs data. Second, the number of parameters must remain small enough so that calibration is tractable. Finally, the whole blood circulation must be taken into account, and hepatectomy dynamically modeled. Consequently, a closed-loop lumped model (also called 0D model, see section 1.2), taking into account the liver and groups of organs, is presented.

Moreover, pressure and flow in the main vessels of the liver have been recorded for different resection percentages. An interesting finding of these experiments was the following: at the resection time, waveform changes were observed repeatedly in the pressure and flow measured in the hepatic artery. These changes differ for 75% and 90% hepatectomy. Since it is hypothesized that there is a link between liver architecture and hemodynamics, and since liver architecture is important to understand liver regeneration, there is a strong interest in explaining these changes in pressure and flow waveforms.

Chapter 5 focuses on the hepatic artery tree lumped model in the liver lobes. After 75% liver resection, one main liver lobe remains. Thus, the post-resection pressure and flow measured in the hepatic artery are used to choose the liver lobe hepatic artery tree lumped model and to estimate the parameters. Two lumped models are tested. The parameter estimation is performed with the unscented Kalman filter algorithm.

Once the hepatic artery tree model is chosen such that it gives good approximation of the observed waveform, chapter 6 focuses on the dynamical change of pressure and flow in the hepatic artery, for the different percentages of liver resection. A mathematical model able to reproduce this phenomenon must satisfy several requirements. First, it has to be able to capture wave propagation. A network of vessels modeled by systems of the one-dimensional (1D) hyperbolic Euler equations is a natural candidate in this respect. The liver being perfused by both arterial and venous blood, the model should be able to address both kinds of vessels. In addition, since during surgery some vessels can be clamped, the model and the numerical scheme should be able to handle the limit of vanishing cross-section area. A kinetic scheme is proposed to solved the hyperbolic Euler equations, in particular because of its interesting capability to preserve the positivity of the cross-section area. This scheme was originally developed for the Saint-Venant shallow water equations. To our knowledge, this is the first time that it is used to model collapsible vessels.

Second, as mentioned previously, the liver receives about 25% of the cardiac output [Lau07], hepatectomy may also influence the systemic circulation. Therefore the network of 1D models is embedded within closed-loop model of the whole circulation, including the liver, using the models studied in the previous chapters.

Different groups have worked on liver hemodynamics modeling, at different scales and for various applications. Liver lobule porous models have been proposed, to model glucose transport and metabolism [RWH+15], to study the influence of a vascular septum and tissue permeability [DVS+14], including in cirrhosis [PDC+15] or to simulate the impact of deformation on pressure-flow relation [BLRS10]. At the organ scale, liver π lumped models for multiple vascular generations have been used to study the hypothermic machine perfusion [VDPtHV+04, DMS14].

A lumped model of the splanchnic and liver circulation has been proposed to illustrate the link between hepatic venous pressure increase, vessel contractility and liver interstitial fluid [CR92]. Models have been developed on transport and diffusion of a compound in the liver [SKN+14], including whole-body pharmacokinetics models [SSK+15] or to study tumor detection with Magnetic Resonance Images [BWKM+07]. Convection is based on resistive models of the different generations of arterial and venous trees. In [LJJ+14], the liver arterial and venous trees geometry is based on CT-scans. The flow in the trees is modeled using Bernouilli equation for the first generations, and a porous media approach for the smallest vessels. Hepatic artery flow 3D CFD simulations for rigid and flexible walls have been performed in [CK14] to study direct drug-targeting. 3D CFD flow in vascular trees simulation have been proposed to model Magnetic Resonance Images [JKE+14]. The simulated MR images are compared to experimental images.

Liver models have also been developed to study the impact of liver surgery. Flow behavior for different H-Graft diameters has been studied with a resistive model and compared to clinical observations in [RRS+87]. A 3D CFD simulation has been performed in the portal vein before and after right lobe hepatectomy in [HSBH12]. The geometry included superior mesenteric and splenic veins merging in portal vein and three portal vein branches. Constant velocities boundary conditions were prescribed in the mesenteric and splenic veins and zero pressure was imposed at the outlets. The surgery was simulated by changing the geometry. Similarly,

for a two-lobe liver lumped model, driving conditions were kept unchanged before and after hepatectomy. Various resection sizes and two different surgical techniques have been simulated using a resistance model, based on cast reconstruction, of rat liver vasculature [DDWC+12]. The results have indicated portal-hyperperfusion after resection and demonstrated that probably better outcomes are expected with one of the two 90% resection techniques. Most of these works do not consider the dynamics induced by the surgery or the interaction with the rest of the circulation.

Chapter 4

Experimental data explained by closed-loop lumped modeling

This chapter proposes to explain with a closed-loop lumped model the hemodynamics changes observed during liver surgeries in twelve pigs. The portal venous tree is modeled with a pressure-dependent variable resistor. The variables measured, before liver ablation, are used to tune the model parameters. Then, the liver partial ablation is simulated with the model and the simulated pressures and flows are compared with post-operative measurements. Fluid infusion and blood losses occur during the surgery. The closed-loop model presented accounts for these blood volume changes. Moreover, the impact of blood volume changes and the liver lobe mass estimations on the simulated variables is studied. The different post-operative states, observed in experiments, are reproduced with the proposed model. Thus, an explanation for inter-subjects post-operative variability is proposed. The presented framework can easily be adapted to other species circulations and to different pathologies for clinical hepatic applications.

The chapter is organized in the following manner. Section 4.1 presents the available experimental measurements, the cardiovascular and liver models and their parametrization. Section 4.2 shows partial hepatectomy simulation results and comparison with measurements. The model capabilities are discussed at the end of this chapter.

The results presented in this chapter lead to the accepted manuscript : C. Audebert, M. Bekheit, P. Bucur, E. Vibert, I.E. Vignon-Clementel, *Partial hepatectomy hemodynamics changes: experimental data explained by closed-loop lumped modeling.* Journal of Biomechanics 2017.

Contents

4.1 Methods 65
4.1.1 Liver surgery - experimental measurements 65
4.1.2 0D closed-loop model 66
4.1.3 Parameter tuning procedure 70
4.2 Results 73
4.2.1 Pre-resection stage 73
4.2.2 Liver partial resection simulation 73
4.3 Discussion and conclusions 77

4.1 Methods

4.1.1 Liver surgery - experimental measurements

As detailed in part I, hepatectomies are performed on several pigs to study the hemodynamics impact. Here, the hepatectomy surgery procedure is rapidly recalled as well as the measurements used (see part I for details). The pig liver is composed of five lobes, usually considered as three main lobes [CWHM+03]: left lobe, median lobe (subdivided in left medial and right medial lobes) and right lobe (subdivided in right lateral and caudate lobes). The median and left lobes are resected. Since the median lobe is around twice the size of left and right lobes, around 75% hepatectomy is performed.
During surgery, several measurements are continuously recorded. Three pressures and three flows are the basis of parameter tuning and model testing. These measurements are averaged over 20 seconds during a stable state of the surgery. Pre-resection and post-resection (immediately after surgical clamping) states are considered. The carotid artery (CA), portal vein (PV) and central venous (CV) pressures are measured. The later is a surrogate for the hepatic vein (v) pressure. The flows are recorded in the aorta above the celiac trunk (celiac aorta), the hepatic artery (HA) and the portal vein. Cardiac output (CO) is estimated assuming celiac aorta flow is around 60% of CO [LFLH81] (assuming humans and pigs flow distributions are similar [SMH+12]). Heart rate is computed from the carotid artery pressure measurement.
Before and after the surgery a CT-scan is performed with a Siemens Somatom AS definition 128 machine. Image acquisitions are done before, 15, 35, 55 and 75 seconds after injection of 75 ml of iohexol 350mg/ml (Omnipaque, GE Healthcare) with a rate of 5 ml per second. From the CT-scans liver volumes are estimated. After ablation, the removed liver is weighted; left and median lobe masses are then assessed. Some parameters in the model are mass dependent, therefore the liver lobe masses and the total liver mass are required. Four different estimations are proposed.

A1 From the pre-operative CT-scan, the total liver mass, as well as the planned resected mass and the remaining mass are estimated (Figure 4.1). The estimated remaining mass corresponds to the right lobe mass, while the planned resected mass corresponds to the sum of left and median lobe masses. To obtain the left and median lobe masses, the planned resected mass is split assuming the left lobe mass is one third of the planned resected mass (Figure 4.1).

A2 The total liver mass is estimated from the pre-operative CT-scan. The left and median lobes are weighted after the resection. The right lobe mass is deduced from the difference of the two previous estimations.

A3 The left and median lobes are weighted after the resection. The right and left lobe masses are assumed similar. The total liver mass is the sum of the lobe masses.

A4 The left and median lobes are weighted after the resection. The right lobe mass is estimated with the post-operative CT-scan. The total liver mass is the sum of the lobe masses.

Mass estimation	A1	A2	A3	A4
Total liver mass	Estimate with pre-op CT-scan	Estimate with pre-op CT-scan	Sum of lobe masses	Sum of lobe masses
Left lobe mass	1/3 Planned resected mass (pre-op CT-scan)	Weight after resection	Weight after resection	Weight after resection
Right lobe mass	Planned remaining mass (pre-op CT-scan)	Total mass minus left and median lobe masses	Equal to left lobe mass	Estimate with post-op CT-scan
Median lobe mass	2/3 Planned resected mass (pre-op CT-scan)	Weight after resection	Weight after resection	Weight after resection

Table 4.1: The different mass estimations description of the total liver, left lobe, right lobe and median lobe. Their degree of certainty increases, and conversely their degree of predictability decreases from A1 to A4: preop calculation, peri-op calculation possible, post-op calculation.

The estimations degree of certainty increases and conversely their degree of predictability decreases from A1 to A4. Table 4.1 sums up the different mass estimations.

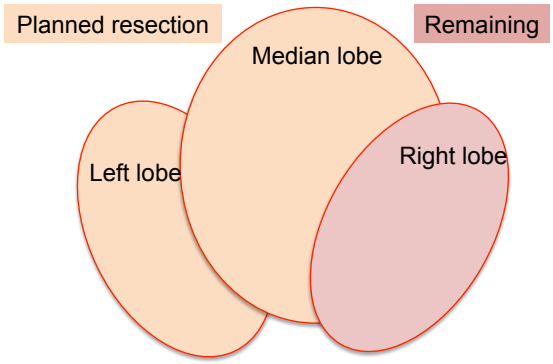

Figure 4.1: Schematic representation of planned resected and remaining parts of the liver, for 75% partial hepatectomy on pig.

4.1.2 0D closed-loop model

A 0D hemodynamics model of the entire cardiovascular system [LL05, SSW+03] is coupled to a new model of liver that is structured by lobes. The model aims to represent hepatectomy, i.e. the resection but also other related phenomena. Hence, only the involved organs are included, resulting in five blocks (figure 4.2).
Lungs ($i = L$), digestive organs ($i = DO$) and other organs ($i = OO$) are represented by

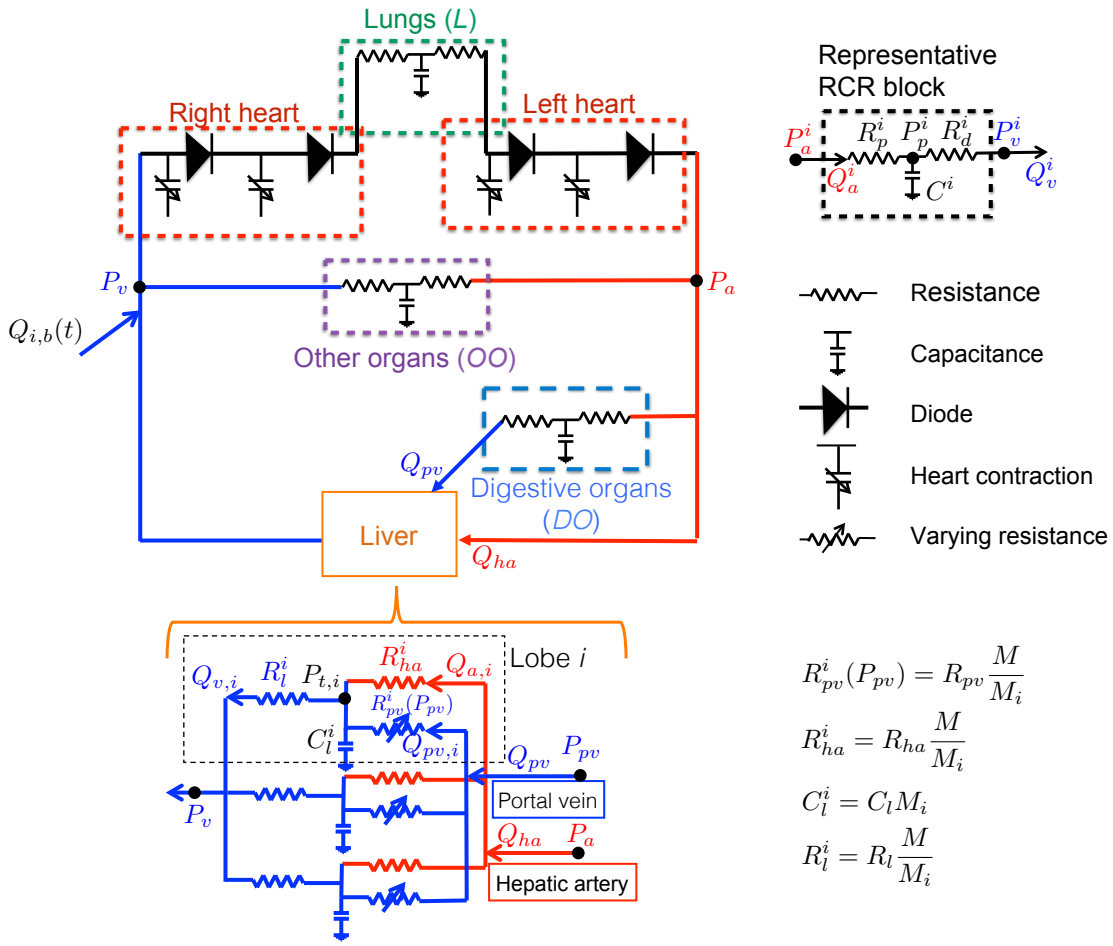

Figure 4.2: Schematic representation of the 0D closed-loop cardiovascular and liver blood circulations. RCR block and liver lobe i parameters are shown. $Q_{i,b}$ is the infused or removed flow to account for blood volume changes.

three-element Windkessel models:

$$\begin{cases} C^i \dfrac{dP_p^i}{dt} & = Q_a^i - Q_v^i \\ R_p^i Q_a^i & = P_a^i - P_p^i \\ R_d^i Q_v^i & = P_p^i - P_v^i \end{cases} \tag{4.1}$$

where for block i, Q_a^i and Q_v^i are arterial and venous flows, P_a^i, P_p^i and P_v^i are arterial, proximal and venous pressures, R_p^i, R_d^i and C^i are proximal and distal resistances and capacitance (figure 4.2).

Heart model The heart model is based on [SS74, PMD+97, LTHL09, BF13]. To obtain smooth, yet sharp, transitions between open and closed valves, logistic functions are used for valves. The heart chamber equations read:

$$\begin{cases} \dfrac{dV_i}{dt} &= Q_{in,i} - Q_{out,i} \\ P_i &= E_i(t)(V_i - V_{0_i}) \\ Q_{out,i} &= G_i(P_i - P_{out,i})(P_i - P_{out,i}), \end{cases} \tag{4.2}$$

where i denotes either the right atrium (RA), right ventricle (RV), left atrium (LA) or left ventricle (LV); V_i and V_{0_i} are respectively the volume and unloaded volume of the heart chamber i; $Q_{in,i}$ and $Q_{out,i}$ are the incoming and outgoing flows; P_i is the heart chamber pressure; $P_i - P_{out,i}$ is the pressure across the valve; E_i is the elastance function, defined by $E_i(t) = E_{a_i} e(t)^{\alpha_i} + E_{b_i}$ with $\alpha_i = 1$ if $i = RA, LA$ and $\alpha_i = 0.5$ if $i = RV, LV$, as in [PCB+15]. E_{a_i} and E_{b_i} are the amplitude and baseline elastances respectively, and e is a normalized time-varying function of the elastance, defined as follows for the ventricles:

$$e(t) = \begin{cases} \dfrac{1}{2}\left[1 - \cos\left(\pi \dfrac{t}{T_{vc}}\right)\right] & 0 \le t \le T_{vc} \\ \dfrac{1}{2}\left[1 + \cos\left(\pi \dfrac{t - T_{vc}}{T_{vr}}\right)\right] & T_{vc} < t \le T_{vc} + T_{vr} \\ 0 & T_{vc} + T_{vr} < t \le T_{cc}, \end{cases} \tag{4.3}$$

and for the atria:

$$e(t) = \begin{cases} \dfrac{1}{2}\left[1 + \cos\left(\pi \dfrac{t + T_{cc} - t_{ar}}{T_{ar}}\right)\right] & 0 \le t \le t_{ar} + T_{ar} - T_{cc} \\ 0 & t_{ar} + T_{ar} - T_{cc} < t \le t_{ac} \\ \dfrac{1}{2}\left[1 - \cos\left(\pi \dfrac{t - t_{ac}}{T_{ac}}\right)\right] & t_{ac} < t \le t_{ac} + T_{ac} \\ \dfrac{1}{2}\left[1 + \cos\left(\pi \dfrac{t - t_{ar}}{T_{ar}}\right)\right] & t_{ac} + T_{ac} < t \le T_{cc}, \end{cases} \tag{4.4}$$

where T_{cc} is the duration of the cardiac cycle. The durations of the ventricular and atrial contractions and relaxations are denoted by T_{vc}, T_{ac}, T_{vr} and T_{ar} respectively; t_{ac} and t_{ar} are the times when the atria begin to contract and relax, respectively. The heart parameter values are given in Table 6.10. The valve conductance is described by the function $G(\Delta P) = \dfrac{G_0}{1 + \exp(-(\Delta P - d))}$ where $G_0 = 0.1\text{cm}^5.\text{dyn}^{-1}.\text{s}^{-1}$, and $d = 0.1\text{dyn/cm}^2$.

Liver model The liver tissue is perfused with venous blood through the portal vein and arterial blood through the hepatic artery and drained by the hepatic veins. The liver main lobes are represented by three blocks in parallel (figure 4.2), related to the left heart (arterial input), digestive organs (venous input) and right heart (venous output) compartments. Within each lobe, the hepatic artery tree is represented by a single resistance. The portal vein tree is modeled by a non-linear resistance to represent pressure (P) dependent resistance (R), the

subscript $_0$ labelling before resection:

$$P - P_0 - K\left(\left(\frac{R_0}{R}\right)^5 - \left(\frac{R_0}{R}\right)^{-0.75}\right) = 0, \tag{4.5}$$

This equation is derived from a vein law relating pressure and area [Sha77, PBS96] (assuming the reference configuration is before liver resection):

$$P - P_0 = K\left(\left(\frac{A}{A_0}\right)^{10} - \left(\frac{A}{A_0}\right)^{-1.5}\right), \tag{4.6}$$

where A is the portal vein cross-section area. Assuming Poiseuille flow, the cross-section area and the resistance are related as follow:

$$R = \frac{8\mu l\pi}{A^2}\,;\ \frac{A}{A_0} = \left(\frac{8\mu l\pi}{R}\right)^{1/2}\left(\frac{R_0}{8\mu l\pi}\right)^{1/2} = \left(\frac{R_0}{R}\right)^{1/2} \tag{4.7}$$

where μ is the blood viscosity and l is the vessel length, these two parameters are assumed unchanged between before and after partial hepatectomy.
Finally, liver tissue and hepatic vein trees are modeled with a capacitance and a resistance [BR81].
The resistances and capacitance in a lobe are assumed, as a first approximation, proportional to lobe mass inverse and lobe mass respectively. Thus, for each lobe:

$$\begin{cases} P_a - P_{t,i} &= R_{ha}\dfrac{M}{M_i}Q_{a,i} \\ P_{pv} - P_{t,i} &= R_{pv}(P_{pv})\dfrac{M}{M_i}Q_{pv,i} \\ P_{t,i} - P_v &= R_l\dfrac{M}{M_i}Q_{v,i} \\ C_l M_i\dfrac{dP_t}{dt} &= Q_{a,i} + Q_{pv,i} - Q_{v,i} \end{cases} \tag{4.8}$$

where P_a, P_{pv}, $P_{t,i}$ and P_v are respectively the pressure for artery, portal vein, ith lobe tissue and venous pressure. $Q_{a,i}$, $Q_{pv,i}$ and $Q_{v,i}$ are hepatic artery, portal vein and hepatic venous flows in lobe i respectively. M and M_i are the liver and lobe i mass estimations. R_{ha}, R_{pv}, R_l are resistances for hepatic artery tree, portal vein tree, and liver tissue and hepatic venous tree. C_l is the liver tissue capacitance per liver mass. The liver tissue properties are assumed the same for all animals, therefore C_l is the only liver non pig-specific parameter.

Partial hepatectomy simulation To model median and left lobes resection, the corresponding hepatic artery and portal vein lobe resistances are multiplied by a function dependent on T_{75}, the resection time:

$$r(t) = \begin{cases} 1 \text{ if } t < T_{75} \\ \exp(5(t - T_{75})) \text{ otherwise} \end{cases} \tag{4.9}$$

Infusion or bleeding modeling During surgery, blood and lymph losses and evaporation due to open-abdomen occur. Anesthetists thus infuse fluid (normal saline or 5% glucose solution). Consequently blood volume is not constant. In the model, systemic venous flow is thus changed dynamically by adding or removing flow to represent bleeding or infusion (Figure 4.2):

$$Q_{i,b}(t) = \frac{V_{i/b}}{D_{i/b}(1+\exp(-0.1(\Delta t - 0.01)))} \quad \text{with } \Delta t = \begin{cases} 1 & T_{i/b} \leq t \leq T_{i/b} + D_{i/b} \\ 0 & \text{otherwise} \end{cases} \tag{4.10}$$

Where $T_{i/b}$ and $D_{i/b}$ are the time and duration of the infusion or bleeding and $V_{i/b}$ is the added or removed volume.

Numerical resolution The model leads to a system of nonlinear differential-algebraic equations, solved with the IDA package from SUNDIALS [SPH15]. A Backward Differentiation Formula is used for time integration, and a Newton method for the resulting nonlinear system.

Statistical tests A test of equivalence compares the model outputs and the measurements. The equivalence test null hypothesis is the dissimilarity of the two populations. Thus, the test assumes the populations are different and uses the data to prove otherwise [RDM05]. A two one-sided t-test (TOST) is chosen and computed with the R function TOST in the "equivalence" package [R D08, Rob16]. The TOST uses as a metric the difference between the two samples. In the following examples, a relative error between the simulations and the measurements is computed and used in the two one-sided t-test (the second sample is null). For the equivalence test, a region of indifference has to be defined; here a 10% relative error is chosen. If the region of indifference is contained in the confidence interval, then the two populations are deemed significantly similar. If not, the null hypothesis is not rejected [RF04].

4.1.3 Parameter tuning procedure

Based on the available cardiac-cycle-averaged measurements and literature data, twenty five parameters are tuned to obtain similar pressures and flows to the measured ones before resection.

Systemic circulation Carotid artery and central vein pressure measurements are used as target arterial (P_a) and venous (P_v) pressures in the model. Combined with the cardiac output, the systemic equivalent resistance is computed: $R_{eq} = (P_a - P_v)/CO$. Similarly, the RCR total resistance for digestive organs (DO) is computed with measured P_a, P_{pv} and Q_{pv}.

$$R_{DO} = \frac{P_a - P_{pv}}{Q_{pv}}$$

The liver tissue pressure (P_t) is estimated assuming that the venous pressure drop between portal vein and liver tissue is 80% of the pressure drop between portal vein and hepatic

Notation	Detail	Value in second
T_{cc}	Cardiac cycle	60s / heart rate (bpm)
T_{vc}	Ventricular contraction duration	$0.34T_{cc}$
T_{vr}	Ventricular relaxation duration	$0.15T_{cc}$
T_{ac}	Atrium contraction duration	$0.17T_{cc}$
T_{ar}	Atrium relaxation duration	$0.17T_{cc}$
t_{ac}	Time atrium begins to contract	$0.8T_{cc}$
t_{ar}	Time atrium begins to relax	$0.97T_{cc}$

Table 4.2: Durations and times for contraction and relaxation of the different cardiac chambers. These parameters are the same for the left and right hearts.

vein ($P_{pv} - P_v$) [DDWC+12]. Combined with the P_a and Q_{ha} measurements, the HA tree resistance is computed:

$$R_{ha} = \frac{P_a - P_t}{Q_{ha}}$$

Similarly, the liver tissue resistance and the initial portal resistance (R_0 in equation (4.5)) are computed:

$$R_l = \frac{P_t - P_v}{Q_{ha} + Q_{pv}}; \quad R_{pv} = \frac{P_{pv} - P_t}{Q_{pv}}$$

The other organs (OO) total resistance is then computed: $R_{OO} = 1/(1/R_{eq} - 1/R_{ha} - 1/R_{DO})$. In the digestive organs RCR model, the proximal resistance is assumed to carry 10% of the total resistance, within ranges in [RJS74, VCFJT10, LAVC+11]. Because of the valve the total proximal resistance cannot be too high for the system to be solved. Therefore, in the other organs RCR model, the proximal resistance carries between 2% and 10% (5% in average) of the total resistance depending on the animals. Capacitances are fixed (same for all pigs). The other organs capacitance is $C^{OO} = 7.36\,10^{-4}\text{cm}^5/\text{dyn}$ (within ranges in [SSS+00]). The portal vein flow is almost not sensitive to heart beat (part I). Therefore, the digestive organs capacitance is manually tuned to obtain a non-pulsating curve, $C^{DO} = 4\,10^{-4}\text{cm}^5/\text{dyn}$. The liver tissue capacitance per mass is fixed with literature $C_l = 1.5\,10^{-5}\text{cm}^5/\text{dyn/g}$ [BR81].

Heart and lung parameters The amplitude and baseline of heart contraction functions are tuned, for each pig, to obtain arterial and venous average pressures measured before resection. The heart contraction times and cardiac cycle are based on the measured heart rate (Table 4.2). Lung parameters are based on [BF13]: $R_p^L = 53.33$ dyn.s/cm^5; $R_d^L = 53.33$ dyn.s/cm^5 and $C^L = 0.05\text{cm}^5/\text{dyn}$.

Table 4.3 presents the closed-loop lumped parameter for each animal as well as the averages and standard deviations over the twelve simulations. The liver mass as well as the liver lobe masses are summed up in Table 4.4.

				Heart			
Animals	HR	Ea_{RA}	Eb_{RA}	Ea_{RV}	Eb_{RV}	Ea_{LV}	Eb_{LV}
Units	1/min	dyn/cm^5	dyn/cm^5	dyn/cm^5	dyn/cm^5	dyn/cm^5	dyn/cm^5
iF01	98	160	100	800	110	2000	280
iF02	80	160	60	800	70	2000	270
iF03	97	160	140	800	150	2000	370
iF06	85	160	100	800	110	2000	250
iF08	84	160	80	800	90	2000	270
iF09	93	160	5.00	800	15	2000	400
iF10	83	160	50	800	60	1900	360
iF11	92	160	10	800	20	2000	230
iF12	100	160	10	800	20	2000	180
iF14	80	160	40	800	50	2000	400
1F16	100	80	40	770	50	2000	330
iF2A	90	160	30	800	50	2000	470
Average	90	153	55	798	66	1992	318
std	8	23	42	9	42	29	85
	Other Organs		Digerstive Organs		Liver		
Animals	R_p^{OO}	R_d^{OO}	R_p^{DO}	R_d^{DO}	R_{ha}	R_{pv}	R_l
Units	dyn.s/cm^5	dyn.s/cm^5	dyn.s/cm^5	dyn.s/cm^5	dyn.s/cm^5	dyn.s/cm^5	dyn.s/cm^5
iF01	94.5	1794.5	465	4184	3.91e4	1.32e2	2.93e1
iF02	151.00	1359.00	344	3098	1.69e4	1.40e2	2.89e1
iF03	50.00	1397.00	555	4996	5.96e4	1.34e2	3.06e1
iF06	120	1089	293	2639	1.78e4	1.74e2	3.71e1
iF08	70	631	326	2938	1.21e4	1.12e2	2.20e1
iF09	100.6	2355.6	620.8	5587.2	2.21e4	7.50e2	1.43e2
iF10	74	2671	402	3618	1.71e4	5.48e2	1.08e2
iF11	89	805	522	4704	2.12e4	9.27e2	1.80e2
iF12	79.5	715.6	558	5026	2.10e4	8.56e2	1.64e2
iF14	97	1876.2	489	4403	1.47e4	2.07e2	3.85e1
1F16	105	3945	589	5302	5.64e4	1.96e2	4.42e1
iF2A	119	3070	575	5175	3.85e4	2.70e2	5.84e1
Average	95.8	1809.1	478.3	4305.8	2.81e4	3.71e2	7.36e1
std	26.7	1030.5	111.9	1006.7	1.64e4	3.10e2	5.83e1
Average	95.8	1809.1	478.3	4305.8	2.81e4	3.71e2	7.36e1
std	26.7	1030.5	111.9	1006.7	1.64e4	3.10e2	5.83e1

Table 4.3: 0D closed-loop model parameter values for each animal as well as the average and standard deviation. The parameters common to all animals are: Ea_{LA} = 200 dyn/cm^5; Eb_{LA} = 400 dyn/cm^5; $V_{RA,0}$ = 4 ml; $V_{RV,0}$ = 10 ml; $V_{LA,0}$ = 4 ml; $V_{LV,0}$ = 5 ml; $C_{O0} = 7.36\,10^{-4}$ cm^5/dyn; $C_{D0} = 3\,10^{-4}$ cm^5/dyn.

Animals	M (g)	M_{ll} (g)	M_{ml} (g)	M_{rl} (g)
iF01	980	160	430	390
iF02	847	170	507	170
iF03	738	195	360	183
iF06	832	157	463	212
iF08	997	517	208	272
iF09	821	160	455	206
iF10	824	187	422	215
iF11	828	179	414	235
iF12	826	148	460	218
iF14	755	188	430	137
1F16	992	260	440	292
iF2A	918	167	415	336
Average	863.17	207.33	417.00	238.83
std	88.26	101.79	74.68	72.15

Table 4.4: Mass parameter values (using A4 estimation) for 0D closed-loop model for each animal as well as the average and standard deviation.

4.2 Results

Hepatic surgeons are particularly interested in specific pressure and flow values hypothesized to be linked to liver failure. Thus, here the variables of interest are: arterial pressure, portal vein pressure, the venous pressure drop $P_{pv} - P_v$ across the liver, portal vein flow and hepatic artery flow. Simulated and measured values are compared for these variables.

4.2.1 Pre-resection stage

The tuning procedure described above (section 4.1.3), based on pre-resection measurements, gives good agreement between pre-resection simulated and measured values. Figure 4.3 displays the simulated pressures and flows of interest against the measured ones in logarithmic scale. The dots in figure 4.3 are nicely aligned along the curve $y = x$ illustrating the good match between the results and measurements, for all pigs. Parameters are tuned for each animal, thus the inter-animal variability is well captured. Standard deviations for measured and simulated variables are: 10.4 mmHg for arterial pressure, 2.4 mmHg for portal vein pressure, 3.1 mmHg for the venous pressure drop across the liver, 0.06 L/min and 0.18 L/min for hepatic artery and portal vein flow rates respectively.

4.2.2 Liver partial resection simulation

Impact of liver lobe mass estimations The post-resection simulated variables are impacted by the estimation of the liver lobe masses. Thus, the simulations are run, with the four different mass estimations (Table 4.1), for twelve different pigs and compared with measurements. Table 4.5 shows mean and standard deviation of the relative error for the different variables and mass estimations. The arterial pressure and portal vein flow are almost

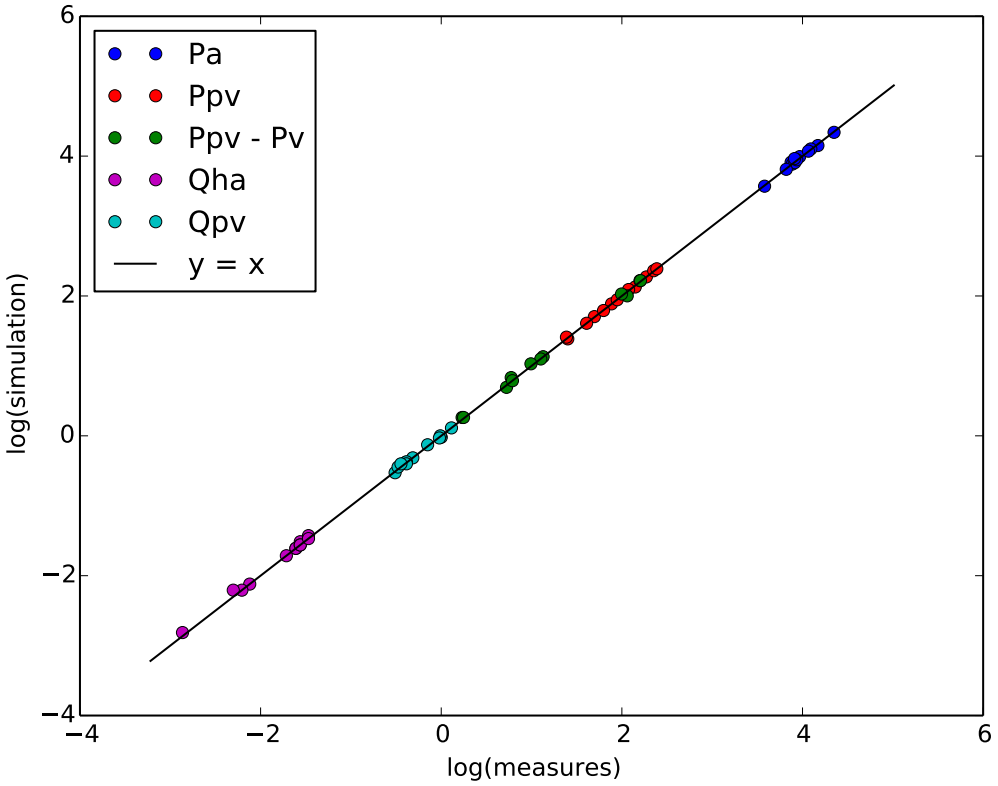

Figure 4.3: Pre-resection measurements vs simulation values in log/log scale, for each variable (unique color) and for each animal (one dot). Pressures are in mmHg and flow rates are in L/min.

Mass estimation	A1	A2	A3	A4
P_a	0.2 (0.18)	0.2 (0.18)	0.21 (0.18)	0.2 (0.18)
P_{pv}	0.28 (0.19)	0.46 (0.57)	0.47 (0.46)	0.37 (0.26)
$P_{pv} - P_v$	0.39 (0.26)	0.74 (0.89)	0.56 (0.49)	0.46 (0.38)
Q_{ha}	0.63 (0.59)	0.65 (0.75)	0.38 (0.27)	0.27 (0.27)
Q_{pv}	0.48 (0.62)	0.42 (0.59)	0.4 (0.6)	0.44 (0.6)

Table 4.5: Mean and standard deviation (in parenthesis) of relative error $\mathcal{E}_{rel}$ for all the 12 simulations, $\mathcal{E}_{rel} = |X_{simu} - X_{mes}| \,/\, |X_{mes}|$ with X_{simu} the simulated and X_{mes} the measured post-resection variable.

not impacted by the lobe mass differences (at most 20% difference). The lobe mass estimations have a significant impact on portal vein pressure (at most 68% difference), the venous pressure drop across the liver (at most 90% difference), and hepatic artery flow (140% maximum difference). The last mass estimation gives the smallest relative errors (in average), thus this mass estimation is kept for the rest of the simulations. As expected, it is the mass estimation the least predictive (A4) that gives the best simulation results.

Hepatectomy simulation The simulation results averages for twelve pigs are compared to the measurements (Figure 4.4) before and after resection. After liver resection, on average, 45% increase of portal vein pressure and 98% increase in pressure drop are measured. A small decrease in arterial pressure of 12% is observed. Moreover, a large decrease in hepatic artery flow, 74%, and a smaller decrease in portal vein flow, 30%, are measured. In the model, in average, 66% increase for portal vein pressure and 110% increase for pressure drop are simulated. The fact that these pressures increase is coherent with the measurements, but these increases are overestimated. The arterial pressure decrease is only 3%. The model underestimates the decrease of portal vein flow (5%), but captures well the HA flow decrease of 75%.

Taking into account changes in blood volume During surgery, the total volume of blood in the circulation varies. Estimating its loss or gain is complex. However, pressures are strongly linked to the circulating blood volume. Thus, the changes observed in arterial pressure measurements are used to estimate the change in blood volume. The volume added or removed is chosen such that the simulated post-resection arterial pressure corresponds to the measurement. Therefore a decrease of 12% in arterial pressure is obtained with the model. Figure 4.4 displays the simulated variables, taking into account the change in blood volume, averaged over twelve pigs. Pressures are largely impacted by changes in blood volume. The model agrees well with the measurements for portal vein pressure and venous pressure drop, with increases of 43% and 82% respectively. Hepatic artery flow is still correctly simulated, with a 79% decrease, and portal vein flow is improved, with 23% decrease, however is still overestimated.

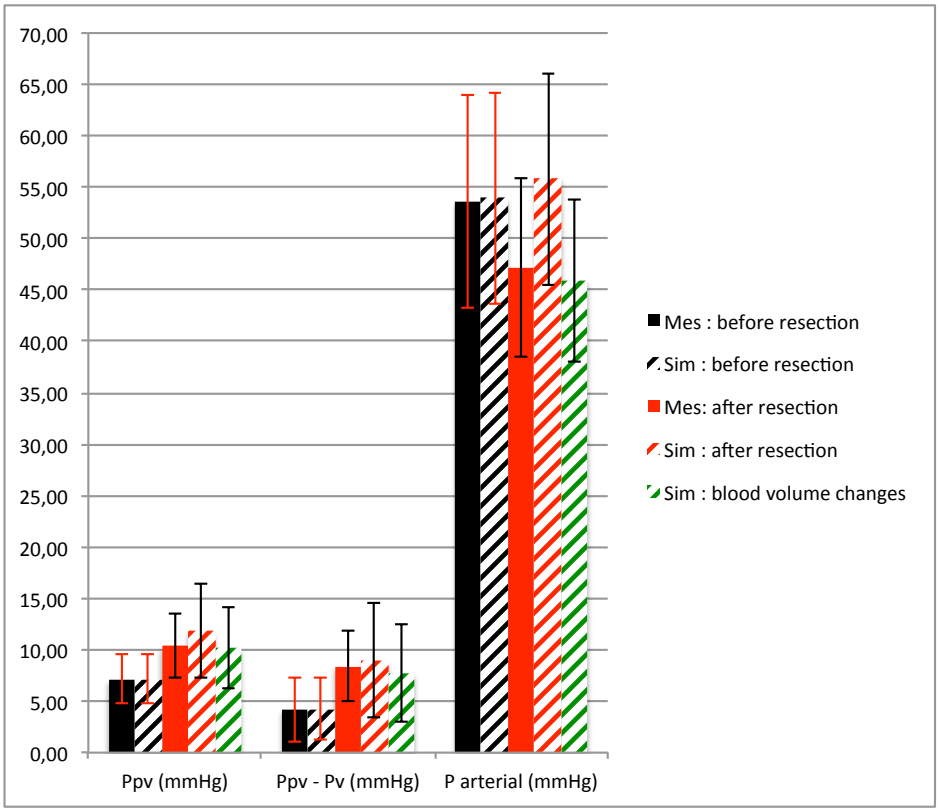

(a) Pressures

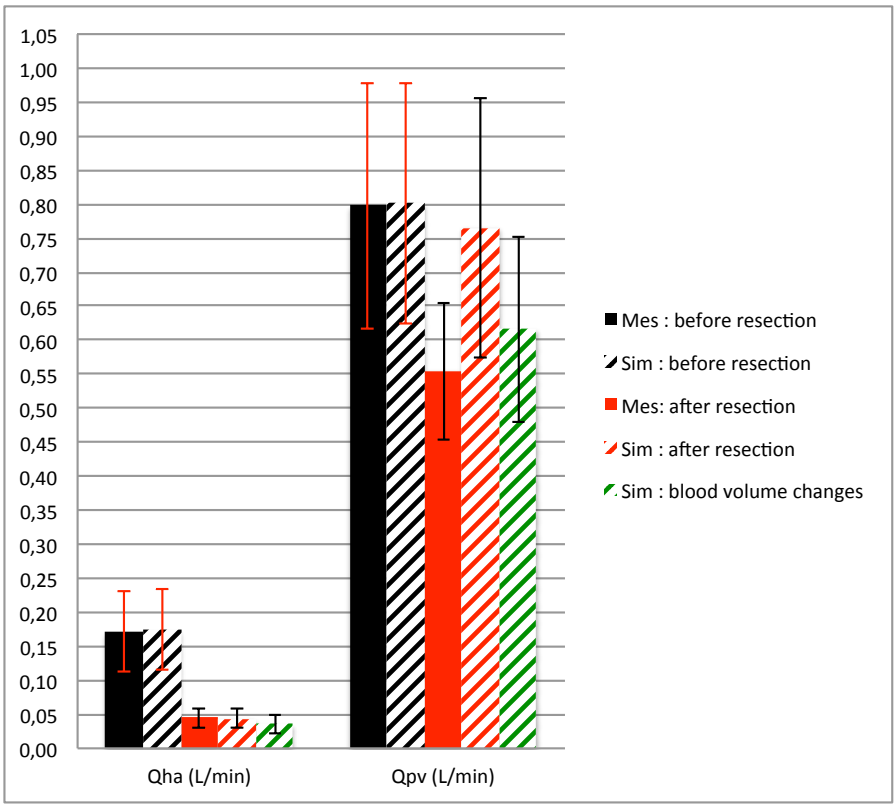

(b) Flows

Figure 4.4: Measurements (full) and simulations (dash) at different states of the surgery: pre-resection, post-resection. Simulations with (dashed green) and without (dashed red) blood volume changes are represented for the A4 mass estimation.

	Before resection	After resection	
		Blood volume constant	Blood volume changes
p-value	$3.3\ 10^{-23}$	0.94	0.027
result	Rejected	Not rejected	Rejected

Table 4.6: p-values for TOST test between the 12 simulated post-resection variables and measurements. The simulations include or not the changes in blood volume.

Similarity of measured and simulated populations The model ability to reproduce the animal population variability is verified with a two one-sided t-test. The A4 mass estimation is used to perform the simulations (section 4.1.1). The test is performed with and without blood volume changes. For each variable of interest and each simulation the relative error is computed. The test is performed on the obtained relative error vectors. The results and p-values are given in Table 4.6. According to the test p-values the null hypothesis is rejected for the pre-resection simulation, with 10% relative error for indifference region. More precisely, the simulated variables and the measurements, before resection, are significantly similar. The null hypothesis is not rejected for post-resection simulation without blood loss changes, with 10% relative error for indifference region. Meaning, there is insufficient evidence to reject the null hypothesis. This result may occur, because the model output and the measurements really differ or because the sample size is too small to conclude. Finally, with a 10% relative error indifference region, post-resection simulation with blood volume changes and measurements are significantly similar: the null hypothesis is rejected (Table 4.6). Taking into account blood volume changes knowing the change in arterial pressure, improves model outputs.

4.3 Discussion and conclusions

Measurements explained by modeling The behavior of the measured pressures and flows during 75% hepatectomy are analyzed using the model. The observed hepatic artery flow decrease corresponds exactly to the increase of the hepatic artery tree resistance due to the 75% liver resection. A main mechanism to regulate the liver inflow is the hepatic arterial buffer response (HABR). This mechanism consists in the hepatic artery dilation or constriction to compensate for the changes in the portal vein flow (see section 1.1.2 for details). Here, the hepatic artery flow is correctly simulated with the model, without HABR being needed. After 75% partial hepatectomy on pigs, the HABR does not seemed activated. At leading order, the liver arterial system behaves as $\Delta P = RQ$, with ΔP the arterial pressure drop, which remains almost constant, R the liver resistance and Q is the hepatic artery flow. The 75% liver resection induces the hepatic artery tree resistance increase of 75%, thus explaining the decrease of hepatic artery flow. The arterial pressure is not impacted by the liver resection because the hepatic artery and liver resistances are small compared to the rest of the systemic circulation. However, in average, it decreases by 12% in the measurements. This decrease is a consequence of the blood loss, as proven with the model. Portal vein flow measurements, in average, decrease by 30%. The main decrease is due to blood (volume) loss. This is reinforced by the fact that animals with larger blood losses have a more important portal vein flow

decrease. However the simulations show that liver resection tends to decrease portal flow by around 5%. The measured portal vein pressure and venous pressure drop increase by 45% and 98% respectively. The portal pressure increase is expected given the increase of portal vein tree and liver resistances due to resection. However it is compensated by three mechanisms: interaction with the rest of the circulation which causes portal vein flow to decrease, the lessen increase in portal vein tree resistance due to dilation and the general pressure decrease due to blood loss. Indeed, the simulations without blood volume change predict a 66% increase of portal pressure and adding the blood losses the increase is 43%. If the venous pressure remains constant during surgery, the pressure drop would increase by 110% as simulated with the model. However, the measured central venous pressure decreases by 33%. Thus, the blood losses lead to all venous pressures decrease, and an increase in the estimated pressure drop estimated as 82% in the simulations.

Sensitivity and variability The liver lobe mass estimations impact the post-resection simulated variables due to the fact that the liver lobe resistances and capacitances depend on lobe masses. The mostly impacted variables are portal vein pressure, the venous pressure drop and HA flow. This is expected since arterial pressure and portal flow are strongly dependent on heart and digestive organs parameters respectively. A better estimation of the liver lobe masses may improve post-resection simulated variables. The mass estimation (A4) gives the best results, however this estimation is not predictive. In order to be predictive, the liver lobe segmentation with CT-scan requires improvement to obtain better liver lobe masses estimation.

Moreover, several events happen during the surgery due to surgical acts, anesthetists interventions etc. Here, the model demonstrates that taking into account the change in blood volume improves the simulated post-resection prediction, knowing e.g. the change in arterial pressure measurements.

In terms of variability, the simulated results are in good agreement with the measurements, both for pre-resection and post-resection with blood volume changes, according to the two one side t-tests. The tests also show that taking into account blood volume changes significantly improved the model outputs agreement with the measurements.

Pressure and flow changes due to hepatectomy without any volume change are also simulated with the model. Theses results may represent the state after the surgery, once the blood volume is back to the pre-resection volume. Under this assumption, the portal pressure and pressure drop, important for liver failure [AAB+13], may be underestimated with intraoperative measurements. Thus, for a 75% liver ablation, the model predicts an increase, in the following post-operative days of 110% instead of 82% for the venous pressure drop across the liver and 66% instead of 43% for portal pressure.

The simulation results for each animal are presented in Table 4.3. Among animals, various post-resection behaviors are obtained with the simulations. For example, without change in blood volume, for animal iF03 portal vein flow is almost unchanged (decrease by 1.7 %) compared to iF12 for which it decreases by 13% (Table 4.3). The simulated blood volume change is adapted on an animal basis to the arterial pressure change. For animal iF02 a loss of 200 ml is simulated compared to animal iF08 for which a volume infusion of 200 ml is

modeled (Table 4.3). Therefore, the model is able to simulate the different hemodynamics states that occur after liver resection.

Future work In summary, this work presents the first dynamical model of liver ablation. Its validation based on pig data is promising; the model is able to capture and explain the main features of hemodynamics changes due to the surgery as well as its variability among pigs, and may give insights about other states (e.g. day post-surgery) when measurements are difficult to take. The hepatic arterial buffer response does not seem required to explain the data. Future work will include the adaptation of the liver model to human liver anatomy. Moreover, in this work, several pressure and flow measurements were available at different stages of the surgery. The pre-resection measurements were used for parameter tuning. In patient surgeries less measurements are available. Furthermore, the model and measurements in this work are for a healthy (pig) liver. However the liver of the patients treated with partial hepatectomy is generally not healthy. For example, collateral circulations can appear [PV05], and the liver resistance and capacitance parameters can change. Thus, future work is needed to integrate these considerations. Despite this, the framework in place can easily be adapted to include various measurements and different pathologies for clinical applications. Finally, the model can be a basis to compute how to control the portal flow in order to avoid liver-failure related hemodynamics ranges [IYT+07, VCZ14, SBSC+11, AAB+13].

Animals	iF01	iF2	iF3	iF6	iF8	iF9	iF10	iF11	iF12	iF14	iF16	iF2A
P_a (mmHg)												
Sim: pre	63.5	50	48.7	49.7	35.5	60.5	54.2	51.8	58.6	45.2	76.7	52.7
Mes: pre	64.8	48.1	48.8	50.1	35.9	59.9	52.9	51.2	58.3	45.6	77.4	50.0
Sim: post constant vol	64.1	52.4	49.4	51.5	36.6	63.7	57.9	53.6	60.6	48	78.3	53.6
Mes: post	60.8	31.9	51.4	43.8	34.9	55.1	54.1	45.8	51.5	42.1	53.0	41.6
Sim: post vol change	56	28.5	49.4	38.5	41.3	52.3	50.4	43.9	49.9	48	53.7	39.2
Vol change (ml)	-200	-700	0	-400	200	-300	-200	-300	-300	0	-500	-400
P_{pv} (mmHg)												
Sim: pre	6.6	5.5	7.0	8.4	6.0	8.1	9.7	10.6	10.9	4.0	5.0	4.1
Mes: pre	6.6	5.5	7.0	8.6	6.0	8.0	9.7	10.5	10.9	4.1	5.0	4.0
Sim: post constant vol	8.2	10.0	9.1	12.6	7.8	16.6	17.3	17.9	19.1	8.7	8.5	6.5
Mes: post	10.6	7.8	10.6	9.6	10.4	9.0	15.1	13.6	11.5	14.0	8.8	3.6
Sim: post vol change	7.4	6.3	9.1	10.0	8.7	14.2	15.5	15.2	16.3	8.7	6.4	5.1
Vol change (ml)	-200	-700	0	-400	200	-300	-200	-300	-300	0	-500	-400
$P_{pv} - P_v$ (mmHg)												
Sim: pre	2.0	2.3	1.3	3.1	1.3	7.4	7.6	9.2	9.2	2.2	3.0	2.8
Mes: pre	2.1	2.2	1.3	3.1	1.3	7.8	7.4	9.0	9.1	2.2	3.0	2.7
Sim: post constant vol	3.6	6.8	3.4	7.3	3.2	15.9	15.3	16.5	17.4	6.9	6.5	5.2
Mes: post	7.4	5.5	8.8	4.2	4.9	6.6	13.6	13.9	10.2	12.7	7.7	5.5
Sim: post vol change	3.4	4.6	3.4	6.1	3.5	13.7	13.7	14.0	14.9	6.9	5.0	4.2
Vol change (ml)	-200	-700	0	-400	200	-300	-200	-300	-300	0	-500	-400
Q_{ha} (L/min)												
Sim: Pre	0.12	0.22	0.06	0.2	0.2	0.21	0.24	0.18	0.21	0.23	0.11	0.11
Mes: Pre	0.12	0.21	0.057	0.2	0.2	0.21	0.23	0.18	0.21	0.23	0.11	0.1
Sim: Post constant vol	0.05	0.04	0.01	0.05	0.06	0.05	0.06	0.05	0.05	0.04	0.03	0.04
Mes: Post	0.06	0.06	0.017	0.05	0.03	0.04	0.05	0.05	0.07	0.03	0.04	0.04
Sim: Post vol change	0.04	0.02	0.01	0.04	0.06	0.04	0.05	0.04	0.04	0.04	0.02	0.03
Vol change (ml)	-200	-700	0	-400	200	-300	-200	-300	-300	0	-500	-400
Q_{pv} (L/min)												
Sim: pre	0.98	1	0.59	1.12	0.73	0.68	0.88	0.64	0.69	0.67	0.97	0.67
Mes: pre	1	0.99	0.6	1.12	0.73	0.67	0.86	0.62	0.68	0.68	0.98	0.64
Sim: post constant vol	0.96	1	0.58	1.1	0.71	0.61	0.81	0.56	0.6	0.64	0.95	0.66
Mes: post	0.61	0.31	0.53	0.65	0.56	0.46	0.68	0.5	0.55	0.59	0.66	0.56
Sim: post vol change	0.84	0.52	0.58	0.78	0.8	0.49	0.69	0.45	0.49	0.64	0.64	0.48
Vol change (ml)	-200	-700	0	-400	200	-300	-200	-300	-300	0	-500	-400

Table 4.7: Simulation results (Sim) and measurements (Mes) for the 12 different pigs before resection (pre), after resection with constant blood volume (post constant vol) and after resection with constant blood volume (post vol change) for : arterial pressure P_a, portal vein pressure P_{pv}, venous pressure drop across the liver $P_{pv} - P_v$, hepatic artery flow Q_{ha} and portal vein flow Q_{pv}. The amount of volume added or removed for the simulation is given (vol change line).

Chapter 5

Liver lumped model

In the previous chapter 4, the proposed model reproduces the averaged post-resection measurements, using the pre-resection measurements for parameter estimation. In the previous model, the liver model has a lobar structure and the lobe vascular trees are assumed similar. Moreover, the lobe parameters are assumed mass-dependent. In this chapter, these assumptions are kept and the hepatic artery tree model of one liver lobe is improved to reproduce the observed flow waveform in the hepatic artery.
The flow waveform in the hepatic artery is studied with a lumped model imposing the measured pressure in the hepatic artery. After the 75% partial hepatectomy only one main liver lobe remains (see Part I for details). Therefore, the post-resection hepatic artery measurements (pressure and flow) are the basis for parameter estimation of the hepatic artery tree model in one liver lobe. The unscented Kalman filter algorithm is used for parameter estimation. Once the lobar parameters are known, with the assumption that parameters are mass-dependent, a pre-resection liver model is built. The pre-resection simulation results are then compared to the measurements.

This chapter is organized in the following manner. In section 5.1, two models are proposed for the hepatic artery tree in a liver lobe and the inverse problem is defined. In section 5.2, the results of the parameter estimation procedure are shown. Then, the two proposed models are compared and the pre-resection liver model is constructed. The simulation results are compared to pre-resection measurements. Discussion and conclusions end this chapter.

Contents

5.1 Methods 83
5.1.1 Hepatic artery tree model 83
5.1.2 Parameter estimation 85
5.2 Results 85
5.2.1 CR-model and RCR-model 85
5.2.2 Pre-resected liver model 85
5.3 Discussion and conclusions 88

$$\frac{CR_pR_d}{M}\dot{Q_{ha}}(t) + \frac{R_p + R_d}{M}Q_{ha}(t) = CR_d\dot{P_{ha}}(t) + P_{ha}(t) - P_t$$

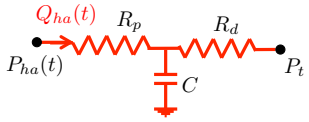

$$\frac{R}{M}Q_{ha}(t) = P_{ha}(t) - P_t + RC\dot{P_{ha}}(t)$$

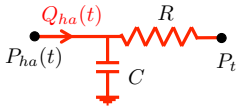

Figure 5.1: Schematic representation of the CR and RCR Windkessel models. The model equations are recalled, where the resistance and capacitance are mass dependent parameters.

5.1 Methods

5.1.1 Hepatic artery tree model

As mentioned before, the pig liver is composed of three main lobes [CWHM+03]. Two of the three lobes are removed during the 75% partial hepatectomy. The hepatic artery tree is composed of three main branches and after the liver resection only one of them remains. The hepatic artery pressure and flow are measured during the surgery. Assuming the three liver lobes have similar hepatic artery tree architectures, the post-resection measurements can be used to identify the hepatic artery tree model and the model parameters.

The liver lobe hepatic artery tree is composed of medium and small arteries as well as capillaries. The model requires to represent the elasticity and storage capacity of the larger arteries and the dissipation of the smaller arteries and capillaries. Moreover, to enable parameter estimation, a model with a small number of parameters is required. In this work the inertia is neglected. From [SLH11], two lumped models are considered, a CR-Windkessel model and a RCR-Windkessel model (Figure 5.1). These two models, are simple enough for parameter estimation and give relatively good approximation of arterial network [SLH11, WES71].

The boundary conditions are the hepatic artery pressure and the liver tissue pressure. The hepatic artery flow is the output of the model. The liver tissue pressure is assumed constant over time. During the surgery the central venous pressure and the portal vein pressure are measured (see part I). Using 20-second averaged pressure, the time-averaged tissue pressure is computed, assuming the liver tissue and the hepatic veins carry 20% of the pressure drop between the portal vein and the central venous pressures [DDWC+12]. The hepatic artery pressure (time-varying) is imposed using Fourier series (30 coefficients) to approximate the measurements (Figure 5.2). The liver lobe resistances are assumed proportional to the inverse of the lobe mass. While, the capacitance is assumed proportional to the lobe mass. Thus, mass parameters are estimated. The remaining lobe mass is a fixed parameter and it is estimated using the post-operative CT-scan.

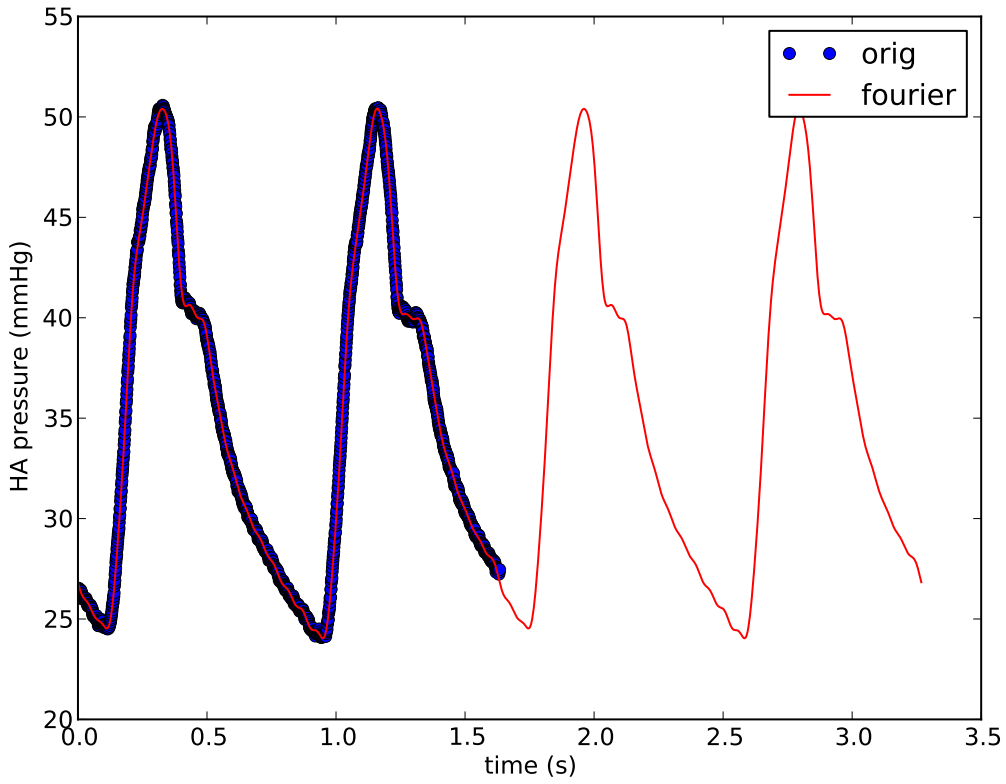

Figure 5.2: Hepatic artery pressure over time: measurements (dot) and approximation obtained with 30 coefficients Fourier series (solid line).

5.1.2 Parameter estimation

The unscented Kalman filter (UKF) is used to estimate the parameters. Details on this method can be found in [PFGVC14, BMG12, MC11, JUDW95]. Appendix A recalls the inverse problem and UKF algorithm definitions. The hepatic artery pressure and the tissue pressure are the model inputs. The hepatic artery pressure over time measurements are displayed in Figure 5.6. The measurements of the hepatic artery flow are used as observations to estimate the CR or RCR parameters.

5.2 Results

5.2.1 CR-model and RCR-model

The C and R parameters of the CR model are estimated with the UKF algorithm. Figures 5.3 and 5.4 display the results for four animals (green lines). The observations curves are well fitted (except of pig 5) and the parameter values converge after few cardiac cycles.
Then, the UKF algorithm is used to estimate the RCR parameters of the hepatic artery tree model for the same four animals (blue lines). Figure 5.3 and 5.4 show the results. The observations curves are well fitted for the first three subjects. For pig 5, some parts of the observations curve are mismatched. The parameter values converge rapidly after few cardiac cycles.

With both models, after few cardiac cycles, the parameters have converged and the observations curve is reasonably matched for all animals. For each animal (except of pig 5), the estimation of CR resistance R and of the RCR distal resistance R_d are similar. The capacitance estimation for the CR model is smaller than for the RCR model. The main difference between the CR and RCR simulations is the amplitude of the hepatic artery flow. It seems that adding a proximal resistance improves the match between simulations and measurements. Relative errors between measurements and simulation results are computed to quantify the difference between the two models:

$$\mathcal{E}_{+\infty} = \frac{\|Q_{ha_{obs}} - Q_{ha_{sim}}\|_{+\infty}}{\|Q_{ha_{obs}}\|_{+\infty}} \; ; \; \mathcal{E}_2 = \frac{\|Q_{ha_{obs}} - Q_{ha_{sim}}\|_2}{\|Q_{ha_{obs}}\|_2}$$

The averaged errors over the four animals for CR model are $\mathcal{E}_{+\infty,CR} = 0.44$ and $\mathcal{E}_{2,CR} = 0.33$ and for the RCR model $\mathcal{E}_{+\infty,RCR} = 0.2$ and $\mathcal{E}_{2,RCR} = 0.16$. Therefore the RCR Windkessel model is chosen to represent the hepatic artery tree in a liver lobe.

5.2.2 Pre-resected liver model

Now that the hepatic artery tree model has been selected, a complete liver lumped model is proposed. The model includes the portal vein trees, liver tissue and the hepatic vein trees (Figure 5.5). The portal vein tree is represented by a single (constant) resistance and the liver tissue and the hepatic vein trees are modeled by a capacitance and a resistance. The model

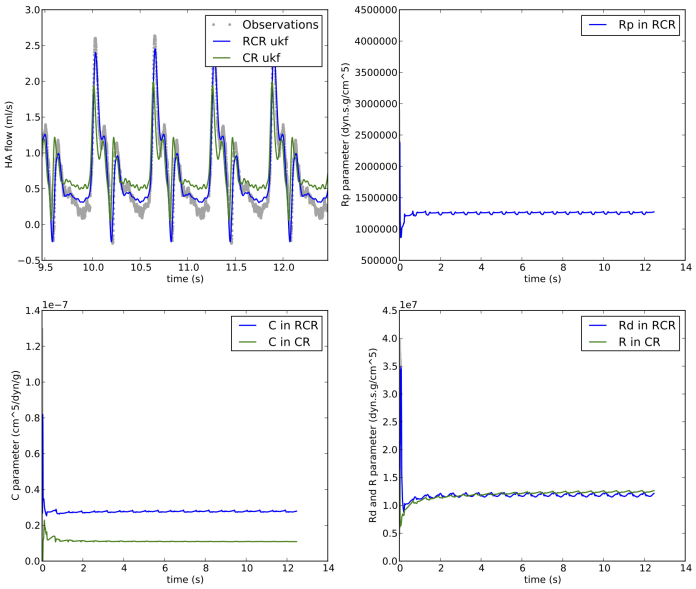

(a) Pig 1

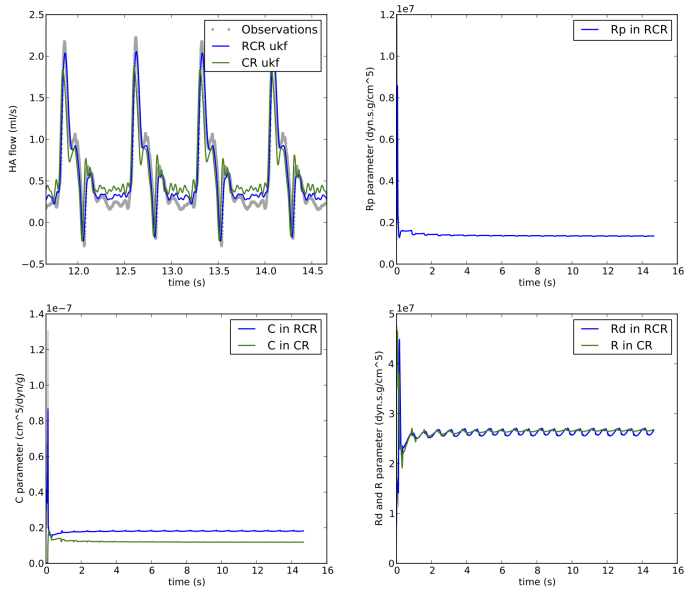

(b) Pig 2

Figure 5.3: Unscented Kalman filter results for CR (green solid line) and RCR (blue solid line) models, for two animals. For each figure: top left: hepatic artery flow measured (grey dot) and simulated (solid line), with both models, for few cardiac cycles after parameters convergence; top right: R_p parameter estimation over time for the RCR model; bottom left: C parameter estimation over time for CR and RCR model; bottom right: R and R_d parameter estimations over time for CR and RCR model respectively. The grey zone is the geometric variance of the estimated parameter.

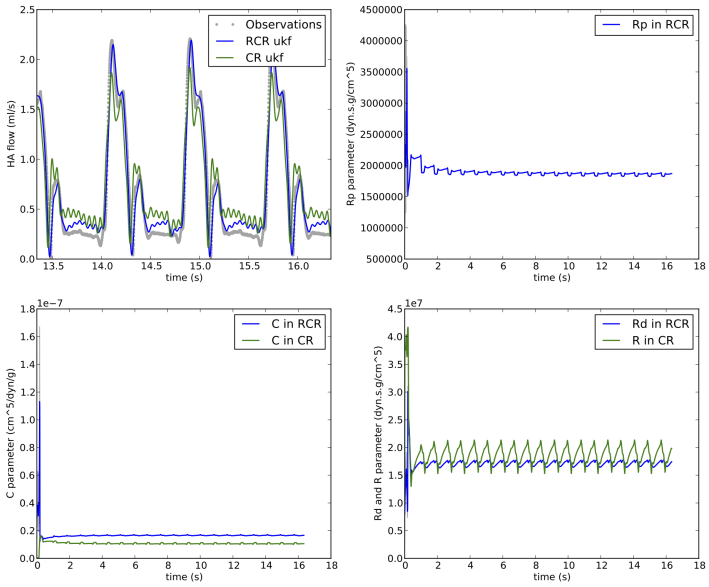

(a) Pig 4

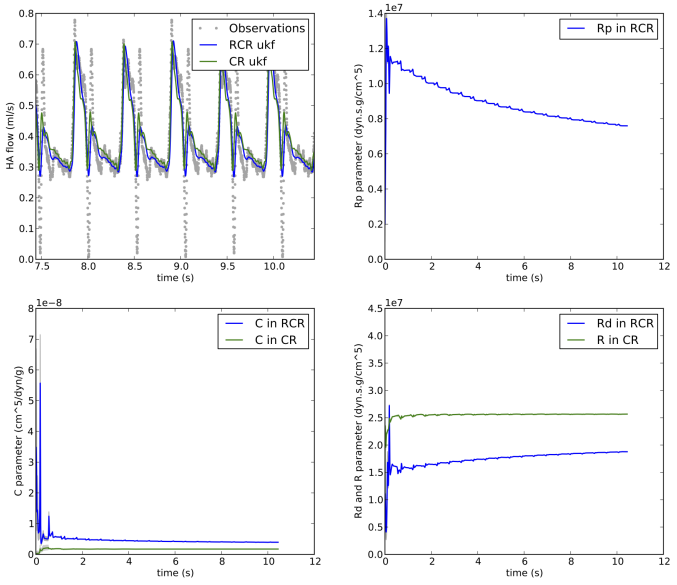

(b) Pig 5

Figure 5.4: Unscented Kalman filter results for CR (green solid line) and RCR (blue solid line) models, for two animals. For each figure: top left: hepatic artery flow measured (grey dot) and simulated (solid line), with both models, for few cardiac cycles after parameters convergence; top right: R_p parameter estimation over time for the RCR model; bottom left: C parameter estimation over time for CR and RCR model; bottom right: R and R_d parameter estimations over time for CR and RCR model respectively. The grey zone is the geometric variance of the estimated parameter.

equations read:

$$\begin{cases} P_{ha} - P_{ha,i} & = R_{p_{ha}} Q_{ha,i}/M_i \\ P_{ha,i} - P_{t,i} & = R_{d_{ha}} Q_{ha_1,i}/M_i \\ C_{ha} M_i \dfrac{dP_{ha,i}}{dt} & = Q_{ha,i} - Q_{ha_1,i} \\ P_{pv} - P_{t,i} & = R_{pv} Q_{pv,i}/M_i \\ P_{t,i} - P_v & = R_l Q_{v,i}/M_i \\ C_l M_i \dfrac{dP_t}{dt} & = Q_{ha1,i} + Q_{pv,i} - Q_{v,i} \end{cases} \tag{5.1}$$

where P_{ha}, P_{ha_i} are respectively the hepatic artery pressure and the pressure after the hepatic artery tree proximal resistance in lobe i. P_{pv}, $P_{t,i}$ and P_v are respectively the pressure for portal vein, ith lobe tissue and venous pressure. $Q_{ha,i}$, $Q_{ha_1,i}$, $Q_{pv,i}$ and $Q_{v,i}$ are hepatic artery flow, hepatic artery flow arriving to liver tissue, portal vein and hepatic venous flows in lobe i respectively. M_i is the lobe i mass estimation. $R_{p_{ha}}$ and $R_{d_{ha}}$ are proximal and distal mass-resistances for hepatic artery tree. R_{pv} and R_l are mass-resistances for portal vein tree, and liver tissue and hepatic venous tree. C_{ha} and C_l are the capacitances per liver mass for the hepatic artery tree and the liver tissue respectively (Figure 5.5).
Lobar parameters are set in the following manner, assuming the intrinsic lobe parameters do not change during the surgery. R_{pv}, R_l and C_l are estimated, with the pre-resection measurements, in the same manner as described in chapter 4. The hepatic artery parameters $R_{p_{ha}}$, $R_{d_{ha}}$ and C_{ha} are estimated as detailed above 5.1, with the post-operative measurements. The remaining parameter is the liver lobe mass. The lobe masses are estimated with the resected mass (the two removed lobes are weighted after the surgery) and with the post-operative CT-scan (for the remaining liver mass).

The forcing conditions are the portal vein flow (Q_{pv}), the venous pressure (P_v) and the hepatic artery pressure ($P_{ha}(t)$). The portal vein flow and the venous pressure are assumed constant over time. For these two conditions, the pre-resection measurements averaged over 20 seconds are imposed (Table 5.1). The hepatic artery pressure curve over time measured before liver resection is approximated with Fourier series and it is used as forcing condition. The hepatic artery pressure measurements curves before and after the liver resection are plotted in Figure 5.6.
For each animal, the simulation is run and the resulting hepatic artery flow is then compared to the hepatic artery flow over time measured before liver resection. Figure 5.7 shows the simulated hepatic artery flows and pre-resection measurements for the four animals. The simulated hepatic artery flow waveforms do not match well the pre-resection measurements, for the four animals. However, the resistance seems correctly set (except for pig 5), as well as the individual key shape features.

5.3 Discussion and conclusions

The RCR-Windkessel model parameters are successfully estimated with the UKF algorithm. The hepatic artery flow measured after 75% partial hepatectomy in four pigs is well matched with an RCR-Windkessel model given the hepatic artery pressure over time and an estimation of the liver tissue pressure (constant over time). From the estimated parameters for one liver

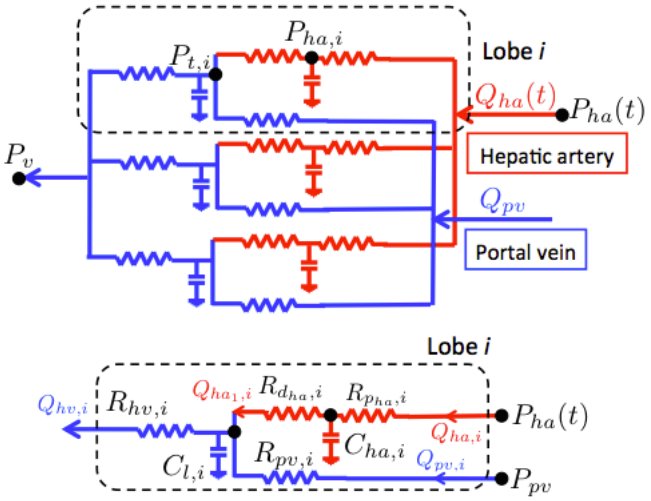

Figure 5.5: Schematic representation of pre-resection 3-lobes liver lumped model.

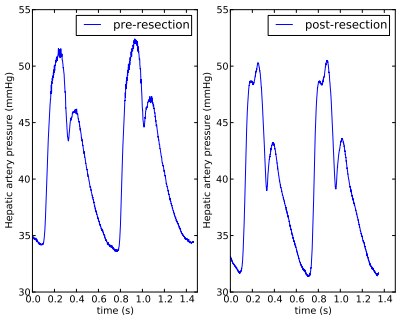

(a) Pig 1

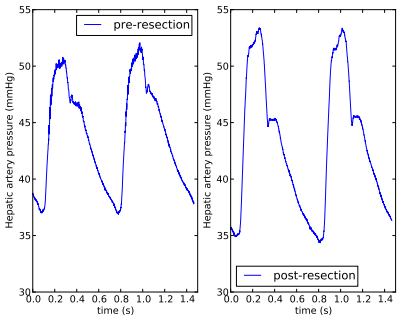

(b) Pig 2

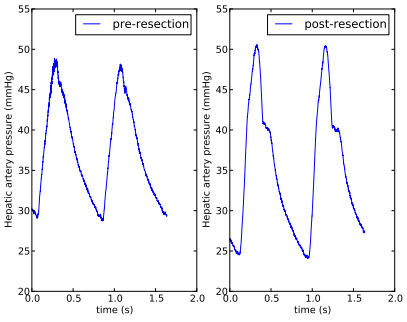

(c) Pig 4

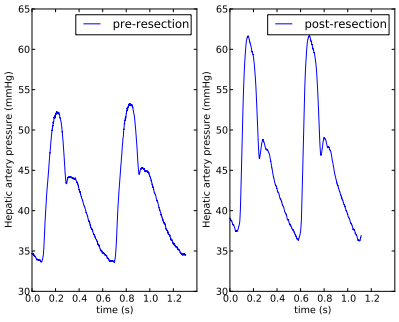

(d) Pig 5

Figure 5.6: Hepatic artery pressure (mmHg) measurements over two cardiac cycles, before and after liver resection for four pigs.

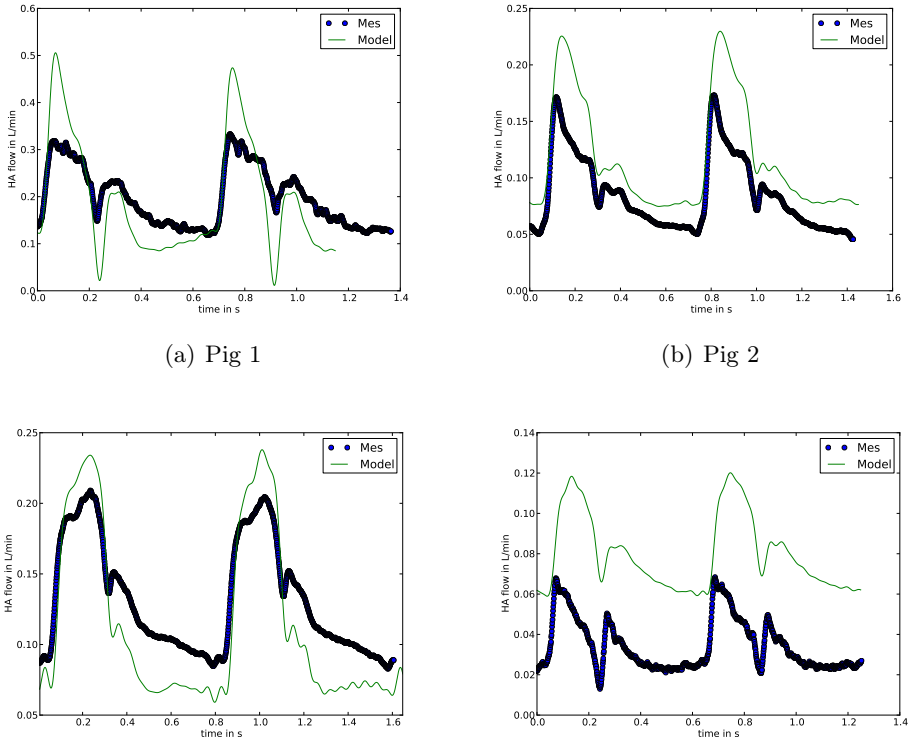

(a) Pig 1

(b) Pig 2

(c) Pig 4

(d) Pig 5

Figure 5.7: Hepatic artery flow (l/min) over two cardiac cycles, 3-lobe model simulation results (solid line) and pre-resection measurements (dot) for four pigs.

Pig	1	2	4	5
	Post-resection			
Tissue pressure (mmHg)	6.3	2.6	6.1	3.6
Right lobe mass (g)	212	292	351	183
	Pre-resection			
Venous pressure (mmHg)	5.5	2	5.9	5.8
Portal vein flow (l/min)	1.13	0.98	0.74	0.6
Left lobe mass (g)	157	260	156	195
Median lobe mass (g)	463	440	391	360

Table 5.1: Imposed boundary conditions and fixed parameters for forward and inverse problems.

lobe, the parameters for the three-lobe model are estimated, assuming that: 1) the hepatic artery tree of the three lobes are similar; 2) the lobe capacitance is proportional to lobe mass; 3) the lobe resistance is proportional to lobe mass inverse. The pre-resection hepatic artery flow measurements and the simulation results with the three lobes model do not match well. Several hypotheses can explain the mismatch between the predicted pre-operative results and the measurements. First, the parameters can change due to the surgery, as vessel dilation or other phenomena can occur. Then, the parameters proportionality to lobe mass or lobe mass inverse may be incorrect. Finally, the structure of the hepatic artery tree may differ from a liver lobe to another. In rats, the portal vein and hepatic vein vascular structure are lobe-specific [DDWC+12]. Therefore, it may be the same for the hepatic artery tree.
From this study, the link between hepatic artery pressure and flow is better understood. Indeed, the hepatic artery flow measured after liver resection is reproduced with an RCR Windkessel model (imposing the measured pressure in the hepatic artery and an estimation of the pressure in liver tissue). However, the pre-resection hepatic artery flow is only grossly recovered from the post-resection parameters estimation.
To reproduce the change of waveform between before and after the liver resection, the pressure and the flow need to be simulated (as both are changing). Moreover, to study waveform changes it is natural to consider a model capable to deal with wave propagation. In the next chapter, a 1D-0D closed-loop model is proposed to model the change of waveforms in the hepatic artery during partial hepatectomy. The hepatic artery tree lumped model proposed here is used in the next chapter, since it grossly reproduces the pre-resection waveform and that it gives good approximation of the post-resection flow waveform.

Chapter 6

Kinetic scheme for arterial and venous blood flow

This chapter presents comparisons of a closed-loop 1D-0D model with real measurements obtained after partial hepatectomy in pigs. To solve the 1D Euler equations of hemodynamics a kinetic scheme is introduced. First, several benchmark tests show that the kinetic scheme compares well with more standard schemes used in the literature, for both arterial and venous wall laws. In particular, it is shown that it has a good behavior when the section area of a vessel is close to zero, which is an important property for collapsible or clamped vessels. Then, the application to liver surgery shows that a model of the global circulation, including 0D and 1D equations, is able to reproduce the change of waveforms observed after different levels of hepatectomy. This may contribute to a better understanding of the change of liver architecture induced by hepatectomy.

The chapter is organized as follows. In Section 6.1, the hyperbolic equations are recalled and the kinetic scheme is described, along with tube laws for artery and vein walls, the boundary and coupling conditions. The kinetic scheme is validated on benchmark cases, for both arterial and venous flows. In Section 6.2, the closed-loop 0D-1D model is presented and the effects of partial hepatectomy are studied numerically and compared with experimental observations. Section 6.3 ends the chapter, with some conclusions and perspectives.

The results presented in this chapter lead to the accepted manuscript : C. Audebert, P. Bucur, M. Bekheit, E. Vibert, I.E. Vignon-Clementel, J-F. Gerbeau, *Kinetic scheme for arterial and venous blood flow, and application to partial hepatectomy modeling.* Computer Methods in Applied Mechanics and Engineering 2017.

Section 6.1.3 and two of the four arterial benchmarks (Common carotid artery and Thoracic aorta) presented in section 6.1.5 are exclusively published in this thesis chapter.

Contents

6.1 Kinetic scheme for arterial and venous blood flow 95
6.1.1 The Euler equations of hemodynamics 95
6.1.2 The kinetic scheme 96
6.1.3 Arteries and veins tube laws 98
6.1.4 Boundary treatments 102
6.1.5 Benchmark test cases 103
6.2 Application to hepatectomy 115
6.2.1 A closed-loop model 115
6.2.2 Discussion 124
6.3 Conclusions 126

6.1 Kinetic scheme for arterial and venous blood flow

6.1.1 The Euler equations of hemodynamics

Blood flow in large vessels of the cardiovascular system can be represented with a collection of one-dimensional systems of nonlinear equations

$$\left\{\begin{array}{rcl} \partial_t A + \partial_x(Au) & = & 0 \\ \partial_t(Au) + \partial_x(\kappa A u^2) + \dfrac{A}{\rho}\partial_x p & = & Ag - f(A, A_0, u), \end{array}\right. \tag{6.1}$$

The first equation corresponds to mass conservation and the second to momentum conservation. $x \in \mathbb{R}$ denotes the coordinate along the longitudinal axis of the portion of vessel, $t \in \mathbb{R}^+$ is the time, $A(x,t)$ is the vessel cross-section area, $u(x,t)$ is the mean velocity of blood through the corresponding cross-section, ρ is the fluid density assumed constant, g denotes the gravity along the longitudinal axis, $f(A, A_0, u)$ is a friction term, and κ is a momentum-flux correction coefficient, assumed to be equal to 1 in this work.

These equations have been used by many authors (e.g. [HL73, GPCP90, Olu99, FLQ03, SFPF03, VT04, MAP+07, AKM+11, WDF+12, KLH+15, ATR+16] to only name a few). Many variants exist, for example in the treatment of dissipation, viscoelasticity, curvature, momentum-flux correction coefficient, *etc.* Here we choose the simplest form of these different components, adding complexity through gravity and dissipation as needed by the test cases. The mean pressure $p(x,t)$ in a cross-section is related to the cross-section area through an algebraic constitutive law

$$p(x,t) = P_0(x) + \psi\left(A(x,t), A_0(x), \beta(x)\right),$$

where $A_0(x)$ is a reference area, $P_0(x)$ is the pressure when $A(x,t)$ is equal to $A_0(x)$, $\beta(x)$ is a parameter representing the vessel stiffness, and ψ is a given function characterizing the "tube law". The details regarding the tube law for this work can be found in [FLQ03, FQV09] for arteries, and in [Sha77, PBS96, BP02, MMT12] for veins. Eliminating the pressure from system (6.1) gives

$$\left\{\begin{array}{rcl} \partial_t A + \partial_x(Au) & = & 0 \\ \partial_t(Au) + \partial_x(Au^2) + \dfrac{A}{\rho}(\partial_A\psi)\partial_x A & = & Ag - f(A, A_0, u) \\ & - & \dfrac{A}{\rho}\left(\partial_x P_0 + (\partial_{A_0}\psi)\partial_x A_0 + (\partial_\beta\psi)\partial_x\beta\right) \end{array}\right. \tag{6.2}$$

In order to write the system in conservative form, the term $\dfrac{A}{\rho}(\partial_A\psi)\partial_x A$ is reformulated

$$\frac{A}{\rho}(\partial_A\psi)\partial_x A = \frac{1}{\rho}\partial_x\left(\int_{\varepsilon A_0}^{A(x,t)} a\partial_a\psi(a,A_0,\beta)da\right) = \partial_x\left(\int_{\varepsilon A_0}^{A(x,t)} c^2(a)da\right) \tag{6.3}$$

where ε is a constant whose value will be discussed later, and $c(A) = \sqrt{\frac{A}{\rho}\partial_A\psi}$ is the wave

speed. With this reformulation, system (6.2) becomes

$$\left\{\begin{array}{rcl} \partial_t A + \partial_x(Au) & = & 0 \\ \partial_t(Au) + \partial_x(Au^2) + \partial_x\left(\displaystyle\int_{\varepsilon A_0}^{A(x,t)} c^2(a)da\right) & = & Ag - f(A,A_0,u) - \dfrac{A}{\rho}\Big(\partial_x P_0 \\ & + & (\partial_{A_0}\psi)\partial_x A_0 + (\partial_\beta\psi)\partial_x\beta\Big) \end{array}\right. \tag{6.4}$$

When the reference cross-section area A_0, the stiffness parameter β and the pressure P_0 are assumed to be constant in space, the system reads

$$\left\{\begin{array}{rcl} \partial_t A + \partial_x(Au) & = & 0 \\ \partial_t(Au) + \partial_x(Au^2) + \partial_x\left(\displaystyle\int_{\varepsilon A_0}^{A(x,t)} c^2(a)da\right) & = & Ag - f(A,A_0,u). \end{array}\right. \tag{6.5}$$

6.1.2 The kinetic scheme

Many numerical methods have been used in the literature to address the solution of (6.5). In the arterial case, we refer to the recent overview presented in [BNB+15], where six different methods were compared: discontinuous Galerkin, locally conservative Galerkin, Galerkin least-squares finite element, finite volume, finite difference MacCormack, and a simplified trapezium rule method (STM). In the venous case, a Godunov scheme has been used in [BP02], an ADER (Arbitrary Accuracy DERivative Riemann problem) scheme in [MMT12], and a Runge-Kutta discontinuous Galerkin scheme in [MF10].

In the present work, a kinetic scheme is adopted for both arterial and venous flows. A motivation for this method, which was initially proposed for the Saint-Venant equations [ABP00], is its capability to provably preserve the positivity of the cross-section area, which is especially relevant in collapsible vessels. To our knowledge, this is the first time this scheme is used in hemodynamics for collapsible vessels. It was recently used for arterial flow in [DL13].

A kinetic interpretation of system (6.5) is obtained by introducing a linear microscopic kinetic equation equivalent to the macroscopic model [Per02]. A real function χ defined on $\mathbb{R}$ is introduced. It is compactly supported and verifies the following properties

$$\left\{\begin{array}{l} \chi(-w) = \chi(w) \geq 0 \\ \displaystyle\int_{\mathbb{R}} \chi(w)dw = \int_{\mathbb{R}} w^2\chi(w)dw = 1. \end{array}\right. \tag{6.6}$$

Here, this function is defined by $\chi(w) = \frac{1}{2\sqrt{3}}\mathbf{1}_{|w|\leq\sqrt{3}}$, but other choices are possible [Per02]. A distribution function $M(x,t,\xi)$ is introduced

$$M(x,t,\xi) = \frac{A}{\gamma}\chi\left(\frac{\xi - u}{\gamma}\right),$$

with $\gamma^2 = \dfrac{1}{A}\displaystyle\int_{\varepsilon A_0}^{A(x,t)} c^2(a)da$. The wave speed c will be further specified in the next section for arterial and venous blood flows. In the kinetic formalism, the variable ξ represents the

microscopic particle velocity.

Consider first the case without source terms. The equation verified by M and the system (6.5) are linked with the following result [Per02]: the functions A and u are solutions to the Euler equations (6.5), if and only if $M(x,t,\xi)$ is solution to the kinetic equation

$$\partial_t M + \xi \partial_x M = \mathcal{Q}(x,t,\xi), \tag{6.7}$$

where $\mathcal{Q}(x,t,\xi)$ is a collision term that satisfies

$$\int_{\mathbb{R}} \mathcal{Q} d\xi = \int_{\mathbb{R}} \xi \mathcal{Q} d\xi = 0.$$

The link between the microscopic density function and the macroscopic variable is given by the two relations

$$\int_{\mathbb{R}} M d\xi = A, \quad \int_{\mathbb{R}} \xi M d\xi = Au. \tag{6.8}$$

Let Δt and Δx denote the time and space steps respectively. Let (A_i^n,u_i^n) denote an approximation of $(A(x_i,t_n),u(x_i,t_n))$, with $t_n = n\Delta t$ and $x_i = i\Delta x$. The unknown (A_i^n,u_i^n) is solution to a finite volume kinetic scheme deduced from the kinetic interpretation of the equations. Let M_i^n be the discrete particles density, defined by

$$M_i^n = M_i^n(\xi) = \frac{A_i^n}{\gamma_i^n} \chi\left(\frac{\xi - u_i^n}{\gamma_i^n}\right),$$

with $\gamma_i^n = \left(\frac{1}{A_i^n}\int_{\varepsilon A_0}^{A_i^n} c^2(a)da\right)^{\frac{1}{2}}$. Equation (6.7) is approximated by an upwind scheme

$$M_i^{n+1,-} = M_i^n - \frac{\Delta t}{\Delta x}\xi\left(M_{i+\frac{1}{2}}^n - M_{i-\frac{1}{2}}^n\right),$$

with $M_{i+\frac{1}{2}}^n = M_i^n \mathbf{1}_{\xi\geq 0} + M_{i+1}^n \mathbf{1}_{\xi\leq 0}$.

Then A_i^n and $(Au)_i^n = A_i^n u_i^n$ are computed with (6.8)

$$X_i^{n+1} = \begin{pmatrix} A_i^{n+1} \\ A_i^{n+1}u_i^{n+1} \end{pmatrix} = \int_{\mathbb{R}} \begin{pmatrix} 1 \\ \xi \end{pmatrix} M_i^{n+1,-} d\xi. \tag{6.9}$$

The kinetic scheme reads

$$X_i^{n+1} = X_i^n - \frac{\Delta t}{\Delta x}(\mathcal{F}_{i+\frac{1}{2}}^n - \mathcal{F}_{i-\frac{1}{2}}^n), \tag{6.10}$$

with $\mathcal{F}_{i+\frac{1}{2}}^n = \int_{\mathbb{R}} \xi \begin{pmatrix} 1 \\ \xi \end{pmatrix} M_{i+\frac{1}{2}}^n d\xi$.

Given the function χ chosen above, the following integrals can be computed in closed form

$$\begin{array}{ll} \int_{\xi\geq 0}\left[\xi^p\frac{A}{\gamma}\chi\left(\frac{\xi-u}{\gamma}\right)\right]d\xi & = \frac{1}{2\sqrt{3}}\frac{A}{\gamma(p+1)}\left[(\xi\gamma+u)^{p+1}\right]_{\xi=\max(\frac{-u}{\gamma};-\sqrt{3})}^{\xi=\max(\frac{-u}{\gamma};\sqrt{3})} \\ \int_{\xi\leq 0}\left[\xi^p\frac{A}{\gamma}\chi\left(\frac{\xi-u}{\gamma}\right)\right]d\xi & = \frac{1}{2\sqrt{3}}\frac{A}{\gamma(p+1)}\left[(\xi\gamma+u)^{p+1}\right]_{\xi=\min(\frac{-u}{\gamma};-\sqrt{3})}^{\xi=\min(\frac{-u}{\gamma};\sqrt{3})} \end{array} \quad p=1,2 \quad (6.11)$$

which gives the expression of the flux $\mathcal{F}$. Details on kinetic interpretation and numerical scheme can be found in appendix C.

In presence of a source term, we adopt the simple strategy of an explicit treatment

$$X_i^{n+1} = X_i^n - \frac{\Delta t}{\Delta x}(\mathcal{F}_{i+\frac{1}{2}}^n - \mathcal{F}_{i-\frac{1}{2}}^n) + \Delta t^n S(X_i^n), \quad (6.12)$$

where $S(X_i^n) = (0, gA_i^n - f(A_i^n, A_0, u_i^n))^T$.

Under the CFL condition $\Delta t \max_i(|u_i^n| + \sqrt{3}\gamma_i^n) \leq \Delta x$, following the same arguments as in [ABP00] for the shallow water equations, it can be proved that the scheme (6.12) preserves the positivity of the cross-section area, i.e $A_i^n \geq 0$, if this property holds at time zero. A second order extension of (6.12) can be obtained with standard arguments (minmod flux limiter).

Remark 6.1

As mentioned above, A_0 is assumed to be constant in each vessel. If A_0 was space-dependent, for example to account for the vessel tapering, the source term should be carefully treated to obtain a numerical scheme that ensures the equilibrium at rest. A similar issue was addressed for the shallow water equations in [ABB+04] with a technique called "hydrostatic reconstruction". To our knowledge, in the context of blood flow, this question was first addressed in [DL13] and named "dead man equilibrium". It was also addressed in [MMT14] for a different scheme.

6.1.3 Arteries and veins tube laws

Arteries. To our knowledge, two elastic tube laws are reported in literature for artery walls, derived from the linear theory of elasticity. One pressure-area relation is developed using Laplace's law [Olu99] and the other one uses a method based on the string model [FQV09, FLQ03].

The vessel is assumed to be a circular tube, with thin wall in the sense $h_0/r << 1$, where h_0 is the thickness at a reference configuration and r the radius of the tube respectively. Note that the thickness could vary in space, here β is assumed constant in space therefore one assumes $h(x) = h_0$. The loading and the deformation of the wall are assumed axisymmetric and the vessel is tethered in the longitudinal direction.

Under these assumptions, the wall stress is reduced to only circumferential direction (σ_{circ}), and it can be expressed as

$$\sigma_{circ} = E\frac{r - r_0}{(1 - \sigma_\theta\sigma_x)r_0}$$

Where E is Young's modulus in the circumferential direction, r_0 is the radius at zero trans-

mural pressure, $\sigma_\theta = \sigma_x = 0.5$ are the Poisson ratios in the circumferential and longitudinal directions respectively (the biological tissue is assumed incompressible). From Laplace's law, (wall stress: $\tau = (p - P_{ext})r/h_0$, p is the internal pressure and P_{ext} is the external pressure) the following relation is obtained :

$$\tau = \frac{r(p - P_{ext})}{h_0} = \sigma_{circ} = \frac{E}{1 - \sigma_\theta \sigma_x} \frac{r - r_0}{r_0}$$

As the tube is circular, the cross-section area reads $A = \pi r^2$; thus pressure and area are linked with the following algebraic relation [Olu99]

$$p = P_{ext} + \frac{4Eh_0}{3r_0} \frac{r - r_0}{r} = P_{ext} + \frac{4Eh_0\sqrt{\pi}}{3\sqrt{A_0}} \left(1 - \sqrt{\frac{A_0}{A}}\right) \tag{6.13}$$

The other tube law derives from a string model, describing the wall displacement mechanics, under the same assumptions on the tube [FQV09, FLQ03].

$$\rho_w h_0 \partial_t^2 \eta + a\eta - b\partial_z^2 \eta = p - P_{ext} \tag{6.14}$$

where ρ_w is the vessel wall density, $\eta = r - r_0$ is the displacement of the wall with respect to a reference configuration, r and r_0 are respectively the radius of the vessel and the vessel radius in the reference configuration. p and P_{ext} are the internal and the external pressures respectively. In equation (6.14), the first term stands for inertia, proportional to acceleration of the wall. The second term is an elastic-response function and the last term is related to the longitudinal tension acting on the vessel. a and b are positive coefficients, in particular $a = \dfrac{Eh_0}{r_0^2(1 - \nu^2)}$, with ν Poisson's ratio, taken equal to 0.5 (vessel tissue is assumed incompressible). In the arteries, the elastic response is the dominant effect, so the other terms can be neglected. Under these assumptions, an algebraic law relates pressure and area

$$p - P_{ext} = a\eta = \frac{4Eh_0\pi}{3A_0}(r - r_0) = \frac{4Eh_0\sqrt{\pi}}{3A_0} \left(\sqrt{A} - \sqrt{A_0}\right) \tag{6.15}$$

The two relations described before are different. However, for A close to A_0, the first-order approximation of the two laws are similar, indeed

$$\frac{1}{\sqrt{A_0}} \left(1 - \sqrt{\frac{A_0}{A}}\right) = \frac{1}{A_0\sqrt{A_0}} \left(\frac{1}{2}(A - A_0) + o(A - A_0)\right) \tag{6.16}$$

And

$$\frac{1}{A_0} \left(\sqrt{A} - \sqrt{A_0}\right) = \frac{1}{A_0} \left(\frac{1}{2\sqrt{A_0}}(A - A_0) + o(A - A_0)\right) \tag{6.17}$$

Therefore, for A close to A_0, the two algebraic laws (6.13) and (6.15), can be equivalently used for arterial walls. In this work the following relation is used for arterial wall

$$p(t,x) = P_0(x) + \beta_a \left(\sqrt{A} - \sqrt{A_0}\right) \tag{6.18}$$

with

$$\beta_a = \frac{4\sqrt{\pi}Eh_0}{3A_0}, \tag{6.19}$$

where E is the Young's modulus, and h_0 the thickness of the tube. The wave speed is then defined by:

$$c^2 = \frac{\beta_a}{2\rho}\sqrt{A(x,t)}. \tag{6.20}$$

Thus, with the arterial tube law, c^2 is integrable in $A = 0$ and we can choose $\varepsilon = 0$ in (6.3). The kinetic distribution function M is defined by $M(x,t,\xi) = \frac{A}{\gamma}\chi\left(\frac{\xi-u}{\gamma}\right)$, with $\gamma^2 = \frac{1}{A}\int_0^{A(x,t)} c^2(a)da = \frac{\beta_a}{3\rho}A^{\frac{1}{2}} = \frac{2}{3}c^2$ and system (6.5) reads

$$\left\{\begin{array}{rcl} \partial_t A + \partial_x(Au) & = & 0 \\ \partial_t(Au) + \partial_x(Au^2) + \partial_x\left(\frac{\beta}{3\rho}A^{\frac{3}{2}}\right) & = & Ag - f(A, A_0, u), \end{array}\right. \tag{6.21}$$

with equation 6.18 to close the system.

Veins. Veins are collapsible tubes. Indeed the low pressure in the vein vessel makes the influence of the external pressure on the vessel wall significant, such that transmural pressure can become negative and lead the vessel to collapse. The non-linear mechanical behavior of the vein wall is then different than the one in arteries. The vein tube law needs to take into account the collapse phenomena.

Shapiro, Brook and Pedley ([Sha77, PBS96, BP02]) introduced and used the following tube law

$$\psi(A, A_0, \beta) = \beta(x)\left(\left(\frac{A(x,t)}{A_0(x)}\right)^m - \left(\frac{A(x,t)}{A_0(x)}\right)^n\right). \tag{6.22}$$

The parameters m and n are obtained from experimental measurements ([Sha77, FKR72, PBS96]). For veins typical values are $m = 10$ and $n = -3/2$. This tube law combines the property of the tube to be stiff when the tube is distended ($A > A_0$), compliant for a range of intermediate values of A and stiff again for A really small ($A < A_0$). The β coefficient is related to vessel elasticity properties and for linear elastic material Shapiro [Sha77] defines β as follows:

$$\beta = \frac{E}{12(1-\nu^2)}\left(\frac{h}{r}\right)^3 \tag{6.23}$$

Muller and Toro in [MMT12] choose to estimate the vessel stiffness parameter β from the pulse wave velocity. This choice is based on the work of Bassez *et al.* [BFC01], which shows that the vein collapse process is less extreme than describe by relation (6.22) with stiffness coefficient (6.23). The stiffness coefficient is estimated by defining a reference wave speed in the veins as follows:

$$c_0 = c_{0,\max} - (c_{0,\max} - c_{0,\min})\left(\frac{r - r_{\min}}{r_{\max} - r_{\min}}\right)^{\frac{1}{4}}$$

with $r_{\min}$ and $r_{\max}$ are the minimum and maximum vessel radii and $c_{0,max} = 3\text{m/s}$, $c_{0,min} = 1$

m/s are based on experimental measurements. So β parameter is estimated with $c_0 = \sqrt{\frac{\beta}{\rho}(m-n)}$. Finally, the tube law can be written as follows

$$\psi(A, A_0, \beta) = \frac{\rho c_0^2}{m-n}\left(\left(\frac{A(x,t)}{A_0(x)}\right)^m - \left(\frac{A(x,t)}{A_0(x)}\right)^n\right) \tag{6.24}$$

In [KLH+15] Keijsers *et al.* interpolate tube law (6.22) with continuous first order derivative, defined by

$$A = A_0\left[h(p^*)f^+(p^*) + (1-h(p^*))f^-(p^*)\right] \tag{6.25}$$

where $p^* = \dfrac{p - P_{ext}}{\beta}$ is a dimensionless pressure, f^+ and f^- are functions fitting the positive and negative pressure part of the original function respectively and h is a scaling function.

$$\begin{aligned} f^+(p^*) &= \frac{A_0^+}{\pi}\left(\tan^{-1}\left(\frac{p^* - p_a^+}{p_b^+}\right) + \frac{\pi}{2}\right) \\ f^-(p^*) &= B + \frac{A_0^-}{\pi}\left(\tan^{-1}\left(\frac{p^* - p_a^-}{p_b^-}\right) + \frac{\pi}{2}\right) \\ h(p^*) &= \frac{1}{\pi}\left(\tan^{-1}\left(\frac{\gamma p^*}{\pi}\right) + \frac{\pi}{2}\right) \end{aligned} \tag{6.26}$$

with $B, A_0^+, A_0^-, p_a^+, p_a^-, p_b^+, p_b^-, \gamma$ are the fitting constant coefficients.

In the examples below the same tube law as in [PBS96, BP02, MMT12] is adopted

$$\psi\left(A, A_0, \beta_v\right) = \beta_v\left(\left(\frac{A}{A_0}\right)^m - \left(\frac{A}{A_0}\right)^n\right), \tag{6.27}$$

where β_v is an elasticity parameter. With $m = 10$ and $n = -1.5$, that are the values commonly used in the literature, the squared wave speed defined by

$$c^2 = \frac{\beta_v}{\rho}\left(m\left(\frac{A}{A_0}\right)^m - n\left(\frac{A}{A_0}\right)^n\right) \tag{6.28}$$

is not integrable at $A = 0$. This question would deserve a special modeling study. Here, for simplicity, we circumvent this difficulty by taking $\varepsilon > 0$ in (6.3)

$$\begin{aligned} \gamma^2 &= \frac{1}{A}\frac{\beta_v}{\rho}\int_{\varepsilon A_0}^{A(x,t)}\left(m\left(\frac{a}{A_0}\right)^m - n\left(\frac{a}{A_0}\right)^n\right)da \\ &= \frac{\beta_v}{\rho}\left(\frac{m}{m+1}\left(\frac{A}{A_0}\right)^m - \frac{n}{n+1}\left(\frac{A}{A_0}\right)^n - \frac{A_0}{A}\left(\frac{m}{m+1}\varepsilon^{m+1} - \frac{n}{n+1}\varepsilon^{n+1}\right)\right). \end{aligned} \tag{6.29}$$

The value of ε will be discussed in section 6.1.5.

6.1.4 Boundary treatments

Characteristic variables The characteristic variables are computed from the quasi-linear form of system (6.5). For arterial blood flow [FQV09], the characteristic variables are

$$W_+ = u + 4\sqrt{\frac{\beta}{2\rho}}A^{\frac{1}{4}}, \quad W_- = u - 4\sqrt{\frac{\beta}{2\rho}}A^{\frac{1}{4}}. \tag{6.30}$$

For venous blood flow [MMT12], the characteristic variables are

$$W_+ = u + \int_{A_0}^{A} \frac{c(a)}{a}da, \quad W_- = u - \int_{A_0}^{A} \frac{c(a)}{a}da. \tag{6.31}$$

In the following numerical examples, the characteristic variables are approximated with the trapezoidal rule for venous blood flow.

Transmission conditions In presence of a bifurcation, or a change in material properties, conservation of mass is imposed $Q_m = Q_{d_1} + Q_{d_2}$, where $Q = Au$ denotes the flow rate, m the mother vessel and d_1, d_2 the two daughter vessels. Except in some specific cases detailed below, continuity of the total pressure $P_T = \frac{\rho}{2}u^2 + p$ is also imposed $P_{T,m} = P_{T,d_1} = P_{T,d_2}$. These relations are complemented with the relations provided by the outgoing characteristics, as explained e.g. in [FQV09]. The resulting system of nonlinear equations is then solved with a Newton method.

Boundary conditions Different types of boundary conditions are considered in the numerical examples. At the inlet of the open-loop models, either the pressure or the flow rate are imposed. At the outlet, either a constant pressure, an absorbing boundary condition, or a coupling with a 0D model are used. For the absorbing boundary condition, the incoming characteristic variable is assumed constant in time. For the coupling with a 0D model, the differential equations are approximated with an implicit Euler scheme. The continuity of pressure is imposed and these relations are complemented with the information obtained from the outgoing characteristics (which is equivalent to impose the conservation of mass). A Newton method and a parabolic linesearch algorithm are used to solve the resulting system of nonlinear equations. The algorithm to solve the system of equations can be summarized as follow

Time loop:

- Compute 1D boundary conditions from previous time step
- Solve for internal nodes of the 1D domain
- Update outgoing characteristics
- Update boundaries :
  - Solve junction transmission conditions (Newton)
  - Solve 0D model equations (Newton)

Properties	Values
Length L	10 m
Cross-section area A_0	π cm^2
Initial velocity u(x,0)	0 cm/s
Initial pressure P(x,0)	0 dyn.cm^{-2}
Pressure P_0	0 dyn.cm^{-2}
Wall thickness h	0.15 cm
Young's modulus E	4.0 10^5 dyn.cm^{-2}
Elasticity parameter β	4.515 10^5 dyn.cm^{-3}
Blood mass density ρ	1.05 g.cm^{-3}
Blood viscosity μ	0 or 0.04 dyn.cm^{-2}
Friction term K_f	$22\pi\frac{\mu}{\rho}$

Table 6.1: Parameters for the single pulse propagation benchmark test case from [BNB+15].

6.1.5 Benchmark test cases

Arterial flow Various benchmark test cases were proposed in [BNB+15] to compare six numerical methods for 1D blood flow models. Four representative tests are studied in the following paragraphs: a single pulse propagation, a common carotid artery vessel simulation, an upper thoracic aorta vessel simulation and an aortic bifurcation simulation. The kinetic scheme is compared to the results from [BNB+15]. For all the cases, the system (6.5) is solved, with a friction function defined by $f(A, A_0, u) = K_f u(x,t)$, K_f being constant, and gravity is neglected.

Single pulse propagation The first test case is the (non-physiological) propagation of a pulse wave along a tube, with an absorbing outlet boundary condition. Table 6.1 provides the parameters values. The inlet flow is imposed $Q_0(t) = \exp(-10^4(t-0.05)^2)\,\text{cm}^3\text{s}^{-1}$. First, the test is performed with the first order kinetic scheme, and the friction is neglected. In [BNB+15] all the numerical schemes give identical results for this benchmark. The kinetic scheme is here compared with the simplified trapezium rule method scheme (STM). For $\Delta t = 10^{-4}$ s and $\Delta x = 10^{-1}$ cm the resulting pressure curves are shown in Figure 6.1 (blue curve). An excessive numerical diffusion is observed, which is reduced when space and time steps are refined (Figure 6.1 red curve), $\Delta t = 10^{-5}$ s and $\Delta x = 10^{-2}$ cm). The results obtained with the second order in space kinetic scheme, with $\Delta t = 10^{-5}$ s and $\Delta x = 10^{-1}$ cm, are plotted in Figure 6.2 (a). Figure 6.2 (b) shows the results obtained in the viscous case with the second order in space kinetic scheme ($\Delta t = 10^{-5}$ s and $\Delta x = 10^{-1}$ cm). Table 6.2 summarizes the normalized errors for all presented simulations. With the second order kinetic scheme, the results are in excellent agreement with the STM scheme.

Common carotid artery A single vessel coupled to a three-element Windkessel model of the rest of the systemic circulation is used to simulate a common carotid artery. Table 6.3 summarizes the parameter values. The flow is imposed at the inlet. Using the first order

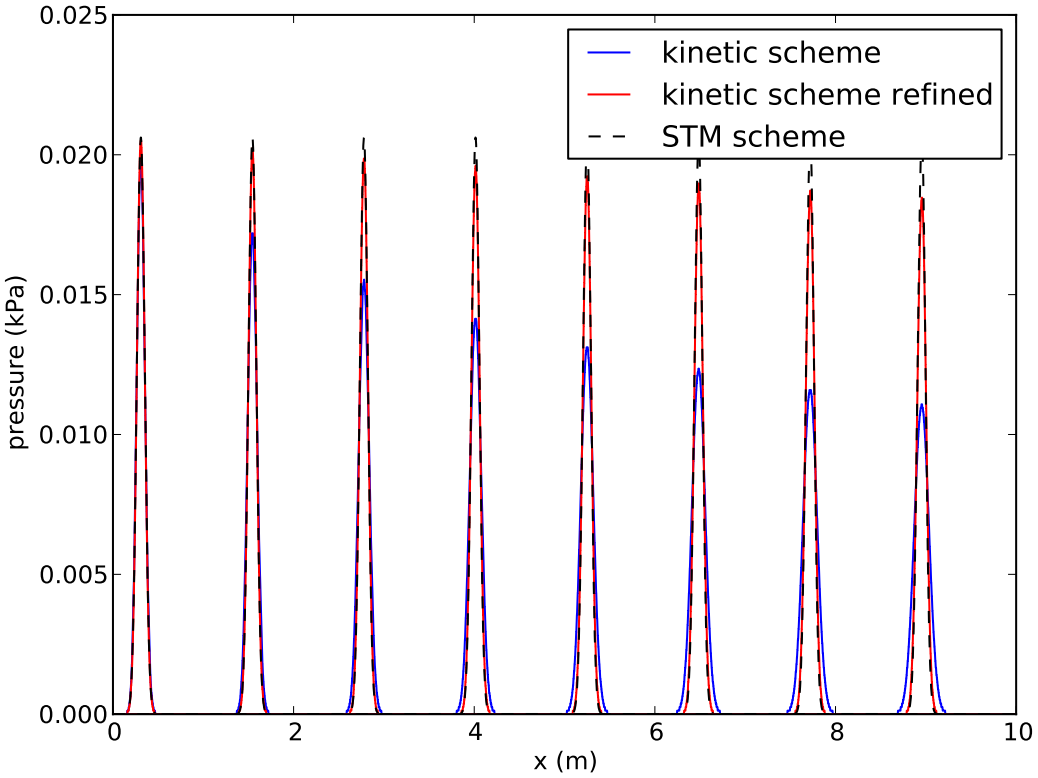

Figure 6.1: Comparison between time and space first order kinetic scheme results with $\Delta x = 0.1$cm, and $\Delta t = 1.0\,10^{-4}$s (blue), with $\Delta x = 0.01$cm, and $\Delta t = 1.0\,10^{-5}$s (red) and numerical results from [BNB+15] (dash black) for the inviscid single pulse propagation test. The pressure over space is represented for different time instants: 0.1s, 0.3s, 0.5s, 0.7s, 0.9s, 1.1s, 1.3s, and 1.5s.

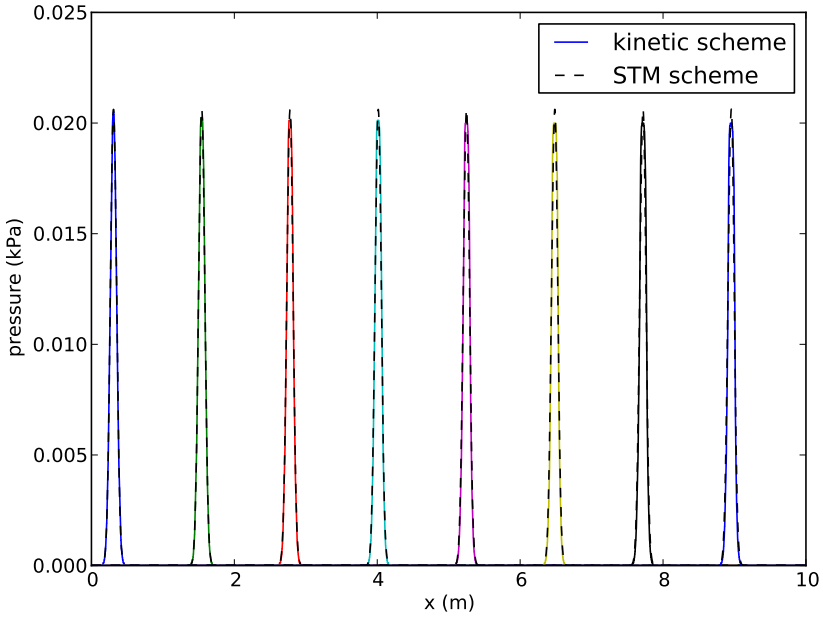

(a) Inviscid blood

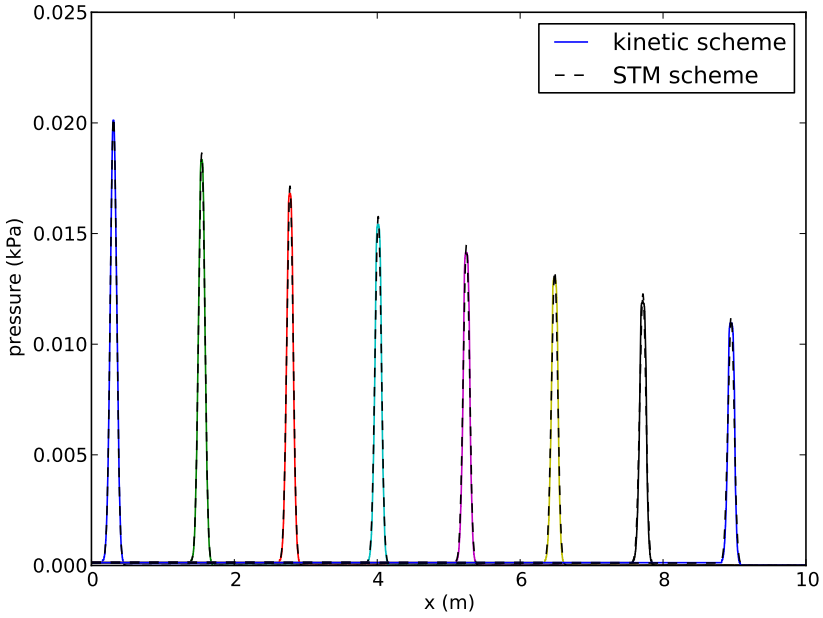

(b) Viscous blood

Figure 6.2: Comparison between first order in time and second order in space kinetic scheme results with $\Delta x = 0.1$ cm, and $\Delta t = 1.0\,10^{-5}$s and numerical results from [BNB+15] with inviscid (a) and viscous (b) blood for the single pulse propagation test. The pressure over space is represented for various times: 0.1s, 0.3s, 0.5s, 0.7s, 0.9s, 1.1s, 1.3s, and 1.5s.

	Case 1		Case 2		Case 3		Case 4	
instants	$\mathcal{E}_{l^2}$	$\mathcal{E}_\infty$	$\mathcal{E}_{l^2}$	$\mathcal{E}_\infty$	$\mathcal{E}_{l^2}$	$\mathcal{E}_\infty$	$\mathcal{E}_{l^2}$	$\mathcal{E}_\infty$
t = 0.1s	0.036	0.043	0.017	0.007	0.007	0.012	0.007	0.012
t = 0.3s	0.145	0.166	0.060	0.024	0.028	0.047	0.029	0.047
t = 0.5s	0.230	0.251	0.104	0.040	0.049	0.073	0.049	0.077
t = 0.7s	0.292	0.314	0.147	0.055	0.067	0.099	0.067	0.101
t = 0.9s	0.343	0.364	0.189	0.069	0.083	0.121	0.083	0.122
t = 1.1s	0.384	0.402	0.229	0.083	0.099	0.140	0.097	0.141
t = 1.3s	0.419	0.438	0.267	0.096	0.111	0.158	0.111	0.158
t = 1.5s	0.448	0.465	0.305	0.109	0.124	0.173	0.122	0.174

Table 6.2: Normalized errors for the single pulse propagation test case; for cases 1,2,3 friction is neglected and case 4 is the viscous blood case. The normalized errors are defined by $\mathcal{E}_{l^2} = \|X_{kin} - X_{STM}\|_{l^2}/\|X_{STM}\|_{l^2}$ and $\mathcal{E}_\infty = \|X_{kin} - X_{STM}\|_\infty/\|X_{STM}\|_\infty$ where X_{STM} is the solution with the 1D STM scheme from [BNB+15] and X_{kin} is the solution obtained with the kinetic scheme. Case 1 presents the results of the first order kinetic scheme with $\Delta x = 0.1$cm, and $\Delta t = 1.0\,10^{-4}$s, case 2 of the first order kinetic scheme with $\Delta x = 0.01$cm, and $\Delta t = 1.0\,10^{-5}$s, case 3 of the first order in time and second order in space kinetic scheme with $\Delta x = 0.1$cm, and $\Delta t = 1.0\,10^{-5}$s, finally case 4 of the first order in time and second order in space kinetic scheme with $\Delta x = 0.1$cm and $\Delta t = 1.0\,10^{-5}$s with a non-zero friction term.

kinetic scheme, with $\Delta t = 10^{-5}$s and $\Delta x = 10^{-1}$cm, pressure, flow, radius change (Δr) and inlet/outlet pressure difference (ΔP) are compared to the STM scheme and the 3D solution from [BNB+15]. The curves are plotted in Figure 6.3. The kinetic scheme is in good agreement with the STM scheme.

In [BNB+15] errors with respect to 3D solution are computed to compare different 1D schemes. The errors are defined by

$$\mathcal{E}_P^{RMS} = \sqrt{\frac{1}{n}\sum_{i=1}^{n}\left(\frac{P_i - \mathcal{P}_i}{\mathcal{P}_i}\right)}, \quad \mathcal{E}_Q^{RMS} = \sqrt{\frac{1}{n}\sum_{i=1}^{n}\left(\frac{Q_i - \mathcal{Q}_i}{\max_j(\mathcal{Q}_j)}\right)} \tag{6.32}$$

$$\mathcal{E}_P^{MAX} = \max_i\left|\frac{P_i - \mathcal{P}_i}{\mathcal{P}_i}\right|, \quad \mathcal{E}_Q^{MAX} = \max_i\left|\frac{Q_i - \mathcal{Q}_i}{\max_j(\mathcal{Q}_j)}\right| \tag{6.33}$$

$$\mathcal{E}_P^{SYS} = \frac{\max(P) - \max(\mathcal{P})}{\max(\mathcal{P})}, \quad \mathcal{E}_Q^{SYS} = \frac{\max(Q) - \max(\mathcal{Q})}{\max(\mathcal{Q})} \tag{6.34}$$

$$\mathcal{E}_P^{DIAS} = \frac{\min(P) - \min(\mathcal{P})}{\min(\mathcal{P})}, \quad \mathcal{E}_Q^{DIAS} = \frac{\min(Q) - \min(\mathcal{Q})}{\max(\mathcal{Q})}, \tag{6.35}$$

where P_i and Q_i are the 1D simulation results at a given space point x_i, $\quad i \in 1...N$, $\mathcal{P}_i$ and $\mathcal{Q}_i$ are the 3D solutions at the same space location. The errors for ΔP and Δr are defined similarly than the for the flow.

The errors for the common carotid test with the kinetic scheme are summed up in table

Properties	Values
Lenght L	12.6 cm
Cross-section area A_0	0.28274 cm^2
Initial velocity u(x,0)	0
Initial pressure P(x,0)	0
Pressure P_0	10.933 10^4 $dyn.cm^{-2}$
Wall thickness h	0.03 cm
Young's modulus E	7.0 10^5 $dyn\ cm^{-2}$
Elasticity parameter β	1.562 10^6 $dyn.cm^{-3}$
Blood mass density ρ	1.06 $g.cm^{-3}$
Blood viscosity μ	0.04 $dyn.cm^{-2}$
Friction term K_f	$8\pi \times \frac{\mu}{\rho}$
Windkessel proximal resistance R_p	2.4875 10^3 $dyn.s.cm^{-5}$
Windkessel distal resistance R_d	1.8697 10^4 $dyn.s.cm^{-5}$
Windkessel capacitance C	1.7529 10^{-5} $cm^5.dyn^{-1}$

Table 6.3: Parameters for common carotid artery benchmark test case from [BNB+15]

6.4. The error ranges found for the kinetic scheme are the same as the errors of the different 1D schemes studied by Boileau *et. al* [BNB+15].

Thoracic aorta The test case represents an upper thoracic aorta with a single vessel coupled to a three-element Windkessel model of the rest of the systemic circulation. The Windkessel and vessel properties are summarized in table 6.5. The inflow is imposed. The simulation is performed with first order kinetic scheme and compared to the results from [BNB+15]. The curves are shown in Figure 6.4 and the error values are in table 6.6. The errors for the kinetic scheme are again similar to the errors from the other 1D schemes studied in [BNB+15]. The kinetic scheme is again in good agreement with the other 1D scheme analyzed in [BNB+15].

Aortic bifurcation The last arterial test is an abdominal aorta branching into two symmetric iliac arteries. The vessel parameters are in Table 6.7. Two three-element Windkessel models represent the rest of the systemic circulation and are coupled to the two 1D iliac arteries. The flow rate is imposed at the inlet. Space and time steps for the kinetic scheme are $\Delta t = 5\,10^{-5}$ s and $\Delta x = 0.1$ cm. The CFL number $(\Delta t \max_i(|u_i^n| + \sqrt{3}\gamma_i^n)/\Delta x)$ remains around 0.63. Figure 6.5 shows pressure, flow rate and radius change for the middle and the end points of the aorta, and the middle point of the iliac artery, compared to the results of 3D simulations and of the 1D scheme STM presented in [BNB+15]. Table 6.8 presents the errors. Again, the kinetic scheme is in very good agreement with the other schemes presented in [BNB+15]. In the three last cases, that are more physiological than the first one, the first order kinetic scheme is sufficient to reach a good accuracy with reasonable discretization steps.

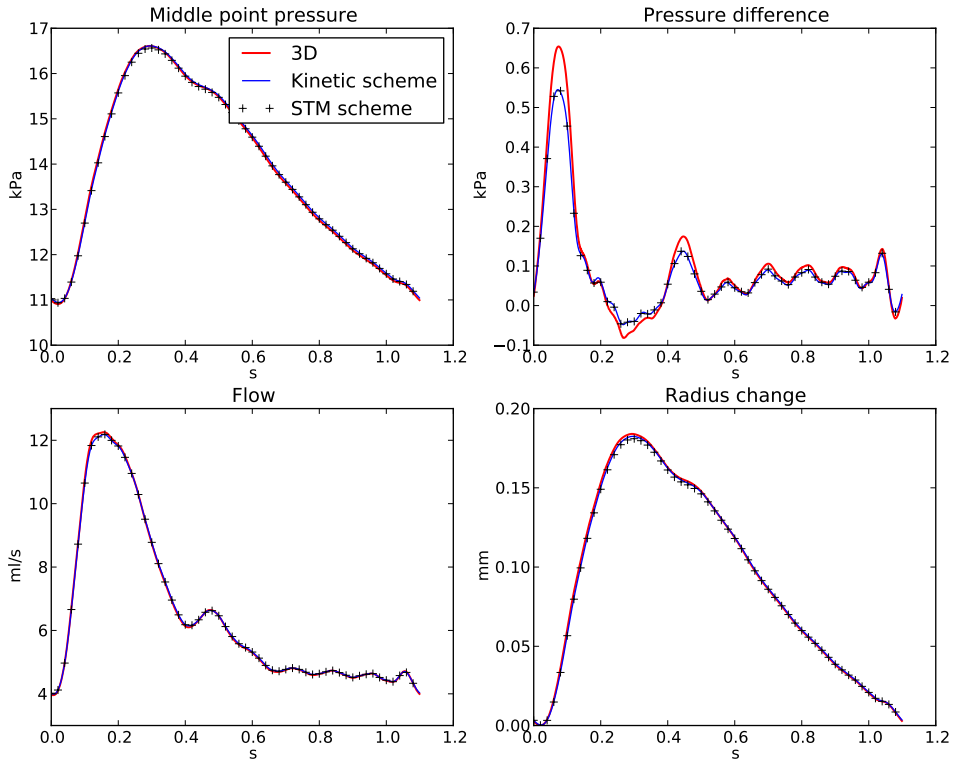

Figure 6.3: Common carotid artery test simulation results with first order kinetic scheme with $\Delta t = 10^{-5}$s and $\Delta x = 0.1$cm over one cardiac cycle compare with STM and 3D simulation solutions from [BNB+15].

Error	First order kinetic scheme
$\mathcal{E}_P^{RMS}$	0.35
$\mathcal{E}_Q^{RMS}$	0.37
$\mathcal{E}_{\Delta r}^{RMS}$	0.8
$\mathcal{E}_{\Delta P}^{RMS}$	4.22
$\mathcal{E}_P^{MAX}$	0.63
$\mathcal{E}_Q^{MAX}$	1.39
$\mathcal{E}_{\Delta r}^{MAX}$	2.18
$\mathcal{E}_{\Delta P}^{MAX}$	15.7
$\mathcal{E}_P^{SYS}$	0.0055
$\mathcal{E}_Q^{SYS}$	-0.60
$\mathcal{E}_{\Delta r}^{SYS}$	-0.85
$\mathcal{E}_{\Delta P}^{SYS}$	-15.38
$\mathcal{E}_P^{DIAS}$	0.33
$\mathcal{E}_Q^{DIAS}$	0.29
$\mathcal{E}_{\Delta r}^{DIAS}$	0.17
$\mathcal{E}_{\Delta P}^{DIAS}$	5.05

Table 6.4: Error with respect to 3D solution in percent as defined in [BNB+15]

Properties	Values
Lenght L	24.137 cm
Cross-section area A_0	4.5239 cm^2
Initial velocity u(x,0)	0 cm/s
Initial pressure P(x,0)	0 $dyn.cm^{-2}$
Pressure P_0	9.46 10^4 $dyn.cm^{-2}$
Wall thickness h	0.12 cm
Young's modulus E	4.0 10^5 $dyn\ cm^{-2}$
Elasticity parameter β	2.23167 10^5 $dyn.cm^{-3}$
Blood mass density ρ	1.06 $g.cm^{-3}$
Blood viscosity μ	0.04 $dyn.cm^{-2}$
Friction term K_f	$22\pi \times \frac{\mu}{\rho}$
Windkessel proximal resistance R_p	1.1752 10^2 $dyn.s.cm^{-5}$
Windkessel distal resistance R_d	1.1167 10^3 $dyn.s.cm^{-5}$
Windkessel capacitance C	1.0163 10^{-3} $cm^5.dyn^{-1}$

Table 6.5: Parameters for upper thoracic aorta benchmark test case from [BNB+15]

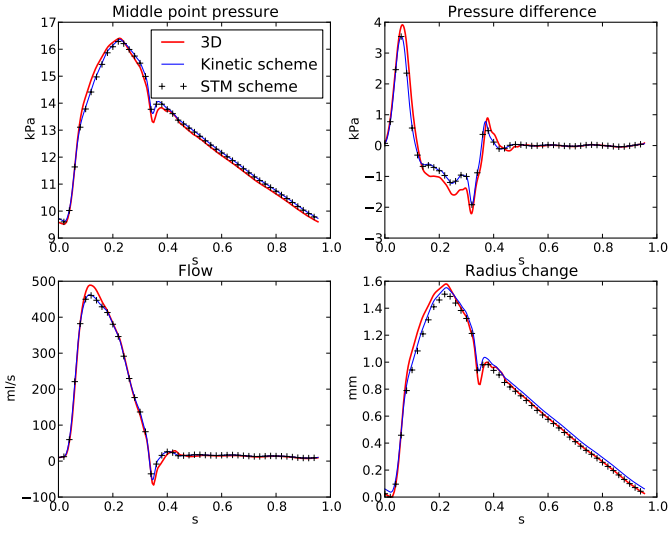

Figure 6.4: Upper thoracic aorta test results obtained with first order kinetic scheme with $\Delta t = 10^{-4}$s and $\Delta x = 0.1$cm over one cardiac cycle compare with the STM and 3D simulation results from [BNB+15].

Error	First order kinetic scheme
$\mathcal{E}_P^{RMS}$	1.30
$\mathcal{E}_Q^{RMS}$	1.75
$\mathcal{E}_{\Delta r}^{RMS}$	2.62
$\mathcal{E}_{\Delta P}^{RMS}$	6.51
$\mathcal{E}_P^{MAX}$	3.0
$\mathcal{E}_Q^{MAX}$	5.74
$\mathcal{E}_{\Delta r}^{MAX}$	7.03
$\mathcal{E}_{\Delta P}^{MAX}$	24.35
$\mathcal{E}_P^{SYS}$	-0.29
$\mathcal{E}_Q^{SYS}$	-5.45
$\mathcal{E}_{\Delta r}^{SYS}$	-1.79
$\mathcal{E}_{\Delta P}^{SYS}$	-9.23
$\mathcal{E}_P^{DIAS}$	1.11
$\mathcal{E}_Q^{DIAS}$	2.97
$\mathcal{E}_{\Delta r}^{DIAS}$	2.30
$\mathcal{E}_{\Delta P}^{DIAS}$	7.35

Table 6.6: Error for thoracic aorta test with respect to 3D solution in percent as defined in [BNB+15]

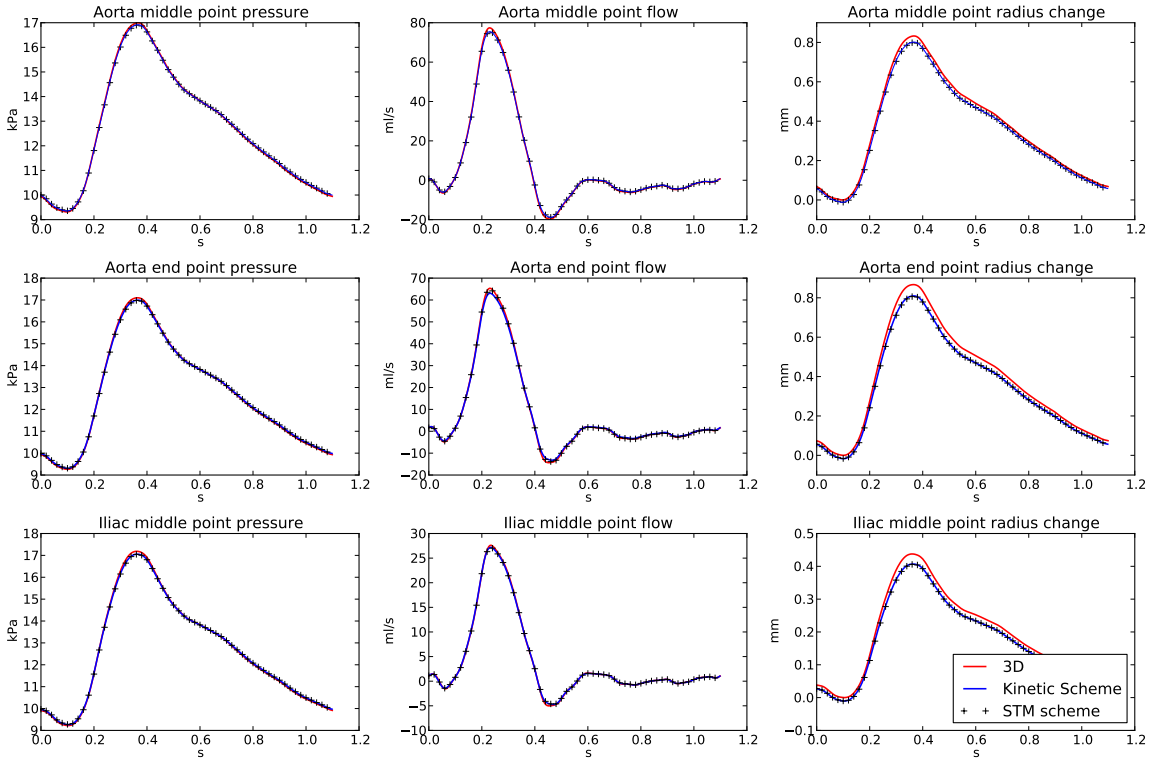

Figure 6.5: Aorta bifurcation test case: kinetic first order scheme results with $\Delta t = 5.10^{-5}$ s and $\Delta x = 0.1$ cm, and 3D and STM scheme results from [BNB+15], over one cardiac cycle.

Properties	Aorta	Iliac
Length L	8.6 cm	8.5 cm
Cross-section area A_0	2.3235 cm^2	1.131 cm^2
Initial velocity u(x,0)	0 cm/s	0 cm/s
Initial pressure P(x,0)	0 $dyn.cm^{-2}$	0 $dyn.cm^{-2}$
Pressure P_0	9.46 10^4 $dyn.cm^{-2}$	9.46 10^4 $dyn.cm^{-2}$
Wall thickness h	0.1032 cm	0.072 cm
Young's modulus E	5.0 10^5 $dyn\ cm^{-2}$	7.0 10^5 $dyn\ cm^{-2}$
Elasticity parameter β	4.671 10^5 $dyn.cm^{-3}$	9.3728 10^5 $dyn.cm^{-3}$
Blood mass density ρ	1.06 $g.cm^{-3}$	1.06 $g.cm^{-3}$
Blood viscosity μ	0.04 $dyn.cm^{-2}$	0.04 $dyn.cm^{-2}$
Friction term K_f	$22\pi\frac{\mu}{\rho}$	$22\pi\frac{\mu}{\rho}$
Windkessel proximal resistance R_p	-	6.8123 10^2 $dyn.s.cm^{-5}$
Windkessel distal resistance R_d	-	3.1013 10^4 $dyn.s.cm^{-5}$
Windkessel capacitance C	-	3.6664 10^{-5} $cm^5.dyn^{-1}$

Table 6.7: Parameters for the aortic bifurcation benchmark test case from [BNB+15].

Error	Midpoint Aorta	End point Aorta	Midpoint Iliac
$\mathcal{E}_P^{RMS}$	0.39	0.42	0.45
$\mathcal{E}_Q^{RMS}$	0.93	1.17	0.53
$\mathcal{E}_{\Delta r}^{RMS}$	2.41	3.99	4.21
$\mathcal{E}_P^{MAX}$	0.67	0.78	0.9
$\mathcal{E}_Q^{MAX}$	2.81	3.64	2.09
$\mathcal{E}_{\Delta r}^{MAX}$	3.87	6.74	7.25
$\mathcal{E}_P^{SYS}$	-0.46	-0.64	-0.77
$\mathcal{E}_Q^{SYS}$	-2.51	-3.51	-1.56
$\mathcal{E}_{\Delta r}^{SYS}$	-3.72	-6.61	-7.03
$\mathcal{E}_P^{DIAS}$	0.4	0.45	0.46
$\mathcal{E}_Q^{DIAS}$	1.15	1.74	1.05
$\mathcal{E}_{\Delta r}^{DIAS}$	-1.42	-1.95	-2.37

Table 6.8: Errors for the aortic bifurcation test case with respect to the 3D solution in percent as defined in [BNB+15].

Venous flow After having been tested on arterial benchmarks, the kinetic scheme is now applied to venous flow, which is more challenging. For collapsible tubes, such as veins, the squared speed wave (eq. 6.28) is not integrable at A=0. This difficulty is avoided by taking $\varepsilon > 0$ in (6.3). In the following numerical simulations, we took the value $\varepsilon = 10^{-3}$. We noticed that the solution was slightly sensitive to the value of ε, but this dependency is reduced when space and time steps are decreased.

Jugular vein collapse The test of the "giraffe jugular vein" was proposed in [PBS96, BP02], and used more recently in [MF10, MMT12]. A single vein is considered with length $L = 200\,\text{cm}$, cross-section area $A_0 = 5\,\text{cm}^2$ and material property parameter $\beta_v = 50$ dyn/cm^2. A constant flow rate is imposed at the inlet and a fixed cross-section area at the outlet. The value of gravity is $g = 980.0$ cm/s^2, and the friction is defined by $f(A, A_0, u) = K_f \sqrt{\frac{A(t,x)}{A_0}} u(t,x)$, with $K_f = 0.96$ cm^2/s. The initial conditions are $A(x,0) = A_0(0.2 + 1.8\frac{x}{L})$ and $u(x,0)A(x,0) = 40\,\text{cm}^3/\text{s}$. The boundary conditions are $u(0,t)A(0,t) = 40\,\text{cm}^3/\text{s}$ and $A(L,t) = 2A_0$. In case of a super-critical inlet, $u(0,t)A(0,t) = 40\,\text{cm}^3/\text{s}$ and $A(0,t) = 0.3825$ cm^2 are the two imposed conditions. The system is solved with the first order kinetic scheme with $\Delta x = 1.0\,\text{cm}$ and $\Delta t = 10^{-4}\,\text{s}$. The CFL number $(\Delta t \max_i(|u_i^n| + \sqrt{3}\gamma_i^n)/\Delta x)$ is around 0.06 for the chosen time and space steps. Here, 201 nodes are used to solve the problem, whereas 1000 nodes were used for the Godunov scheme in [BP02].

The results for $\alpha = A/A_0$ and the velocity u are plotted over the vessel length for $t = 5.7\,\text{s}$ and $t = 50\,\text{s}$ in Figure 6.6. Gravity tends to empty the upstream part of the vessel, thus a super-critical flow appears at the inlet. The vessel cross-section area at the outlet is forced to remain equal to $2A_0$, hence the flow remains sub-critical at the outlet and a shock appears in the middle of the vessel. The position of the shock oscillates until the solution converges. Figure 6.6 shows the solution at time $t = 5.7\,\text{s}$ and the stationary state (time $t = 50\,\text{s}$). The

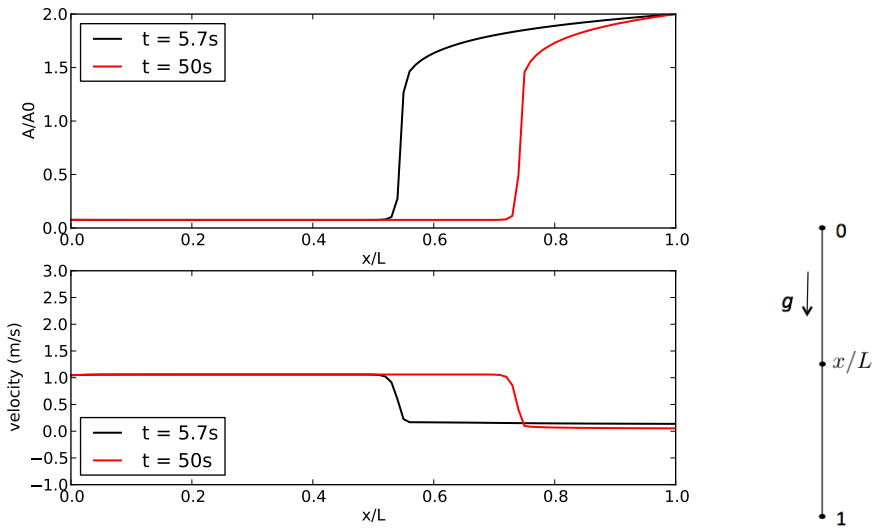

(a) (b)

Figure 6.6: Giraffe jugular vein test: (a) at time t = 5.7s (black) and t=50s (red), simulation results with kinetic scheme ($\Delta t = 10^{-4}$ s, $\Delta x = 1.0$ cm). $\alpha = \dfrac{A}{A_0}$ (top) and velocity in m/s (bottom) are plotted over the vessel length. (b) schematic representation including gravity.

obtained curves are very similar to the curves reported in [MMT12, MF10, BP02]. The front position is $x/L = 0.8$ in [BP02], $x/L = 0.72$ in [MF10], $x/L = 0.74$ in [MMT12]. With our numerical scheme, the front position is $x/L = 0.74$.

Portal vein uncollapse To illustrate the robustness of the kinetic scheme, we propose a new benchmark test case mimicking the uncollapse of the portal vein. During the surgery described in the following section, the surgeons clamp the main vessels perfusing the organ to avoid blood loss. When the clamp is in place, the vessel is collapsed. Once sutures are done, they remove the clamp. The proposed test is mimicking the uncollapse of the portal vein, just after the clamp removal.

We assume that a cross-section area of 0.5 % of A_0 corresponds to a collapsed vessel. The 1D blood flow equations (6.5) are solved with the vein constitutive law (6.28) in a single vessel, with length $L = 6$ cm, cross-section area $A_0 = 0.8\,\text{cm}^2$ and material parameter $\beta_v = 10$ dyn/cm^2. The initial conditions are set to represent a collapsed vessel due to the clamp in

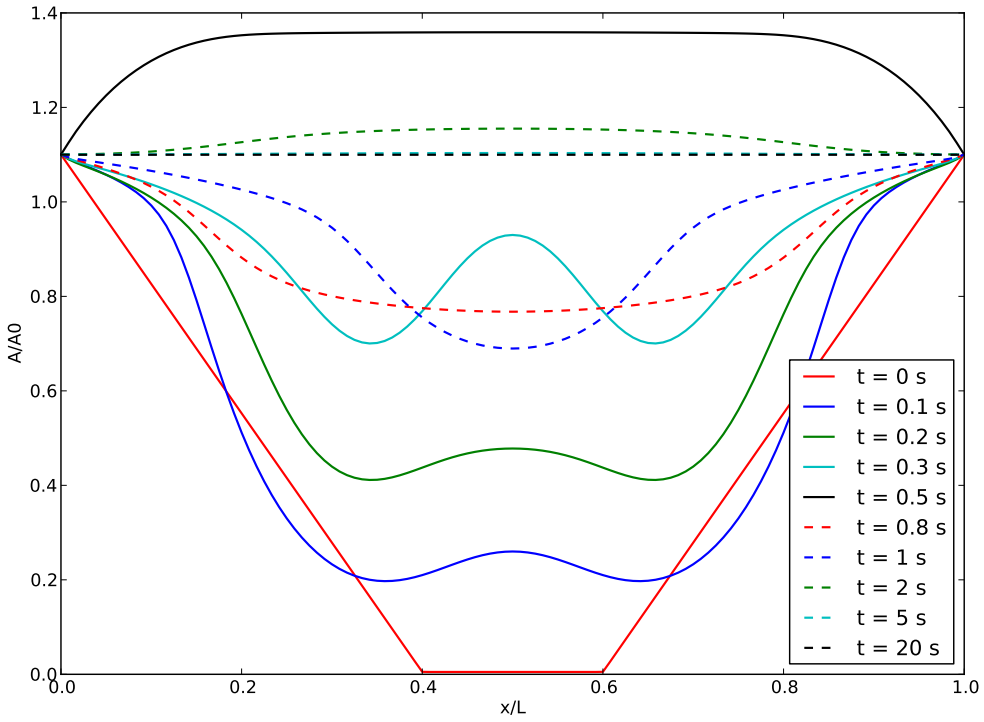

Figure 6.7: Uncollapse of portal vein simulation: $\alpha = \dfrac{A}{A_0}$ is plotted along the vessel at various time instants.

the middle of the tube

$$\begin{aligned} A(x,0) &= \left(1.1 - x\frac{10.95}{4L}\right) A_0 \text{ for } x < 4L/10 \\ A(x,0) &= 0.005 A_0 \text{ for } 4L/10 \leq x \leq 6L/10 \\ A(x,0) &= \left(-1.6375 + x\frac{10.95}{4L}\right) A_0 \text{ for } 6L/10 < x \leq L \\ A(x,0)u(x,0) &= 0 cm^3/s \end{aligned} \tag{6.36}$$

The inlet and outlet pressures are imposed, corresponding to a cross-section area of 1.1 A_0. The pressure corresponding to $A = A_0$ is $P_0 = 1.05$ mmHg, the blood density is $\rho = 1\,\text{g.cm}^{-3}$, the friction term is $f(A, A_0, u) = K_f u(t,x)$, with $K_f = 0.96$ cm^2/s. Gravity is neglected. The first order kinetic scheme is used, with $\Delta x = 0.05$ cm and $\Delta t = 10^{-4}$ s. Figure 6.7 shows the quantity $\alpha = A/A_0$ for various time instants. At time $t = 0$ s, just after unclamping, the vessel is collapsed in the middle. Then, the vessel uncollapses and oscillates around the equilibrium position (see $t = 2$ s and $t = 5$ s in Fig. 6.7) to eventually reach a steady state (see $t = 20$ s in Fig. 6.7).

6.2 Application to hepatectomy

To our knowledge, only a few mathematical models were proposed in the literature to describe the hemodynamics impact of liver surgeries. In [DDWC+12], a cast-based reconstruction of the rat liver vasculature was performed to compute the resistance in the different vascular trees. Various sizes of virtual resection were studied with a resistance model and two 90% resection techniques were compared. The results indicated a portal hyperperfusion after resection and demonstrated that probably better outcomes could be expected with one of the two resection techniques. In [HSBH12], a 3D simulation was performed in the portal vein after right lobe hepatectomy. The geometry, based on medical imaging data, included superior mesenteric and splenic veins merging in portal vein and three portal vein branches. Constant velocities boundary conditions were prescribed in the mesenteric and splenic veins and zero pressure was imposed at the outlets. The right lobe hepatectomy was simulated changing the geometry. Similarly, for a two-lobe liver 0D model, driving conditions were kept unchanged before and after hepatectomy.

The model proposed in the present work differs from these two approaches from several aspects that will be detailed below. Our strategy is to propose a model of moderate complexity which can be parameterized to match measurements, but with a sufficient level of realism to be able to capture non-trivial phenomena observed in animal experiments.

6.2.1 A closed-loop model

To be able to consider waveform changes as a result – and not as an input – of the simulations, a closed-loop model is proposed including 1D and 0D compartments. Although this approach is not new, models of that sort, calibrated with experimental measurements, are not numerous in the literature. Closed-loop models, including 0D-1D-3D vessels, were proposed in [BF13] to study the impact of aortic insufficiency on the local hemodynamics of a cerebral aneurysm, and in [LTHL09] to study the effects of arterial and aortic valvular stenoses. Closed-loop 0D-1D models, including arteries and veins, were proposed in [MS15, MT14]. The latter article focused on head and neck, to study possible connections between the venous vasculature and a class of neurodegenerative diseases. The simulation results were compared to Phase-Contrast MRI flow data.

The closed-loop model proposed in this work is represented in Figure 6.8. The main arteries are modeled with the 1D Euler equations described above. The arterial and venous trees at each outlet, as well as the pulmonary circulation and vena cava, are modeled with three-element Windkessel models. The heart and the liver are also represented by 0D models. The main features of each of these compartments are now detailed.

For the 1D models, the length, the cross-section area A_0 and the bifurcation angles are estimated from CT-scans of the pigs which underwent the surgical operations (CT-scans were done with a Siemens Somatom AS definition 128 machine).

At the bifurcation, the continuity of total pressure is enforced as explained in Section 6.1, except at the bifurcation between the abdominal aorta and the celiac trunk, and when the celiac trunk bifurcates into the hepatic and the splenic arteries. In these two bifurcations, the condition proposed in [FLQ03] is adopted: $P_{T,d_1} = P_{T,m} - 2\,\mathrm{sign}(u_{d_1})u_{d_1}^2\sqrt{2(1-\cos(\alpha_1)}$,

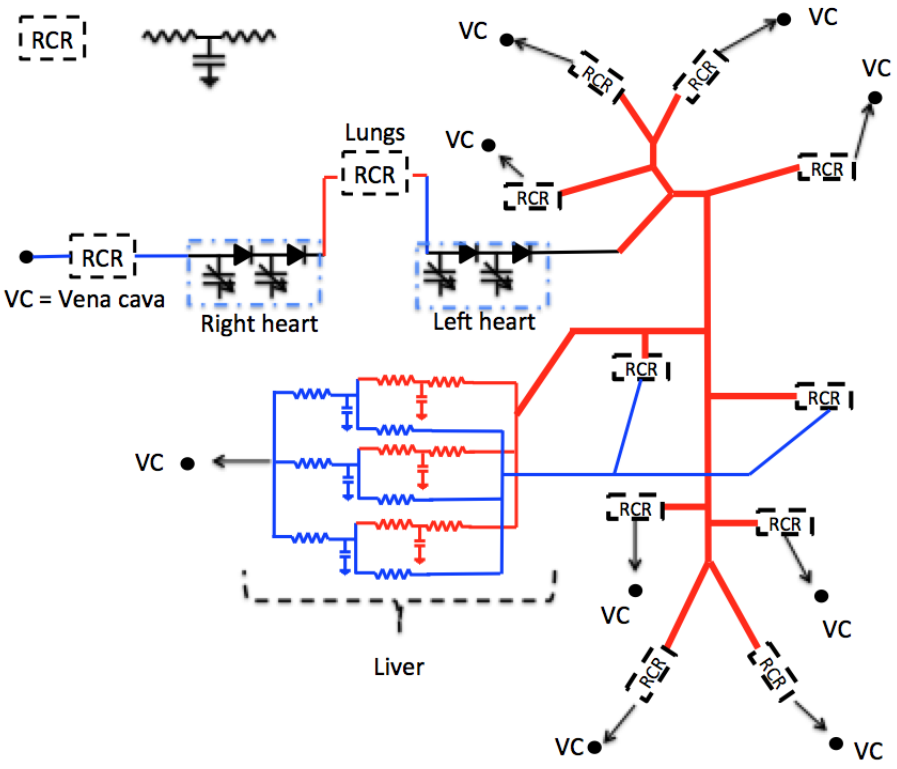

Figure 6.8: Schematic representation of the 1D-0D closed-loop model. 1D blood flow is simulated in the thick lines arteries while thin lines represent the 0D model connections. All RCR units and the liver are linked (thin arrows) to the vena cava (VC).

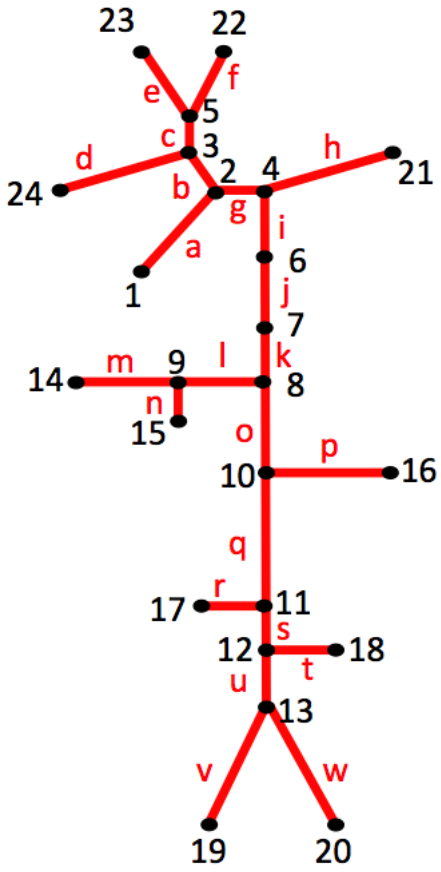

Figure 6.9: 1D arteries node number and arteries id; see Table 6.9 for their parameter values.

id	Name	l (cm)	A_0 (cm^2)	β/ρ (cm/s^2)	N_{el}
a	Ascending aorta	3.5	2.54	2.07 10^5	35
b	Brachiocephalic trunk	2.92	0.46	4.88 10^5	30
c	Aortic arch A	0.36	0.39	5.34 10^5	5
d	Right subclavian	8.5	0.20	7.96 10^5	85
e	Right common carotid	11.8	0.12	1.24 10^6	120
f	Left common carotid	11.9	0.15	9.79 10^5	120
g	Aortic arch B	0.68	2.30	2.17 10^5	7
h	Left Subclavian	12	0.31	6.01 10^5	120
i	Thoracic aorta A	9.1	2.06	2.30 10^5	91
j	Thoracic aorta B	9.5	1.43	2.75 10^5	95
k	Thoracic aorta C	9.5	0.81	3.66 10^5	95
l	Celiac trunk	0.66	0.29	6.22 10^5	7
m	Hepatic artery	5	0.10	1.45 10^6	50
n	Splenic artery	12.8	0.10	1.45 10^6	130
o	Abdominal aorta A	1.7	0.80	3.69 10^5	17
p	Mesenteric artery	3	0.36	5.57 10^5	30
q	Abdominal aorta B	3.55	0.80	3.69 10^5	36
r	Right Renal	3.65	0.18	8.63 10^5	37
s	Abdominal aorta C	0.5	0.78	3.72 10^5	5
t	Left renal	1.37	0.24	6.95 10^5	14
u	Abdominal aorta D	8	0.57	4.36 10^5	80
v	Right iliac	2.9	0.29	6.33 10^5	29
w	Left iliac	2.8	0.34	5.74 10^5	28

Table 6.9: Parameters for the 1D vessels of the pig cardiovascular model. The first column contains the id number of the artery (Figure 6.9), the second the name of the artery, the third l its length in cm, the fourth its cross-section area A_0 in cm^2 from CT-scan, the fifth is the vessel elasticity coefficient β (defined in equation (6.19)) divided by the fluid density ρ, and the last one the number of elements used to discretize the vessel.

where α_1 is the angle of the branches d_1 with respect to the mother vessel.

The elasticity parameters are computed with the following formula [Olu99]

$$\frac{Eh_0}{r_0} = a\exp(br_0) + c, \tag{6.37}$$

where E is the Young's modulus, h_0 and r_0 are the vessel thickness and radius when $A = A_0$. This formula is scaled in order to obtain a pressure in the carotid artery which is similar to the one measured in pigs. The parameters are: $a = 6.0\ 10^6 \text{g.s}^{-2}\text{.cm}^{-1}$, $b = -22.53\text{cm}^{-1}$ and $c = 2.595\ 10^5 \text{g.s}^{-2}\text{.cm}^{-1}$. The values for each artery can be found in Table 6.9.

The total resistances for RCRs are computed with $R_{tot} = \dfrac{\Delta P}{Q}$, by a combination of flow splits from [LFLH81], assuming pig and human flow splits are similar, and of available pressure and flow measurements. These total resistances are then separated into proximal R_p and distal R_d resistances, assuming the proximal resistance carries 10% of the total resistance in each RCR, within the ranges used in [RJS74, VCFJT10, LAVC+11]. The total systemic capacitance is fixed at 4.10^{-4} $\text{cm}^5\text{.dyn}^{-1}$ as reported in [SSW+03] for pig circulation, further split based on the number of large arteries represented by each compartment according to [Lom14]. Table 6.11 summarizes RCR parameter values.

The liver model is based on the pig anatomy. The pig liver consists of three separate lobes and is perfused by venous blood, through the portal vein, and arterial blood, through the hepatic artery. The three lobes are represented by three 0D models in parallel, connected to the heart through the 1D models, and to the digestive organs through the venous input connected to the RCR models of the splenic and mesenteric arteries. The vascular tree sizes are assumed proportional to the perfused tissue mass. A larger vascular tree has a smaller resistance, therefore the lobar resistances of the hepatic artery tree, the portal vein tree and the liver tissue are assumed inversely proportional to the lobe mass. The lobar capacitances of the hepatic artery tree and the liver tissue are assumed proportional to the lobe mass. The proximal to total resistance ratios of the hepatic artery tree reflect the lobar architecture differences [DDWC+12]. The values of the liver parameters are reported in Table 6.13.

The heart model is the same than in the 0D closed-loop model described in chapter 4 paragraph 4.1.2.

Hepatectomy simulation in the 1D-0D closed loop model The system of equations (6.5) is solved for the large arteries, with the first order kinetic scheme, with $\Delta x = 0.1$cm and $\Delta t = 10^{-4}$s (see Table 6.12). Gravity is neglected and the friction function is defined as $f(A, A_0, u) = K_f u(x,t)$, with $K_f = 3\ \text{cm}^2/\text{s}$. The initial conditions are $p(x, t = 0) = 45$ mmHg and $u(x, t = 0) = 5.0\ \text{cm/s}$.

Before hepatectomy, the 1D-0D closed loop model is tuned with the available measurements. Given the variability between subjects, the parameters are not tuned to represent a specific animal but to obtain representative pressures and flow rates. Figure 6.10 shows the measured carotid pressure curves over time for the four animals and the simulated curve. The first cardiac cycles at the left hand side of Figure 6.13 show the pressure and flow rates in the hepatic artery, to be compared with the experimental measurements represented in Figure 6.11. Given the intersubject variability, we considered that we reached a qualitative and quantitative

Heart chamber	Right atrium	Right ventricle	Left atrium	Left ventricle
E_a (dyn/cm^5)	80	750	200	1600
E_b (dyn/cm^5)	110	100	400	350
T_c (s)	0.145	0.289	0.145	0.289
T_r (s)	0.145	0.128	0.145	0.128
t_c (s)	0.68	-	0.68	-
t_r (s)	0.824	-	0.824	-
V_0 (cm^3)	4	10	4	5
	R_p (dyn.s/cm^5)	R_d (dyn.s/cm^5)	C (cm^5/dyn)	
Lungs	53	53	0.03	
Vena cava	10	10	0.004	

Table 6.10: Parameter for heart, lungs and vena cava 0D models. E_a is the contraction function amplitude, E_b the contraction function baseline, T_c is the duration of contraction, T_r is the duration of relaxation, t_c and t_r are the times when the atria begin to contract and relax, respectively and V_0 is the unstressed volume of the chamber. R_p and R_d are the proximal and distal resistances of the RCR model and C is the capacitance.

id	out	R_p (dyn.s/cm^5)	R_d (dyn.s/cm^5)	C (cm^5/dyn)
n	15	953	8584	2.0 10^{-5}
p	16	864	7780	4.0 10^{-5}
r	17	1189	10705	2.0 10^{-5}
t	18	1196	10762	2.0 10^{-5}
v	19	1655	1490	8.0 10^{-5}
w	20	165	14907	8.0 10^{-5}
h	21	1069	9622	6.0 10^{-5}
f	22	1288	11592	4.0 10^{-5}
e	23	1311	11806	4.0 10^{-5}
d	24	1063	9566	6.0 10^{-5}

Table 6.11: Parameters for the outlets RCR models. The first column contains the id of the artery, the second node id, the third R_p the proximal resistance, the fourth R_d the distal resistance, and the last one the capacitance.

Time step (s)	10^{-5}
Mesh size (cm)	0.1
initial pressure $p(x, t = 0)$ (dyn.cm^{-2})	$6.0\,10^4$
initial velocity $u(x, t = 0)$ (cm/s)	5
P_0 (dyn.cm^{-2})	$6.6\,10^4$
K_f (cm^2/s)	3
ρ (g.cm^{-3})	1.05

Table 6.12: 1D-0D closed-loop simulation parameters, time and space discretization parameters, initial conditions for 1D part, P_0, friction parameter and fluid density values.

Liver lobes	Right lobe	Middle lobe	Left lobe
Mass (g)	250	500	180
R_p/R_{tot} arterial tree	0.1	0.5	0.1
	Arterial tree	Portal vein tree	Tissue + Hepatic veins
Mass resistance (g.dyn.s/cm^5)	1.9 10^7	1.86 10^5	7.44 10^4
Mass capacitance (cm^5/dyn/g)	3.0 10^{-8}	-	1.5 10^{-5}
	Hepatectomy parameters		
75% clamping time T_{75} (s)	8		
90% clamping time T_{90} (s)	16		
r (%)	35		

Table 6.13: Liver 0D model parameters. First the different lobe masses are given and the ratio between proximal and total resistances in each lobe for the hepatic artery RCR model. Then, mass resistance and mass capacitance are given for hepatic artery tree, portal vein tree, tissue and hepatic vein tree, followed by the clamping parameters. r is the right lobe resected mass %.

agreement sufficient for our purpose.

The influence of partial hepatectomy on these hepatic artery waveforms is then studied by simulating partial hepatectomy in the model. In pig surgery, partial ablation is done in two steps. In a first stage, two of the three liver lobes are removed, corresponding to approximately 75% ablation. Part of the remaining lobe is removed in a second step to reach a final ablation around 90%. The percentages of ablation are based on initial liver volume. In the model, the first stage is taken into account by dynamically increasing the corresponding lobe resistances and decreasing the corresponding capacitances, to simulate the 75% hepatectomy

$$R(t) = \begin{cases} R \text{ if } t < T_{75} \\ R \exp(5(t - T_{75})) \text{ otherwise} \end{cases} \qquad C(t) = \begin{cases} C \text{ if } t < T_{75} \\ C \exp(-5(t - T_{75})) \text{ otherwise} \end{cases} \tag{6.38}$$

where T_{75} is the time instant of the clamping, and R and C are the values before clamping. Then, to simulate the second part of the surgery, the remaining lobe mass is decreased, simulating a larger ablation resulting in a 90% hepatectomy. The remaining lobe mass is given by

$$M(t) = \begin{cases} M \text{ if } t < T_{90} \\ M\left(1 - r + \dfrac{r}{1 + \exp(-5(t - T_{90}))}\right) \text{ otherwise} , \end{cases} \tag{6.39}$$

where M is the initial lobe mass, T_{90} is the time of the second clamp, and r is the percentage removed in the remaining lobe. The parameters for the simulated hepatectomies are given in Table 6.13.

Typical changes in waveform occurring at 75% hepatectomy have been observed in several animals; Figure 6.11 shows four examples. The pressure amplitude goes up (between 5 and 10 mmHg). For the flow rate, although there is some variability in the pre-hepatectomy shape, after the clamping two characteristic changes can be observed besides the mean value decrease:

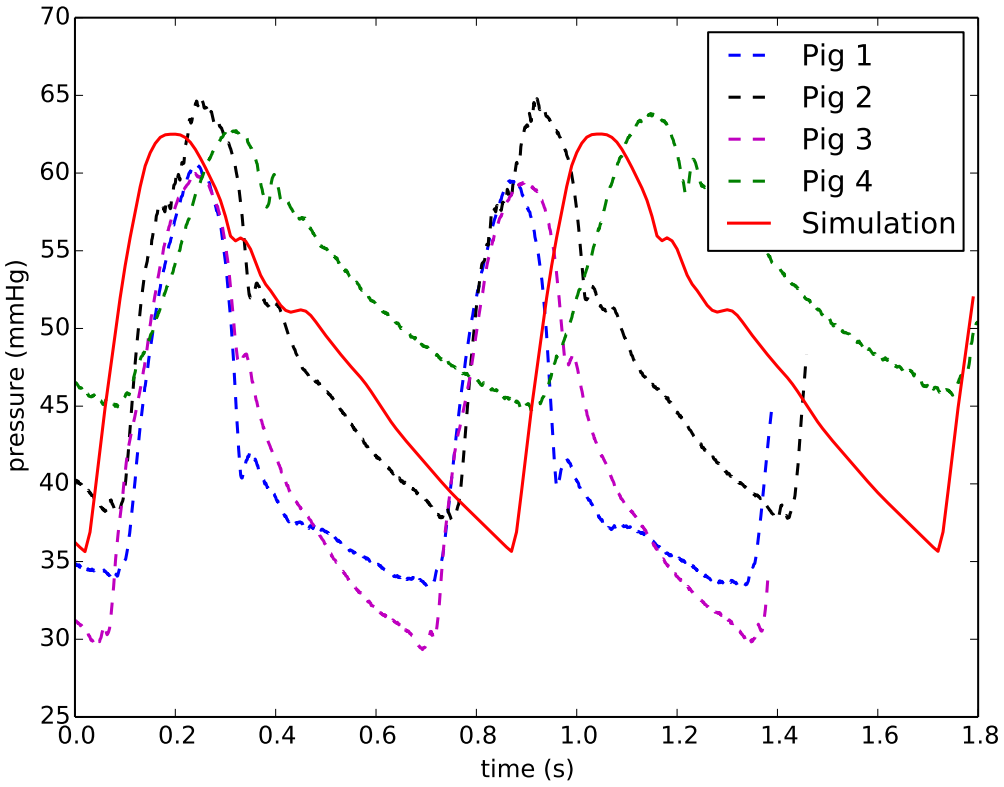

Figure 6.10: Carotid pressure over two cardiac cycles: measurement curves for four pigs (dashed lines) and 1D-0D closed-loop model simulated curve (solid line).

the first peak is sharper, meaning the second peak is lower than before hepatectomy, and diastolic flow is at low values for longer. By contrast, no major changes in waveform have been observed for 75% to 90% hepatectomy, as shown in the experimental curves for two different pigs in Figure 6.12. Apart from a small mean flow decrease, in some pigs such as pig 4, the flow rate minimum that follows systole becomes lower than the flow in diastole.

The two hepatectomies are simulated one after the other with the 1D-0D model. Figure 6.13 shows the simulated pressure and flow rate in the hepatic artery. For the 75% hepatectomy, the increase of pressure is well captured by the model and the typical changes of the flow waveform are well reproduced. For the simulated 75% to 90% hepatectomy, the pressure does not change and a small decrease in the mean and minimum flow appear (Figure 6.13 (b)) as in the experimental curves (Figure 6.12). Thus, the 1D-0D model is in good agreement with the experimental observations before and after clamping, both for 75% and 75% to 90% hepatectomies.

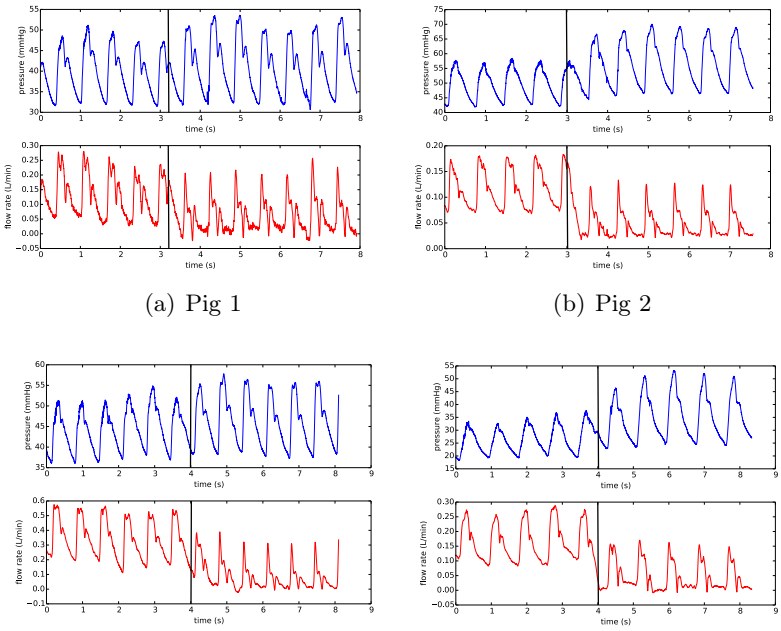

(a) Pig 1 (b) Pig 2

(c) Pig 3 (d) Pig 4

Figure 6.11: Experimental measurements of hepatic artery pressure and flow rate during 75% hepatectomy for four different pigs, the dark lines indicating the clamping time.

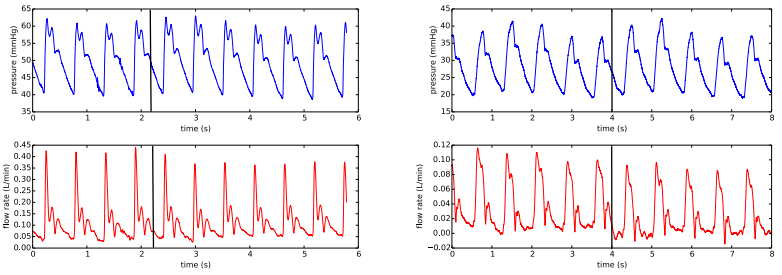

(a) Pig 3 (b) Pig 4

Figure 6.12: Experimental measurements of hepatic artery pressure and flow rate during 75% to 90% hepatectomy for two different pigs, the dark lines indicating the clamping time.

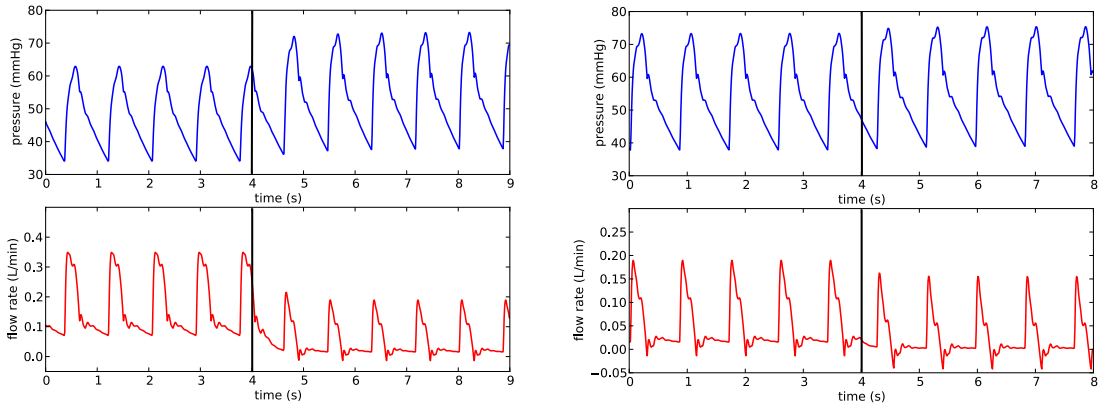

(a) 75% hepatectomy simulation

(b) 75% to 90% hepatectomy simulation

Figure 6.13: 1D-0D closed-loop model results: hepatic artery pressure (mmHg) and flow rate (L/min) during 75% simulated hepatectomy and 75% to 90% simulated hepatectomy, the dark lines indicating the time of simulated clamping.

6.2.2 Discussion

It is quite remarkable that the 1D-0D model can predict the pressure and flow rate waveform changes for both 75% and 75% to 90% hepatectomies. This may be an indication that the waveforms are related to the liver architecture. To further understand this link, parameter sensitivity analysis can help to explain the changes in pressure amplitude and in flow waveform during the 75% hepatectomy. Generalized sensitivity functions (GSFs) analysis help identify correlations between parameters and the distribution over time of the information on parameters contained into the model outputs. Generalized sensitivity functions definitions are given in Appendix B. Details on sensitivity analysis can be found in [TC99, BBD+07, MXPW11, PFGVC14]. By definition, a GSF starts at value zero and ends at value one. The increase in-between is not necessary monotonic; if important correlations between parameters exist oscillations occur. The time interval where the sharpest increase occurs is when most information on the parameter is contained into the model output. The GSF is computed before and after the simulated 75% hepatectomy.

The GSFs of the total resistance and capacitance for flow and pressure in the hepatic arterial trees are plotted in Figures 6.14 and 6.15. Before hepatectomy, pressure and flow are sensitive to resistance during the entire cardiac cycle. This result is expected as resistance impacts mean pressure and flow. The pressure is more sensitive to the capacitance during its rising phase. The sharper increase of capacitance GSF after 75% hepatectomy indicates that the pressure amplitude is especially sensitive to capacitance. Between before and after 75% hepatectomy, capacitance is divided by approximately four.

Before 75% hepatectomy, the flow is sensitive to resistance and capacitance during the entire cardiac cycle. After 75% hepatectomy, the flow is more sensitive to the capacitance between 0.3 s and 0.45 s, corresponding to the sharp decrease in the flow curve.

Thus, the change in parameters due to the 75% hepatectomy – resistance increases by

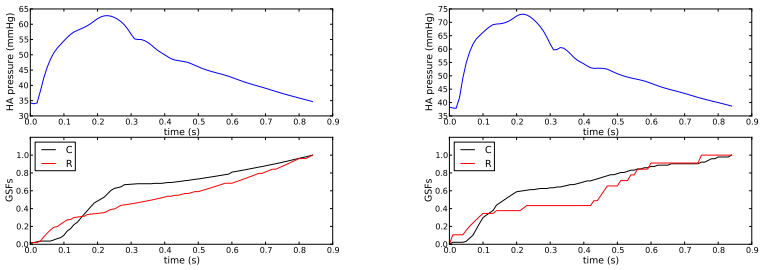

(a) Before partial hepatectomy (b) After 75% hepatectomy

Figure 6.14: Pressure GSF of hepatic arterial trees for the resistance and the capacitance

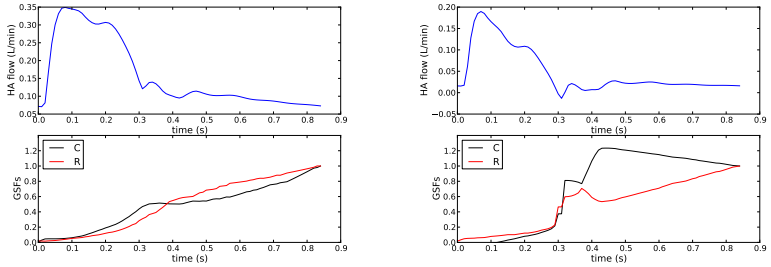

(a) Before partial hepatectomy (b) After 75% hepatectomy

Figure 6.15: Flow rate GSF of hepatic arterial trees for the resistance and the capacitance

around 75% and capacitance decreases by around 75% – seems to explain the changes in pressure and flow waveforms. To confirm this hypothesis, the pre-hepatectomy model is run but with hepatic artery resistance and capacitance parameters multiplied and divided by four respectively, as if each lobe was 75% smaller. The new simulations are compared with the previous ones after the 75% hepatectomy, in Figure 6.16. Contrarily to pressures, the flow rates differ. Therefore, the change of global parameter values – total liver resistance and capacitance – can explain the change in pressure amplitude but it is not enough to obtain the sharp change observed in the flow waveform.

The fact that changes in hepatic artery flow waveform during experiments are observed for 75% hepatectomy but not for 90% hepatectomy, can be explained by the change in architecture in the blood vessel trees. Indeed, in the first hepatectomy, two of the three liver lobes are removed, which leads to an important architecture change. For the second hepatectomy, the remaining lobe mass is decreased and the vessel tree architecture does not change as much. In the model, the simulation of the first stage corresponds to an impedance change from 3 RCRs in parallel to a single RCR. For the second stage, the impedance remains the one of a single RCR; only the remaining lobe model parameters are changed, due to mass proportionality assumptions.

In summary, the modeling choices linking the liver resistances and capacitances to the mass and to the lobar structure of the liver allowed us to reproduce the changes in the experimentally

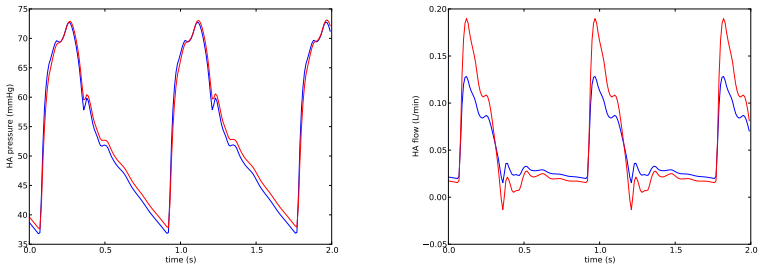

(a) Hepatic artery simulated pressure (b) Hepatic artery simulated flow

Figure 6.16: Simulated pressure and flow in the hepatic artery, with reduced capacitance and increased resistance in each of the 3 lobes (blue) and with previous parameters after the simulated 75% hepatectomy (red).

observed signals. Thus, the study and reproduction of hepatectomy with a model enable us to better understand experimental observations and propose a novel link between architecture and flow. Monitoring waveform changes during post-hepatectomy regeneration could thus be a surrogate for the underlying architectural changes, which are currently not possible to non-invasively quantify.

6.3 Conclusions

In this chapter, the kinetic scheme, mainly used for the Saint-Venant equations in the literature, was successfully adapted to blood flow models. This scheme proved to have a very good behavior for arterial and venous benchmark tests. In particular, its theoretical properties of positivity make it especially well adapted to simulate collapsible vessels.

The scheme was then used to simulate complex behaviors occurring during liver surgeries. First, an idealized test representing the unclamping of the portal vein was proposed. Then the effects of partial hepatectomies on the hepatic artery pressure and flow waveforms were studied with a 1D-0D closed-loop model. Interestingly, the changes observed experimentally on pigs were correctly captured for different percentages of hepatectomy. To the best of our knowledge, these experimental observations were never reported before in the literature. The capability of the model to represent this complex behavior allowed us to propose possible explanations of the observed phenomenon.

Future work will be devoted to a finer characterization of the change of the liver architecture during hepatectomy, in particular for hepatic artery (chapter 5), and to the adaptation of the model to humans.

Chapter 7

Perspectives

In the following section, future work to improve the modeling of liver hemodynamics is presented. In collaboration with Noémie Boissier (INRIA, Mamba), a procedure is proposed to couple micro and macro scale models to improve liver hemodynamics simulation during liver resection and model the liver regeneration, in section 7.1. In section 7.2, liver model improvements are proposed to continue the investigation on the hepatic artery flow and pressure waveforms started in chapters 5 and 6.

7.1 Liver micro-architecture impact on macro hemodynamics

In chapter 4, the averaged hepatic artery flow as well as liver pressures measurements are matched with a 0D closed-loop model, where the portal vein trees are represented by a non-linear pressure dependent resistance. However, the portal vein flow is overestimated with this model.
The presented work has focused on the pre and post liver resection hemodynamics, the data recorded on the days after partial hepatectomy have not been used. The liver regeneration cannot be modeled only by increasing the lobe mass, more information about the vascular structure and tissue regeneration is required. Thus, more knowledge on the micro-architecture and micro-structure of the liver may improve the liver hemodynamics simulation during liver resection and allow to model the liver regeneration.

After the 75% liver resection, the animals are kept under observation for three to seven post-operative days. After seven days, the remaining liver has grown and the liver weight is similar to the pre-operative one. The liver total volume is evaluated with CT-scan before and after surgery and at post-operative days one, three and seven (depending on animals). The average and standard deviation volumes are presented in Figure 7.1. The total hepatic inflow is also measured at these different time instants (Figure 7.2). The growth of the liver is not linear as shown in figure 7.1 and the same dynamics is followed by the total liver inflow (Figure 7.2).
During the surgery, liver biopsy samples are taken and stained, using an H&E staining, to be analyzed. Histological slices, in two different pigs are displayed in figure 7.3. In the two animals the observations are different: no dilatation of sinusoids is observed on the left slice, whereas dilation of sinusoids is observed on the right slice. These 2D slices could lead to wrong hypotheses depending on the vessel cutting angle. However, considering that the sinusoids dilate after partial hepatectomy and during regeneration seems a plausible assumption. Indeed, the total liver inflow does not change much in comparison with the change of liver mass due to the partial resection, and then to regeneration. Therefore, in the micro-architecture, the pressure difference between portal vein and central vein should

increase drastically, leading to dilation in the liver micro-architecture. For example, with the portal vein resistance depending on portal pressure (model proposed in chapter 4), after 75% partial hepatectomy the portal vein tree radii increase by about 10 to 20 percent (assuming Poiseuille flow to link radius and resistance). From the observation of the 2D slices, the dilatation seems located in some parts, and especially in the lobule central area (Figure 7.3 right).

Several works in biology exist on the impact of different percentages of partial hepatectomy on liver micro-structures, on rats and pigs [DHM+06, IYT+07]. After partial hepatectomy, the sinusoid and intersinusoid diameters increase and decrease respectively [DHM+06]. In [IYT+07], hepatic centrilobular necrosis is observed after 70% partial hepatectomy in pigs. Moreover, during the liver regeneration, cell proliferation is not uniform in the lobule. The cells in the center of the lobule (pericentral cells) are the last to proliferate [Rab77]. The proliferation of the endothelial cells (blood vessel wall cells) starts only on the second or third day after liver resection [Mic07].

The changes of liver micro-structures due to partial hepatectomy and regeneration process are difficult to take into account with macro-scale models. However, using micro-scale liver lobule models, the changes of macro-scale parameters, like the lobe resistances, can be assessed. With a mathematical model, different scenarios can be tested, and the impact of micro-architecture changes on liver hemodynamics can be investigated [Boi17]. The different scenarios that could be considered are the following: 1. No change in micro-architecture radius; 2. all sinusoids dilate, the radii increase of 20%; 3. Only the central area dilates, the sinusoid radii increase by 20%, corresponding to 30% of the lobule; 4. The central and midzonal areas dilate, the radii increase by 20%, corresponding to 70% of the lobule.
To consider the changes occurring in the micro-architecture, a spatial representation of the architecture is needed. From the biopsy samples, statistically representative 3D lobule model can be developed, as already proposed for mice liver lobule in [HBB+10]. The statistically representative pig lobule micro-architecture is generated from blood vessel networks, positions of hepatocytes, *etc* [HBB+10, HHF+14].
In pig liver tissue a vascular septum surround the lobule [STC99]. The septum will be added to the model. With this model, the boundary conditions can be set assuming no flow at the border due to the septum. Then only central veins and portal triads boundary conditions are needed. Using the post-operative day biopsy samples, representative lobule at different stages of the liver regeneration can be constructed. The hemodynamics of the micro-circulation in the 3D lobule is modeled assuming Poiseuille flow in each edge, with mass conservation at each node. Pries law is used, to take into account the effective viscosity depending on the capillary radius, and on the percentage of red blood cells in it. The imposed boundary conditions are the portal triad flow and the central vein pressure. With the computed flow and pressure in the representative lobule, the equivalent resistance R_{lobule} of the lobule can be calculated: $R_{lobule} = \Delta P / Q_{in}$, with ΔP the pressure different across the lobule and Q_{in} the total lobule inflow. From the lobule resistance and the liver volume estimation, the liver lobe resistances can be computed.
Then, with the liver lobe resistances, the closed-loop 0D model can compute the liver hemodynamics at the different stages of the surgery: before and after partial hepatectomy

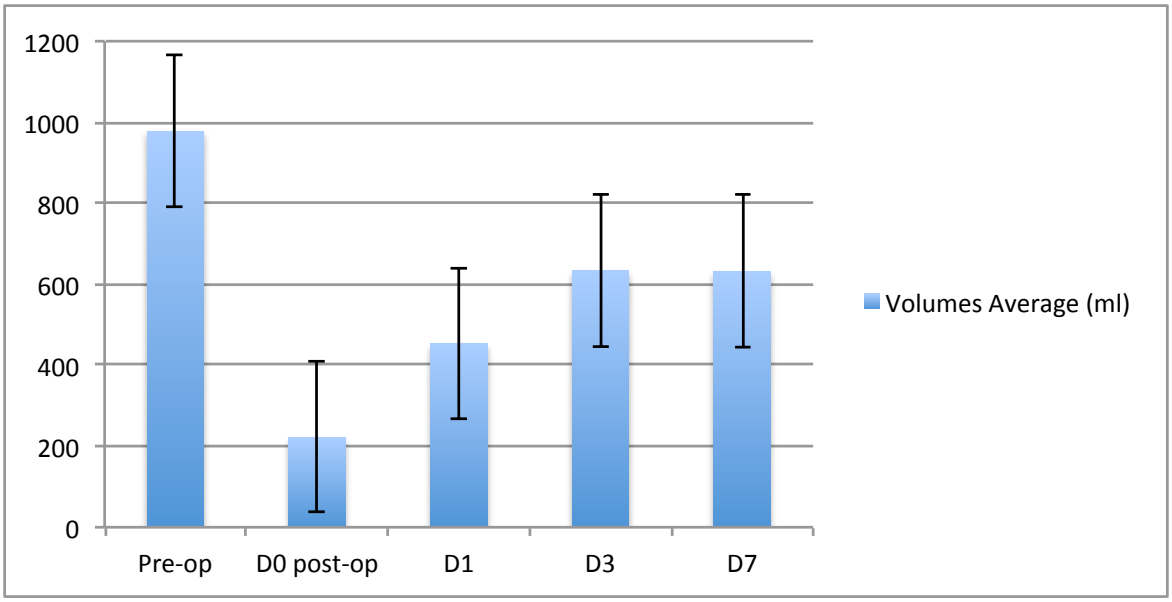

Figure 7.1: Average and standard deviation of liver volume estimation from CT-scan for the different time instants of the surgical protocol.

Scenario 1	Scenario 2	Scenario 3	Scenario 4
No change in the micro-architecture radius	Change of radius in the micro-architecture of 20 percent everywhere	Change of radius in the central area part (30 percent of the lobule) of 20 percent	Change of radius in the midzonal and central areas (70 percent of the lobule) of 20 percent

Table 7.1: Description of the proposed scenarios for micro-architecture changes after partial hepatectomy.

and the different post-operative days. This procedure will be done for the different scenarios proposed for the micro-architecture changes due to liver resection and regeneration. The proposed procedure couples micro and macro scale models to improve liver hemodynamics simulation during liver resection and regeneration.

7.2 Hepatic artery tree model

In chapter 4, the liver lobe hepatic artery tree is modeled with a single resistance. With this model, the post-resection averaged flow in the hepatic artery was well predicted (knowing the pre-resection flow). Understanding and reproducing the flow and pressure waveforms in the hepatic artery is more challenging.
Chapter 5's work on lumped liver model and parameter estimation has shown that the RCR model represents well the post-resection liver hepatic artery tree. Assuming mass proportionality of the parameters and that the liver lobe hepatic artery trees are similar, a

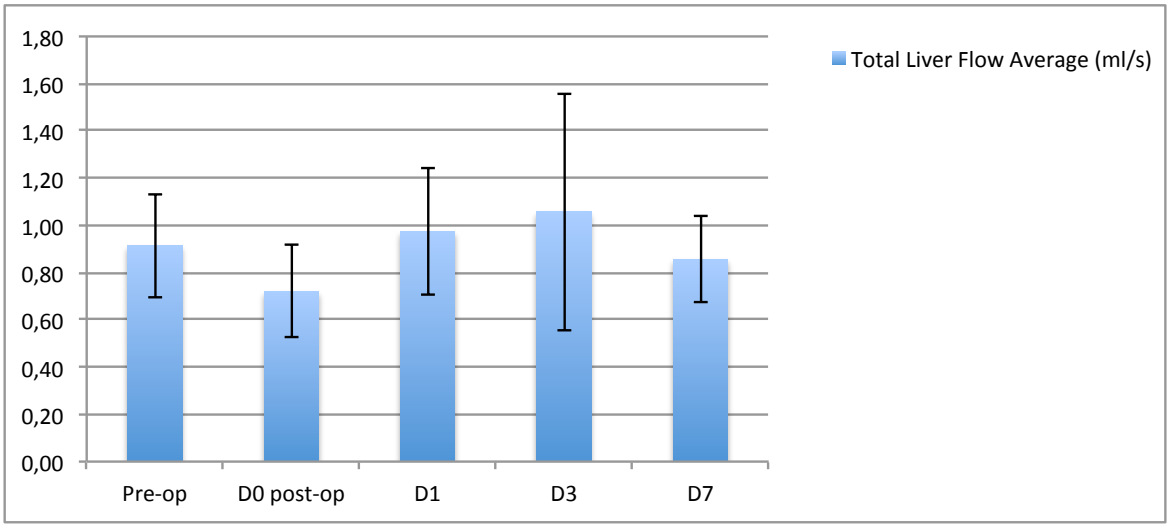

Figure 7.2: Average and standard deviation of liver inflow (hepatic artery plus portal vein flow) for the different time instants of the surgical protocol.

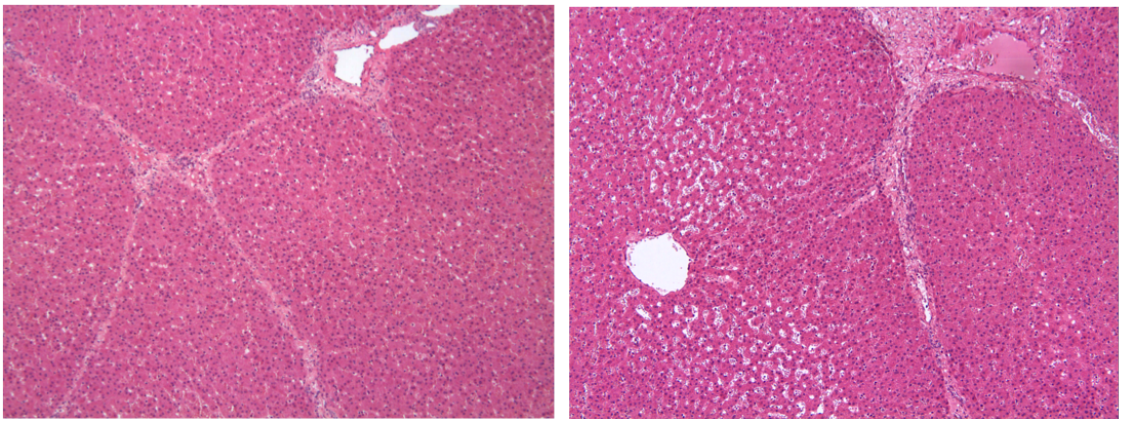

(a) No dilatation (b) Dilatation of the sinusoids

Figure 7.3: H&E stained histological pig slices showing differences in the micro-architecture seven days after 75% partial hepatectomy. (a) No dilatation after partial hepatectomy is observed; (b) dilatation of the sinusoids after partial hepatectomy is seen in the middle of the lobule.

pre-resection liver model is proposed. However the simulation results of this model mismatch the pre-resection measurements.
The 1D-0D closed-loop model, presented in chapter 6, with three RCR model in parallel modeling the hepatic artery trees, is able to reproduce qualitatively the waveform changes observed during the liver surgeries on pigs. In the 1D-0D closed-loop model, the proximal resistance caries 10% of the total resistance in the left and right liver lobes and 50% in the median lobe. Therefore, the hepatic artery trees of the lateral liver lobes and the median lobe are not exactly the same.
According to the proposed models, better knowledge on the differences between the hepatic artery tree architecture in each liver lobe may give clues to improve the liver model and better reproduce pre and post liver resection measurements in the hepatic artery.
In [DDWC+12], combining vascular corrosion casting, micro-CT scanning and image processing, 3D-reconstructions of rat liver vasculature have been presented. The 3D-reconstructions of the different liver lobes have been shown. The mean radius for portal vein and hepatic vein vascular trees, over the generations, for the different lobes has been presented. For the same generation, the mean radius is not the same for all the lobes. Unfortunately the same graph for the hepatic artery tree has not been shown. Vascular cast of the pig liver has been proposed in [CWHM+03], but no details on the hepatic artery tree in liver lobes are given.
From a 3D-reconstruction of the hepatic artery tree for each lobe of a pig liver, the architecture differences can be assessed. And with the differences of radius between the tree generation, the ratio of proximal to total resistance, in RCR model, could be estimated. Including lobe differences may improve the liver model and thus the reproduction of the hemodynamics measurements in the hepatic artery.
[CWHM+03] reported three main lobes in the pig liver, subdivided in five lobes. In the proposed model the 3 main lobes are represented with three electrical circuits in parallel. Including the smaller lobes in the model may improve the simulated waveform. However, adding the smaller lobes will increase the difficulty of the parameter estimation.

Part III

Indocyanine green fluorescence transport in blood and processing by the liver

Chapter 8

Introduction

The liver function can be evaluated with blood sample analysis, quantifying the increase of bilirubine for example. The indocyanine green (ICG) is a dye eliminated exclusively by the liver [AKL+12, HdGN+13]; therefore it is used to assess liver function. The ICG clearance, presented as plasma disappearance rate is, presently, the most reliable method to estimate the hepatic 'function'. In fact, this biomarker combines the effect of liver perfusion and functions. Moreover, the blood analysis requires time and therefore is not instantaneously available during liver surgery. The liver surgery (partial hepatectomy and liver transplantation) are the only curatives treatments for advanced liver disease (see chapter 1). The principal lethal complications after these surgeries are the post-operative liver failure, after major partial hepatectomy, and the small-for-size syndrome, after partial liver transplantation. Both complications are related to a poor pre- or intra-operative evaluation of the function of the remnant or transplanted liver. Therefore a tool for the assessment of liver function intra-operatively is interesting for clinicians.
The liver function can be divided in two steps, the uptake by the liver cells (the removal of the compound from the blood) and the excretion into the bile. A good understanding of ICG processing by the liver may improve the liver function assessment and help clinical decision. In addition, contrast agents, tracers or chemical injections are largely used in medicine for CT-scans, contrast agent for Magnetic Resonance Images, or direct drug tumor targeting. Therefore, mathematical modeling of a compound transport in the main blood vessels and through organ vascular trees has many applications. Mathematical models and numerical simulations are good tools to better understand the transport of ICG to the liver as well as its processing by the liver, in healthy and pathological situations.

Several works exist on transport and diffusion of a compound (a tracer (CFDA SE), an antibiotic spiramycin, midazolam, caffeine or insulin) in the liver [SKN+14], using pharmacokinetic models and including the whole-body PBPK (physiologically based pharmacokinetics) [SSK+15], or for tumor detection with Magnetic Resonance Images modeling [BWKM+07]. In these works, the transport in the arterial and venous trees has been based on resistive models. A model of contrast fluid transport in liver vascular trees and in liver tissue has been proposed in [JRLB14, LJJ+14]. The flow in the upper part of the vascular tree has been modeled with Bernoulli equations and in the smaller vessels porous media model has been used. Direct drug-targeting has been studied in [CK14] with hepatic artery flow 3D CFD simulation for rigid and flexible walls.
The transport in blood and the supply of substrates to tissue have been modeled in [D'A07, DQ08]. 1D models have been used for blood flow and mass transport. Then, these models have been coupled to 3D porous media model for tissue perfusion. The multi-scale models have been used to represent metabolic processes such as those induced by exercise, that take place at different scales (from cells to whole body scales). Other groups have also proposed numerical schemes to solve 1D arterial flow and mass transport equations in

few vessel and in vessel network: a Roe type energy balanced solver has been developed in [MGN15] and a stabilized discontinuous Galerkin approximations with a Taylor basis has been proposed in [KWH13].
Regarding ICG, its concentration in the blood circulation has been studied using pharmacokinetic models. Including compartments for pulmonary circulation, systemic circulation, gut and liver, a minimal physiological model for liver uptake and excretion rate estimation has been developed in [WKA11]. Parameter estimation has been based on arterial ICG concentration over time in dogs that are awake and under anesthesia. The ICG clearance sensitivity to uptake and excretion rates has been studied. Since anesthesia tends to decrease cardiac output, the impact of a reduced flow on the estimated parameter has been also analyzed. Their results suggest that ICG uptake is limited by hepatic cells uptake capacity and bile excretion and not by the blood flow.
The ICG plasma disappearance rate has been largely studied. In particular, a two compartments pharmacokinetic model validated on healthy liver has been proposed in [GKB+83]. Then, the same model has been studied for patients with liver cirrhosis, and a tri-exponential function to better describe the elimination of ICG from plasma has been proposed [BTTB91]. In [OKJB94], two fractions of ICG contained in dye preparations have been taken into account, suggesting that the two fractions disappearing rates are different. Measurements in pigs have been performed, and two types of model have been considered, including or not a temporary storage compartment to determine if taking into account extrahepatic, extravascular distribution is required to explain the measurements. In all these models, the liver is represented with a single compartment, therefore the exchanges between the different liver tissues are not modeled. In [AYIC06], the pharmacokinetics of ICG in cancerous tumor is modeled. After tumor cell injection under the skin of rats, the pharmacokinetic parameters have been estimated with ICG tumor tissue concentration measurements, using the extended Kalman filter. The exchange rate between blood and tissue is estimated, and edematous and necrotic tissue rates are compared. The model parameters may be useful for tumor differentiation. Finally, the liver tissue ICG concentration has been less studied than plasma disappearing rate. In [STK+96] and then in [EDSC+99] near-infrared spectroscopy has been used to estimate hepatic ICG concentration over time on rabbits liver. A sum of two exponential functions has been used to match the measurement curves. Two parameters have been estimated, one for dye uptake from plasma and a second for dye removal from the liver. The changes of uptake and excretion parameters due to different treatments (colchicine, vessel occlusion ...) have also been analyzed [EDSC+99].

In this work the transport in blood of a compound as well as the processing of ICG by the liver is studied. The liver is perfused with arterial and venous blood, thus the modeling of the transport of a compound from the aorta to the liver is challenging. To our knowledge models of compound transport from the aorta to the liver, including the transport through digestive organs, hepatic artery and portal vein have not been studied.
Chapter 9 focuses on the transport of ICG in the blood. The 1D-0D hemodynamics model developed in chapter 6 is used to compute the fluid dynamics. Then, the transport in the 1D domain is numerically solved using an upwind scheme with slope limiters. Two approaches are proposed to model the transport of a compound through the organs' vascular trees. The

model results are compared to indocyanine green fluorescence measurements in liver vessels (part I). Different liver configurations are also considered (after liver resection, in case of hepatic vein obstruction). The goal is to better understand the dynamics of a compound from its intravenous injection to when it reaches the two liver vessels (hepatic artery and portal vein).
Moreover what is influencing this dynamics requires investigation. These questions are motivated by various medical applications. For example, in CT angiography acquisition with contrast, a time for arterial acquisition (depending on the targeted arteries) and another time for portal vein have to be given. Therefore how the time difference of peak intensity is affected by liver, digestive organs and spleen is an interesting question for clinicians. First investigations on that topic are proposed in chapter 9.
Chapter 10 focuses on a precise description of the ICG processing by the liver, including three compartments for the liver model (sinusoids, hepatocytes and bile canaliculi). Contrary to the previous works, this model enables to precisely quantify the different exchanges between liver tissuess. The model is based on ordinary differential equations and parameters are estimated with an inverse problem resolution based on the unscented Kalman filter. The model output sensitivity is studied and the inverse problem resolution is verified on synthetic data. Then, the parameters are identified based on the measurements from [EDSC+99] in rabbits. They are estimated for different liver states, and their link with liver function is investigated. The model predictions are then tested under different liver hypoperfusions.
With only the tissue dynamics, the information on liver excretion function is limited. To our knowledge, for the first time, the ICG fluorescence measurements in liver vessels as well as in liver tissue and common bile duct are recorded. This is performed during pig surgery, namely before or after partial hepatectomy (see part I) to test if it is possible to evaluate peri-operatively liver functional changes. These measurements enable to develop a mathematical model representing the ICG processing from the uptake from blood by the hepatocytes to ICG excretion into bile. Here, to reproduce the ICG measurements, the three compartments for the liver model are required. Chapter 11 extends the model developed in chapter 10 adding a common bile duct compartment. The ICG fluorescence in liver vessels is used as input for the models. To our knowledge, for the first time, different processes for ICG exchange between blood and hepatocytes are proposed and studied with mathematical models. The model output sensitivity to parameters is analyzed. Then, parameter estimation is performed using a population approach with the Monolix software [Mon]. The link between model parameters and liver function is investigated for healthy liver and after partial hepatectomy of varying extent.
Finally, chapter 12 presents the adaptation of the model proposed in chapter 11 for clinical application. Since more information is available during pig surgery, the procedure is first tried out with the measurement subset that would be available in the clinics. A feasibility study is then performed on a few patient measurements after liver transplantation. Several modeling options able to reproduce the observed ICG fluorescence are presented. A new framework is thus established to quantitatively analyze ICG fluorescence dynamics. It consists of the development of a specific pharmacokinetics model and its parameter identification. The aim is to provide a novel estimation of the liver function(s) peri-operatively.

Chapter 9

Compound transport from the heart to the liver

The transport in blood of a compound using the previously developed 1D model (chapter 6) for large arteries is proposed in this chapter. Different numerical tests investigate the transport of a compound in the blood circulation and through the liver vascular trees. Simulation results are qualitatively compared to indocyanine green fluorescence measurements recorded during the partial hepatectomy surgery on pigs (see Part I). The goal is to better understand the dynamics of a compound from its intravenous injection to when it reaches the two liver vessels (hepatic artery and portal vein).
First, the 1D hemodynamics and transport equations for the large arteries and the models for transport through organs are presented. Then, the numerical methods for the resolution of transport in the 1D domain and through the organs are detailed. Finally, the method is verified on test cases, then different situations are simulated: the transport through heart and lungs, the venous return of the compound, the transport after partial hepatectomy, the liver venous outflow blockage.

Contents

9.1 Transport models 141
9.1.1 Transport in large arteries 141
9.1.2 Transport in organs 141
9.1.3 Transport through the liver vascular trees 144
9.1.4 Compound venous return 144
9.2 Numerical resolution 146
9.2.1 Numerical scheme for transport in large arteries 146
9.2.2 Numerical scheme for transport in organs 148
9.3 Results 148
9.3.1 Numerical tests in large arteries 148
9.3.2 Hepatic artery, portal vein and liver lobes concentrations 153
9.4 Discussion and conclusions 159

9.1 Transport models

9.1.1 Transport in large arteries

Euler equation of hemodynamics. Blood flow in large vessels of the cardiovascular system is computed with the hemodynamics model described in chapter 6. The hemodynamics equations are recalled briefly, the details can be found in chapter 6.

$$\begin{cases} \partial_t A + \partial_x(Au) & = 0 \\ \partial_t(Au) + \partial_x(Au^2) + \dfrac{A}{\rho}\partial_x p & = -f(A, A_0, u) \end{cases} \tag{9.1}$$

The first equation stands for mass conservation and the second one for momentum conservation. $A(x,t)$ is the vessel cross-section area, $u(x,t)$ and $p(x,t)$ are the mean velocity and pressure for the corresponding area. The coordinate along the axial axis of the vessel is denoted by $x \in \mathbb{R}$, $t \in [0; +\infty[$ is the time and $f(A, A_0, u)$ is a friction term. The area and pressure are related with the following algebraic constitutive law

$$p(x,t) = P_0 + \beta\left(\sqrt{A} - \sqrt{A_0}\right) \tag{9.2}$$

with A_0 a reference area, P_0 the pressure when $A = A_0$ and β is a coefficient related to the elasticity properties of the vessel. The details on the modeling choices, boundary conditions and numerical scheme can be found in chapter 6.

Transport equations. The transport of a chemical in a one-dimensional vessel equations are derived from reduced transport-diffusion equations [D'A07, FQV09]. The mass transport is modeled in an axisymmetric cylindrical vessel, neglecting diffusion terms. The vessel wall are assumed impermeable and the concentration profile is assumed flat. Under these assumptions, the mass transport equation reads

$$\partial_t(AC) + \partial_x(uAC) = 0 \tag{9.3}$$

With $C(x,t)$ the cross-sectional average concentration.

9.1.2 Transport in organs

Two approaches are studied to model the transport of a compound through a vascular tree. The first approach consists of the analytical computation of the tree transit time, under simplifying assumptions on the structure of the tree. In the second approach, ordinary differential equations model the transport and dispersion of the compound globally through the vascular trees.

Transit time and structured trees. Structured trees are usually proposed to compute an equivalent impedance, to obtain a boundary condition to 1D or 3D hemodynamics equations [Olu99, SOT07, CGT13, VT04, VCFJT06]. Here, organs transit times are computed with structured trees.

As a first approximation and to simplify the calculation, arterial and venous trees are assumed symmetric. Moreover, for one organ, the arterial and venous trees are assumed identical. Usually, for asymmetric trees, two scaling factors describe the daughter vessels radius (r_{d_1} and r_{d_2}) as a function of the parent vessel radius (r_{pa}). In [Olu99, SOT07, Zam99, Mur26] the following relations are reported: $r_{d_1} = \alpha r_{pa}$ and $r_{d_2} = \beta r_{pa}$, with $\alpha = (1+\gamma^{k/2})^{-1/k}$, $\beta = \alpha\sqrt{\gamma}$ and $\gamma = \dfrac{r_{d_2}^2}{r_{d_1}^2}$, where k is called the radius exponent. The exponent value may depend on the vessel radius. Various studies exist in the literature [SNFS63, Pol92] and the radius exponent is found to vary from 2.0 to 3.0. In this work, the trees are assumed symmetric, so $\gamma = 1$, $\beta = \alpha = 2^{-1/k}$. The radius r_i of generation i is assumed to verify $r_i = \alpha^i r_0$. Therefore, the parameters describing the tree structure are: the number of generations N, the length to radius ratio $\lambda = l/r$, the root radius r_0 and the parameter α that describes the tree structure.

Knowing the tree transit time, the transport in a symmetric tree can be analytically solved. Indeed, in a symmetric tree all the pathways are the same. Moreover, the arterial and the venous trees are assumed similar. With these assumptions, the quantity at the output (Q_{ty_o}) of the arterial-venous trees depends on the input quantity (Q_{ty_i}) and on the tree transit time (τ) in the following manner: $Q_{ty_o}(t) = Q_{ty_i}(t - 2\tau)$. The delay is 2τ, because the arterial and venous vascular trees transit time is τ.
The delay τ expression is the sum of all the conduit transit times along one pathway: $\tau = \sum_{j=0}^{N} l_j/u_j$, with l_j and u_j respectively the length and velocity in generation j. Assuming branches are cylinders of constant area, $u_j = q_j/A_j = q_j/(\pi r_j^2) = q_j/(\pi(\alpha^j r_0)^2)$, with q_j the flow in branches of the j^{th} generation. The tree is symmetric, thus $q_j = q_0/2^j$, with q_0 the inlet flow. τ can be expressed as follow:

$$\tau = \sum_{j=0}^{N} (\pi(\alpha^j r_0)^2) l_j 2^j/q_0 = \pi\lambda r_0^3/q_0 \sum_{j=0}^{N} ((\alpha^j)^3 2^j) \tag{9.4}$$

with $\lambda = l_j/r_j$ the length to radius ratio. Finally,

$$\tau = \pi r_0^3 \lambda/q_0 \left((2\alpha^3)^{N+1} - 1\right)/(2\alpha^3 - 1) \tag{9.5}$$

The transit time τ is inversely proportional to the inflow and it depends on the vascular tree structure. Since k varies from 2.0 to 3.0, and $\alpha = 2^{-1/k}$, $2\alpha^3 < 1$. The limit of τ when N tends to infinity is $\pi r_0^3 \lambda/q_0(1 - 2\alpha^3)$.

Series of well-mixed compartment. With the second approach the transport through a network of small vessels is modeled by a series of well-mixed compartments, described by exponential functions [BAW66, BG84, TWM16]. The transport and the dispersion are represented by the convolution of the input concentration with two exponential functions, assuming a series of 2 compartments represents the organ vascular trees (Figure 9.1). The equation reads

$$C_{output}(t) = (C' * h)(t) = (C_{input} * h * h)(t) \tag{9.6}$$

Where C_{input}, C' and C_{output} are respectively the incoming, the intermediate and the exiting concentrations over time, $*$ stands for the convolution product and $h(t) = \frac{1}{\tau}e^{-t/\tau}$ is the transfer function for each compartment (Figure 9.1).

Equation (9.6) is equivalent to the system of ordinary differential equations

$$\begin{cases} \tau\dfrac{dC'}{dt} & = C_{input}(t) - C' \\ \tau\dfrac{dC_{output}}{dt} & = C' - C_{output} \\ C'(t=0) & = C_{output}(t=0) = 0 \end{cases} \tag{9.7}$$

The transport in arterial and venous trees of the organ, leads to a delay as well as the dispersion of the input concentration curve. These phenomena are mimicked with the system of equation (9.7).

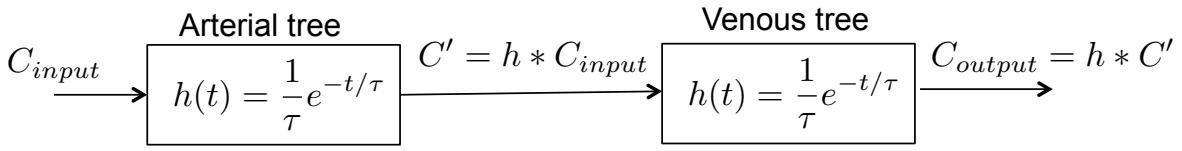

Figure 9.1: Schematic representation of the transport of compound through the organs vascular trees (arterial tree followed by venous tree).

Comparison of the two approaches. The advantage of the first approach, computing the transit time with a structured tree, is that the transit time depends explicitly on the flow and the tree structure. Therefore, flow changes impact the transport through organs. However, the first approach models only the compound convection, no dispersion is included. To add dispersion, an asymmetric tree should be considered. For asymmetric trees, the transit times can be computed recursively. However, in both cases (symmetric and asymmetric) the transit times computation depends on the vascular tree structure. Thus, knowledge on the tree structure is required to accurately compute the transit time.

The second approach takes into account the convection and the dispersion. Moreover, the model depends only on one constant parameter τ, which is related to the ratio of compartment volume per flow rate, both assumed constant over time. With this approach, a change of flow rate is not taken into account. However, in this work the second approach is chosen because of the simplicity of implementation, the poor knowledge on organs vascular tree structure and the importance of dispersion.

Coupling 1D domain and organs vascular trees transport. For each outlet (except the hepatic artery outlet) of the 1D domain, the system (9.7) is solved, where C_{input} is the concentration curve from the 1D domain, $C_{input} = C^{1D}_{outlet}$ (see Figure 9.2). Moreover, the product is intravenously injected, then transported through the heart chambers and the lungs

vascular trees before reaching the aorta. Therefore, the system of equation (9.7) is also solved to model the compound passage through heart and lungs (Figure 9.2).

9.1.3 Transport through the liver vascular trees

The compound arrives to the liver through the hepatic artery and the portal vein. It is first transported through digestive organs (corresponding to the mesenteric artery outlet of the 1D domain) and through the spleen (corresponding to the splenic artery outlet of the 1D domain) (see Figure 9.2). Then, it arrives to the portal vein (blue arrow in Figure 9.2). The hepatic artery and portal vein trees join in the liver tissue and the compound exits the liver through tissue and hepatic veins vascular trees (Figure 9.2) (see chapter 1). When two trees (1 and 2) join at the entry of a third one (3), mass conservation has to be ensured, thus the following relation is imposed: $q_1 C_{output,1} + q_2 C_{output,2} = q_3 C_{input,3}$, with q_i the flows (solution of the 1D-0D system of equations).
The pig liver is composed of three main lobes (see Part I); each lobe is assumed to be composed of three vascular trees: the hepatic artery tree (HA), the portal vein tree (PV) and the liver tissue and hepatic vein tree (HV). To model the transport in each liver lobe tree the following equation is solved:

$$\tau \frac{dC_{output}}{dt} = C_{input}(t) - C_{output}$$

where $C_{input}(t)$ is the incoming concentration over time, from other organs or exiting the 1D domain (Figure 9.2) and C_{output} is the concentration over time exiting the compartment.

9.1.4 Compound venous return

The blood circulation is a closed-loop system, thus after being transported through an organ, the compound returns to the heart and then to the aorta.
The venous concentration is computed with the quantity of compound exiting the organ compartments: $Q_v C_v = \sum C_{output,i}\, q_i$, with q_i the venous tree outlet flow (solution of the hemodynamics 1D-0D system of equations) and $C_{output,i}$ is the concentration exiting the i^{th} compartment (solution of eq. (9.7)).
To model the return of the compound to the heart, the input concentration (imposed to the heart and lungs compartment) includes the venous concentration (Figure 9.2), following this relation: $C_{input} Q_{Ao} = C_{inj}(t) Q_{Ao} + C_v Q_v$. Where C_{input} is the input concentration of the heart-lungs compartment, C_v is the venous concentration and C_{inj} is the compound injection concentration. The aorta and venous flows are Q_{Ao} and Q_v respectively (solution of the hemodynamics 1D-0D system of equations).

In this work, the compound of interest is indocyanine green (ICG), which is eliminated exclusively by the liver [AKL+12, HdGN+13]. Thus, to mimic this elimination the quantity exiting the liver is excluded from the quantity returning to the heart. Therefore, the assumption that all the product is eliminated after the first passage in the liver is made. This assumption is a first approximation to compare the product concentration over time with and without venous return. A more complex model is required to represent the various mechanisms involved in the elimination of the ICG by the liver. The chapters 10 and 11 focus on this topic.

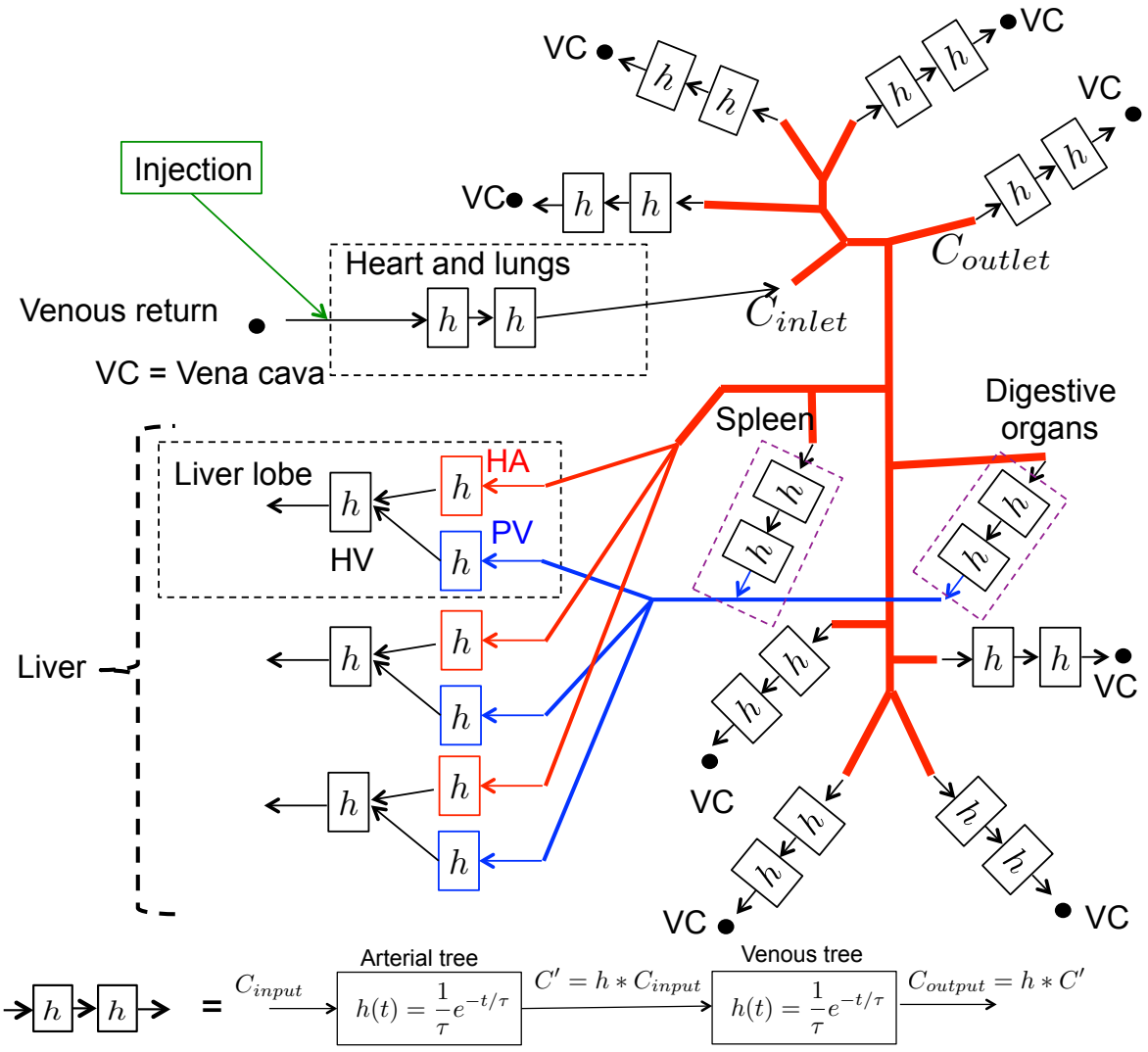

Figure 9.2: Schematic representation of the transport of compound through the large arteries (thick lines) and the organs vascular trees. All product exiting the organs (except the liver) is transported back to the heart and lungs compartment.

9.2 Numerical resolution

9.2.1 Numerical scheme for transport in large arteries

The Euler equation system for hemodynamics (9.1) is solved independently of the transport equation (9.3). Chapter 6 details the hemodynamics equations numerical resolution. The transport equation (9.3) is solved with a finite volume scheme, based on the hemodynamics solution. An upwind scheme with slope limiters is chosen to avoid numerical diffusion. Moreover this scheme is stable under a CFL condition. The chosen slope limiter is the monotonized central-difference limiter (MC), because it fits a wide class of problems [SD12, LeV02, VL77]. The numerical scheme can be written as follow:

$$A_i^{n+1}C_i^{n+1} = A_i^n C_i^n + \frac{\Delta t}{\Delta x_i}(\mathcal{F}_{i-\frac{1}{2}} - \mathcal{F}_{i+\frac{1}{2}}) \tag{9.8}$$

With $i \in \{1, ..., N-1\}$, where A_i^n and C_i^n are respectively approximation of $A(x_i, t^n)$ and $C(x_i, t^n)$, $x_i = i\Delta x_i$ and $t^n = n\Delta t$, where Δx_i and Δt are space (which can be different between vessels) and time steps respectively. A_i^n and A_i^{n+1} are known from the hemodynamics equations resolution. The scheme fluxes are defined by:

$$\begin{aligned}\mathcal{F}_{i-\frac{1}{2}} = \quad & 0.5u_{i-1/2}^n \left((1+\theta_{i-1/2})A_{i-1}^n C_{i-1}^n + (1-\theta_{i-1/2})A_i^n C_i^n\right) \\ & +0.5|u_{i-1/2}^n| \left(1 - \frac{\Delta t}{\Delta x_i}|u_{i-1/2}^n|\right) \phi(r_{i-1/2})(A_i^n C_i^n - A_{i-1}^n C_{i-1}^n)\,,\end{aligned} \tag{9.9}$$

where $u_{i-1/2}^n = 0.5(u_{i-1}^n + u_i^n)$ and $\theta_{i-1/2} = \begin{cases} 1 & \text{if } u_{i-1/2} \geq 0 \\ -1 & \text{if } u_{i-1/2} < 0 \end{cases}$.
And $r_{i-1/2}$ is defined by

$$r_{i-1/2} = \begin{cases} \dfrac{A_{i-1}^n C_{i-1}^n - A_{i-2}^n C_{i-2}^n}{A_i^n C_i^n - A_{i-1}^n C_{i-1}^n} & \text{if } u_{i-1/2} \geq 0 \\ \dfrac{A_{i+1}^n C_{i+1}^n - A_i^n C_i^n}{A_i^n C_i^n - A_{i-1}^n C_{i-1}^n} & \text{if } u_{i-1/2} < 0 \\ 0 & \text{if } |A_i^n C_i^n - A_{i-1}^n C_{i-1}^n| < \varepsilon \text{ or } i = 1 \text{ or } i = N \end{cases} \tag{9.10}$$

In this work $\varepsilon = 10^{-8}$. The function ϕ depends on the slope limiter choice. Here the monotonized central-difference limiter (MC) induces that ϕ is defined by [SD12]:

$$\phi(r) = \max\left(0, \min\left(\frac{1+r}{2}; 2; 2r\right)\right) \tag{9.11}$$

Remark 9.1
With these scheme fluxes, the upwind scheme is without slope limiter between boundary nodes ($i = 0, N$) and the first internal nodes ($i = 1$, $N-1$).

Boundary conditions. Similarly to the hemodynamics scheme (chapter 6), the boundary and transmission conditions are treated separately, and the different types of boundaries are: inlet (a), outlet (b), multi-tube (c) and bifurcation (d) interface. The inlet concentration

$C_{inlet}(t)$ over time is imposed (boundary (a)). In the following examples, the inlet concentration is the injected concentration $C_{inlet} = C_{inj}$ or the heart-lungs compartment output concentration (eq. (9.7)) $C_{inlet} = C_{output}^{heart-lungs}$. The inlet boundary $i = 0$ concentration is given by:

$$A_0^{n+1}C_0^{n+1} = A_0^nC_0^n + \frac{\Delta t}{\Delta x_0} \begin{array}{l} \left[u_0^n \left(A_0^nC_{inlet}(t^n)\mathbf{1}_{u_0^n \geq 0} + A_0^nC_0^n\mathbf{1}_{u_0^n<0}\right)\right. \\ \left. -u_{1/2}^n \left(A_0^nC_0^n\mathbf{1}_{u_{1/2}^n \geq 0} + A_1^nC_1^n\mathbf{1}_{u_{1/2}^n<0}\right)\right] \end{array}. \tag{9.12}$$

The assumption that no compound can enter through the outlets is imposed, and an outlet boundary condition (b) is defined as

$$A_i^{n+1}C_i^{n+1} = A_i^nC_i^n + \frac{\Delta t}{\Delta x_i} \begin{array}{l} \left[u_{i-1/2}^n \left(A_{i-1}^nC_{i-1}^n\mathbf{1}_{u_{i-1/2}^n \geq 0} + A_i^nC_i^n\mathbf{1}_{u_{i-1/2}^n<0}\right)\right. \\ \left. -u_i^n \left(A_i^nC_i^n\mathbf{1}_{u_i^n \geq 0}\right)\right] \end{array} \tag{9.13}$$

REMARK 9.2
The assumption that no compound can enter from the outlets may be incorrect. Indeed, if the velocity becomes negative some compound should re-enter the 1D domain. The outlets of the 1D-domain are assumed to be sinks.

The multi-tube interface (boundary (c)) is treated with an upwind scheme. M denotes the mother node (outlet of the mother vessel) and d for daughter node (inlet of the daughter vessel) and the velocity at the interface is $u_{Int}^n = 0.5(u_M^n + u_d^n)$. We have

$$A_M^{n+1}C_M^{n+1} = A_M^nC_M^n + \frac{\Delta t}{\Delta x_M} \begin{array}{l} \left[u_{M-1/2}^n \left(A_{M-1}^nC_{M-1}^n\mathbf{1}_{u_{M-1/2}^n \geq 0} + A_M^nC_M^n\mathbf{1}_{u_{M-1/2}^n<0}\right)\right. \\ \left. -u_{Int}^n \left(A_M^nC_M^n\mathbf{1}_{u_{Int}^n \geq 0} + A_d^nC_d^n\mathbf{1}_{u_{Int}^n<0}\right)\right] \end{array}. \tag{9.14}$$

And for the daughter vessel the formula is similar

$$A_d^{n+1}C_d^{n+1} = A_d^nC_d^n + \frac{\Delta t}{\Delta x_d} \begin{array}{l} \left[u_{Int}^n \left(A_M^nC_M^n\mathbf{1}_{u_{Int}^n \geq 0} + A_d^nC_d^n\mathbf{1}_{u_{Int}^n<0}\right)\right. \\ \left. -u_{d+1/2}^n \left(A_d^nC_d^n\mathbf{1}_{u_{d+1/2}^n \geq 0} + A_{d+1}^nC_{d+1}^n\mathbf{1}_{u_{d+1/2}^n<0}\right)\right] \end{array} \tag{9.15}$$

With these formulas the conservation of compound mass between the two vessels is ensured. The last type of boundary is the bifurcation (boundary (d)), one mother vessel denoted by M and two daughter vessels denoted by d_1 and d_2. The interface velocities are defined as follow

$$u_{Int_k}^n = 0.5(u_M^n + u_{d_k}^n) \quad k = 1, 2. \tag{9.16}$$

In order to ensure the compound mass conservation at the bifurcation, the following fluxes are defined

$$A_{d_k}^{n+1}C_{d_k}^{n+1} = A_{d_k}^{n}C_{d_k}^{n} + \frac{\Delta t}{\Delta x_{d_k}} \quad \left[u_{Int_k}^{n}\left(A_M^n C_M^n \mathbf{1}_{u_{Int_k}^n \geq 0} + A_{d_k}^n C_{d_k}^n \mathbf{1}_{u_{Int_k}^n < 0}\right)\right. \\ \left. -u_{d_k+1/2}^{n}\left(A_{d_k}^n C_{d_k}^n \mathbf{1}_{u_{d_k+1/2}^n \geq 0} + A_{d_k+1}^n C_{d_k+1}^n \mathbf{1}_{u_{d_k+1/2}^n < 0}\right)\right] \tag{9.17}$$

with $k = 1{,}2$. And for the mother vessel:

$$A_M^{n+1}C_M^{n+1} = A_M^n C_M^n + \frac{\Delta t}{\Delta x_M} \quad \left[u_{M-1/2}^{n}\left(A_{M-1}^n C_{M-1}^n \mathbf{1}_{u_{M-1/2}^n \geq 0} + A_M^n C_M^n \mathbf{1}_{u_{M-1/2}^n < 0}\right)\right. \\ -u_{Int_1}^{n}\left(A_M^n C_M^n \mathbf{1}_{u_{Int_1}^n \geq 0} + A_{d_1}^n C_{d_1}^n \mathbf{1}_{u_{Int_1}^n < 0}\right) \\ \left. -u_{Int_2}^{n}\left(A_M^n C_M^n \mathbf{1}_{u_{Int_2}^n \geq 0} + A_{d_2}^n C_{d_2}^n \mathbf{1}_{u_{Int_2}^n < 0}\right)\right] \tag{9.18}$$

9.2.2 Numerical scheme for transport in organs

First, the transport in the large arteries is solved with the scheme detailed in section 9.2.1. Then, for each outlet the system (9.7) is solved with an Euler implicit scheme:

$$\begin{aligned} C'^{n+1} &= \frac{1}{1+\Delta t/\tau}\left(C'^{n} + \Delta t C_{input}^{n+1}/\tau\right) \\ C_{output}^{n+1} &= \frac{1}{1+\Delta t/\tau}\left(C_{output}^{n} + \Delta t C'^{n+1}/\tau\right) \end{aligned} \tag{9.19}$$

For the liver lobe trees the equation is solved similarly:

$$C_{output}^{n+1} = \frac{1}{1+\Delta t/\tau}\left(C_{output}^{n} + \Delta t C_{input}^{n+1}/\tau\right) \tag{9.20}$$

where C_{input}^{n+1} is the concentration at the entry of the compartment and C_{output}^{n+1} is the concentration exiting the compartment.

9.3 Results

9.3.1 Numerical tests in large arteries

The numerical scheme, for the 1D domain, described in the section 9.2.1 is verified with different test cases without considering the transport through compartments or venous return. First a single vessel is considered. Then a bifurcation is studied. Finally, the transport in a network of arteries is presented. For each test case, parameters for hemodynamics equations are required. For the single vessel test, the hemodynamics is solved for the common carotid and the thoracic aorta benchmarks from Boileau et al. [BNB+15]. In these cases, the inlet flow is imposed (time-varying and constant flow are considered), and the vessel is coupled to a three-element Windkessel model of the rest of the systemic circulation. For the bifurcation test case, the hemodynamics parameters are from the aortic bifurcation test case proposed in [BNB+15]. The hemodynamics boundary conditions are, the inlet flow (time-varying and constant flow are considered), and the two daughter vessels are coupled to two three-element

Windkessel models. The arterial network test case hemodynamics is solved with the pig blood circulation 1D-0D model presented in chapter 6. The 1D-0D closed-loop model hemodynamics is considered as well as the same model with a constant inlet flow (open-loop model). For all cases, the parameters as well as the transmission and boundary conditions for the resolution of the hemodynamics are recalled in chapter 6.

Next, for the transport equations, the inlet concentration boundary condition (a) is a Gaussian over time: $C_{inlet}(t) = \exp(-5(t - t_i)^2)$, with different t_i.

Single vessel. The hemodynamics equations are solved in a single vessel and three different inlet flows are considered. First a constant inlet flow is imposed to the thoracic aorta vessel (Figure 9.3 top left). Then a realistic time varying inlet flow is imposed to a common carotid vessel (the inlet flow remains positive over one cardiac cycle (Figure 9.3 middle left)). Finally, a thoracic aorta vessel is considered with a time varying realistic inlet flow, which becomes negative over one cardiac cycle (Figure 9.3 bottom left). Figure 9.3 (left) shows the inlet flows over time. Figure 9.3 (right) displays the concentration over time for three different positions in the vessel for the different test cases, as well as the input concentration.
With a constant flow, the initial Gaussian is transported at constant velocity as expected (without numerical diffusion, Figure 9.3 top right). The simulation and the analytic solution are in excellent agreement. With a time dependent positive flow, the Gaussian shape is modified due to the non-constant velocity in time (Figure 9.3 middle). Since the flow remains positive, the compound is always transported forward in the vessel. On the contrary, the Gaussian shape of the imposed concentration is completely lost for a time-dependent and possibly negative blood flow as shown in Figure 9.3 (bottom). At time $t = 3s$ the flow is positive and the compound enters the vessel (green curve Figure 9.3 (bottom right)). Then the flow decreases and become negative then null, the concentration is almost constant. Just before $t = 4s$ the flow increases rapidly and the compound start entering the vessel again. The plateaus in the concentration curve are explained by the small or negative flow during the cardiac cycle.

Aortic bifurcation. The second numerical test is the transport in a bifurcation, two different inlet flows are imposed: a constant flow and a realistic aortic flow. Figure 9.4 (left) shows the inlet flows over time. Figure 9.4 (right) displays the compound concentration over time in the bifurcation for different locations as well as the inlet concentration.
When the inlet flow is constant, the analytic solution is also plotted. Similarly to the previous case, when the inlet flow is constant over time, the Gaussian is transported with a constant velocity (without numerical diffusion) and the simulation is in good agreement with the analytic solution. The realistic aortic flow is time varying and possibly negative (Figure 9.4 bottom left). In this case, compared to the single vessel thoracic aorta case, the flow remains strictly negative during a part of the cardiac cycle. The compound in the blood is therefore transported forward, then backward in the vessel. The concentration curve over time decreases and increases due to these variation of blood flows. The inlet concentration Gaussian shape is thus lost (Figure 9.4 bottom right). For both inlet flows, the concentration over time in the two daughter vessels are the same. This result is expected as the bifurcation

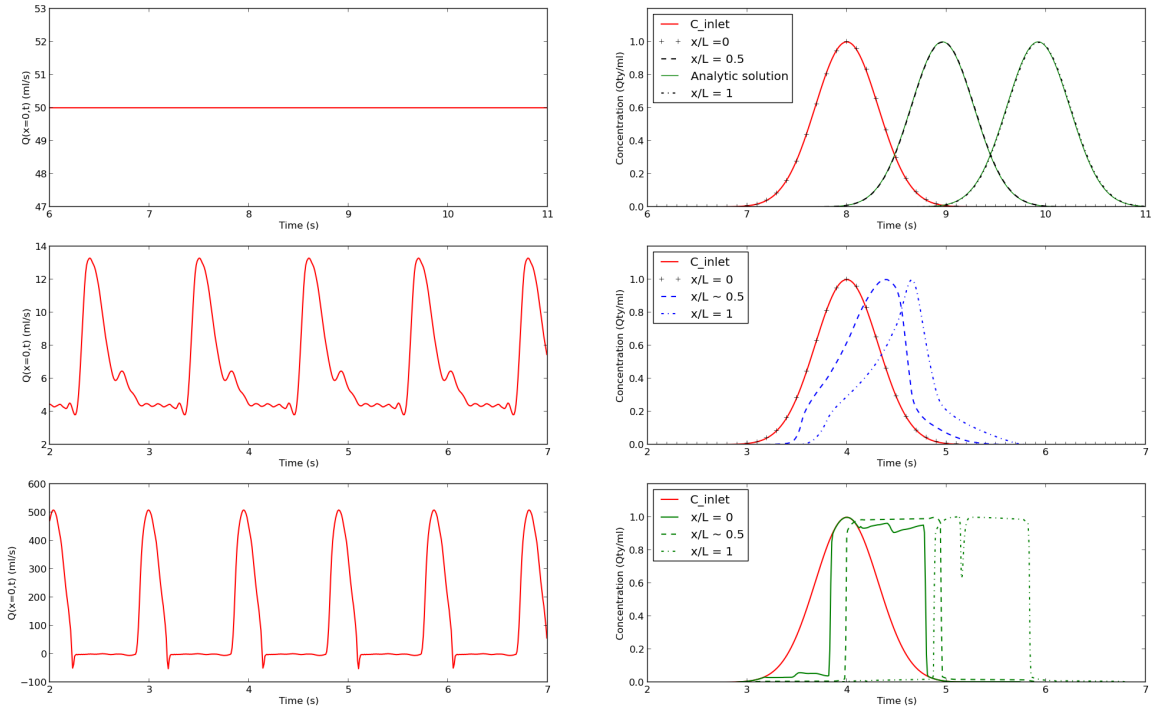

Figure 9.3: Transport in a single vessel, for different inlet flows. The imposed inlet flow over time is shown on the left side. The inlet concentration (C_{inlet}) as well as the concentration over time for three different locations in the vessel (right): the first node ($x/L = 0$); the middle of the vessel ($x/L \simeq 0.5$) and the outlet ($x/L = 1$). When a constant inlet flow is imposed, the analytic solution is also plotted.

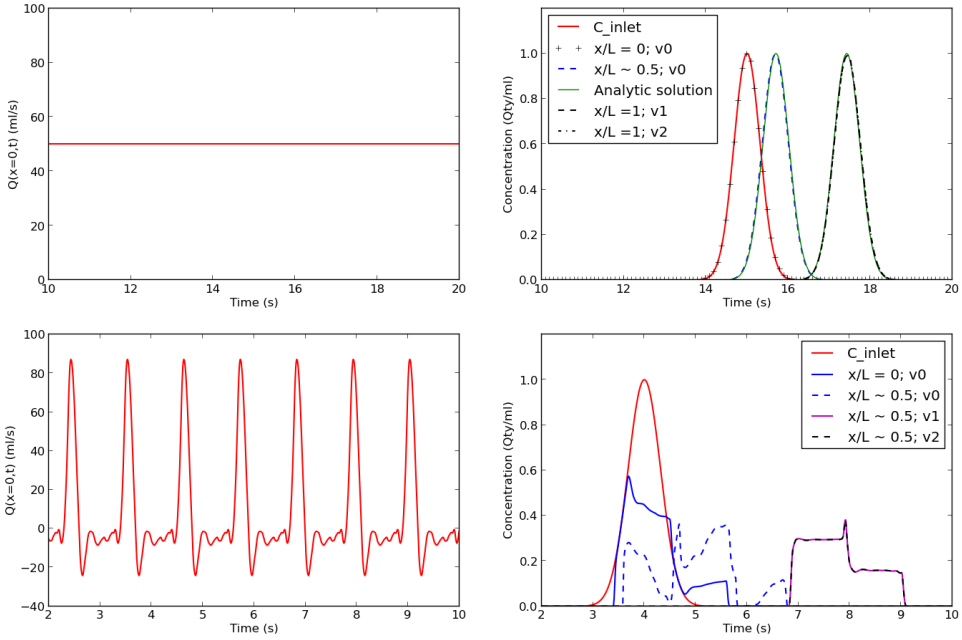

Figure 9.4: Transport in a bifurcation, for two different inlet flows. The imposed inlet flow over time is shown on the left side. The inlet concentration (C_{inlet}) as well as the concentration over time for three different locations in the bifurcation (right): the first node ($x/L = 0$; v_0); the middle of the mother vessel ($x/L \simeq 0.5$; v_0) and the middle or end of the daughter vessels ($x/L \simeq 0.5$; $v_1; v_2$ or $x/L = 1$; $v_1; v_2$). When a constant inlet flow is imposed, the analytic solution is also potted.

is symmetric. The model and the numerical scheme are verified with a constant value of blood flow. However, in reality the blood flow is not constant in time (especially in large arteries). The obtained concentration curves with time varying flow are different from the concentration measurements displayed in literature [PRM+06, TWM16]. Model limitations will be discussed later.

Systemic circulation. The transport of a compound in the blood of 23 main arteries of the pig systemic circulation is simulated. The hemodynamics equations are solved by a 1D-0D closed-loop model (chapter 6). A second test is also studied with a constant inlet flow ($Q(x = 0,t) = 50$ml/s, open loop model). Figure 9.5 shows the concentration over time in the thoracic and abdominal aorta (top), as well as in the two carotid arteries (bottom) for both inlet flows. For a constant inlet flow (Figure 9.5 left), the compound is transported forward, without dispersion between the thoracic and the abdominal aorta. Indeed, in this portion of vessels there is no bifurcations (only multi-tube interfaces). Since the left and right carotid arteries bifurcation is not symmetric, the compound concentration differs between the two

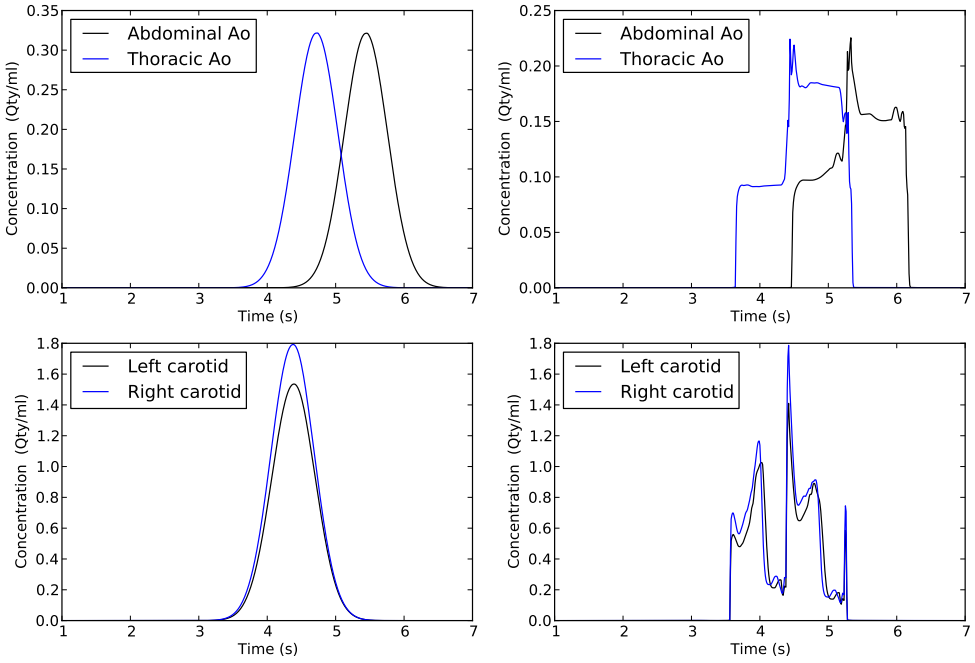

Figure 9.5: Concentration over time for constant inlet flow (left) and for 1D-0D closed-loop model flow (right) at different locations of the 23 arteries system: the thoracic aorta and the abdominal aorta (top); the left and right common arteries (bottom).

vessels. The concentration is lower in the left carotid artery. However, the timing of peaks in both carotid arteries are similar.

As shown previously the Gaussian shape is lost when the velocity is not constant over time. When the velocity is low or negative the concentration of compound remains constant or decreases (Figure 9.5 right). Similar sharp increase and decrease of concentration in the thoracic and abdominal aorta are repported in a human arterial network with 94 arteries in [MGN15].

The model aims at explaining the indocyanine green measurements in the hepatic artery and the portal vein (part I). Figure 9.6 displays the measurement curves (for one typical animal), as well as the simulated hepatic artery concentration over time with constant and time-varying blood velocity (1D-0D model for hemodynamics). In the simulation with time-dependent velocity large oscillations appear, that are not observed in the measurements curve (Figure 9.6 (a) and (b)). Oscillations are not related to numerical instabilities but correspond to each cardiac cycle. As previously mentioned, the blood time varying velocity is the cause of the oscillations. Indeed with a constant inflow, no oscillations appear (Figure 9.6 (b)). The one-dimensional equations for transport seem to miss a mixing phenomena (due to the different velocities in the vessel area), this limitation will be discussed later. For the next

Compartment	τ in second
Liver lobe HA/PV/HV trees	5
Digestive organs	8
Spleen	8
Heart and lungs	2
Other organs	30

Table 9.1: τ parameters for each organ compartment (Figure 9.2)

simulations, a constant inlet flow is considered to easily compare the simulation results and the measurements.

9.3.2 Hepatic artery, portal vein and liver lobes concentrations

After intravenous injection of indocyanine green (ICG), the hepatic artery and portal vein fluorescence are measured over time in pigs (see Part I). The measured fluorescence is assumed linked to the concentration of ICG in the vessels. The measurements for two different animals are shown in figure 9.7. Since the measurements are intensities and not concentrations, the simulation results are qualitatively compared to these measurements (dispersion, delay between curves ...).
The 23 arteries 1D-0D model (see chapter 6) is used with a constant inlet flow $Q(x = 0,t) = 50\text{ml/s}$. The injected concentration is a Gaussian $C_{inj}(t) = 10\exp(-0.5(t - 4.0)^2)$, that models the rapid intravenous injection (around 2 seconds).
The parameter τ for each well-mixed compartment is fixed (see Table 9.1).
Compared with the other well-mixed compartment the liver lobe compartments represent smaller vascular trees, therefore the transit time is smaller. The transit times of the spleen and digestive organs compartments are fixed to obtain a delay between hepatic artery and portal vein maximum concentrations similar to the measured one (section 2.2.2). Finally, the other organs and heart-lungs compartment parameters are fixed to obtain a circulation time near forty seconds. This time is reported in literature for 30 kg children [Sec36].
First, the simulated concentration and measurements in the hepatic artery and the portal vein over time are compared. The impact of heart-lungs compartment, and of the compound venous return is studied. Then, two liver configurations, that may occur after liver surgery, are simulated: post-hepatectomy liver and right hepatic vein flow blockage.

Intravenous injection and venous return. The concentration in the hepatic artery and in the portal vein are simulated with the 23 arteries model and organ compartments. The simulation is done with and without the heart-lungs compartment (Figure 9.8), without venous return. In the measurements, a two-second intravenous injection leads to a ten-second large curve in the hepatic artery (Figure 9.7). The passage through heart chambers and lungs vascular tree explains this observation (Figure 9.8). The two simulations show the difference between an intravenous injection and an injection that would be performed in the aorta for example.

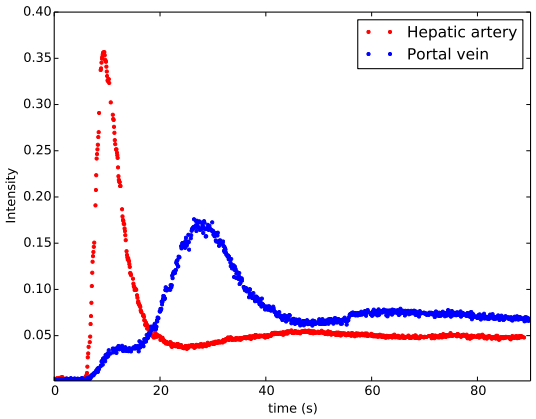

(a) ICG fluorescence measurements

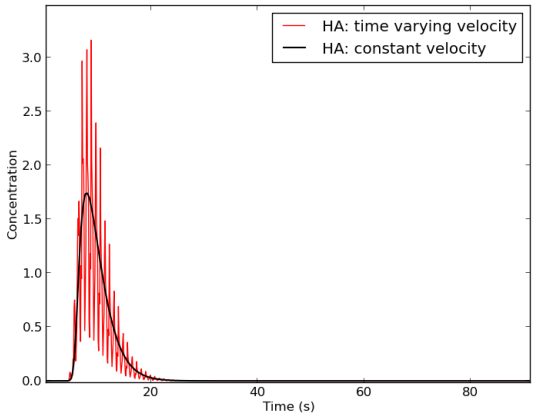

(b) Simulation with 1D-0D closed-loop model and with a constant inlet flow (open loop)

Figure 9.6: ICG fluorescence measurements (normalized by the reference intensity) and simulated concentration over time in the hepatic artery.

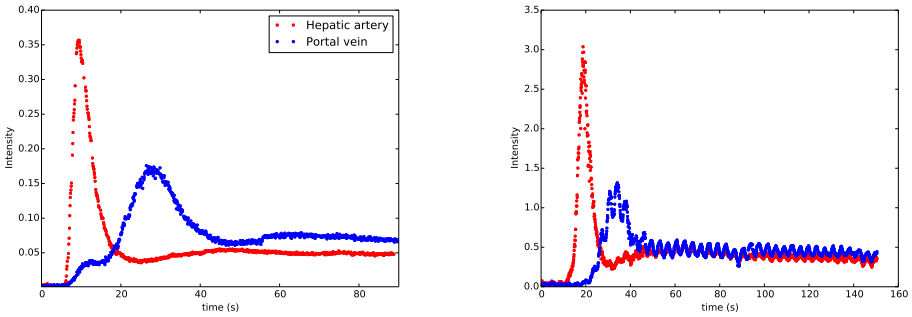

(a) Pig 1 (b) Pig 2

Figure 9.7: ICG fluorescence measurements (normalized by the reference intensity) over time in the hepatic artery and the portal vein for two animals.

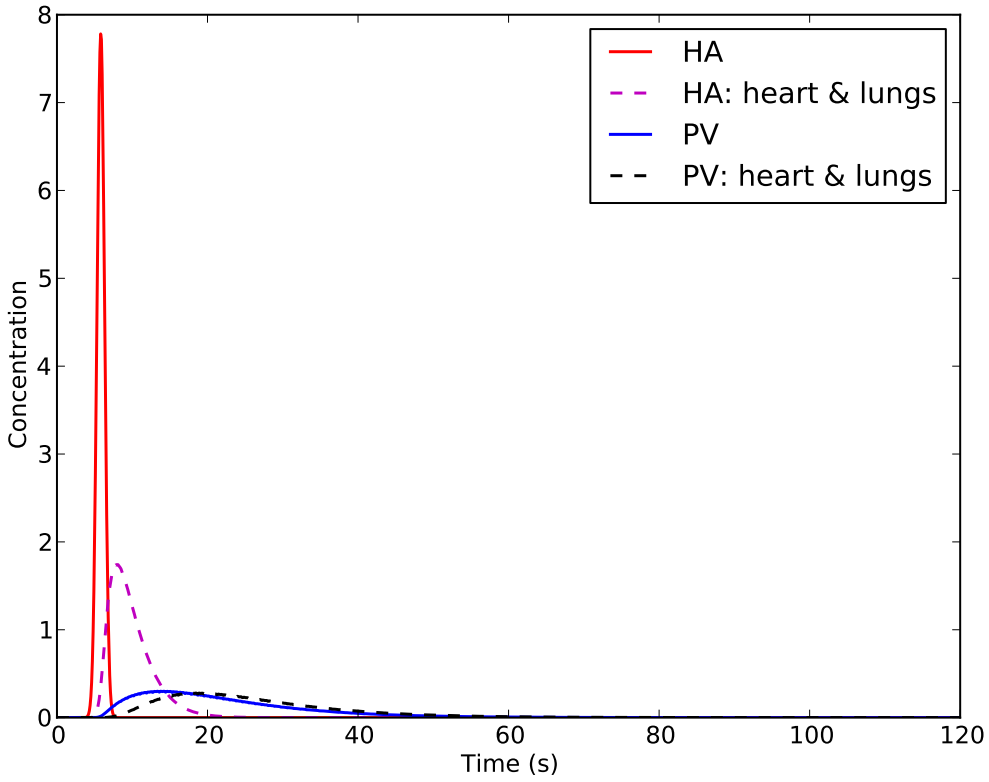

Figure 9.8: Simulated compound concentration over time in the hepatic artery and the portal vein without (full) and with (dashed) heart and lungs compartment. The simulations are obtained with the 1D-0D pig systemic circulation with constant inflow (open-loop model).

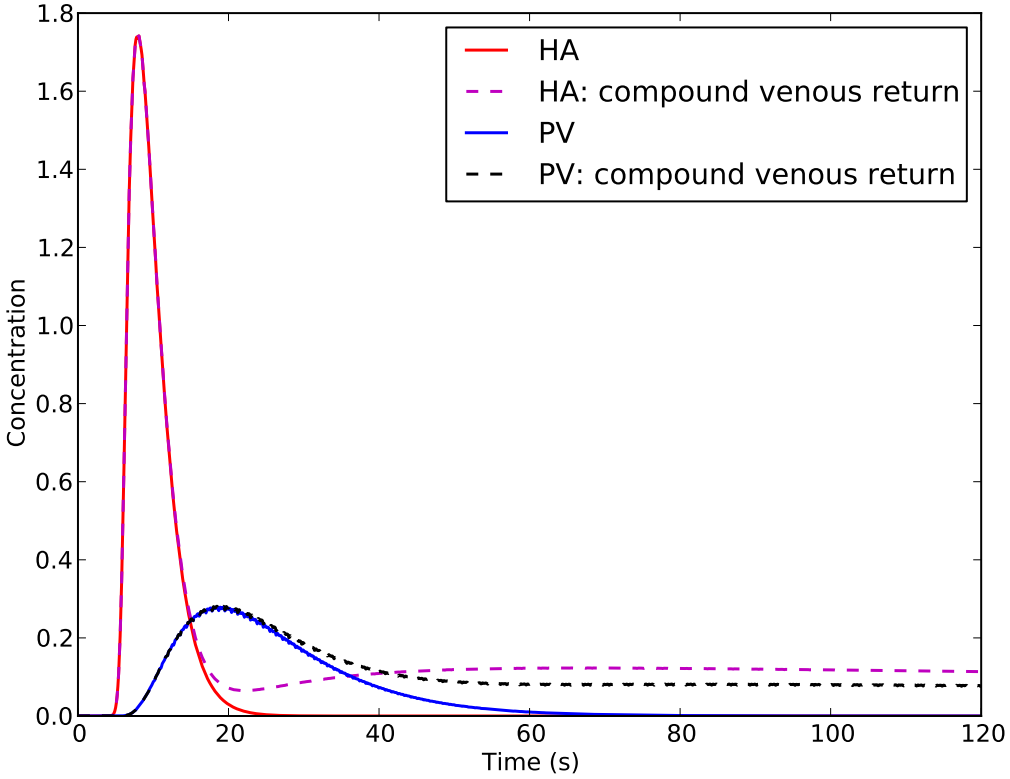

Figure 9.9: Simulated product concentration in the hepatic artery and the portal vein accounting or not for the product venous return over time. Simulations obtained with 1D-0D pig systemic circulation with constant inflow.

In the measurements (Figure 9.7), after the first peak the concentration in the vessel is not null. This observation may be explained by the compound venous return. To test this assumption, the simulation is performed with compound venous return. Figure 9.9 shows the simulated hepatic artery and the portal vein concentration over time. After the first peak a smooth decrease is obtained when the compound venous return is taken into account. On the contrary without it, after the first peak the concentration is back to zero (Figure 9.8). Thus, the compound venous return seems to explain the second part of the measurement curves. For the rest of the simulations the compound venous return and the heart-lungs compartment are included.

Partial hepatectomy and liver vessels concentration. The intravenous ICG injection was done before and after a 75% liver resection on pig 1. The measured ICG fluorescence curves are displayed in Figure 9.10 (normalized by the reference intensity). The simulation of the 75% liver resection is done with the 1D-0D model as detailed in chapter 6. The

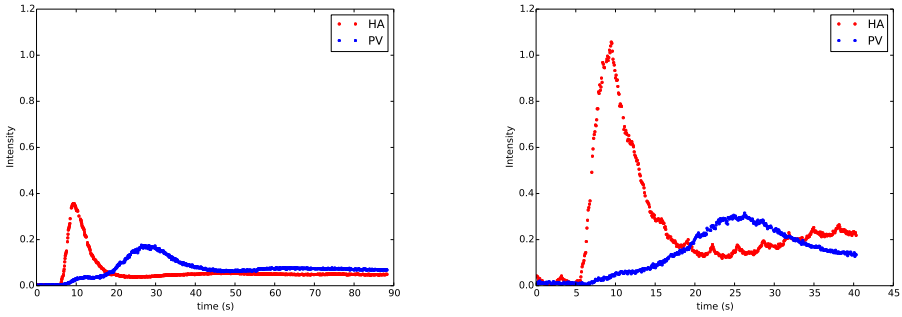

(a) Before liver resection

(b) After liver resection

Figure 9.10: ICG fluorescence measurements over time in the hepatic artery and the portal vein for the same animal, before and after 75% liver resection.

parameters are the same as in the previous simulations. Figure 9.11 shows the simulated hepatic artery and portal vein concentrations over time before and after partial hepatectomy. In the measurements, after partial hepatectomy the difference between the maximum values of hepatic artery and portal vein intensities is larger than before partial hepatectomy. A similar result is obtained in the simulations. After liver resection, the maximum concentration in the hepatic artery is higher and in the portal vein it is slightly increased.

Hepatic vein blockage. After partial hepatectomy or after a liver transplant the hepatic vein corresponding to a liver region may be resected. Therefore, the corresponding region is subject to an outflow blockage, meaning blood cannot be drained easily from this region. In such situation, after indocyanine green (ICG) injection, the ICG intensity in these liver regions is significantly lower than in the liver region without outflow blockage [KSI+13]. To mimic the outflow blockage, the resistance and capacitance of the liver tissue and hepatic vein vascular trees, in one of the liver lobe (the right main lobe), are drastically increased and decreased respectively. The change of resistance and capacitance leads to back-flow in the portal vein of the corresponding liver lobe. When portal vein back-flow occurs in a lobe, the concentration at the end of the portal vein tree is assumed equal to the concentration exiting the hepatic artery tree. This concentration is then transported (with the same ODE equation as before) to the liver common portal vein (due to the back-flow). The tissue concentration is computed, ensuring mass concentration. Figures 9.12, 9.13 and 9.14 show the concentration over time in the different liver lobes, exiting HA and PV compartments, in the tissue and exiting HV compartment, with and without outflow blockage.
In the right lobe, the compound does not appear in the tissue and does not exit the hepatic vein compartment. The compound arriving through the hepatic artery is transported backward through the lobe portal vein tree. Therefore, the concentration in the common portal vein and then in the other lobes is increased. Since the parameter τ is the same in all lobes, the same concentration is simulated in the left and the median lobes. In [KSI+13] the ICG intensity is compared between liver region with and without venous occlusion (measured in liver resection

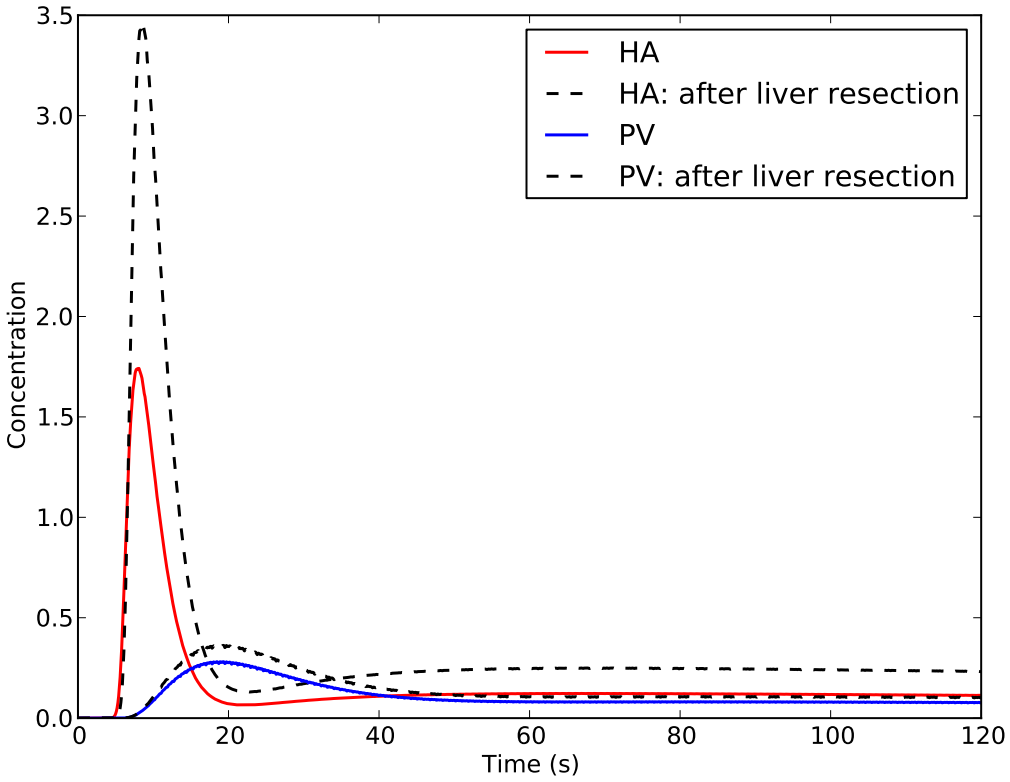

Figure 9.11: Simulated compound concentration in the hepatic artery and the portal vein over time before and after 75% liver resection simulation. The simulations are obtained with 1D-0D pig systemic circulation with constant inflow.

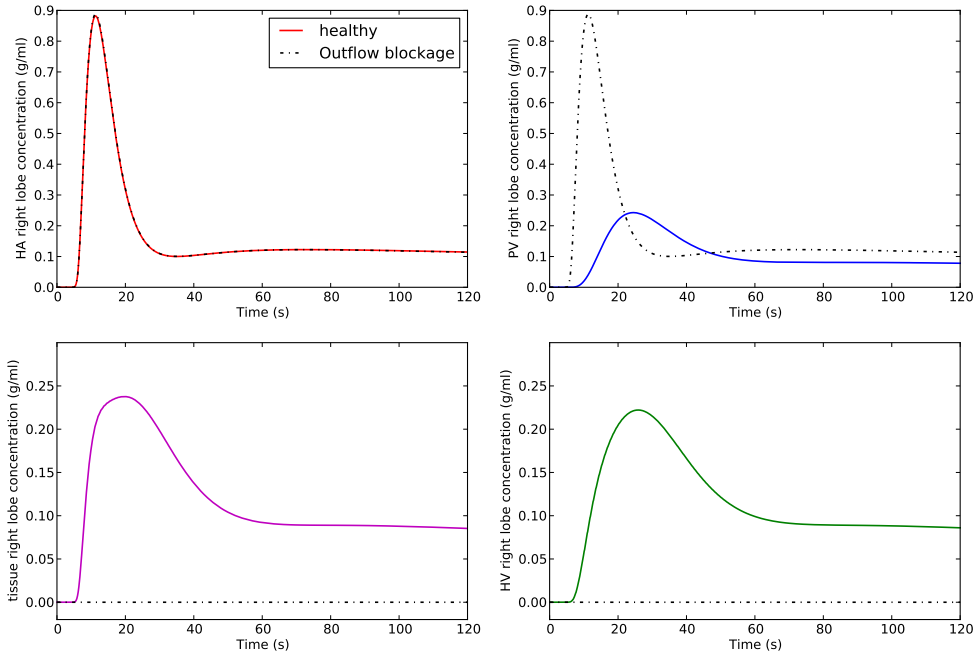

Figure 9.12: Concentration over time in the right liver lobe without (solid line) and with outflow blockage (dash-dot line). Concentration over time exiting the hepatic artery (HA) (top left), the portal vein (PV) (top right) and the liver tissue concentration (bottom left) as well as the hepatic vein (HV) (bottom right) compartment.

patients and recipients and donors of liver transplantation). The measured ICG concentration was significantly lower in the liver region with venous occlusion than in the region without it. The same behavior is qualitatively reproduced here, ICG concentration in the right lobe is lower than in the other liver lobes.

9.4 Discussion and conclusions

The 1D-0D blood flow model developed in the previous chapter 6 is used to investigate the transport of a compound in blood. Simplifications are made to model the transport through the organs using well-mixed compartments. The numerical tests have highlighted the differences between constant and time-dependent velocity transport in blood. The typical ICG intensity curves measured in the liver vessels, in several animals, have a smooth shape similar to a Gaussian (part I). With time-dependent blood velocity the 1D model is not reproducing the same type of smooth shape. Indeed, as the blood velocity may become negative, the compound is not only transported forward in the vessels and sharp increases and decreases of the compound concentration appear. The compound transport is a three

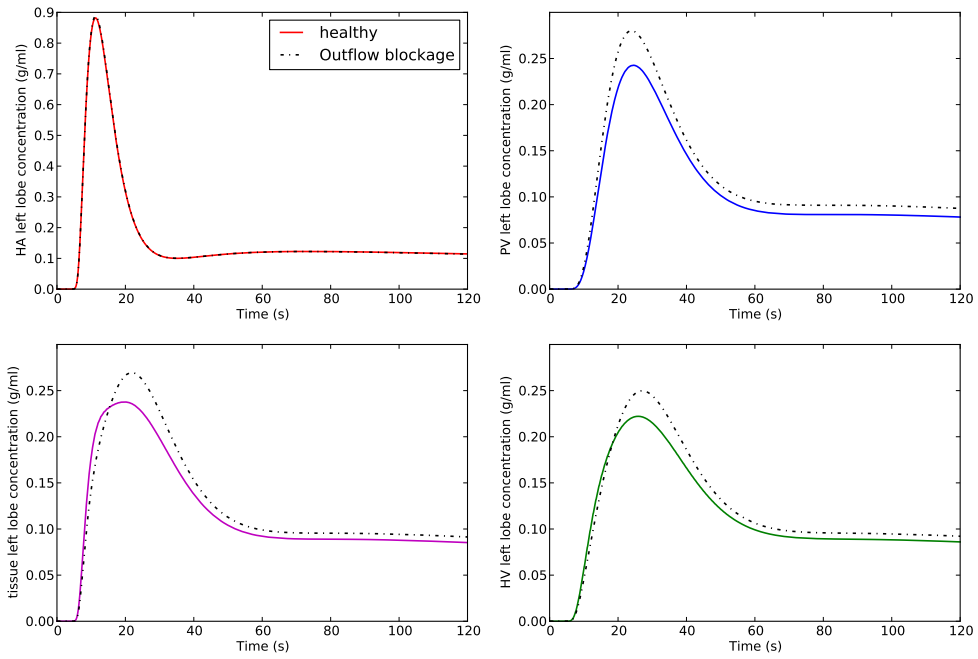

Figure 9.13: Concentration over time in the left liver lobe without (solid line) and with outflow blockage (dash-dot line). Concentration over time exiting the hepatic artery (HA) (top left), the portal vein (PV) (top right) and the liver tissue concentration (bottom left) as well as the hepatic vein (HV) (bottom right) compartment.

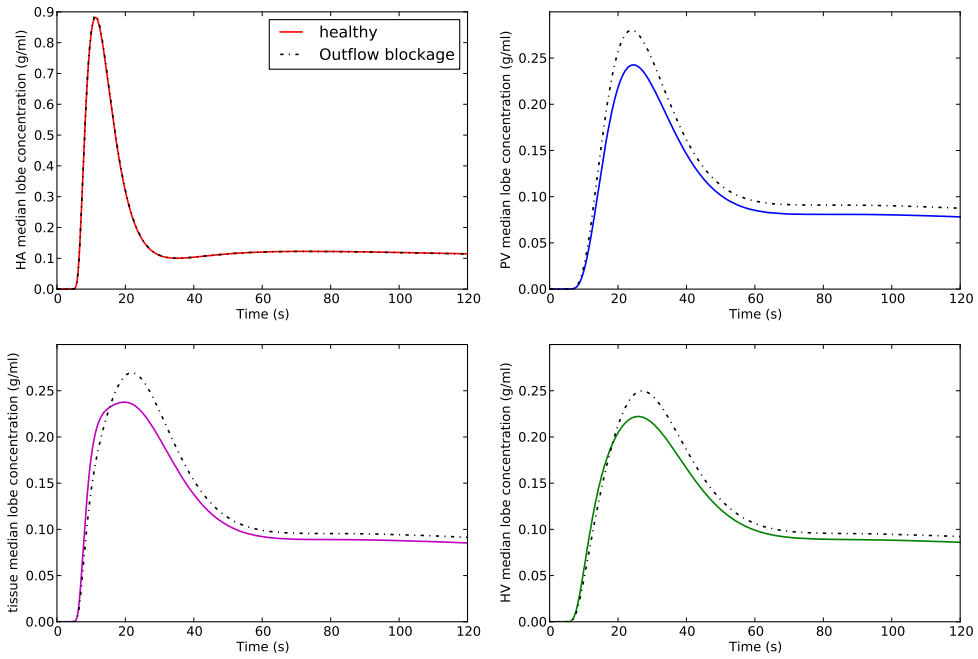

Figure 9.14: Concentration over time in the median liver lobe without (solid line) and with outflow blockage (dash-dot line). Concentration over time exiting the hepatic artery (HA) (top left), the portal vein (PV) (top right) and the liver tissue concentration (bottom left) as well as the hepatic vein (HV) (bottom right) compartment.

dimensional phenomenon, therefore the concentration is not constant within the section. The one-dimensional equations for transport, with a flat profile, do not account for the variation of concentration in the vessel cross-section. With a non-flat velocity profile the compound is transported with different velocities in the section area. Thus, between systole and diastole, mixing phenomena might happen (due to the different velocities in the vessel section). Here, these mixing phenomena are missed, because the sectional average concentration is simulated. The oscillation appearance requires more investigations. In the future, the comparison of 3D transport simulations averaged over the section with 1D transport simulations may explain these oscillations. Future work on 1D transport equations, maybe with a non-flat profile, are required to improve the simulated transport of compound with non-constant velocity.
The impact of intravenous injection and compound venous return on the concentration curves has been shown. Both phenomena are important to reproduce the measurements. The heart-lungs compartment explains that the two-second intravenous injection becomes a ten-second large concentration curve in the hepatic artery. While, the venous return of the compound explains that after the first peak of concentration in the blood vessels, the compound concentration decreases slowly (instead of a quick return to zero concentration). The elimination of ICG from blood by the liver has been modeled assuming all the product is eliminated after the first passage in the liver. To improve this assumption, the presented model could be coupled to a more accurate model for the processing of ICG by the liver (such models are presented in the chapters 10 and 11).
This work is a first step to better understand the transport of a compound in the blood circulation, and more specifically in the liver. A more precise modeling of transport through organs is likely to improve the results. For example, computing a transit time that depends dynamically on the flow and/or the organ size would give a more realistic model.
To conclude, this work has proposed a simple model for compound transport, using the previously developed 1D-0D model for blood flow. The model enables to investigate, with numerical simulations, different situations occurring after liver surgery. The model qualitatively reproduces the observed and reported behavior of indocyanine green intensity measurements after liver resection or liver venous occlusion.

Chapter 10

Model and Methods to assess liver function from ICG fluorescence measurements

In the previous chapter the transport of indocyanine green (ICG) to the liver has been modeled. This chapter presents a pharmacokinetic model for ICG processing by the liver. Assessing the liver function during liver surgery is difficult due to the time for blood sample analysis. Moreover, the blood analysis informs on the overall hepatic function. Therefore, ICG fluorescence measurements present an interesting real-time alternative. However, only intensity level changes or time-to-peak intensity are usually extracted from such data (Part I), or at most fit by phenomenological curves [STK+96, EDSC+99]. This chapter proposes to extract more information from the liver intensity dynamics by interpreting it through a dedicated pharmacokinetics model. The estimation of the pharmacokinetic model parameters may lead to an evaluation of the liver function. This chapter presents a first step: sensitivity analysis and parameter estimation methods are proposed and applied on synthetic data and on measured data from literature [EDSC+99]. The impact of different liver conditions on model parameters is also studied.

This chapter is organized in two main sections. First, the model equations, the sensitivity analysis functions and the parameter estimation algorithm are presented in section 10.1. Then, in section 10.2, the data from [EDSC+99] and the model parameters that are fixed based on the literature are detailed. Next, the methods are validated on synthetic data and applied on the measured data. Finally, section 10.3 concludes this chapter, with a discussion on the results.

Contents

10.1 Methods 165
10.1.1 Pharmacokinetic model of ICG transport 165
10.1.2 Sensitivity analysis 166
10.1.3 Parameter estimation method 166
10.2 Results 167
10.2.1 Available data for parameter estimation 167
10.2.2 Sensitivity on synthetic data 168
10.2.3 Parameter estimation on noisy synthetic data 170
10.2.4 Parameters estimation on real data 175
10.3 Discussion and conclusions 179

10.1 Methods

10.1.1 Pharmacokinetic model of ICG transport

The presented model aims at representing the transport of indocyanine green (a fluorescent dye) in blood and its processing by the liver. After blood injection the ICG exits the body exclusively through the liver [AKL+12, HdGN+13]. The ICG goes through the liver, composed by mainly three types of tissue (chapter 1); a) the blood vessels, in particular the sinusoids, which are the smallest blood vessels of the liver, where exchanges occur, b) the hepatocytes which are the liver cells, that take the ICG from the sinusoids blood and excrete it into the bile canaliculi, and c) the bile canaliculi, small canals that transport bile to the common bile duct.
To represent the ICG concentration dynamics over time, a pharmacokinetic model is developed. The compartments taken into account are the sinusoids, the hepatocytes, the bile canaliculi and the rest of the blood circulation. The compound is assumed to be injected in the rest of the blood circulation, then it arrives to the liver through the hepatic artery (ha) and the portal vein (pv) and it enters the liver through the sinusoids. A passive exchange is assumed between sinusoids and hepatocytes (no energy consumption). The ICG is secreted from the hepatocytes into bile canaliculi, with a process assumed active and possibly saturating. The saturation is modeled by parameter S in the following equations. If S times the concentration in the hepatocytes is larger than one, then the secreted amount of ICG is independent of ICG concentration in hepatocytes. Then, the ICG exits the liver through the hepatic veins and returns to the rest of the blood circulation, or reaches the common bile duct, with the bile flow through the bile canaliculi. The liver amount of ICG is assumed to be the sum of the amounts in sinusoids, hepatocytes and bile canaliculi compartments. Figure 10.1 shows a schematic representation of the model. Notation for parameters and concentrations are summarized in table 10.1. The model equations read

$$\begin{cases} \frac{d}{dt}(V_{blood}C_{blood}) &= (F_{ha}+F_{pv})C_s - (F_{ha}+F_{pv})C_{blood} \\ \frac{d}{dt}(V_sC_s) &= (F_{ha}+F_{pv})C_{blood} - (F_{ha}+F_{pv})C_s - K_{sh}(C_s - C_h) \\ \frac{d}{dt}(V_hC_h) &= K_{sh}(C_s - C_h) - \frac{K_{hb}}{1+SC_h}C_h \\ \frac{d}{dt}(V_{bc}C_{bc}) &= \frac{K_{hb}}{1+SC_h}C_h - F_bC_{bc} \end{cases} \tag{10.1}$$

And the liver amount of ICG is defined as follows:

$$V_LC_L = V_sC_s + V_hC_h + V_{bc}C_{bc} \tag{10.2}$$

The system of equations (10.1) - (10.2) is solved with the IDA package, a part of SUNDIALS (Suite of Nonlinear and Differential/Algebraic Equation Solver) [SPH15]. The time-integration is done with the Backward Differentiation Formula (BDF) method; the non-linear algebraic system is then solved with a Newton method.

Notation	Signification
blood	Rest of blood circulation
s	Sinusoids
h	Hepatocytes
bc	Bile Canaliculi
L	Liver
ha	Hepatic artery
pv	Portal vein
b	Bile
V_i	Volume of i^{th} compartment
C_i	Concentration of i^{th} compartment (arbitrary units AU)
F_i	i^{th} flow rate (Volume/Time)
K_{sh}	Exchange coefficient between sinusoids and hepatocytes (Volume/Time)
K_{hb}	Excretion coefficient from hepatocytes to bile canaliculi (Volume/Time)
S	Saturation parameter (1/Concentration; 1/AU)

Table 10.1: Notation and units.

10.1.2 Sensitivity analysis

The sensitivity analysis aims at qualifying the sensitivity of the model output (observations) to the model parameters. This tool is used to identify the parameters that are likely to be estimated or not from the available observations. Two sensitivity tools are used: the traditional sensitivity and the generalized sensitivity functions. Details about sensitivity analysis are given in Appendix B and in [TC99, MXPW11, BBD+07, PFGVC14]. The time interval, where the sharpest increase appears in the generalized sensitivity function, is where most information on the parameter is contained into the observations [BBD+07]. In this work, the sensitivity functions are computed with the IDAS solver, which is a part of SUNDIALS [SPH15]. The two sensitivity tools are local analysis thus the initially chosen parameters impact the sensitivity functions. Therefore, the sensitivity analysis is performed for two different sets of parameters, representing two regimes of the dynamical system.

10.1.3 Parameter estimation method

Sensitivity analysis informs about parameter estimation problem difficulties, according to available measurements. Once the parameters to be reasonably estimated are known, an algorithm to find these parameters based on the available measurements also needs to be chosen. The Unscented Kalman Filter (UKF) algorithm is here used for parameter estimation (the methods is detailed in [JUDW95]). Inverse problems definition and UKF algorithm details can be found in Appendix A. UKF algorithm consists of two steps: the state mean and covariance forward propagation by solving the model equations and the correction of state mean and covariance with the noisy observations (model output transformation). Here, the forward model is fast and easy to solve therefore the UKF algorithm technique is well adapted. Moreover UKF provides second-order accuracy for mean propagation forward (contrary to extended Kalman filter) [JUDW00, MC11, PFGVC14]. The parameter estimation, in UKF,

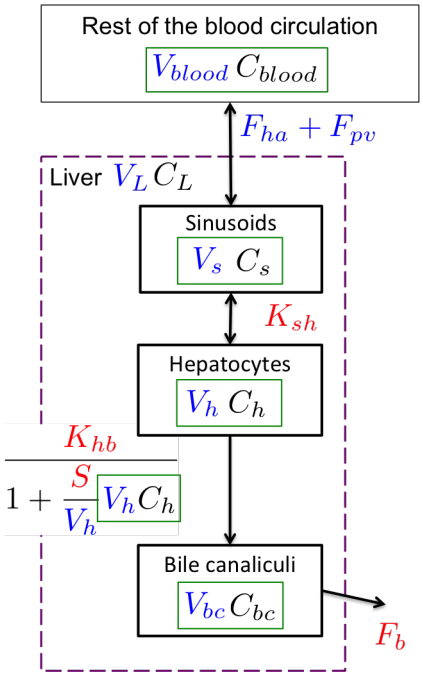

Figure 10.1: Model schematic description. The parameters in blue are the ones fixed with literature or non-ICG measurements, in red the estimated parameters by the resolution of an inverse problem, and the state variables are framed in green.

is based on a prior confidence. The two coefficients, σ^2_{obs} and σ^2_{init}, are standing for the confidence in the measurements and in the initial guess respectively. These two coefficients may impact the UKF results. Therefore, in the next section, different initial guesses with varying confidence are considered.

10.2 Results

10.2.1 Available data for parameter estimation

In [EDSC+99], El-Desoky *et al.* give typical indocyanine green curves of concentration over time in the rabbit liver. The goal here is to use these measurements to identify the model parameters.

All the parameters are not estimated with the unscented Kalman filter: some are fixed from literature or from non-ICG measurements, as detailed below. The curves in [EDSC+99] are in arbitrary units. Thus, in this work, the amount unit is concentration arbitrary unit times volume in ml (AU.ml).

In [EDSC+99], the injected ICG quantity is given. However, since the concentration function are in arbitrary units, the bolus function is unknown. Here, the initial time (t=0s) is assumed to be just after the bolus injection in the blood circulation. Therefore, a non-zero initial value for ICG amount in the blood compartment is assumed, and the ICG amount in the other compartments is set to zero. Finally, El-Desoky *et al.* measured the hepatic artery and

portal vein flows, hence the parameters F_{ha} and F_{pv} are known ($F_{ha} = 0.25$ ml/s and $F_{pv} = 1.5$ ml/s) (Figure 10.1 in blue). All compartment volumes are fixed based on the literature (Figure 10.1 in blue) as follows.
The total circulating volume is assumed to be 56 ml/kg of the animal body weight [DHM+01]. The weight of the rabbit, considered in [EDSC+99], is 2.9 kg in average. Therefore, the rabbit average blood volume is assumed equal to 160 ml. The rabbit liver weight is reported to be 2.7% of body weight in [WLZ47]. The liver is mainly composed of blood or water. Therefore, the liver mass density is chosen close to blood density (1 g/ml). Finally, the rabbit liver volume estimation is 80 ml. [HHF+14] reports, in a hepatic lobule (definition in Part I), the sinusoids and the bile canaliculi volumes, in percentage of the tissue volume. The results are extended to the whole liver and the remaining volume is assumed to be the hepatocytes volume. The estimated volumes are then, for the sinusoids, 12.3 ml, for the hepatocytes 65 ml and for the bile canaliculi 2.7 ml. The remaining parameters to estimate are K_{sh}, K_{hb}, S and F_b (Figure 10.1 in red).

In the next sections, the sensitivity of the liver amount (equation (10.2)) to these four parameters is analyzed. Then, to verify the approach, the inverse problem is solved with noisy synthetic data as observation (meaning that the data are generated by the model itself, adding noise). Finally, measurements curves from [EDSC+99] are used to estimate the four parameters.

10.2.2 Sensitivity on synthetic data

The sensitivity of ICG amount in the liver compartment (equation (10.2)) to the parameters K_{sh}, K_{hb}, S and F_b is studied. The other parameters are set as explained in the previous section.
The initial conditions are: in the blood compartment $V_{blood}C_{blood} = 83000$ AU.ml and set to zero in the other compartments. The sensitivity analysis is a local analysis that depends on the set parameters. Therefore, two different parameter sets are studied to consider different types of observations curve.
In the first case, a fast decrease of ICG in the liver occurs (Figure 10.2 left), due to a small saturation parameter S. The first parameter set of the synthetic observations curve is: $K_{sh} = 1.0$ ml/s, $K_{hb} = 6.5$ ml/s, $S = 0.001$ 1/AU and $F_b = 0.05$ ml/s. In the second case, a bigger saturation parameter is chosen, leading to a slower decrease of liver ICG amount (Figure 10.4 left). The second case parameter set is: $K_{sh} = 1.0$ ml/s, $K_{hb} = 6.5$ ml/s, $S = 0.2$ 1/AU and $F_b = 0.05$ ml/s.
The first case represents the regime where $SC_h << 1$, while the second one represent the regime where $SC_h >> 1$. Thus, the exchange coefficient $\frac{K_{hb}}{1+SC_h}C_h \sim K_{hb}C_h$ in the first case, and $\frac{K_{hb}}{1+SC_h}C_h \sim K_{hb}/S$ in the second case.
The generalized sensitivity functions are plotted by pairs, assuming the other parameters are known. Analyzing generalized sensitivity functions two by two enables to better understand the correlations between parameters.

Case 1: The liver amount of ICG over time and the traditional sensitivity functions are shown in Figure 10.2 over 1500 seconds. The traditional sensitivity functions (Figure 10.2 right), for parameters K_{hb}, S and F_b have a single peak (negative or positive). The peak position is around when the ICG amount in the liver is maximal. The K_{sh} sensitivity function has two peaks (one positive and one negative, smaller in absolute value). One at the beginning of the simulation, like the other parameters, and one later in time. It reveals the instant times where changes in parameters have an important impact on model solution.
In Figure 10.3, generalized sensitivity functions (GSFs) are plotted over 1500s, assuming two of the four parameters are known. The oscillations in GSFs reveal correlations between parameters. Three of the six plots have important oscillations (Figure 10.3 D, E and F). The parameters K_{hb} and F_b, K_{hb} and S, as well as F_b and S, are likely to be correlated, especially the last pair. Moreover, K_{sh} and K_{hb}, K_{sh} and F_b, as well as K_{sh} and S are not correlated (Figure 10.3 A, B and C) and they are likely to be estimated, knowing the liver ICG amount. The time interval, where a sharp increase of GSFs occurs, informs where most information about a parameter is contained into observations. Therefore, when S and F_b are known (Figure 10.3 A), most information on K_{sh} parameter seems to be during the increasing part of liver amount (between 0s and 200s) (Figure 10.2 left). The sharper increase, between 200s and 800s, in K_{hb} GSF, reveals that the observation is more sensitive to this parameter, when the ICG start to decrease (Figure 10.2 left). When the S and K_{hb} parameters are known (Figure 10.3 B), F_b GSF increase is sharper between 200s and 600s. Thus, most information, about the F_b parameter, is contained when the ICG amount in the liver decreases substantially. The same observation is made for the S parameter, when K_{hb} and F_b are known (Figure 10.3 C). To summarize, the first part of the ICG liver amount contains most information about the K_{sh} parameter (between 0 and 200 seconds). Moreover, when the ICG amount decreases significantly, the observation is most sensitive to K_{hb}, S and F_b. Therefore, the correlation between the parameters K_{hb}, S and F_b is expected, since the same part of the observation is the most sensitive to these parameters.

Case 2: The traditional sensitivity function curves and liver amount of ICG are shown in Figure 10.4 over 1500 seconds. The traditional sensitivity functions have a single maximum or minimum for all parameters. The extrema are, for K_{hb} and S, at the end of the simulation. F_b traditional sensitivity function values remain constant and far from zero after 200 seconds. This time interval corresponds to the decrease in the observations curve (Figure 10.4 left). Thus, the second part of the curve is more sensitive to F_b parameter than the first part. The K_{sh} traditional sensitivity function extremum is at the beginning of the simulation (Figure 10.4 right), when the liver ICG amount is maximal (Figure 10.4 left). Therefore, the changes in parameter K_{sh} mainly impact the first part of the ICG liver amount curve. The second part of the observations curve is more sensitive to F_b, K_{hb} or S changes.
Figure 10.5 shows generalized sensitivity functions for pairs of parameters, when the two others are known. S and K_{hb} GSFs present much higher values and important oscillations (25 times more than in the previous case). Such GSFs reveal important correlations between the two parameters (Figure 10.5 E). Small correlations between F_b and K_{hb}, and S and F_b are likely according to GSFs (Figure 10.5 D and F). In this case, K_{sh} and K_{hb}, K_{sh} and F_b, as

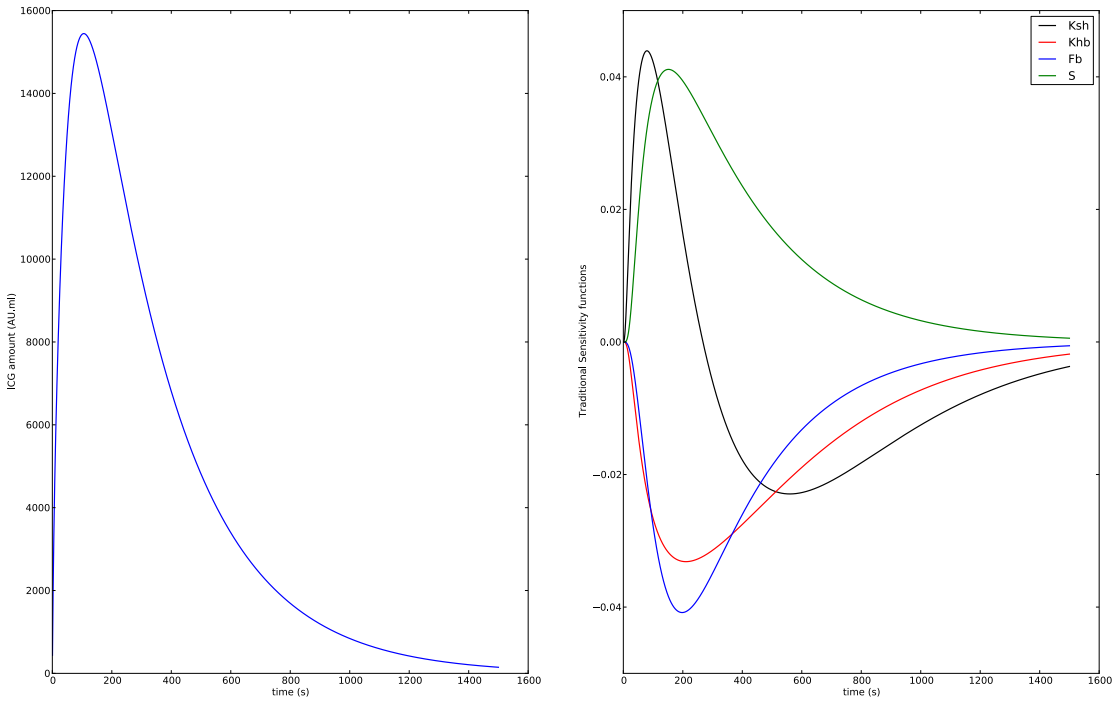

Figure 10.2: **Case 1: Traditional sensitivity function** Left: ICG amount in the liver over time. Right: Traditional sensitivity functions for K_{sh}, K_{hb}, S and F_b parameters.

well as S and K_{sh} are not correlated (Figure 10.5 A, B and C). The sharp increase in K_{sh} GSFs between 0 and 200 seconds (Figure 10.5 A, B and C), reveals that most information, about K_{sh}, is contained into the beginning of the observations curve. For K_{hb}, F_b and S parameters most information is contained between 200 seconds and the end of the simulation (Figure 10.5 A, B and C).
To sum up, in the curve of ICG amount in the liver, most information, on K_{sh}, is contained in the increasing part of the curve, and the second part of the curve informs on the S, K_{hb} and F_b parameters.

The two cases have different sensitivity functions. However for both of them, K_{hb} and S parameters are likely to be correlated (much more in the second case). Moreover, in the observations curve, most information about K_{sh} is contained in the increasing part, and the decreasing part contains information about the other parameters.

10.2.3 Parameter estimation on noisy synthetic data

The inverse problem on synthetic data is performed to confirm the previous observations on sensitivity functions. Synthetic data are generated by choosing a set of parameters and solving the model equations (the direct problem). The resulting amount in the liver, with added noise, can thus be taken as a synthetic observation. If the inverse procedure works

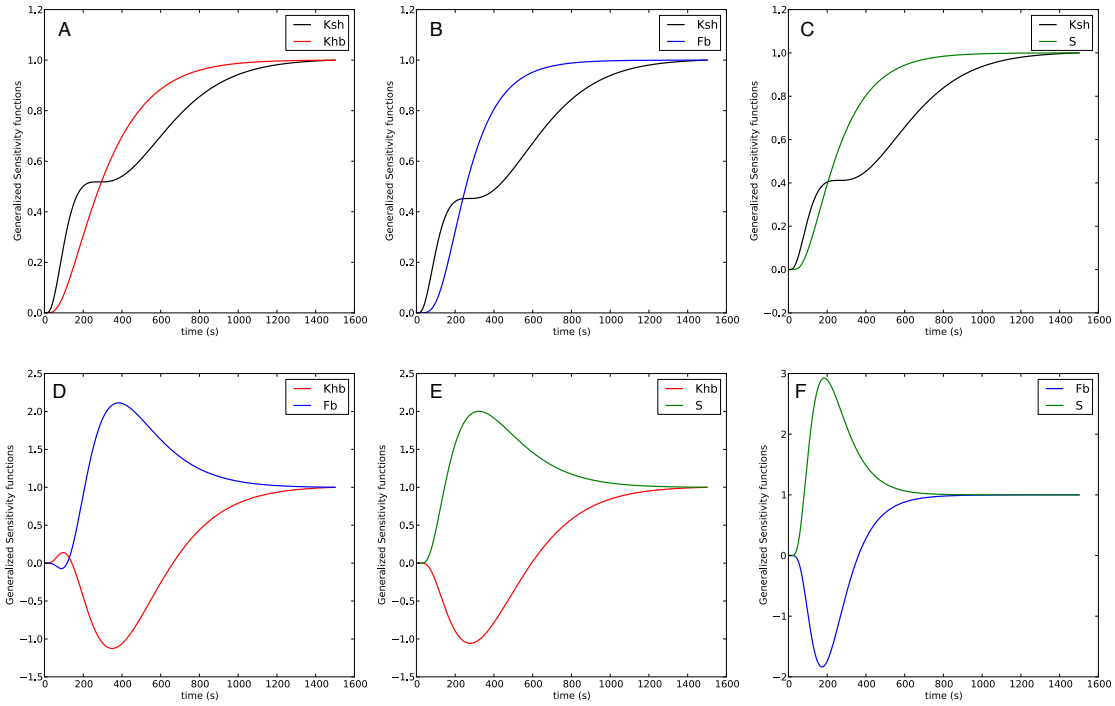

Figure 10.3: **Case 1: Generalized sensitivity functions** Generalized sensitivity functions for two parameters, with the two other parameters fixed, for all pairs of parameters K_{sh}, K_{hb}, S and F_b. A: F_b and S are fixed; B: K_{hb} and S are fixed; C: K_{hb} and F_b are fixed; D: K_{sh} and S are fixed; E: F_b and K_{sh} are fixed; F: K_{sh} and K_{hb} are fixed.

well, one should recover as estimated parameters the chosen set. A Gaussian noise of zero mean and with a given variance is chosen (the chosen variance corresponds to $\sigma^2_{obs} = 0.02$). The time step of the observations is 0.5s, and the final time is 1500s. The initial conditions are always set to the correct ones. The initial amount in the blood compartment is set to $V_{blood}C_{blood} = 83000$ AU.ml and set to zero in other compartments. For all the inverse problems, the UKF algorithm is performed three times in a row. First, UKF is performed with the initial guess $((K_{sh}, K_{hb}, S, F_b)_0 =$ (10.0, 65.0, 0.01, 0.5)) and the confidence parameter $\sigma^2_{init} = 1.0$. Then, UKF is run again with the estimation of the first run and a reduced confidence $\sigma^2_{init} = 0.5$. Finally, the UKF is run a third time, with the estimates of the second run and the confidence is decreased $\sigma^2_{init} = 0.3$. The results are presented with geometric mean +/- geometric standard deviation (grey zone) over time for each run (first : blue, second : red and third : green).

Case 1: First, all parameters are tried to be estimated, three runs of the algorithm are done, as explain previously. The UKF results are shown in Figure 10.6. K_{sh} and F_b are well estimated (Figure 10.6 C and F), while S and K_{hb} are poorly estimated (Figure 10.6 D and E). Indeed, the final estimated values are: $K_{sh} = 0.87$ ml/s (true 1.0 ml/s, initial guess 10.0 ml/s), $K_{hb} = 782.4$ ml/s (true 6.5 ml/s, initial guess 65.0 ml/s) and $S = 4.21\ 10^{-6}$ 1/AU (true

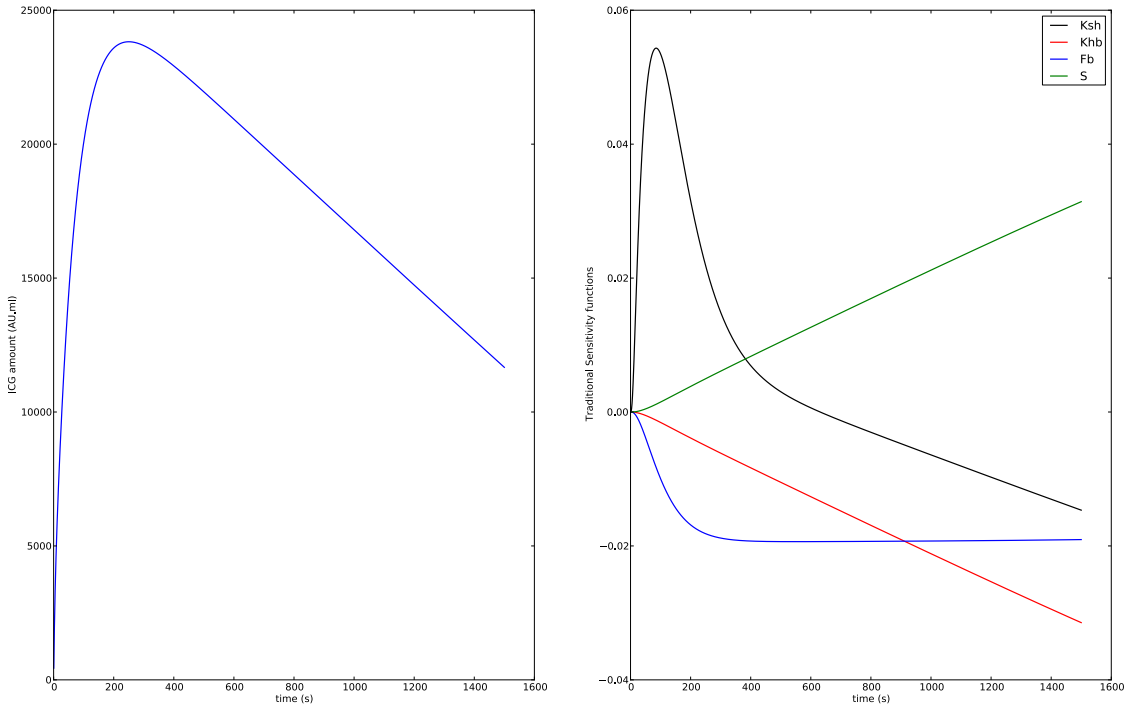

Figure 10.4: **Case 2: Traditional sensitivity function** Left: ICG amount in the liver over time. Right: Traditional sensitivity functions for K_{sh}, K_{hb}, S and F_b parameters.

0.001 1/AU, initial guess 0.01 1/AU) and $F_b = 0.048$ ml/s (true 0.05 ml/s, initial guess 0.5 ml/s). The direct model equations are solved, fixing the parameters with UKF final estimates, (Figure 10.6 B). The observations curve is not perfectly fitted as shown in Figure 10.6 B.

Then, the same procedure is used, assuming the bile flow parameter (F_b) is known. The results of the inverse problems are shown in Figure 10.7. For all parameters, the converged value is close to the known value. Moreover, the observations curve is well fitted (Figure 10.7 B). The final estimated values are: $K_{sh} = 0.98$ ml/s (true 1.0 ml/s, initial guess 10.0 ml/s), $K_{hb} = 7.8$ ml/s (true 6.5 ml/s, initial guess 65.0 ml/s) and $S = 0.007$ 1/AU (true 0.001 1/AU, initial guess 0.01 1/AU). The parameter estimation is thus improved when the bile flow F_b parameter is known.

Now, assuming the parameter K_{sh} is known, the other parameters are estimated with the same procedure. The results are shown in Figure 10.8. All estimated parameters are close to the known values. The S parameter value is overestimated and the confidence in this parameter is small (the grey zone in Figure 10.8 E is large). The observations curve is well fitted (Figure 10.8 B). The final estimates are: $K_{hb} = 6.52$ ml/s (true 6.5 ml/s, initial guess 65.0 ml/s), $S = 0.005$ 1/AU (true 0.001 1/AU, initial guess 0.01 1/AU) and $F_b = 0.052$ (true 0.05 ml/s, initial guess 0.5 ml/s). With synthetic observations, the four parameters cannot be estimated. However if K_{sh} or F_b are known the other parameters are well estimated and the observations curve is well matched.

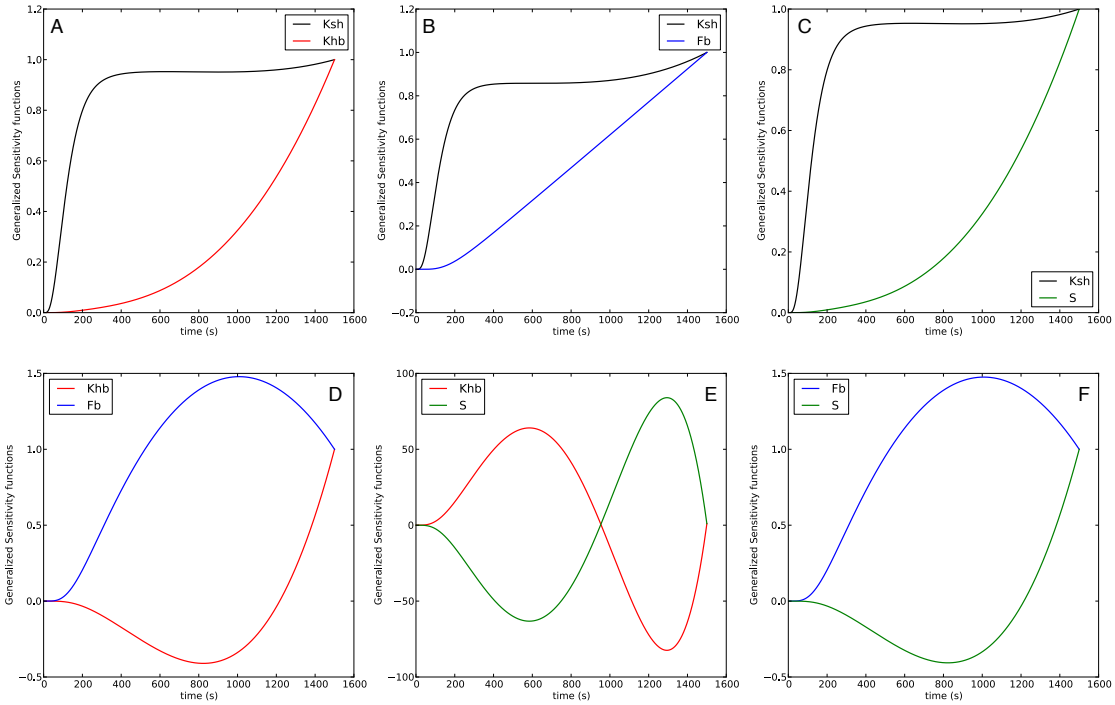

Figure 10.5: **Case 2: Generalized sensitivity functions** Generalized sensitivity functions for two parameters, with the two other parameters fixed, for all pairs of parameters K_{sh}, K_{hb}, S and F_b. A : F_b and S are fixed; B : K_{hb} and S are fixed; C : K_{hb} and F_b are fixed; D : K_{sh} and S are fixed; E : F_b and K_{sh} are fixed; F : K_{sh} and K_{hb} are fixed.

Case 2: The second regime of the dynamical system is now studied with the same procedure. First, the inverse problem is performed to estimate all parameters (see Figure 10.9). The estimated parameter K_{sh} is close to the known value, while K_{sh} and F_b estimates explode (Figure 10.9 D and F). Moreover, the S parameter is poorly estimated (Figure 10.9 E). The final estimated values are: $K_{sh} = 1.47$ ml/s (true 1.0 ml/s, initial guess 10.0 ml/s), $K_{hb} = 9.5\ 10^5$ ml/s (true 6.5 ml/s, initial guess 65.0 ml/s), $F_b = 2.1\ 10^4$ ml/s (true 0.05 ml/s, initial guess 0.5 ml/s) and $S = 0.001$ 1/AU (true 0.2 1/AU, initial guess 0.01 1/AU). The observations curve is not fitted correctly as shown in Figure 10.9 B.

When F_b is known, the inverse problems results are shown in Figure 10.10. K_{sh} is well estimated (Figure 10.10 C), the final value is $K_{sh} = 1.0$ ml/s (true 1.0 ml/s, initial guess 10.0 ml/s). However, K_{hb} and S are overestimated (Figure 10.10 D and E), the final values are $K_{hb} = 18.4$ ml/s (true 6.5 ml/s, initial guess 65 ml/s) and $S = 0.58$ 1/AU (true 0.2 1/AU, initial guess 0.01 1/AU). Despite the poor estimation of two parameters, the observations curve is well fitted (Figure 10.10 B). Computing the ratio $\frac{K_{hb}}{S}$, for the estimates and the known values, the following results are obtained:

$$\left(\frac{K_{hb}}{S}\right)_{estimate} = 31.7 \quad \left(\frac{K_{hb}}{S}\right)_{known} = 32.5$$

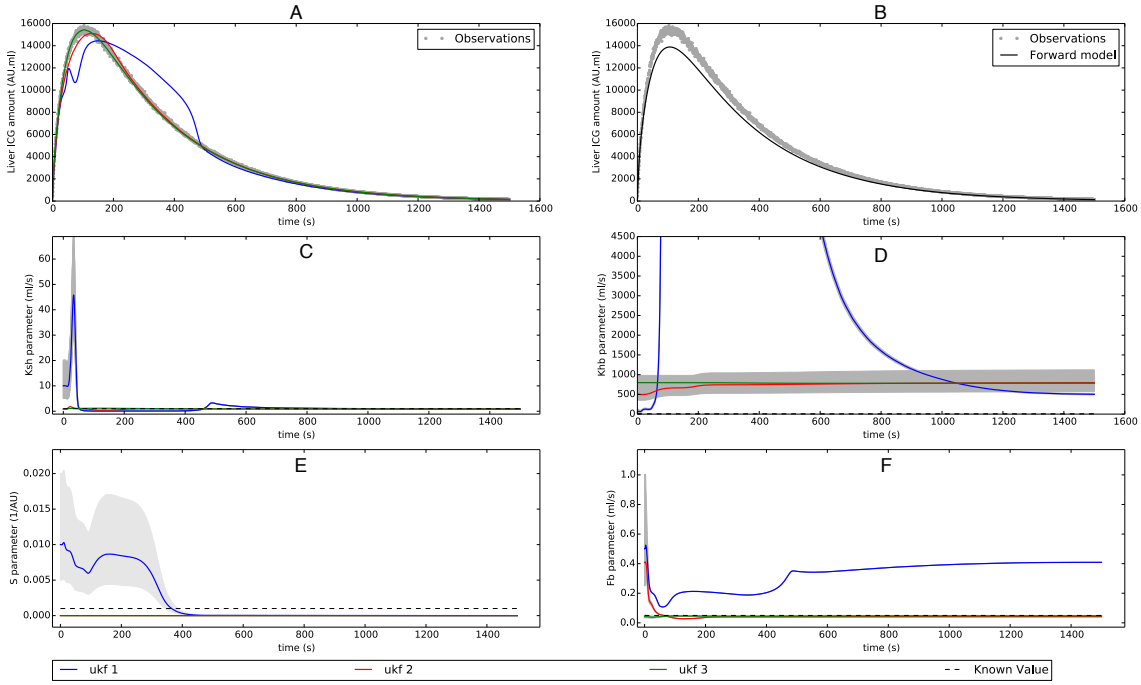

Figure 10.6: Case 1 : All parameters are estimated. A : ICG amount in the liver over time, observations curve (grey) and results from UKF runs (solid line); B : ICG amount in the liver over time, observations curve (grey) and model direct solution with parameters from UKF estimation (black solid line). Geometric mean (solid line) of the estimated parameters evolution over time and +/- geometric standard deviation (grey zone) for: K_{sh} (C); K_{hb} (D); S (E) and F_b (F).

From sensitivity analysis, the parameter K_{hb} and S are known to be correlated. The ratio of the two estimated parameter is close to the known values ratio. Moreover, the observations curve is well fitted, even with the overestimated parameters K_{hb} and S. Therefore, in this regime, it is likely that the observation is sensitive to the ratio $\frac{K_{hb}}{S}$, when F_b is known.

Then, K_{sh} is fixed, and estimation of the other parameters is performed with the same procedure; three runs of UKF algorithm (Figure 10.11). K_{hb} and S estimations converge to close values of the known parameters. The known values are a little underestimated. The observations curve is well fitted (Figure 10.11 B). F_b is correctly estimated. The final estimates are: $K_{hb} = 5.95$ ml/s (true 6.5 ml/s, initial guess 65.0 ml/s), $S = 0.18$ 1/AU (true 0.2 1/AU, initial guess 0.01 1/AU) and $F_b = 0.052$ ml/s (true 0.05 ml/s, initial guess 0.5 ml/s). Like for the first regime, with synthetic observations the four parameter cannot be estimated and the observations curve is mismatched. When F_b or K_{sh} is known, then the parameter estimation is improved and the observations curve is well matched. When F_b is known, the unsatisfactory estimation of S and K_{hb} is explain by the high correlation between these two parameters in this regime, as shown by the sensitivity analysis.

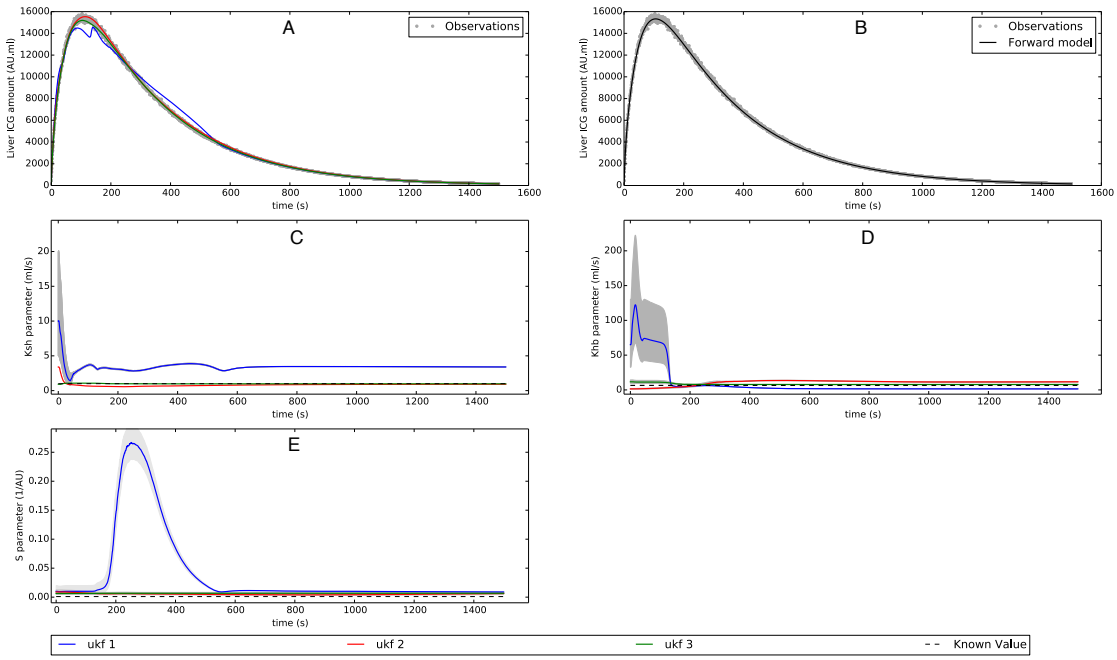

Figure 10.7: Case 1: F_b parameter is known. A: ICG amount in the liver over time, observations curve (grey) and results from UKF runs (solid line); B: ICG amount in the liver over time, observations curve (grey) and model direct solution with parameters from UKF estimation (black solid line). Geometric mean (solid line) of the estimated parameters evolution over time and +/- geometric standard deviation (grey zone) for: K_{sh} (C); K_{hb} (D) and S (E).

According to the inverse problems on synthetic observation and to the sensitivity analysis, the estimation of the four parameters is unlikely with the curve of ICG amount in the liver. However, fixing F_b or K_{sh} leads to parameter estimation that results in a well fitted observation curve. In the next section the model parameters are estimated using two curves from in-vivo data [EDSC+99]: one curve is more like the second case regime (bile ligation group) and the second curve is similar to the first case regime curve (control group). Therefore, to estimate the model parameters with the bile ligation group curve the parameter F_b is fixed and with the control group curve the parameter K_{sh} is fixed based on the estimation from the bile duct ligation group.

10.2.4 Parameters estimation on real data

El-Desoky *et al.* employed near infrared spectrometry (NIRS) to evaluate the ICG concentration in rabbit liver [EDSC+99]. The data are collected on 36 rabbits, separated in 6 groups. Here, two of these groups are used for parameter estimation; the control group and the bile duct ligation group. In [EDSC+99], indocyanine green concentration over time curves for all groups, are fitted with a sum of two exponential functions: $-Ae^{-\alpha t} + Be^{-\beta t}$. In the paper, the parameters α and β mean and standard deviation are reported. Moreover, a

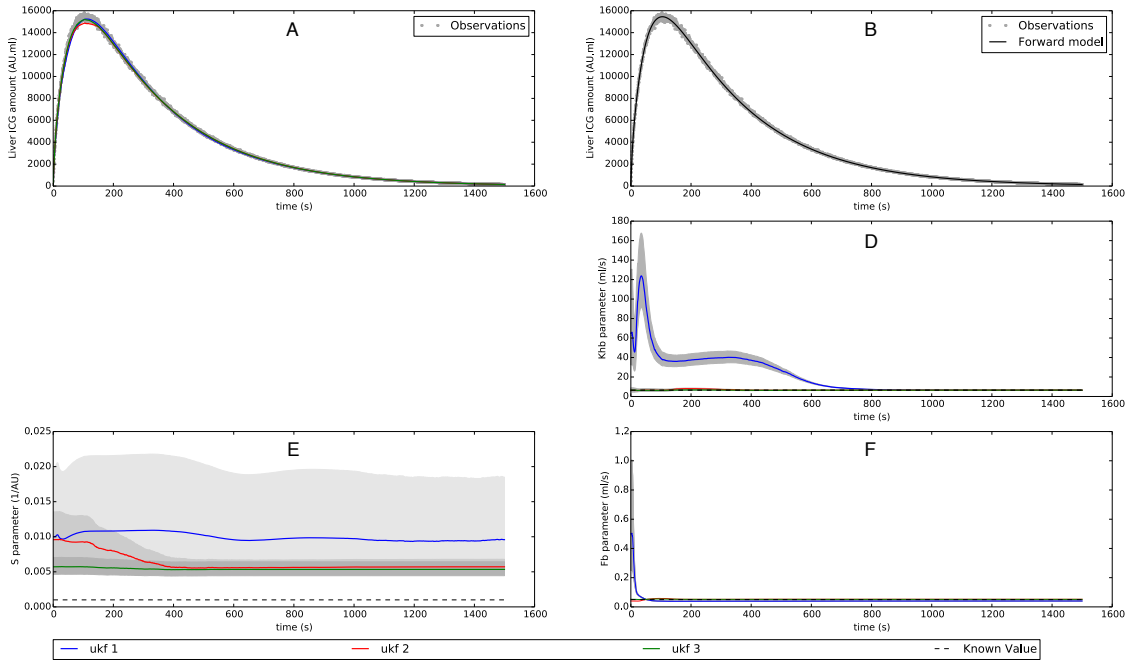

Figure 10.8: Case 1: K_{sh} parameter is known. A: ICG amount in the liver over time, observations curve (grey) and results from UKF runs (solid line); B: ICG amount in the liver over time, observations curve (grey) and model direct solution with parameters from UKF estimation (black solid line). Geometric mean (solid line) of the estimated parameters evolution over time and +/- geometric standard deviation (grey zone) for: K_{hb}(D); S (E) and F_b (F).

typical curve is drawn for each group. This curve is used to identify A and B. The curves from the paper start from non-zero values. In this work, the amount of ICG in the liver at time t = 0s is assumed null, because the initial time is assumed to be just after bolus injection. Thus, no ICG has arrived to the liver yet.

To obtain observations curves starting at zero, the curves from [EDSC+99] are shifted in time. The shift in time does not change α and β values, but new values for A and B = A are found. α and β parameters are chosen, in the given range, such that the obtained curve is close to the drawn curve in [EDSC+99]. The liver ICG amount is obtained by multiplying the concentration curve by the estimated liver volume (80 ml). A Gaussian noise is added to take into account the inter-subject variability of the group. Therefore, $\sigma^2_{obs} = 0.02$ is known.

According to the inverse problem on synthetic data results, the four parameters are unlikely to be all estimated. Therefore, first the parameters K_{sh}, K_{hb}, and S are estimated with the bile ligation group curve. Indeed, for this group, the bile flow rate is known, equal to zero.

To estimate the initial amount of ICG in blood compartment, several UKF algorithm runs are performed, with the bile ligation group curve as observation. $F_b = 0$ ml/s, thus no ICG exits the system, and the sum of all compartments amount of ICG at the end of the

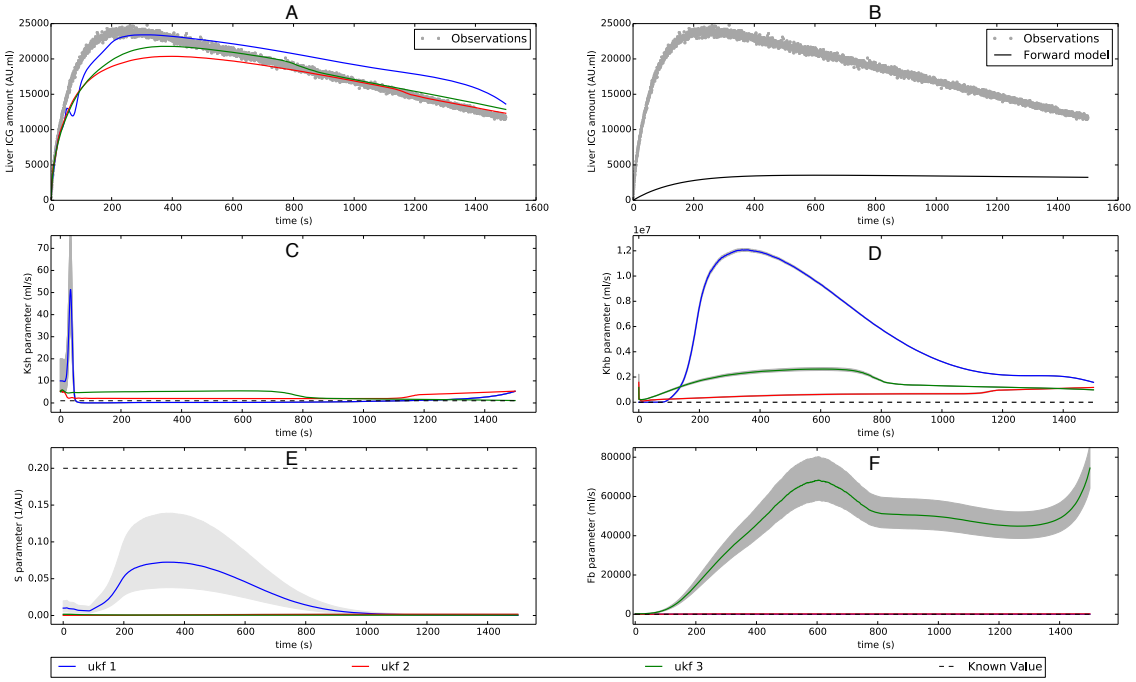

Figure 10.9: Case 2: all parameters are estimated. A: ICG amount in the liver over time, observations curve (grey) and results from UKF runs (solid line); B: ICG amount in the liver over time, observations curve (grey) and model direct solution with parameters from UKF estimation (black solid line). Geometric mean (solid line) of the estimated parameters evolution over time and +/- geometric standard deviation (grey zone) for: C: K_{sh} D: K_{hb} E: S and F: F_b

simulation should be the initial amount injected. After several runs of UKF, the value $V_{blood}C_{blood}(t = 0) = 82960.0$ is found. This value is used for the rest of the simulations. Different initial guesses for parameters and initial confidence are considered, similarly to the synthetic data examples.

With the bile ligation group curve as observation, the estimated parameters are: $K_{sh} = 49.6$ ml/s, $K_{hb} = 0.56$ ml/s $S = 1.4$ 1/AU. Figure 10.12 shows the solution curve of the forward problem, with this set of parameters. The observations curve is well fitted (relative error: $\frac{\|A_{model} - A_{obs}\|_2}{\|A_{obs}\|_2} = 0.02$, where the ICG amount in the liver is denoted by A).

Then, the parameter K_{sh} is fixed with the value found in the previous inverse problem ($K_{sh} = 49.6$ ml/s). The control group curve is used to estimate the F_b parameter. The parameters S and K_{hb} are also estimated for this group. Indeed, these parameters might be impacted by the bile duct ligation. Different initial guesses and confidence parameters are considered. The algorithm converges and the forward problem curve, obtained with the estimated parameters, is shown in Figure 10.13. The control group curve is correctly fitted

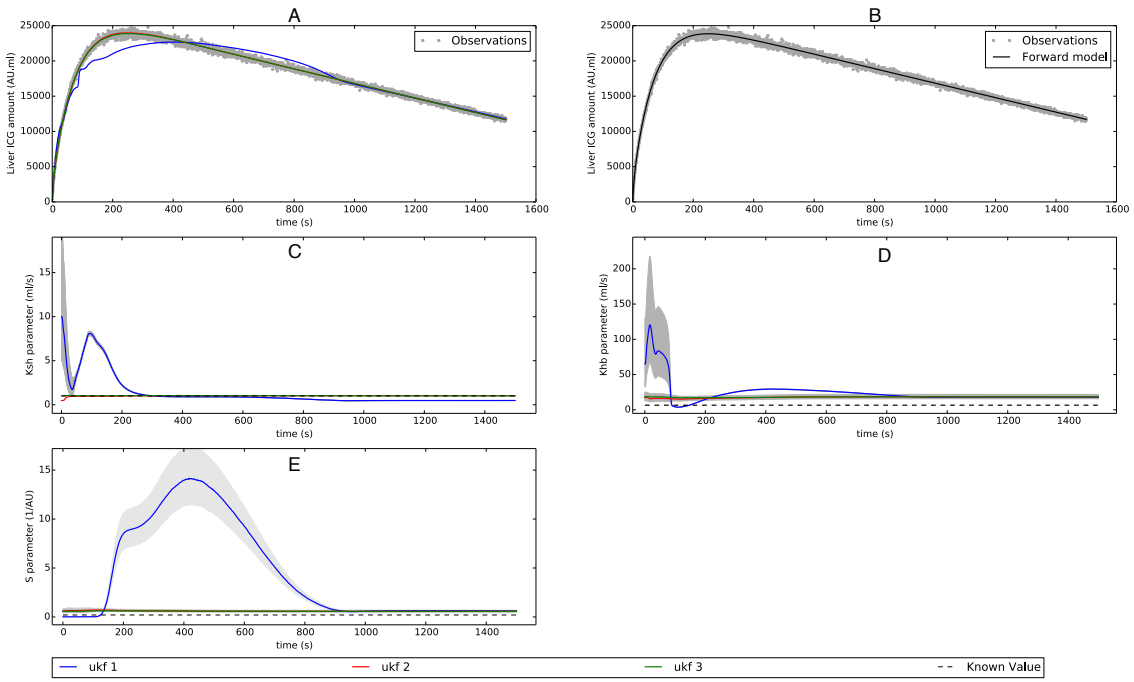

Figure 10.10: Case 2: F_b parameter is known. A : ICG amount in the liver over time, observations curve (grey) and results from UKF runs (solid line); B : ICG amount in the liver over time, observations curve (grey) and model direct solution with parameters from UKF estimation (black solid line). Geometric mean (solid line) of the estimated parameters evolution over time and +/- geometric standard deviation (grey zone) for: K_{sh} (C); K_{hb} (D) and S (E).

(relative error: $\dfrac{\|A_{model} - A_{obs}\|_2}{\|A_{obs}\|_2} = 0.04$, where ICG amount in the liver is denoted by A). The estimates set is $K_{hb} = 0.22$ ml/s, $F_b = 0.098$ ml/s, $S = 0.0018$ 1/AU.

Finally, two more groups from [EDSC+99] are used to further challenge the model, the hepatic artery (HA) occlusion group and portal vein (PV) partial occlusion group. The parameters are set with the control group estimated parameters. Simulations with various inflow are performed. The inflow is decreased by 25% (corresponding to HA occlusion), by 40% (corresponding to PV partial occlusion), by 70% and by 90%. The model solutions are plotted in Figure 10.14, along with the curves from [EDSC+99] average and standard deviation. The model simulation global behavior is similar to the curve from the paper. Indeed, compared to the control group, when the inflow is decreased, the maximum amount of ICG is reduced. Moreover, the time-to-peak (time at maximum value), is increased. However, the large standard deviation of the portal vein partial occlusion group (Figure 10.14 D), makes the results difficult to further analyze.

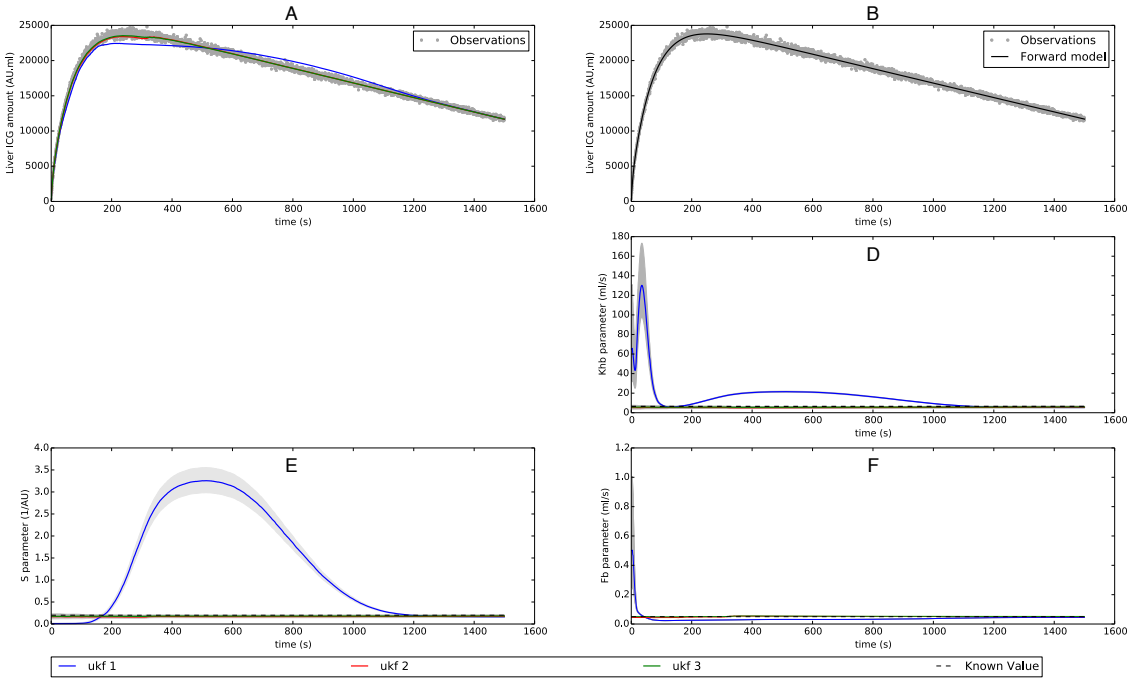

Figure 10.11: Case 2: K_{sh} parameter is known. A: ICG amount in the liver over time, observations curve (grey) and results from UKF runs (solid line); B: ICG amount in the liver over time, observations curve (grey) and model direct solution with parameters from UKF estimation (black solid line). Geometric mean (solid line) of the estimated parameters evolution over time and +/- geometric standard deviation (grey zone) for: K_{hb} (D); S (E) and F_b (F).

10.3 Discussion and conclusions

A mathematical model of indocyanine green processing by the liver has been developed. The liver amount sensitivity to parameters has been studied and the inverse problem to estimate model parameters has been performed.

The mathematical model. Using experimental measurements available in [EDSC+99], the model parameters are estimated. The experimental measurements are well fitted with the proposed model. The liver three compartments representation enables a precise description of ICG processing by the liver. In the model proposed in [STK+96] and used in [EDSC+99], a single compartment describes the liver. Furthermore, that model does not take into account a re-circulation of ICG through the hepatic veins. However, the measurements in [OKJB94] have confirmed that ICG exits the liver through the hepatic veins. The re-circulation is taken into account in the model proposed in [WKA11] and the complete blood circulation has been considered. However, the liver has been represented by a single compartment and the available data are ICG concentration in arterial blood samples, contrary to the liver tissue ICG concentration used here.

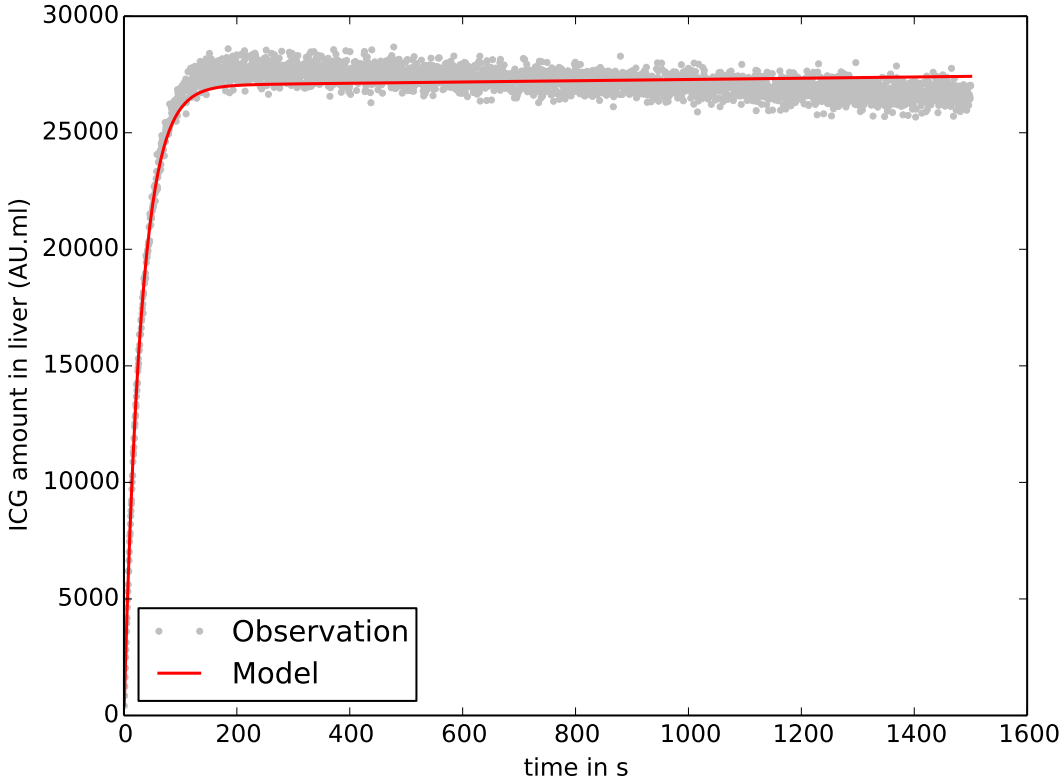

Figure 10.12: Model and observation liver ICG amount over time, for the bile ligation group. Bile ligation data curve from [EDSC+99] with added noise (grey line) and the forward problem solution, with the set of parameters found by theUKF algorithm (solid red line).

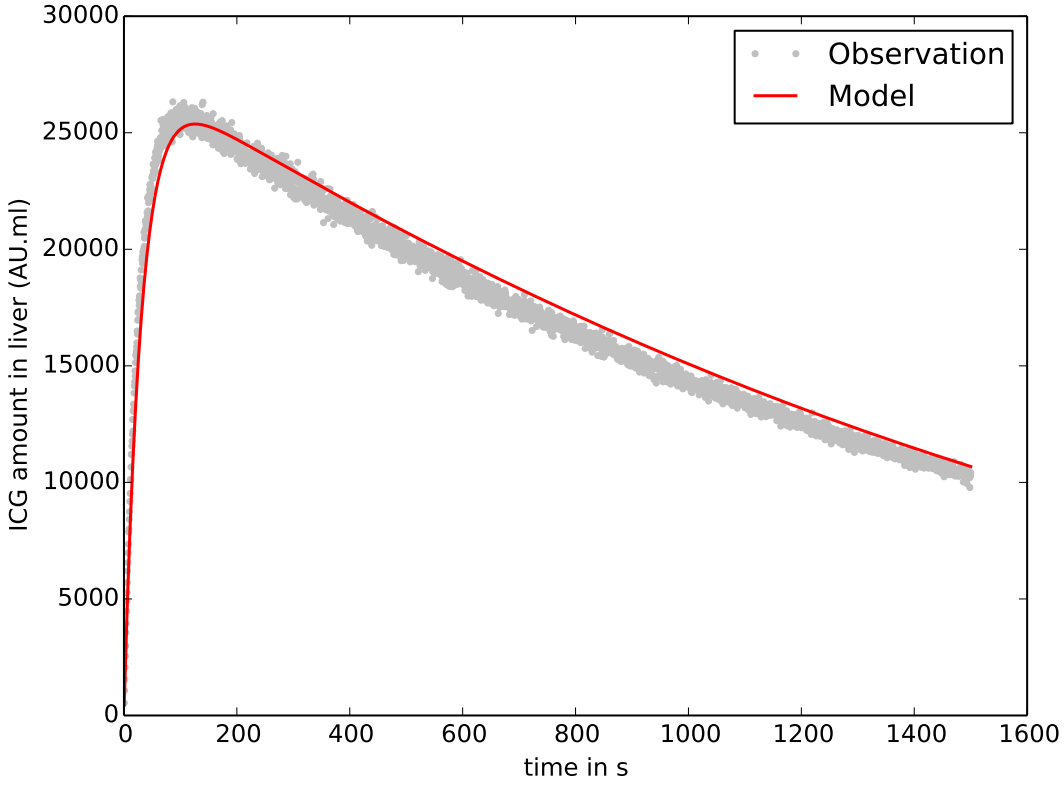

Figure 10.13: Model and observation liver ICG amount over time for control group. Control data curve from [EDSC+99] with added noise (grey line) and the forward problem solution, with the set of parameters found by UKF algorithm (solid red line).

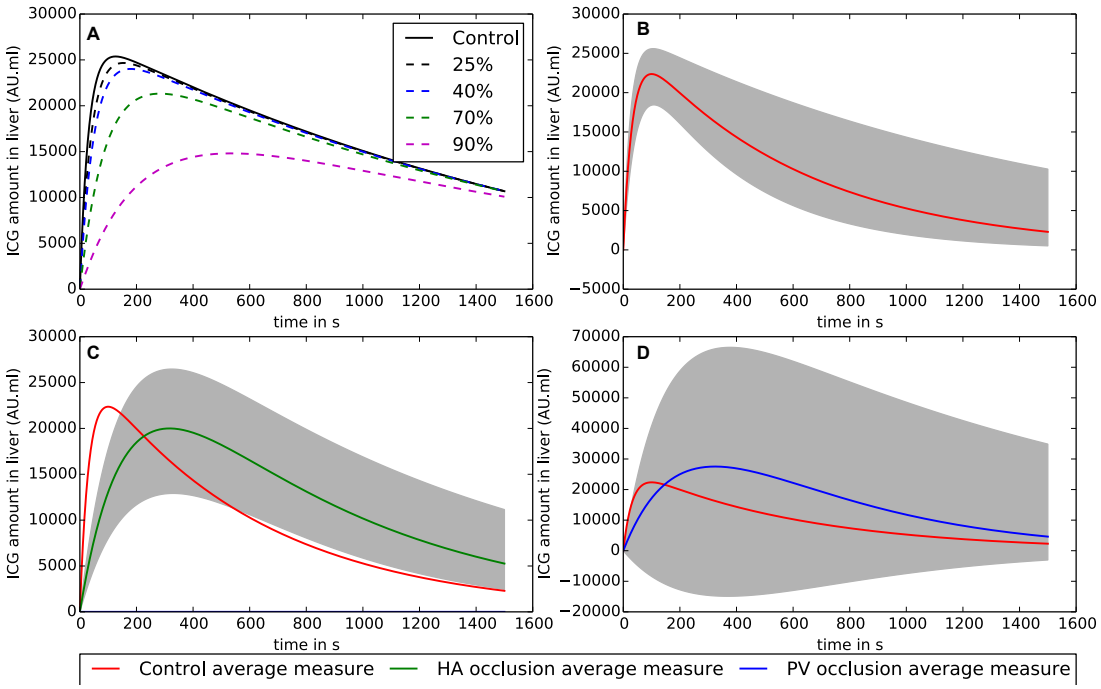

Figure 10.14: Model and observations of liver ICG amount over time for different liver inflows. A: ICG amount over time obtained with the model for different inflows; B: Control group average measure (solid line red) +/- standard deviation (grey zone) and control simulation (solid line black); C: Hepatic artery occlusion (solid black line) group average measure +/- standard deviation (grey zone) and control group average measure (solid red line); D: Portal vein partial occlusion (solid black line) group average measure +/- standard deviation (grey zone) and control group average measure (solid red line). The measurements are from [EDSC+99].

The three compartments in the liver are required to take into account the two exchanges of different nature. The exchange between sinusoids and hepatocytes, where no energy consumption is assumed, and the exchange between hepatocytes and bile canaliculi, where the transport is active, with possible saturation. The simple passive exchange between sinusoids and heptocytes enable to reproduce the measurements curves. The non-linearity for the exchange rate between hepatocytes and bile canaliculi, cannot be replaced with a constant exchange rate, as shown in Figure 10.15. In the control group, this rate varies during the entire simulation time. In the bile ligation group, the value for the first part of the curve (the increase of ICG amount in the liver) and for the second part (the storage of the ICG in the liver) are different. The non-linearity enables to reproduce different behaviors of ICG amount in the liver over time.

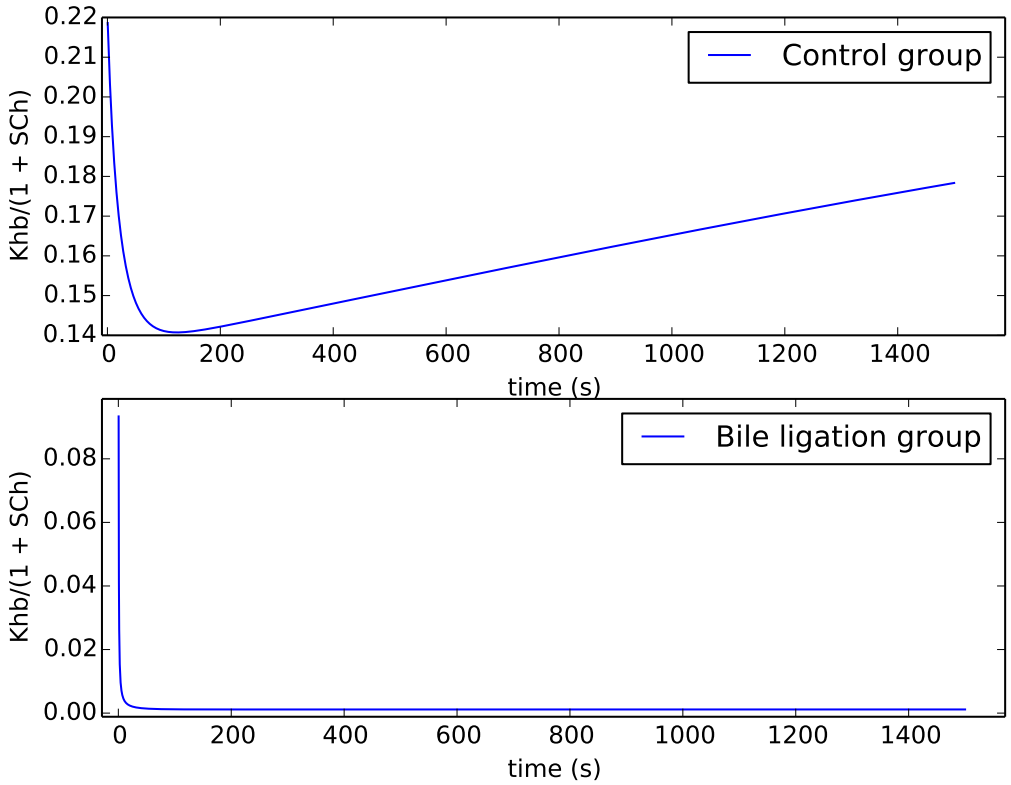

Figure 10.15: Hepatocytes - bile canaliculi exchange coefficient over time. $\frac{K_{hb}}{1 + SC_h(t)}$ coefficient over time for control and bile ligation groups.

Sensitivity analysis. Generalized sensitivity functions have indicated the correlation between K_{hb}, S and F_b parameters. The strongest correlation is between K_{hb} and S, while the exchange rate K_{sh} seems uncorrelated from the others. The inverse problems on synthetic curves tend to confirm the sensitivity analysis. Indeed, in the first case, when all

parameters are estimated, F_b and K_{sh} are correctly estimated. While, S and K_{hb} estimates are unsatisfactory, confirming that the correlation between these two parameters make their estimation difficult. The next inverse problem has revealed that, knowing F_b or K_{sh}, improves the estimation of the other parameters. In the fist case, when K_{sh} is known, the saturation parameter S seems harder to estimate than the other parameters. Moreover, the confidence in its estimation is small (Figure 10.8 E).
In the second case, that corresponds to a regime in which the term SC_h becomes larger than one rapidly, when all parameters are estimated, only K_{sh} is correctly estimated, which is coherent with the sensitivity functions (Figure 10.5). When F_b is known, in the second example, K_{sh} is still correctly estimated and K_{hb} and S are overestimated. However, the ratio of these two parameters, $\frac{K_{hb}}{S}$, is well estimated. In addition, the observations curve is correctly fitted. This result confirms the correlation between K_{hb} and S, even if F_b is known. In this regime, the observation is more sensitive to the parameters ratio than to the parameters. Indeed, as rapidly during the simulation SC_h becomes greater than 1, it leads to $\frac{K_{hb}}{1+SC_h}C_h \simeq K_{hb}/S$. In addition, due to the added noise, more than one set of parameters can fit correctly the noisy observations curve. To conclude, the inverse problem on noisy synthetic data has confirmed the sensitivity analysis conclusions: with the liver ICG amount as observations it is difficult, may be ill posed, to identify the four parameters. However, knowing F_b or K_{sh} parameters, leads to a good estimation of the other parameters, with three runs of UKF algorithm, and the observations curve is well fitted.

Data measurements. Once the approach is verified on synthetic data, the measurements from [EDSC+99] are used as observations. Since the inverse problems and the sensitivity analysis have revealed that the four parameters are unlikely to be all estimated, two different curves, from different groups in [EDSC+99], are used for parameter estimation. The bile ligation group curve seems similar to the second regime type of curve. In that case it is better to fix F_b parameter according to the inverse problem on synthetic observations. Moreover, F_b is known for this group. The control group curve is similar to the first regime curve. According to the inverse problems on synthetic observations it is better to fix K_{sh} in that case. Different parameters are found for the different groups. In the bile ligation group, in comparison with the control group, K_{hb} coefficient is increased by around 2.5, as well as the saturation parameter by around $7.8\,10^2$. The non-linear excretion rate to the bile canaliculi is reduced, when bile ligation occurs, according to the simulation results.
The small decay in bile ligation group measurements curve is not reproduced with the model (Figure 10.12). This small decrease can be due to fluorescence light intensity decay over time. Indeed, if the common bile duct is completely ligature, no ICG can exit the liver, thus no decrease should appear in the curve. In the model, because the bile flow is set to zero ($F_b = 0$) the system will reach a stationary state, in which the amount of ICG in the blood, the sinusoids and the hepatocytes compartments is null and the bile canaliculi ICG amount is constant equal to the initial amount injected (here the initial condition). Since the initial amount is large the stationary state is not reached after 1500s. As a result, with $F_b = 0$ in the proposed model, the ICG amount in the liver never decreases. A small bile flow, because

the bile duct is not entirely ligature can also explain the small decrease in the measurements. Taking into account this decay in the model would likely result in a better estimation of the bile ligation group parameters. This is likely to lead to a better fit of the control group as well, through a better estimation of K_{sh}.
The large standard deviation in the observation of the group with portal vein partial occlusion in [EDSC+99], makes the analysis difficult. However, decreasing the liver inflow in the model, leads to the same behavior than the one reported in [EDSC+99].
With the model, the impact of bile duct ligation on the different liver compartments can be assessed. Figure 10.16 shows the ICG amount over time in the sinusoids, the hepatocytes and the bile canaliculi compartments for the control and the bile ligation groups. In the control group simulation (solid lines), the bile canaliculi compartment contains more ICG than in the bile ligation group (dash lines). A second observation is that in the control group, the ICG quantity decreases in all compartments. While, in the bile ligation group, the ICG is stored in the hepatocytes, and as a consequence also remains in high amount in the sinusoids. This leads to a large amount of ICG in the rest of the blood circulation.

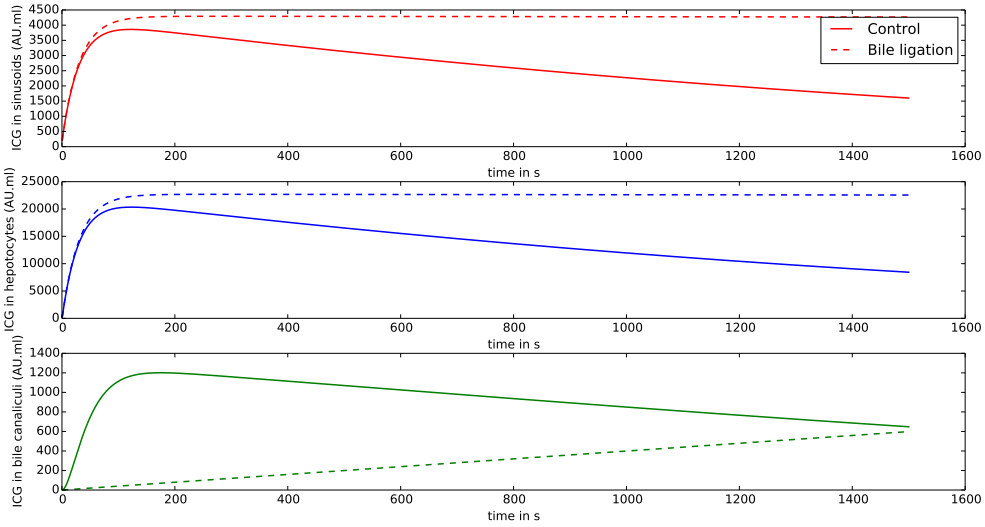

Figure 10.16: Model simulations of ICG amount over time in the different compartments of the liver: sinusoids, hepatocytes and bile canaliculi for the control simulation (solid lines) and the bile ligation simulation (dash lines).

ICG and liver function evaluation. A common test to evaluate the liver function, is the percentage of retention of indocyanine green in blood [MRA74, CHS63]. With the mathematical model, the indocyanine green percentage of retention over time, in the blood compartment, can be compared between the different groups. Three groups are compared, a control group, a bile ligation group, and a reduced liver inflow group. The simulation for the last group is done with the control parameters and a 70% liver inflow reduction (liver inflow in

control is 1.75 ml/s; it is reduced to 0.53 ml/s). Figure 10.17 shows the percentage retention of ICG over time for the different groups. The first decrease is not different between control and bile ligation groups, while the second one is, as shown in Figure 10.17. For the inflow reduction group, compared with the control group, the first part of the curve is different, and slope of the second part is similar.
According to these results, if the unhealthy liver problem is related to bile excretion, after 2min the ICG retention should be similar to the "normal" value. While, if the problem is related to liver perfusion (porto-caval shunts, etc), after 2 or 4 min the percentage of ICG retention should be higher than for a healthy liver. The ICG retention percentage after 15 min, for each group, is summarized in table 10.2. The ICG retention percentage is higher in the bile ligation group than in the inflow reduction group. In addition, in both of these groups, the value is larger than in the control group.

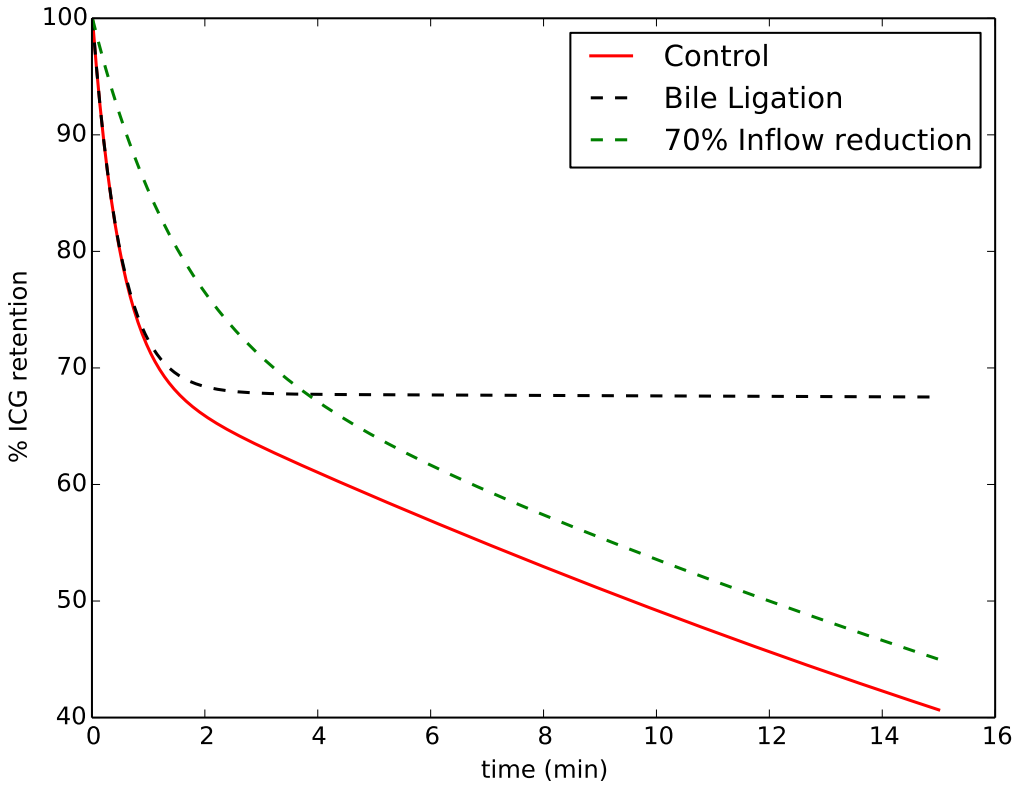

Figure 10.17: Model simulations of % of ICG remaining in blood over 15 min. The simulation is performed for different groups: control group (solid red), bile ligation group (dash line black) and 70% inflow reduction group (dash line green)

To conclude, the sensitivity analysis combined with inverse problem resolution on synthetic data, enable a good understanding of model parameter dependency. The three compartments model for the liver, is able to reproduce the different types of measurements, available in

Groups	% retention indocyanine green at 15min
Control	41
Bile Ligation	67.5
70% inflow reduction	45

Table 10.2: Percentage of ICG retention in blood after 15 min simulation results. With the model the % of ICG remaining in blood compartment after 15 minutes is computed for control group, bile ligation group and 70% inflow reduction group.

[EDSC+99]. Finally, mathematical modeling and numerical simulation of ICG processing by the liver, are promising tools to improve knowledge on the relation between ICG processing and liver function.

Chapter 11

Hepatic elimination of indocyanine green before/after partial hepatectomy in pigs

In the previous chapter (chapter 10), the indocyanine green processing by the liver was studied with data from literature [EDSC+99]. Only the liver signal was available. By contrast, the data measured during the liver surgeries on pigs (see Part I) consist of the signal in the liver but also in the hepatic artery, portal vein and common bile duct. How the hepatic artery and portal vein signals relate was studied in chapter 9. In this chapter they are taken as model inputs. Because more information is available when combining the signals in the liver and the common bile duct, the pharmacokinetic model developed in the previous section is enriched.

Section 11.1 details the measurements available and the different considered models. The methods for model outputs sensitivity to parameters, estimation of parameters and comparison of the different models are also presented. Then, in section 11.2 the sensitivity analysis is carried out for different liver signal dynamics, corresponding to two regimes of the dynamical system. In addition, the model parameters are estimated for three groups: control group, after 75% liver ablation group and after 90% liver ablation group. Section 11.3 comments on the assumptions made for this work and gives some conclusions.

Contents

11.1 Material and methods 191
11.1.1 Available measurements 191
11.1.2 Mathematical models for ICG processing 191
11.1.3 Sensitivity analysis and parameter estimation 196
11.1.4 Comparison of mathematical models 196
11.2 Results 197
11.2.1 Qualitative comparison of ICG fluorescence measurements in the liver . 197
11.2.2 Generalized sensitivity analysis 197
11.2.3 Parameter estimation and model comparison 202
11.3 Discussion and conclusions 204

11.1 Material and methods

11.1.1 Available measurements

The detailed protocol for indocyanine green fluorescence measurements can be found in part I. This chapter focuses on the modeling of the elimination of ICG from the blood to the common bile duct. The ICG measurement in the hepatic artery and the portal vein are inputs for the model. The liver and common bile duct measurements are the observations of the model from which parameters are estimated.
The ICG fluorescence in liver vessels can only be measured for two minutes, but liver and the common bile duct measurements are recorded during twenty to sixty minutes. Therefore an assumption to extend the fluorescence curve in the liver vessels is required. One longer measurement of the ICG fluorescence in the vessels could be recorded. This measurement is used to fit a typical contrast-agent function from literature [PRM+06]. Figure 11.1 shows the ICG measurement and the prolongation functions (equations (11.1)) for both vessels. The prolongation functions read:

$$\begin{aligned} f_{ha}(t) &= 2.2A_{ha}\frac{\exp(-0.04t/60)}{1+\exp -0.05(t-0.483)/60} \\ f_{pv}(t) &= 2A_{pv}\frac{\exp(-0.05t/60)}{1+\exp -0.11(t-0.483)/60} \end{aligned} \tag{11.1}$$

Where A_{ha} and A_{pv} are the last measured values of the two minutes recording in the hepatic artery and portal vein respectively.

The fluorescence is assumed to be linearly related to the concentration. The linear coefficient may differ between the different tissues (blood vessels, liver tissue and common bile duct). The linear coefficient for the common bile duct and the liver tissue are assumed identical. The difference between liver tissue and blood vessels is taken into account by the ratio of these coefficients, called $K_l = a_{vessels}/a_{liver}$ later in the equations. Without any loss of generality, the concentration in the equations are defined up to a multiplicative a_{liver} coefficient. Note that it does not impact parameters, except for coefficient in the non-linear terms (S as well as K_m in model 3 see eq. (11.2) and Figure 11.2).

11.1.2 Mathematical models for ICG processing

To represent the ICG concentration dynamics over time, a pharmacokinetic model is developed, based on the model proposed in chapter 10. The liver tissue is represented by sinusoids, hepatocytes and bile canaliculi compartments. Here a common bile duct compartment is added to take advantage of the signal measured there. The ICG exchange between sinusoids and hepatocytes is not precisely defined in literature. In chapter 10 a passive exchange was assumed. In [WKA11] two active processes drive this exchange. [OKJB94] has reported two fractions of ICG, removed at different rates. A selective uptake across the sinusoids membrane is reported in [DGMP16]. An active process with possible saturation is also described in [Ott98]. Therefore, three different types of exchange are considered in this work: a passive exchange, two active processes, as well as an active process with saturation from sinusoids to hepatocytes and an active process from hepatocytes to sinusoids. Figure

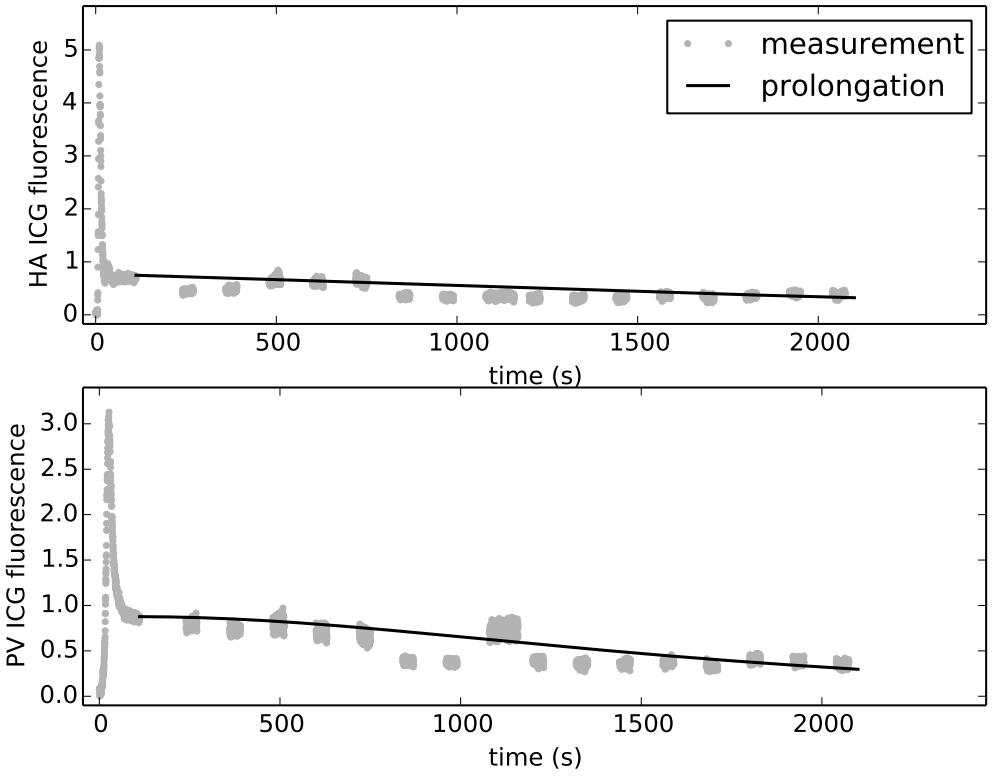

Figure 11.1: Hepatic artery and portal vein indocyanine green fluorescence measurements over 2000s and the prolongation function curve.

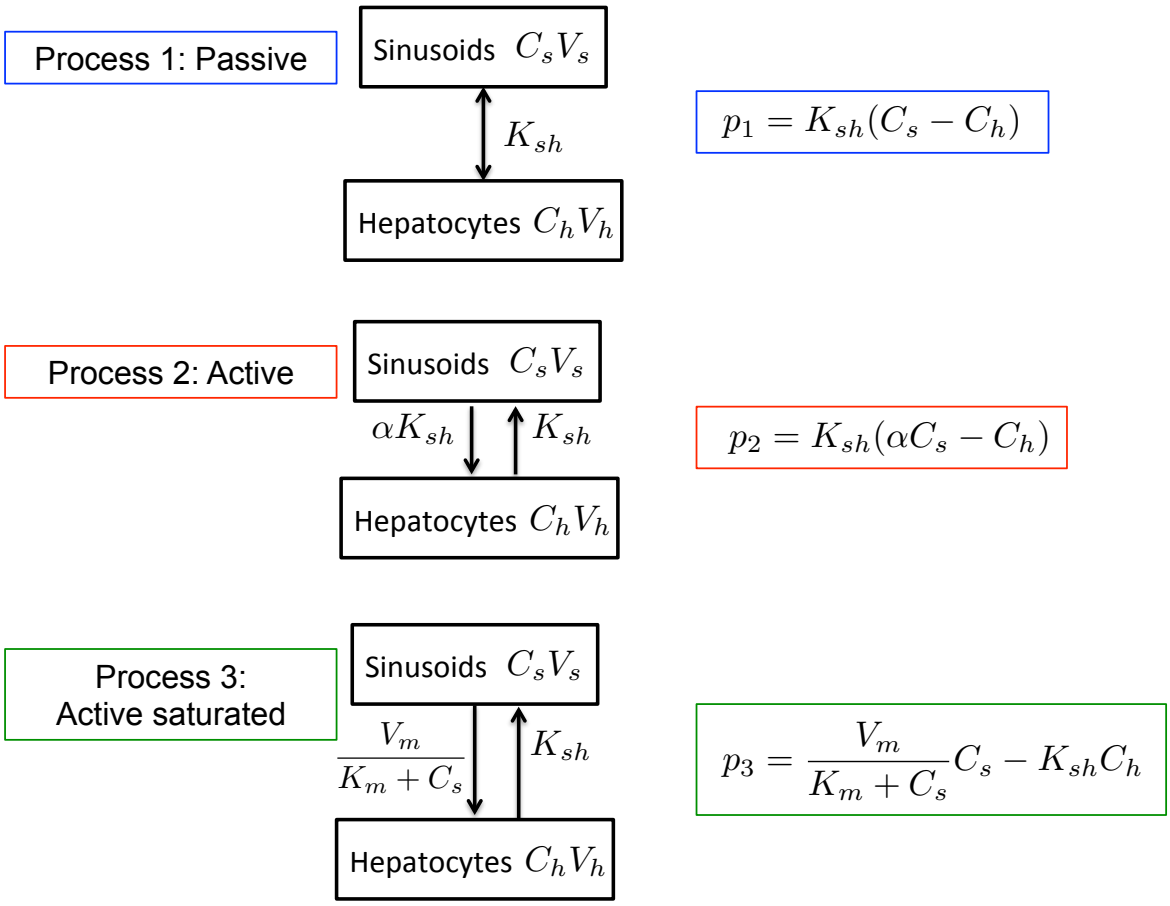

Figure 11.2: Three different types of exchange for ICG between sinusoids and hepatocytes.

11.2 shows a schematic of the three exchange processes.

The ICG excretion process from the hepatocytes to the bile canaliculi is assumed active and possibly saturating, as in the model of chapter 10. Then ICG exits the liver with bile; it flows to the common bile duct. In the measurements, a delay is observed in the appearance of ICG in the common bile duct (see section 2.2.2). To represent this delay, three transit compartments are added [BDG76, SJKK07]. The analytic solution of a series of N compartments is derived in the Appendix E. The liver amount of ICG is assumed to be the sum of the amounts in sinusoids, hepatocytes and bile canaliculi compartments. Figure 11.3 gives a schematic representation of the model. The notation for parameters and concentrations is summarized

in table 11.1. The model equations read:

$$\begin{cases} \frac{d}{dt}(V_s C_s) &= F_{ha} K_l I_{ha} + F_{pv} K_l I_{pv} - (F_{ha} + F_{pv}) C_s - p_i \\ \frac{d}{dt}(V_h C_h) &= p_i - \frac{K_{hb}}{1 + S C_h} C_h \\ \frac{d}{dt}(V_{bc} C_{bc}) &= \frac{K_{hb}}{1 + S C_h} C_h - F_b C_{bc} \\ \frac{d}{dt}(R_1) &= \frac{1}{\tau}(F_b C_{bc} - R_1) \\ \frac{d}{dt}(R_2) &= \frac{1}{\tau}(R_1 - R_2) \\ \frac{d}{dt}(R_3) &= \frac{1}{\tau}(R_2 - R_3) \\ \frac{d}{dt}(V_{cbd} C_{cbd}) &= R_3 - F_b C_{cbd} \end{cases} \tag{11.2}$$

Where p_i is one of the processes considered (Figure 11.2) defined by:

$$p_1 = K_{sh}(C_s - C_h)\,,\; p_2 = K_{sh}(\alpha C_s - C_h)\,,\; p_3 = \frac{V_m}{K_m + C_s} C_s - K_{sh} C_h$$

The only difference between the first and second process is the parameter α. However, this distinction is kept for the parameter estimation.

Notation	Signification
s	Sinusoids
h	Hepatocytes
bc	Bile Canaliculi
L	Liver
ha	Hepatic artery
pv	Portal vein
cbd	Common bile duct
b	Bile
V_i	Volume of i^{th} compartment (ml)
C_i	Concentration of i^{th} compartment (g/ml)
R_i	Delay compartment (g/s)
I_i	Fluorescence measure vessel i (grey level)
F_i	i^{th} flow rate (ml/s)
K_l	Ratio of conversion coefficients from fluorescence to concentration
K_{sh}	Exchange coefficient between hepatocytes and sinusoids (ml/s)
α	Sinusoids proportion uptake in process 2
V_m	Maximum exchange coefficient in process 3 (g/s)
K_m	Saturation concentration in process 3 (g/ml)
K_{hb}	Excretion coefficient from hepatocytes to bile canaliculi (ml/s)
S	Saturation parameter (ml/g)

Table 11.1: Notation table with notation details and unit precision.

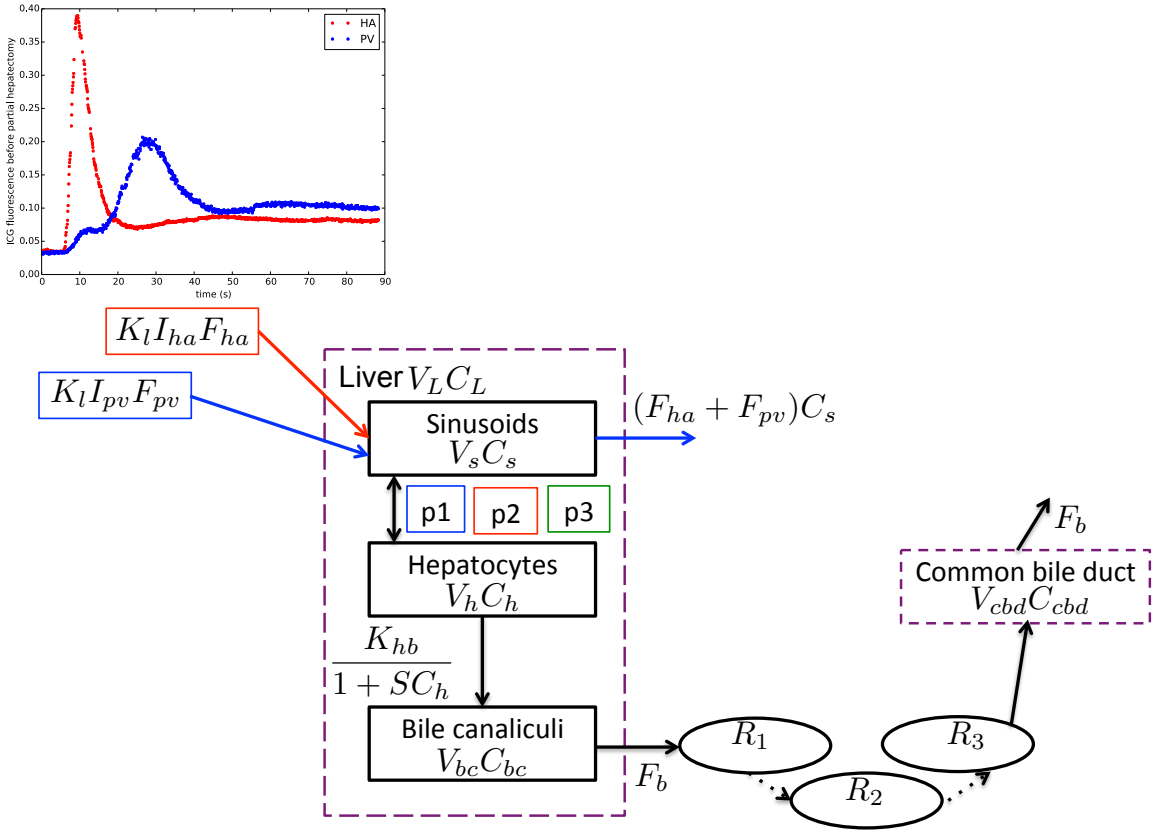

Figure 11.3: Schematic of the ICG phamaco-kinetic model. The dash blocks are the observations. The processes 1 2 and 3 are recalled in figure 11.2.

11.1.3 Sensitivity analysis and parameter estimation

Fixed parameters. The model with processes 1, 2 and 3, has 13, 14 and 15 parameters respectively. The liver volume is estimated with the pre-operative CT-scan. The sinusoids, the bile canaliculi and the hepatocytes compartments volumes are 15.3%, 3.4% and 81.3% of the liver volume [HHF+14]. The hepatic artery flow F_{ha} and the portal vein flow F_{pv} are measured during the fluorescence recording. These two parameters are set to measured values averaged over around 20 seconds (see Part I section 2.2.1).
The remaining parameters are estimated, solving an inverse problem, with the liver tissue and common bile duct ICG measurements as observation. In the model with process 1, the parameters K_l, K_{sh}, K_{hb}, S, τ, F_b and V_{cbd} have to be estimated. While with process 2 the parameter α has to be estimated as well, and with process 3 K_m, V_m estimations are also required.

Sensitivity analysis. The correlation and the sensitivity of model outputs (liver and common bile duct compartments concentration) to parameters is assessed with generalized sensitivity functions. The sensitivity analysis tools are detailed in Appendix B.

Parameter estimation. Three groups of animals are considered, the control group (before liver resection), the 75% liver ablation group and the 90% liver ablation group. In order to evaluate the differences between the parameters estimated in each group, a population approach is used for parameter estimation. For each group the population parameters are estimated with the Monolix software, as well as the parameters for each individual. The population approach algorithm used in Monolix is detailed in Appendix D and in [Mon]. Once the parameters are estimated, the model predictions are compared to the measurements. To do so, the forward model is implemented in a C code. The system of differential equations (11.2) is solved with the IDA package from SUNDIALS (Suite of Nonlinear and Differential/Algebraic Equation Solver) [SPH15]. Backward Differentiation Formula is used to integrate in time the system, and a Newton method solves the resulting nonlinear equations.

11.1.4 Comparison of mathematical models

In order to compare the three different processes, a relative error is computed. The error is defined by:

$$\mathcal{E}_2 = \frac{\|X_i^o - X_i^m\|_2}{\|X_i^o\|_2} \tag{11.3}$$

where X_i^o is the measurement at time t_i and X_i^m is the model output at the same time, for the liver and the common bile duct. The error is computed for each animal and for both measurements, then the average and standard deviation (over all animals and both measurements) is calculated.

11.2 Results

11.2.1 Qualitative comparison of ICG fluorescence measurements in the liver

In the measurements, two different shapes for the liver ICG curve are observed (section 2.2.2). Figure 11.4 shows the two typical shapes for two animals. The increase of the ICG in the liver tissue is different in the two animals. With the mathematical models, the two types of curve can be qualitatively reproduced.
The first part of the curve shape depends on the balance between the liver inflow ($F_{ha} + F_{pv}$) and the hepatocytes uptake coefficient (K_{sh} or αK_{sh} or $V_m/(K_m + C_s)$). If the hepatic uptake is large compared to the inflow (flow-limited case), the ICG goes rapidly to the hepatocytes compartment, and no first peak appears. On the contrary, if the hepatic uptake is lower than the flow (uptake-limited case), then the first part of the liver tissue curve follows the input curve, and a first peak appears. The model results (for each process) are plotted in figure 11.5, with all parameters fixed except the hepatic uptake parameters.
From this first observation and according to the mathematical model results, the presence of a first peak in the liver ICG fluorescence curve could be linked to a poor exchange function between sinusoids and hepatocytes or a large hepatic inflow.

11.2.2 Generalized sensitivity analysis

In the previous section, two types of liver ICG concentration curve have been described, corresponding to two different regimes. The generalized sensitivity analysis is a local analysis, therefore the generalized sensitivity functions are computed for each model with both types of curve. The generalized sensitivity functions are plotted by pairs, assuming the other parameters are known, to study the inter-dependency of parameters. The liver tissue and the common bile duct are considered as the observations.

Model with process 1. In case of a large hepatic uptake, Figure 11.6 shows the model outputs and the generalized sensitivity function (GSF) for K_l, K_{sh}, K_{hb}, S, τ, F_b and V_{cbd} parameters. The oscillation in GSF indicates that correlation between parameters are likely (Appendix B). Small oscillations are observed in the GSFs of K_l and K_{sh}, K_l and K_{hb}, K_l and S. Moreover, the parameters K_{hb} and S, K_{hb} and K_{sh}, K_{sh} and S are also likely to be correlated. The sharp increase of the GSF indicates the time interval where the model output is the most sensitive to the parameter. The model outputs are the most sensitive to τ between 1000 and 2000 seconds; this time interval corresponds to the increase part of the common bile duct curve (Figure 11.6 (a)). The parameter S is sensitive to the second part of the curves, after 1000 seconds. This time interval is when the concentration in the liver has reached a maximum and the common bile duct concentration increases. The model outputs are sensitive to F_b and V_{cbd} at the end of the simulation, between 2000 and 2500 seconds, when the concentration in the liver start to decrease and the increase in the common bile duct curve slows down.

In case of a low hepatic uptake, Figure 11.7 shows the model outputs and the generalized sensitivity functions for the same parameters as the previous case. Less correlation appears

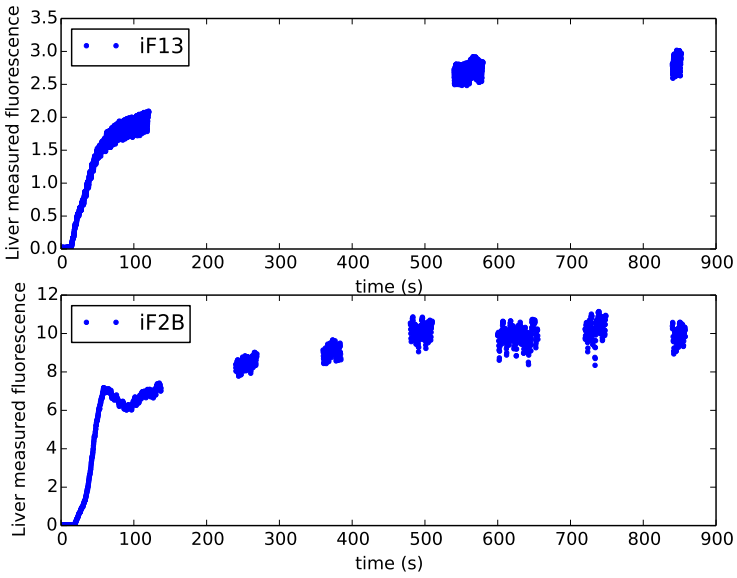

Figure 11.4: Liver ICG fluorescence measurements in two animals over time.

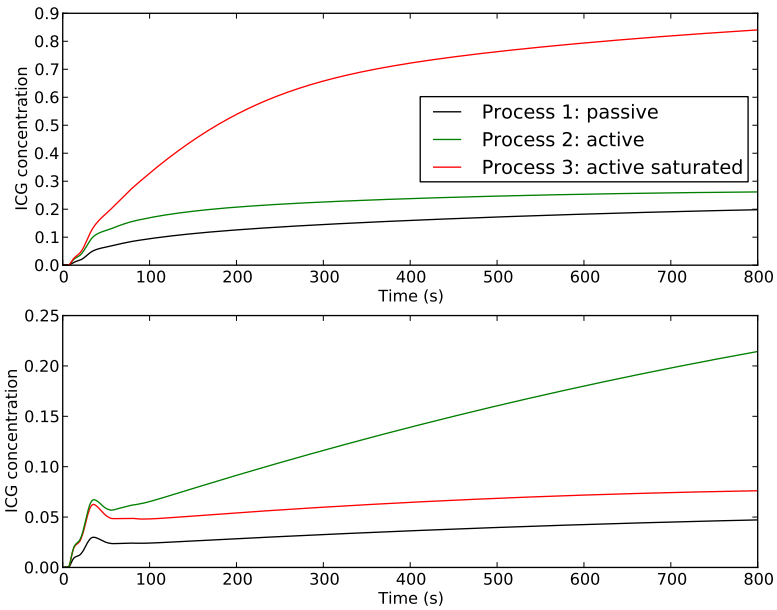

Figure 11.5: Liver ICG concentration simulation with the three different processes, with liver hepatocytes uptake larger (top) and lower (bottom) than liver inflow.

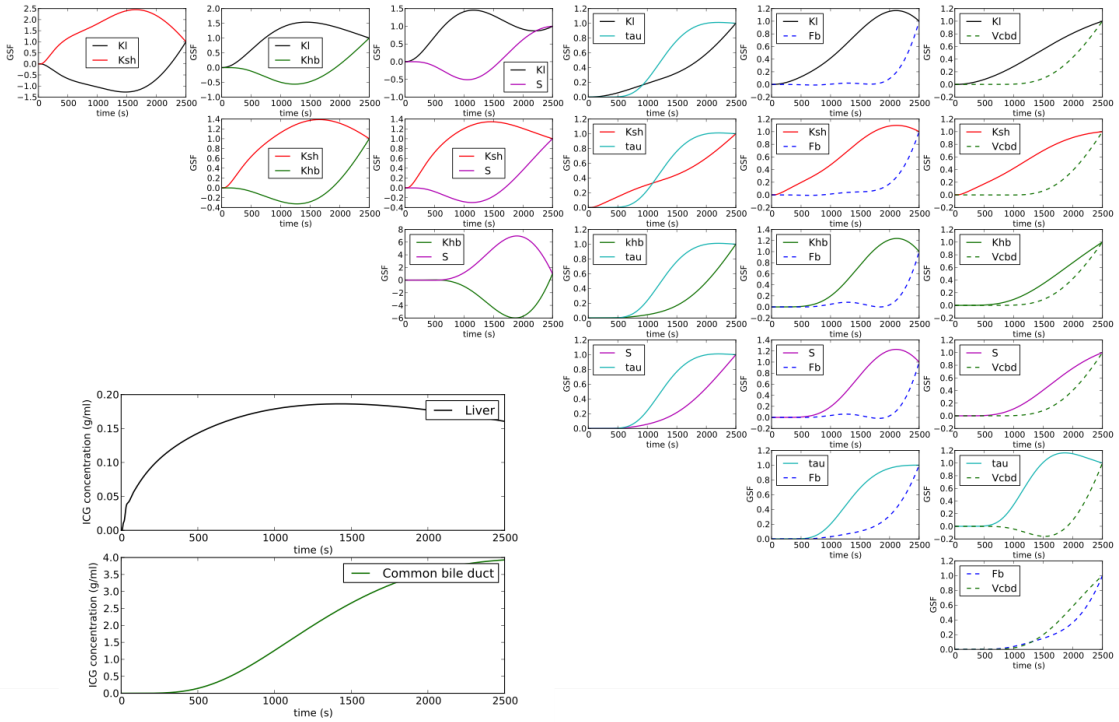

Figure 11.6: Model outputs and generalized sensitivity function for the model with process 1 when the hepatic uptake is larger than the liver inflow.

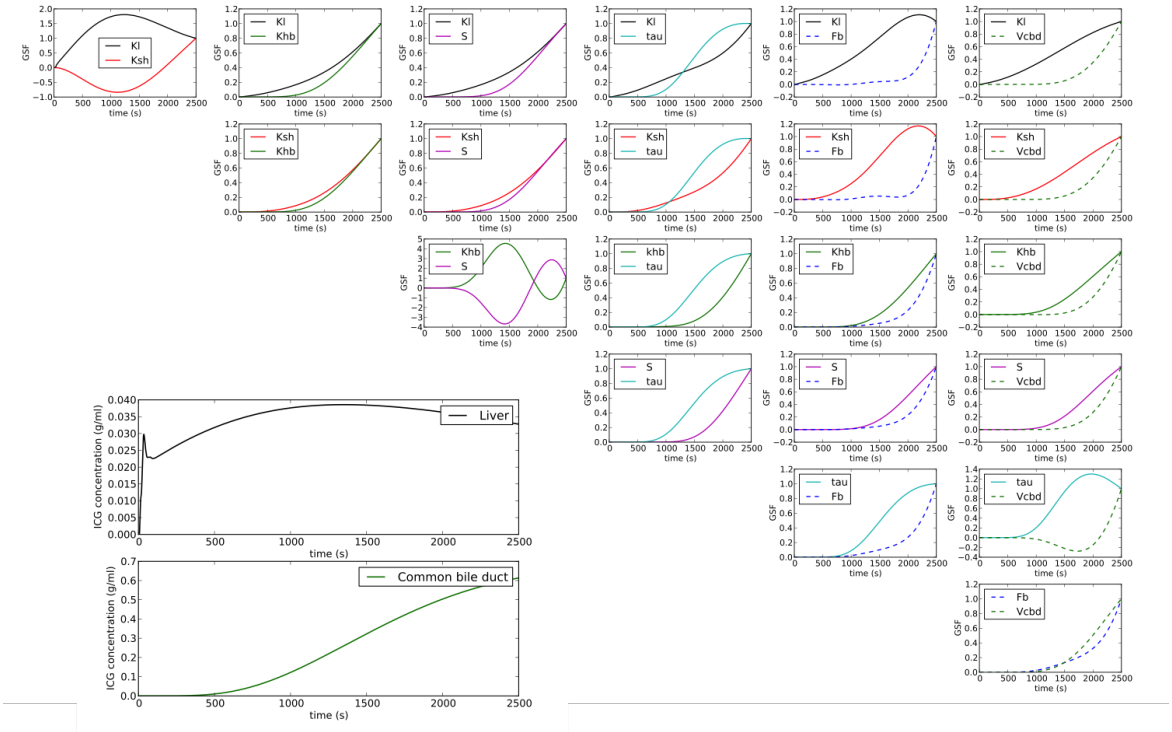

Figure 11.7: Model outputs and generalized sensitivity function for the model with process 1 when the hepatic uptake is lower than the liver inflow.

in this case; only parameters K_l and K_{sh}, as well as K_{hb} and S are likely to be correlated. Similarly to the previous case, the model outputs are sensitive to τ parameter between 1000 and 2000 seconds and to parameters F_b and V_{cbd} at the end of the simulation, between 2000 and 2500 seconds. The observations curves contain most information on S and K_{hb} parameters between 1000 seconds and the end of the simulation, when the liver concentration has reached its maximum (Figure 11.7 (a)).

In both cases, some correlations exist between parameters. Therefore the estimation of parameters may be difficult. With the second type of liver curve (with a low hepatic uptake) less parameters are correlated. In this case, the parameter estimation should be easier. In both cases, the model outputs contain most information about F_b and V_{cbd} once the liver concentration starts to decrease and the common bile duct concentration increase slows down.

Model with process 2. In case of a large hepatic uptake, Figure 11.8 shows the model outputs and the generalized sensitivity functions for K_l, K_{sh}, α, K_{hb}, S, τ, F_b and V_{cbd} parameters. The generalized sensitivity functions for τ, F_b and V_{cbd} are similar to the previous model ones. According to GSFs, correlations are likely between, α and S as well as between S and K_{hb}. Small correlations exist between K_l and K_{sh}, K_l and K_{hb}, K_l and α, K_l and S. Moreover, the non-monotonic increase of GSFs of K_{sh} and α, K_{hb} and α, K_{sh} and K_{hb}, as well as K_{sh} and S indicates small correlations between these parameters.

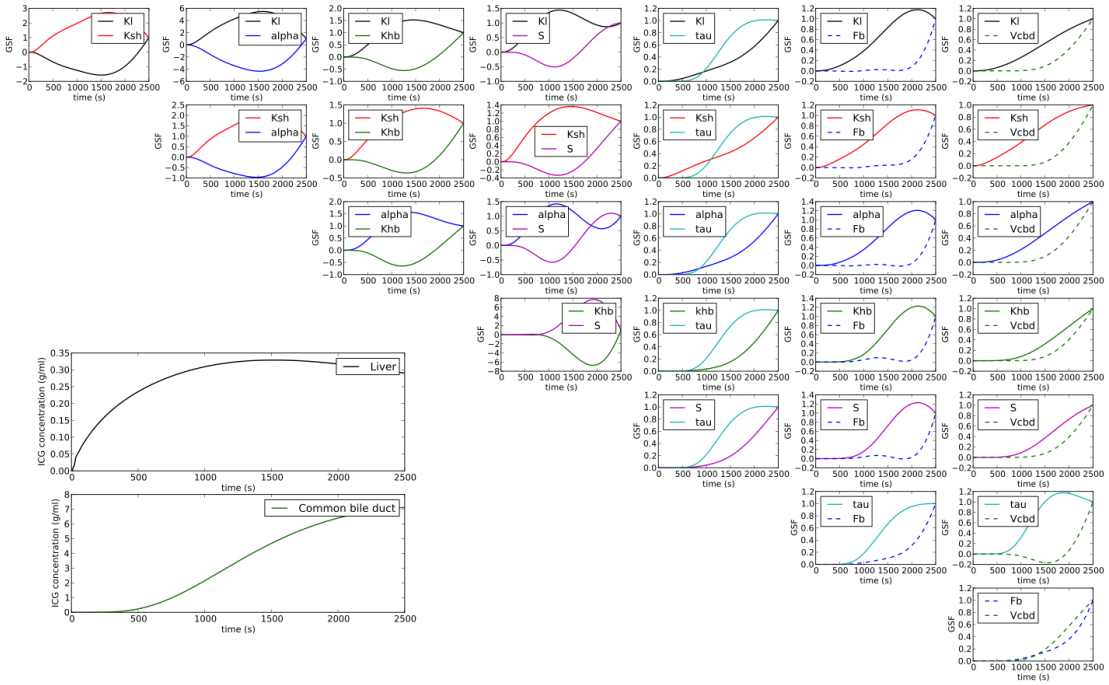

Figure 11.8: Model outputs and generalized sensitivity function for the model with process 2 when the hepatic uptake is larger than the liver inflow.

In case of a low hepatic uptake, similarly to the first model, less oscillations appear in generalized sensitivity functions (Figure 11.9 (b)). Small correlations exist between K_l and K_{sh}, K_l and α, K_{sh} and α. The large oscillations in K_{hb} and S GSFs indicate that the parameters are likely to be correlated. For the other parameters the GSFs are similar to the previous cases.

For both cases, correlation between parameters are likely. Like for the first model, less correlation appears for the second type of liver concentration curve. When the hepatic uptake is low the parameter estimation may be easier, due to less inter-dependency between parameters.

Model with process 3. Like for the two other models, the generalized sensitivity functions and the model output curves are plotted when hepatic uptake is large (Figure 11.10) and when it is low (Figure 11.10). The observation for the parameters common to the three models are similar. In this model, in the first case, oscillations are observed in GSFs, indicating correlations, for parameters K_{hb} and V_m, K_m and K_{hb} as well as K_{sh} and K_{hb}. Similarly, important correlations exist between S and the parameters K_l, V_m, K_m, K_{sh} and K_{hb}. Between other parameters only small correlations are likely.
In the second case, the GSFs increase are almost monotonic, therefore only small correlations between parameters are likely. Like for the other model, with the second type of liver curve as observations, the parameter estimation may be easier than with the first type of curve.

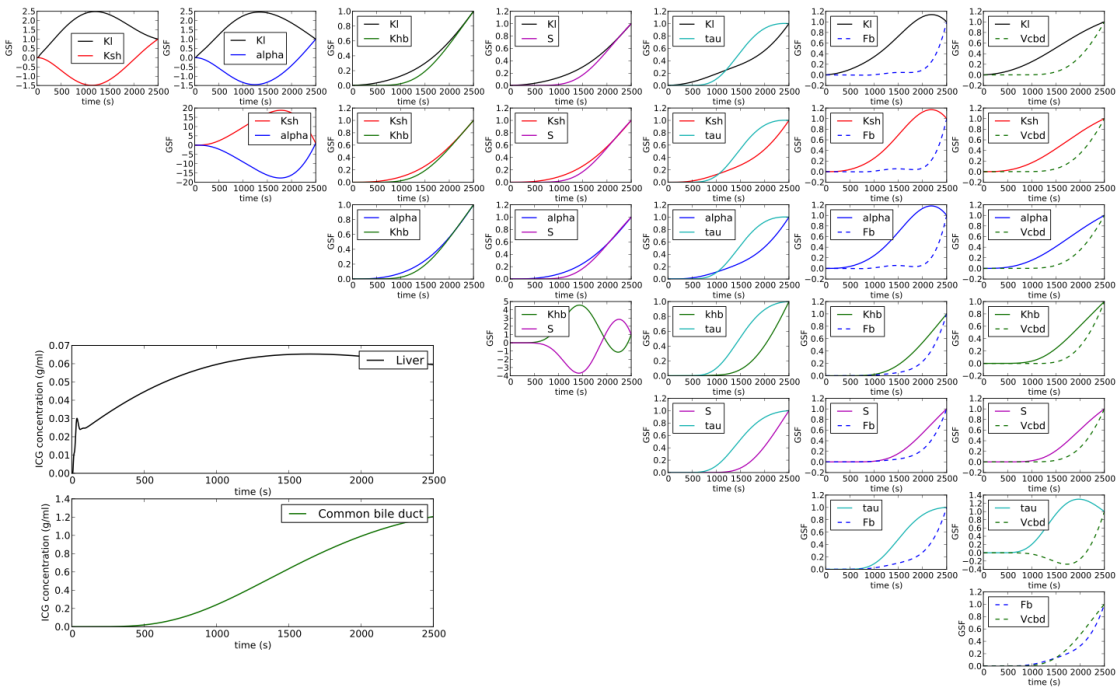

Figure 11.9: Model outputs and generalized sensitivity function for the model with process 2 when the hepatic uptake is lower than the liver inflow.

According to the sensitivity analysis, parameters correlation are likely. The parameters with the highest correlation are K_{hb} and S, as well as V_m and K_m for model 3. The sensitivity analysis does not prove that the parameters are unidentifiable, but it gives information on the relation between parameters. Therefore, using a population approach the model parameters are estimated. The analyzed population parameters are K_{hb} and K_{hb}/S, as well as V_m and V_m/K_m in order to account for the known correlations. These parameters are chosen because they have an impact on the observations curves.

11.2.3 Parameter estimation and model comparison

After estimating the parameters as described in paragraph 11.1.3, for each model, the equations are then solved for each animal. The results are shown in Figures 11.12, 11.13 and 11.14. The three processes are able to fit almost all the measurements. The two animals iF8 and iF1A are less well fitted than the others (Figures 11.12 (a) and (e)). The third process seems to be the only one able to match the observations curve in the liver tissue of animal iF9. The three models are compared, in terms of their error, averaged over all animals (Table 11.2). The third model has the smallest error; however its number of parameters is the highest. Since the maximal difference between the errors is 0.03, it seems no significant advantage is gained by adding parameters.

The population parameters divided by the control population parameters for each group

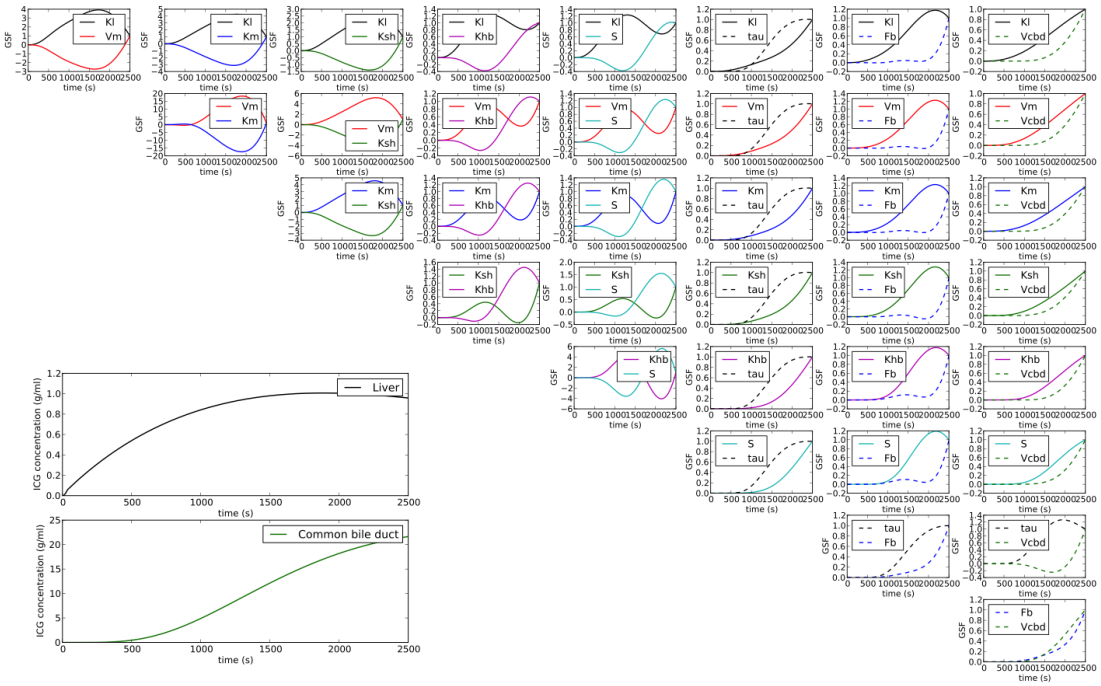

Figure 11.10: Model outputs and generalized sensitivity function for the model with process 3 when the hepatic uptake is larger than the liver inflow.

are summarized in Table 11.3 for the first model, Table 11.4 for the second one and Table 11.5 for the third model. The analysis of these parameters is difficult because of the small number of individuals per population (control: 5, 75%: 2 and 90%:3).

With the estimated parameter, in comparison with the control group, K_{sh} and V_m are increased for 75% liver ablation and they are decreased for the 90% liver ablation group. The hepatic uptake is different in each model. In each model, the uptake parameter (K_{sh} or V_m) value in 75% group is really high, but this group contains only two animals. It seems the hepatocytes uptake is decreased after 90% liver ablation. In all groups the liver inflow is lower than the hepatic uptake parameter (K_{sh} or V_m). However, the ratio $(F_{ha} + F_{pv})/K_{sh}$ or $(F_{ha} + F_{pv})/V_m$ in the control group and after 75% liver ablation is lower than 0.1 for all models. While, for all models, after 90% liver ablation this ratio is between 0.2 and 0.4. After 90% liver ablation it seems that a change of regime occurs as shown in the shape on the liver concentration curves (Figure 11.14).

According to the models, the excretion parameters from the hepatocytes to the bile canaliculi seems impacted by the liver resection. In the first model, K_{hb} coefficient is increased in the 75% liver ablation group, while in the 90% liver ablation group the coefficient is decreased compared to the control group. In the second and third model the excretion coefficient K_{hb} decreases after liver partial ablation. In the three models, K_{hb}/S coefficient is smaller in the partial ablation groups compared with the control group. The reduction of

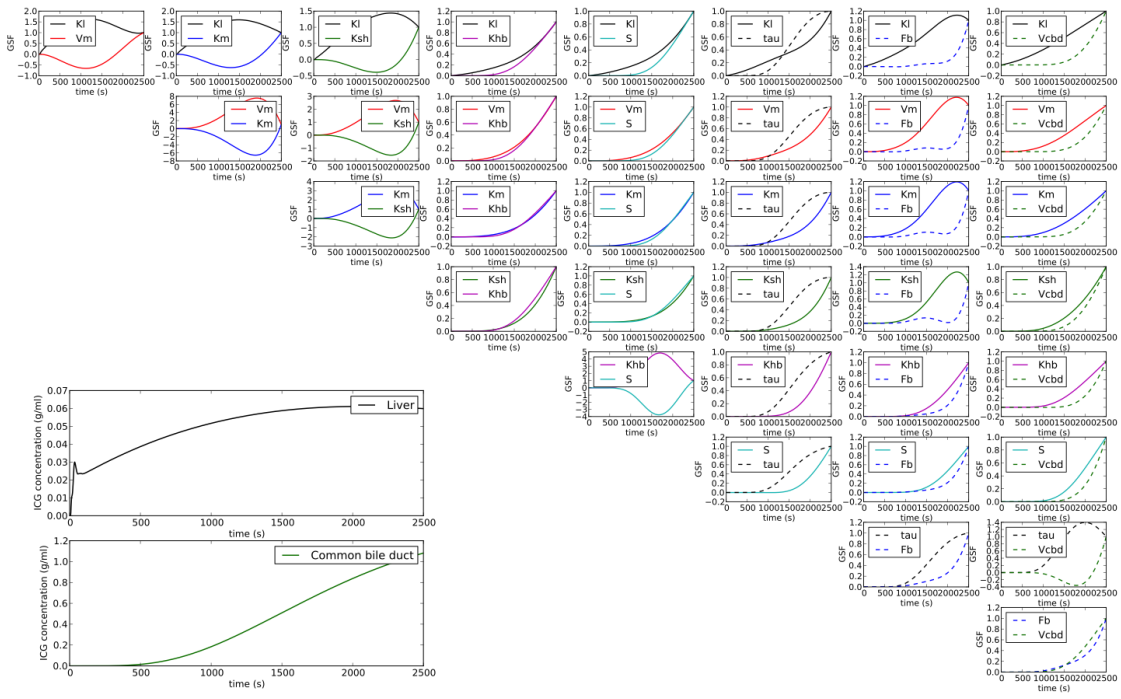

Figure 11.11: Model outputs and generalized sensitivity function for the model with process 3 when the hepatic uptake is lower than the liver inflow.

Error $\mathcal{E}_2$	Average	Std
Model 1	0.17	0.18
Model 2	0.15	0.17
Model 3	0.14	0.17

Table 11.2: Average and standard deviation of the error $\mathcal{E}_2$ (eq. (11.3)) for each model.

K_{hb}/S is larger for a larger liver ablation. The time delay parameter τ is largely increased in the 90% liver ablation group, for all models. Moreover according to the models, the bile flow is reduced after partial ablation. Therefore, the bile excretion seems impacted by liver partial ablation.

The small amount of individuals and the large range of parameter values make the analysis of these results difficult. More data are required to identify parameter ranges that could be linked to liver function, and confirm these tendencies.

11.3 Discussion and conclusions

Input curves prolongation. The assumption on the prolongation of the input curves may impact the model results. In order to investigate this impact three different assumptions are tested: 1) concentration linearly decreases and no ICG remains after 1h; 2) concentration linearly decreases and no ICG remains after 1.5h; 3) concentrations are extended with the

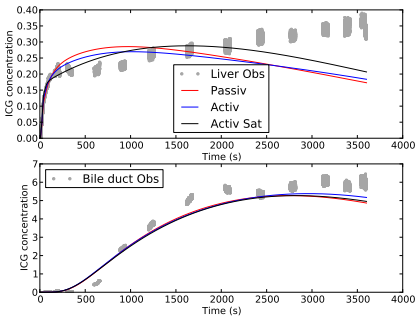

(a) Pig iF8

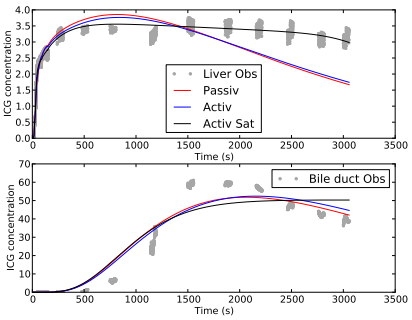

(b) Pig iF9

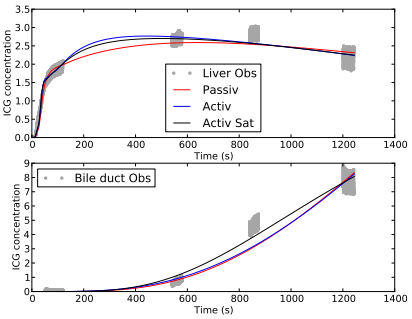

(c) Pig iF13

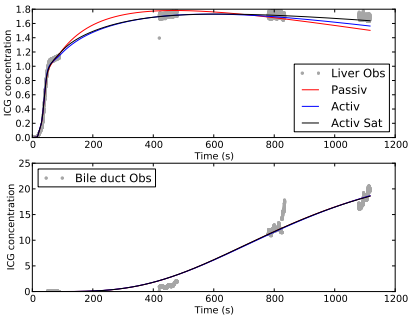

(d) Pig iF14

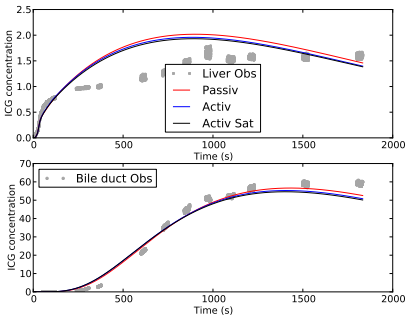

(e) Pig iF1A

Figure 11.12: Model outputs and measurements over time. The parameters are set to Monolix individual estimates. The animals are in the control group.

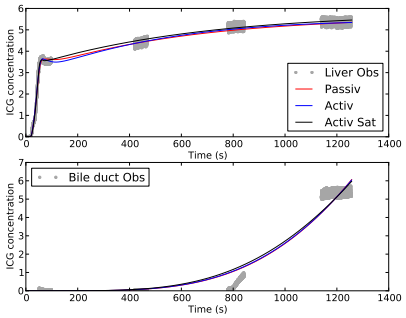

(a) Pig iF16

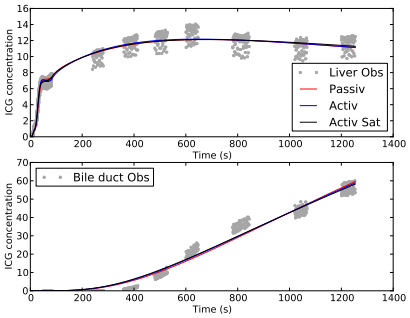

(b) Pig iFC6

Figure 11.13: Model outputs and measurements over time. The parameters are set to Monolix individual estimates. The two animals are in the 75% liver ablation group.

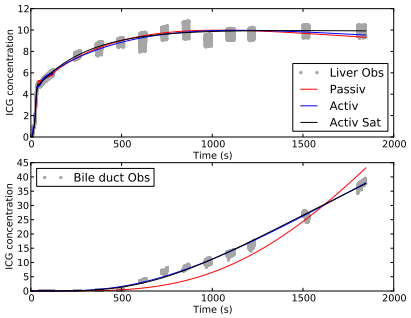

(a) Pig iF1B

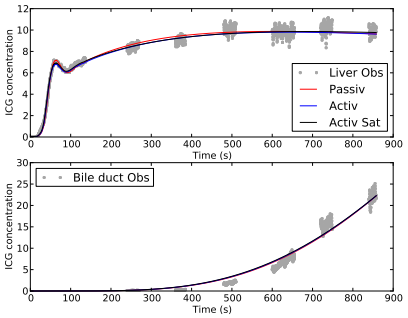

(b) Pig iF2B

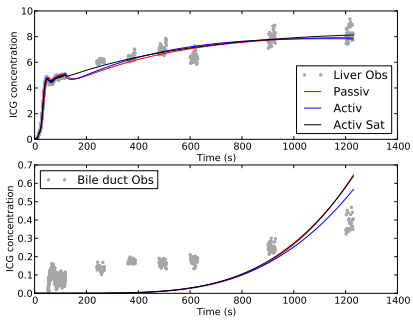

(c) Pig iF3B

Figure 11.14: Model outputs and measurements over time. The parameters are set to Monolix individual estimates. The three animals are in the 90% liver ablation group.

Pop parameter over control pop parameter	75%	90%
K_{sh}	5.1	0.04
K_{hb}	1.2	0.78
K_{hb}/S	0.6	0.38
τ	0.63	4.4
F_b	0.12	0.08

Table 11.3: Population parameter over control population parameter for each group estimated by Monolix for the first model (Figure 11.2).

Pop parameter over control pop parameter	75%	90%
K_{sh}	638	0.04
α	1.2	1.2
K_{hb}	0.8	0.49
K_{hb}/S	0.87	0.35
τ	1.37	3.16
F_b	0.26	0.1

Table 11.4: Population parameters over control population parameters for each group estimated by Monolix for the second model (Figure 11.2).

Pop parameter over control pop parameters	75%	90%
V_m	2.1	0.5
V_m/K_m	1.1	0.13
K_{sh}	0.7	0.22
K_{hb}	0.62	0.43
K_{hb}/S	0.47	0.29
τ	0.94	2.6
F_b	0.2	0.09

Table 11.5: Population parameters over control population parameters for each group estimated by Monolix for the third model (Figure 11.2).

function defined with formulas (11.1). The three assumptions are compared to the longer measurements available (see Figure 11.15): all lie within the noise of the measurements. To evaluate the impact of the different assumptions on the models outputs, the solution is computed for each assumption with fixed parameters and for all models. Figures 11.16 and 11.17 show the ICG concentrations in the liver and in the common bile duct over time. The first part of the input curves is common to each assumption, therefore no differences appear in the initial steep signal increase of the liver concentration curve. Then, the liver concentration curve is impacted by the different prolongations of the input curves. By contrast, no differences are observed before 2000s in the common bile duct concentration for the different assumptions. Even if the differences between the inputs are small, the liver model outputs are sensitive to these differences. Therefore, more measurements are required to validate the prolongation of the input curves. In future work, the model of ICG transport in the entire blood circulation developed in chapter 9 could provide, given an injected dose, the hepatic artery and portal vein entries to the liver over time. However, to obtain such detailed shapes in the initial phase by contrast to what is obtained with a simple model of the rest of the body (like in chapter 10), more work is requited to better model the transfer functions (first investigations on that topic are proposed in chapter 9).

Sensitivity analysis and parameter estimation. The sensitivity analysis has revealed correlations between some parameters. In addition the measurement curves are noisy. Therefore more than one set of parameters may be able to fit the observations curves. In this work three models are proposed to explain the measurements. For each model, parameters have been found that lead to the fit of the observations curves.
The models have been compared computing the error to the observation for each individual. The errors are similar, with a small advantage for the process 3. However, the third model has more parameters than the other models and the fit improvement with the additional parameter is small.

The parameters for three groups have been estimated for each model. The goal was to identify differences in parameters linked to the liver function. The hepatic excretion of ICG into bile and the bile flow seem reduced after liver ablation, with a larger reduction if the liver ablation is larger. By contrast, the uptake from the sinusoids seems to increase for the 75% liver ablation and decrease for the 90% liver ablation, compared to the control group. The small amount of data make the analysis of parameter estimation per group questionable, and more data are required to confirm these results. Experimentally, this is due to the fact that an ICG injection could only be performed before or after surgery on a given animal, and that a number of experimental issues lead to disregard a number of acquisitions. However, this study presents, for the first time, a framework able to explain ICG dynamics measurements in the liver and the bile duct. With more data, this framework may be able to link the model parameters to the liver function, in a variety of conditions. This could lead to a new method to evaluate the liver uptake and excretion functions with indocyanine green measurements, and to reveal if one or the two mechanisms are dysfunctional.

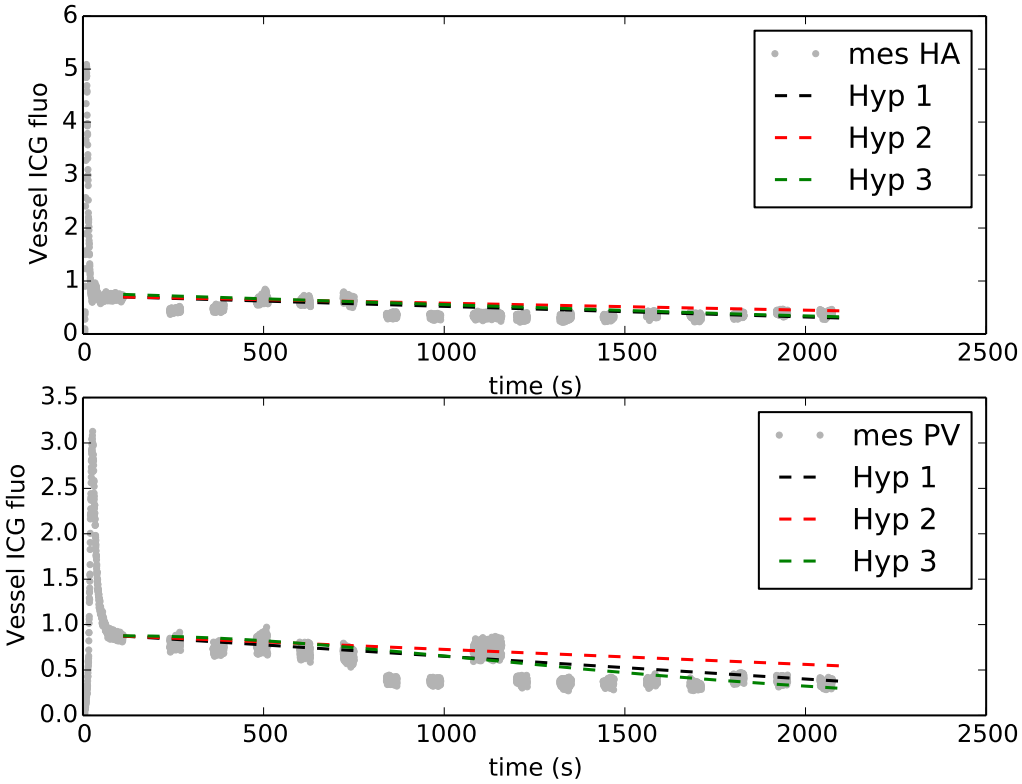

Figure 11.15: Hepatic artery and portal vein indocyanine green fluorescence measurements over 2000s and the prolongation curves for the three hypotheses: 1) concentration linearly decreases and no ICG remains after 1h; 2) concentration linearly decreases and no ICG remains after 1.5h; 3) concentration is extended with the formulas (11.1).

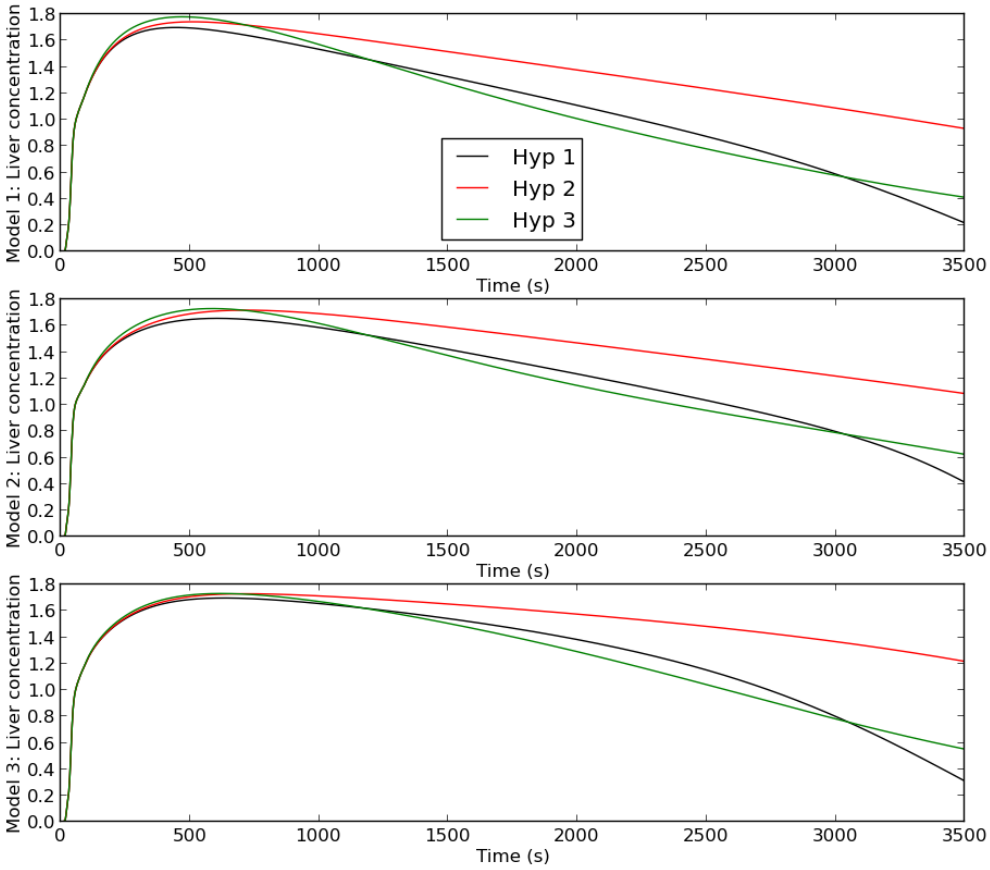

Figure 11.16: Liver compartments ICG concentration over 3500s simulated with the three considered models (top: Model 1; middle: Model 2; bootom: Model 3) for the different assumptions to extend vessel measurements.

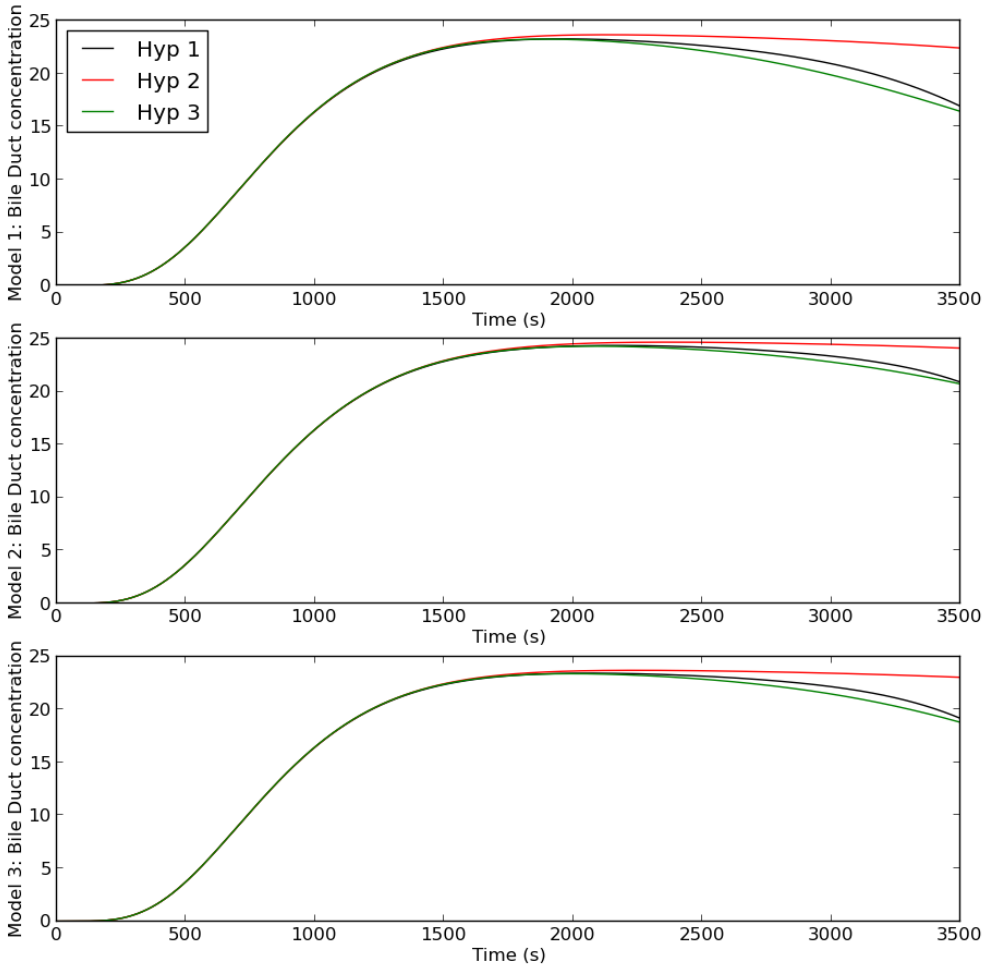

Figure 11.17: Bile duct compartments ICG concentration over 3500s simulated with the three considered models (top: Model 1; middle: Model 2; bootom: Model 3) for the different assumptions to extend vessel measurements.

Chapter 12

Clinical application of indocyanine green measurements

In the previous chapter (chapter 11) indocyanine green measurements had been taken as long as possible (20 to 50 minutes), so that the decline of the signal, which is sensitive to liver function, could be captured. In the clinical peri-operative context, 20 minutes open abdomen measurements are simply not possible: only a few minutes of dynamical measurements can be acquired. In such a short time, no signal raise in the common bile duct can be detected. Therefore, in this chapter the model proposed in chapter 11 is simplified to match the clinical requirements. First, the measurements and the proposed models are presented in section 12.1. Then, in section 12.2, the parameter estimation is performed with few minutes of pig measurements. The flow estimates are compared to the measured ones and the model that gives the best flow estimation is selected for the subsequent patient parameter estimation. Section 12.3 ends this chapter with some conclusions.

Contents

12.1 Material and methods 215
12.1.1 Clinical measurements 215
12.1.2 Mathematical model 215
12.1.3 Parameter identifiable and estimation 216
12.2 Results 221
12.2.1 Parameter estimation with pig ICG measurements and model comparison 221
12.2.2 Parameter estimation patient ICG measurements 224
12.3 Conclusions 225

12.1 Material and methods

12.1.1 Clinical measurements

The indocyanine green blood concentration measurement is clinically used to estimate the liver function [MRA74, CHS63]. Similarly to the context of hepatectomy, after a liver transplantation, once the transplanted liver is in place, the evaluation of the new liver function is important and not easy to measure intra-operatively. The fluorescence of the liver, measured with near infrared spectroscopy, after an indocyanine green injection may evaluate the new liver perfusion and function. For example, the function of the veno-occluded regions is evaluated with ICG in [KSI+13].
In AP-HP hopital Paul Brousse, centre hepato-biliaire (12 Avenue Paul Vaillant Couturier, 94800 Villejuif, France), four patients received indocyanine green intravenous injection after liver transplantation, and fluorescence was measured for a few minutes. No medical decisions were made according to the fluorescence measurements. The measurements are only for observation of the fluorescence. This study was approved by Paul Brousse local scientific board and complies with the French guidelines regarding the scientific research on human subjects. The fluorescence is recorded in the hepatic artery and in the portal vein as well as in the liver tissue with Fluostick^{TM} from the Fluoptics company [Flu]. Image analysis is performed by Fluoptics [Flu]. A quantitative estimation of the liver function is hoped by combining these measurements, mathematical modeling and parameter estimation. The hepatic artery and portal vein flows are not commonly measured in patients. Therefore, the ICG measurements are also used to test if estimation of the liver inflow is possible, which is an important parameter for graft function [VCZ14].

More measurements are available on pigs, and pig is considered a good animal model for liver since its liver to body weight ratio is close to human's [Box80]. Thus, the parameter estimation is first performed with measurements from pig surgeries (see part I). The estimated flows are compared to the measured ones (since these measurements are available). Then, the procedure developed on pig ICG measurements is applied on patient measurements.

12.1.2 Mathematical model

The model proposed in chapter 11 is adapted to the available clinical measurements. Assuming no ICG is excreted into the bile during the two minutes following the injection, the proposed pharmaco-kinetic model includes only sinusoids and hepatocytes compartments. The three processes proposed in chapter 11 to describe the exchange between sinudoids and hepatocytes are considered. Therefore, three simplified models are proposed, described in Figure 12.1. The ICG fluorescence measured in the vessels is imposed as inputs to the model. The sum of sinusoids (s) and hepatocytes (h) ICG amounts is assumed equal to the liver (L) ICG amount.
The ICG fluorescence measurements are assumed linearly related to the ICG concentration: $C = aI$ with C the concentration and I the fluorescence. However, the difference in tissue linear coefficients between fluorescence and concentration in the blood vessel tissue on one hand and liver tissue on the other hand, is taken into account by the ratio of these linearity coefficients $K_l = a_{vessel}/a_{liver}$. Without any loss of generality, the concentration in the

equations are defined up to a multiplicative a_{liver} coefficient. Note that it does not impact parameters, except for the saturation coefficient in Model 3, this parameter is also defined up to a multiplicative coefficient. The models equations read:
Model 1.

$$\begin{cases} \frac{d}{dt}(V_s C_s) & = rFK_l I_{ha} + (1-r)FK_l I_{pv} - FC_s - K_{sh}\left(C_s - C_h\right) \\ \frac{d}{dt}(V_h C_h) & = K_{sh}\left(C_s - C_h\right) \\ C_L & = \frac{C_s V_s + C_h V_h}{V_s + V_h} \end{cases} \tag{12.1}$$

Model 2.

$$\begin{cases} \frac{d}{dt}(V_s C_s) & = rFK_l I_{ha} + (1-r)FK_l I_{pv} - FC_s - K_{sh}\left(\alpha C_s - C_h\right) \\ \frac{d}{dt}(V_h C_h) & = K_{sh}\left(\alpha C_s - C_h\right) \\ C_L & = \frac{C_s V_s + C_h V_h}{V_s + V_h} \end{cases} \tag{12.2}$$

Model 3.

$$\begin{cases} \frac{d}{dt}(V_s C_s) & = rFK_l I_{ha} + (1-r)FK_l I_{pv} - FC_s - \frac{V_m}{K_m + C_s} C_s + K_{sh} C_h \\ \frac{d}{dt}(V_h C_h) & = \frac{V_m}{K_m + C_s} C_s - K_{sh} C_h \\ C_L & = \frac{C_s V_s + C_h V_h}{V_s + V_h} \end{cases} \tag{12.3}$$

Where I_{ha} and I_{pv} are hepatic artery and portal vein fluorescence measurements respectively. F is the total inflow and r is the ratio of hepatic artery flow over total inflow. C_i and V_i are the ICG concentration and volume compartment respectively for the ith compartment ($i = s, h, L$).
The animal liver volume was estimated with the CT-scan. For patients, a liver graft volume estimation is available. Here contrary to the previous chapters 10 and 11, the bile canaliculi volume is neglected. The sinusoids compartment volume is assumed equal to 20% of the liver volume and the hepatocytes compartment accounts for the rest. The parameters to estimate from the liver ICG measurements are F, r, K_l and K_{sh} for the first model. In the second model α has also to be estimated and in the third model V_m and K_m estimations are also required (Figure 12.1).

12.1.3 Parameter identifiable and estimation

Parameter identifiability. For a linear system, the parameter identifiability is assessed for the given measurements with the Laplace transform. This analysis is performed for model 2. The identifiable parameters of model 1 are then deduced taking $\alpha = 1$ in model 2. Model 3 equations are non-linear, which precludes such analysis.
The notation is simplified for the analysis: y_1 is the amount of product in the sinusoids, y_2 is

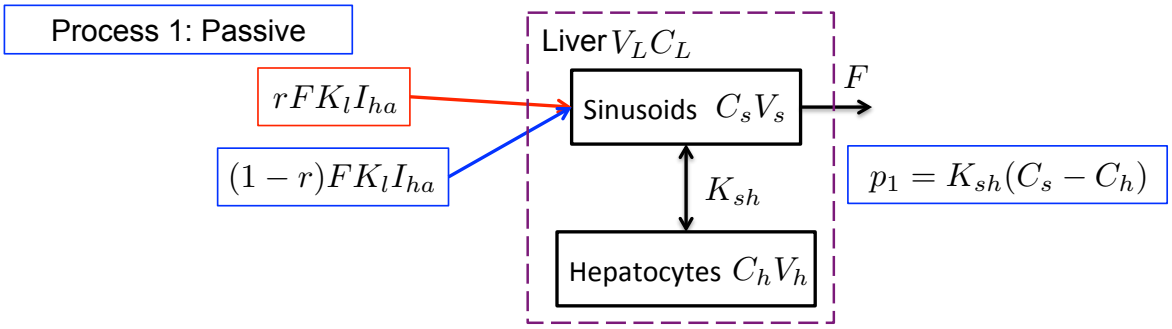

(a) Sinusoids - Hepatocytes: passive exchange

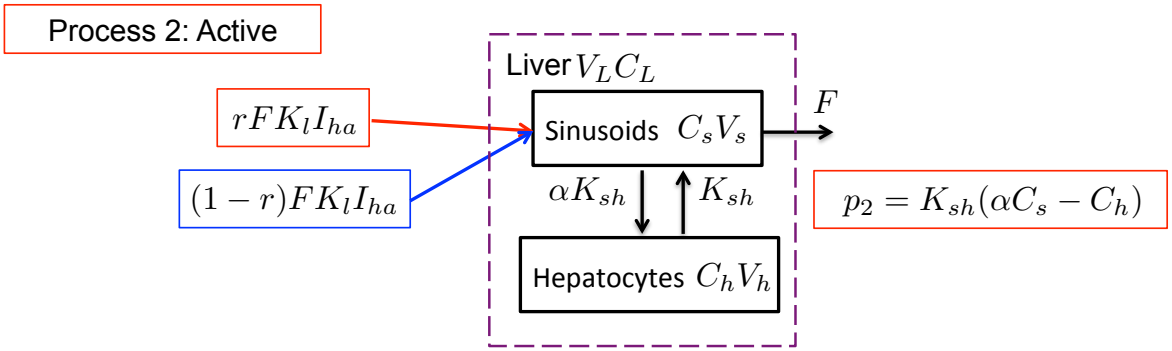

(b) Sinusoids - Hepatocytes: active exchange

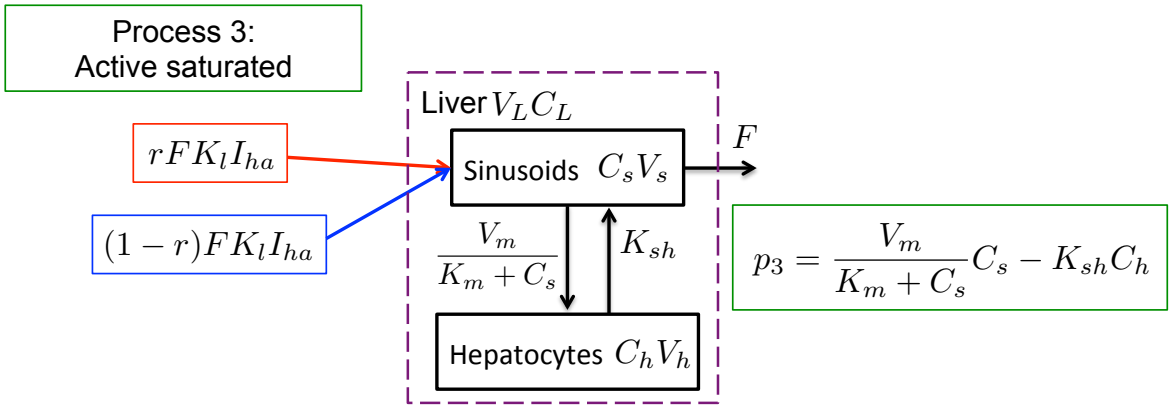

(c) Sinusoids - Hepatocytes: active with possible saturation exchange

Figure 12.1: Schematic representation of mathematical model of liver ICG processing (for 2 minutes following injection). Three processes are considered to represent the exchange between sinusoids and hepatocytes. I_{ha} and I_{pv} are hepatic artery and portal vein fluorescence measurements respectively. The liver compartment ICG concentration is the observation (purple dash lines).

the amount of product in the hepatocytes and z is the observation, i.e. the concentration of compound in the liver. The model equations read:

$$\begin{array}{ll} \dot{y_1} & = FK_l r I_{ha} + FK_l(1-r)I_{pv} - (F/V_s + \alpha K_{sh}/V_s)y_1 + (K_{sh}/V_h)y_2 \\ \dot{y_2} & = \alpha(K_{sh}/V_s)y_1 - (K_{sh}/V_h)y_2 \\ z & = (y_1 + y_2)/(V_s + V_h) \end{array} \tag{12.4}$$

Since the system is linear it can be written as follow:

$$\begin{array}{ll} \dot{Y} & = AY + BIn \\ z & = CY + DIn \end{array} \tag{12.5}$$

With $Y = \begin{bmatrix} y_1 \\ y_2 \end{bmatrix}$ the unknowns of the model and $In = \begin{bmatrix} I_{ha} \\ I_{pv} \end{bmatrix}$ are the input. The matrices are:

$$A = \begin{bmatrix} -(F/V_s + \alpha K_{sh}/V_s) & K_{sh}/V_h \\ \alpha K_{sh}/V_s & -K_{sh}/V_h \end{bmatrix}$$

$$B = \begin{bmatrix} FK_l r & FK_l(1-r) \\ 0 & 0 \end{bmatrix} \quad ; \quad C = 1/(V_s + V_h)[1 \quad 1], \quad D = 0$$

Applying the Laplace transform ($\mathcal{L}$), the system becomes:

$$\begin{array}{ll} s\mathcal{L}(Y) & = A\mathcal{L}(Y) + B\mathcal{L}(In) \\ \mathcal{L}(z) & = C\mathcal{L}(Y) \end{array} \tag{12.6}$$

As a result:

$$(sI_2 - A)\mathcal{L}(Y) = B\mathcal{L}(In) \Rightarrow \mathcal{L}(Y) = (sI_2 - A)^{-1}B\mathcal{L}(In) \Rightarrow \mathcal{L}(z) = C(sI_2 - A)^{-1}B\mathcal{L}(In) \tag{12.7}$$

Defining H by $H(s,\theta) = C(sI_2 - A)^{-1}B$ with θ the model parameters (to be estimated, here K_l, K_{sh}, α, r and F). The parameters are identifiable if

$$H(s,\theta) = H(s,\theta^*) \Rightarrow \theta = \theta^*.$$

With $Dd = s^2 + (F/V_s + K_{sh}(1/V_h + \alpha/V_s))\, s + FK_{sh}/(V_h V_s)$, H is actually given by:

$$H(s,\theta) = \frac{1}{Dd(V_s + V_h)}[FK_l r(s + K_{sh}(1/V_h + \alpha/V_s)) \quad FK_l(1-r)(s + K_{sh}(1/V_h + \alpha/V_s))] \tag{12.8}$$

Naming H components by:

$$h_1(s,\theta) = FK_l r(s + K_{sh}(1/V_h + \alpha/V_s))/(Dd(V_s + V_h))$$

$$h_2(s,\theta) = FK_l(1-r)(s + K_{sh}(1/V_h + \alpha/V_s))/(Dd(V_s + V_h))$$

and writing h_1 and h_2 as rational fractions, one obtains:

$$h_1(s,\theta) = \alpha_1 s + \alpha_2/(\beta_1(s^2 + \beta_2 s + \beta_3))$$

with $\alpha_1 = FK_l r$, $\alpha_2 = \alpha_1 K_{sh}(1/V_h + \alpha/V_s)$, $\beta_1 = (V_s + V_h)$, $\beta_2 = (F/V_s + K_{sh}(1/V_h + \alpha/V_s)$, $\beta_3 = FK_{sh}/(V_h V_s)$. And,

$$h_2(s,\theta) = \gamma_1 s + \gamma_2/(\beta_1(s^2 + \beta_2 s + \beta_3))$$

with $\gamma_1 = FK_l(1-r)$, $\gamma_2 = \gamma_1 K_{sh}(1/V_h + \alpha/V_s)$. Solving $H(s,\theta) = H(s,\theta^*)$ leads to two equations $h_1(s,\theta) = h_1(s,\theta^*)$ and $h_2(s,\theta) = h_2(s,\theta^*)$. From the first equation, the following system is obtained:

$$h_1(s,\theta) = h_1(s,\theta^*) \Rightarrow \alpha_1 s + \alpha_2/(\beta_1(s^2 + \beta_2 s + \beta_3)) = \alpha_1^* s + \alpha_2^*/(\beta_1^*(s^2 + \beta_2^* s + \beta_3^*))$$

$\beta_1 = (V_s + V_h) = \beta_1^*$ because the volumes are fixed parameters. Thus,

$$\begin{aligned}
&\alpha_1 s + \alpha_2/(s^2 + \beta_2 s + \beta_3) = \alpha_1^* s + \alpha_2^*/(s^2 + \beta_2^* s + \beta_3^*) \\
&\Rightarrow (\alpha_1 s + \alpha_2)(s^2 + \beta_2^* s + \beta_3^*) = (\alpha_1^* s + \alpha_2^*)(s^2 + \beta_2 s + \beta_3) \\
&\Rightarrow \alpha_1 s^3 + (\alpha_2 + \alpha_1\beta_2^*)s^2 + (\alpha_1\beta_3^* + \alpha_2\beta_2^*)s + \alpha_2\beta_3^* = \alpha_1^* s^3 + (\alpha_2^* + \alpha_1^*\beta_2)s^2 + (\alpha_1^*\beta_3 + \alpha_2^*\beta_2)s + \alpha_2^*\beta_3
\end{aligned} \tag{12.9}$$

The polynomials are equal, therefore:

$$\begin{cases}
\alpha_1 = \alpha_1^* \\
\alpha_2 + \alpha_1\beta_2^* = \alpha_2^* + \alpha_1^*\beta_2 \\
\alpha_1\beta_3^* + \alpha_2\beta_2^* = \alpha_1^*\beta_3 + \alpha_2^*\beta_2 \\
\alpha_2\beta_3^* = \alpha_2^*\beta_3
\end{cases} \tag{12.10}$$

The first relation gives the following relation for parameters:

$$\alpha_1 = \alpha_1^* \Rightarrow FK_l r = F^* K_l^* r^* \tag{12.11}$$

Now, using eq. (12.11) and assuming parameter values are non-zero:

$$\begin{aligned}
&\alpha_2 + \alpha_1\beta_2^* = \alpha_2^* + \alpha_1^*\beta_2 \\
&\Rightarrow F^*/V_s = F/V_s
\end{aligned} \tag{12.12}$$

Thus $F = F^*$ and F parameter is identifiable. From eq. (12.11) one obtains: $K_l r = K_l^* r^*$.

Next, the third line of the system (12.10) is used:

$$\begin{aligned}
&\alpha_1\beta_3^* + \alpha_2\beta_2^* = \alpha_1^*\beta_3 + \alpha_2^*\beta_2 \\
&\Rightarrow \\
&\alpha_1 F^* K_{sh}^*/(V_h V_s) + \alpha_1 K_{sh}(1/V_h + \alpha/V_s)(F^*/V_s + K_{sh}^*(1/V_h + \alpha^*/V_s)) \\
&= \alpha_1^* F K_{sh}/(V_h V_s) + \alpha_1^* K_{sh}^*(1/V_h + \alpha^*/V_s)(F/V_s + K_{sh}(1/V_h + \alpha/V_s)) \\
&\\
&(F^* = F \text{ and } \alpha_1 = \alpha_1^*) \Rightarrow \\
&F K_{sh}^*/(V_h V_s) - F K_{sh}/(V_h V_s) + K_{sh} F(1/V_h + \alpha/V_s)/V_s - F K_{sh}^*(1/V_h + \alpha^*/V_s)/V_s \\
&= K_{sh}^*(1/V_h + \alpha^*/V_s) K_{sh}(1/V_h + \alpha/V_s) - K_{sh}(1/V_h + \alpha/V_s) K_{sh}^*(1/V_h + \alpha^*/V_s) \\
&\\
&\Rightarrow K_{sh}\alpha = K_{sh}^*\alpha^*
\end{aligned} \tag{12.13}$$

Now, using relation (12.11) and $F = F^*$, and assuming parameter values are non-zero, the fourth line of system (12.10) reads:

$$\begin{aligned}
&\alpha_2\beta_3^* = \alpha_2^*\beta_3 \\
\Rightarrow\ &\alpha_1 K_{sh}(1/V_h + \alpha/V_s) F^* K_{sh}^*/(V_h V_s) = \alpha_1^* K_{sh}^*(1/V_h + \alpha^*/V_s) F K_{sh}/(V_h V_s) \\
&\Rightarrow \alpha = \alpha^*
\end{aligned} \tag{12.14}$$

Because $K_{sh}\alpha = K_{sh}^*\alpha^*$ and $\alpha = \alpha^*$, $K_{sh} = K_{sh}^*$. Therefore K_{sh} is identifiable as well as α. Next, considering the second equation:

$$h_2(s,\theta) = h_2(s,\theta^*)$$

$$\Rightarrow \gamma_1 s^3 + (\gamma_2 + \gamma_1\beta_2^*)s^2 + (\gamma_1\beta_3^* + \gamma_2\beta_2^*)s + \gamma_2\beta_3^* = \gamma_1^* s^3 + (\gamma_2^* + \gamma_1^*\beta_2)s^2 + (\gamma_1^*\beta_3 + \gamma_2^*\beta_2)s + \gamma_2^*\beta_3$$

Thus $\gamma_1 = \gamma_1^* \Rightarrow F K_l(1-r) = F^* K_l^*(1-r^*)$. With relation (12.11) and $F = F^*$, one obtains $K_l = K_l^*$ and then $r = r^*$. Finally, all parameters are identifiable, assuming parameters are not null. Therefore $\alpha_i = \alpha_i^*$, $\beta_i = \beta_i^*$, $\gamma_i = \gamma_i^*$ with $i = 1,2,3$ and

$$H(s,\theta) = H(s,\theta^*) \Rightarrow \theta = \theta^*$$

To conclude, with the liver compartment concentration as observation, the parameters F, r, K_l and K_{sh}, as well as α for the second model are identifiable. This analysis is performed assuming the observations are model outputs and that it is noise free.

Parameter estimation. Model 1 and 2 parameters are identifiable with the ICG concentration in the liver tissue. For model 3, the parameter estimation is first performed on synthetic noisy data to assess the parameter identifiability. Then, the parameters are estimated. For the animal measurement, like in chapter 11, three groups are studied: control (before liver resection), after 75% liver ablation and after 90% liver ablation. The parameters are estimated for the three models. For each animal, the liver inflow estimation is compared to the measurements. A relative error average and standard deviation are then calculated. Since in chapter 11 the three models gave similar results, here the model that gives the best

Average relative error	Model 1	Model 2	Model 3
F error	3.26 (7.62)	10648 (35487) / 2.44(5.74)	0.81 (1.35)
r error	0.56 (0.33)	0.5 (0.36)	0.55(0.33)

Table 12.1: Relative error of flow F and ratio $r = F_{ha}/F$ estimation average and standard deviation over all animals (error $= |X_e - X_m|/X_m$ with X being the flow F or the ratio r; e and m stand for estimation and measurements). In model 2, one animal flow estimation is very high, therefore the error average is computed with and without this animal.

flow estimation is kept. The patient parameters are finally estimated with this model. All parameter estimations in this chapter have been performed with Monolix, as in the previous chapter.

12.2 Results

12.2.1 Parameter estimation with pig ICG measurements and model comparison

Liver inflow estimation and comparison between models. Parameter estimation is first performed, on synthetic noisy data for model 3. With the estimated parameters the synthetic curves are matched. The parameters F and r are well estimated, as well as K_l. The parameters K_{sh}, K_m and V_m are not always correctly estimated. Moreover, more than one set of parameters may fit the noisy observations curve. Therefore, in model 3 the estimated parameters may not be unique. Model 3 parameters estimation is however performed with the measurements.
The individual parameters of each model are estimated, and the direct model is run with them. Figures 12.2, 12.3 and 12.4 show the model results and the measurements. No major differences are observed between the models.

Therefore, the flow F and the ratio r estimations are compared to the measurements for each pig in order to select the model that gives the best flow estimation. The relative error average and standard deviation are summarized in Table 12.1. For one animal the flow estimated value in model 2 is very high. Therefore, in that case, the average and standard deviation are computed with and without this animal parameter. Model 3 gives the best estimation for the flow F (smaller error average and std). However the average error remains high. The error for the ratio estimation is similar for all the models. Model 3 has the highest number of parameters, however because it gives the best estimation for the flow, this model is kept. This improved estimation of the flow may indicate that the exchange between sinusoids and hepatocytes modeled by process 3 is more realistic than the exchange modeled by two other studied processes (Figure 12.1).

Populations parameter estimation. Model 3 parameters are estimated for each population, and the ratio of each group parameters over the control group parameters are presented in Table 12.2. And like in chapter 11 the parameters V_m and V_m/K_m are presented due to the likely correlation between this two parameters. As in the previous chapter, the differences

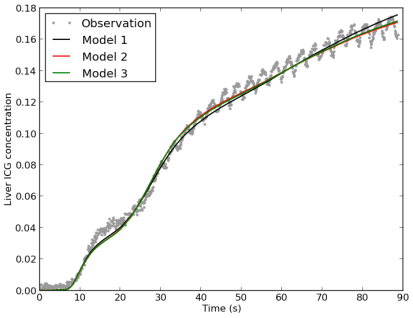

(a) iF8

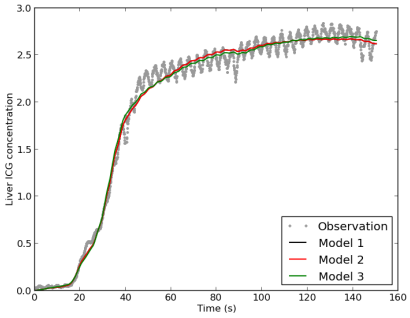

(b) iF9

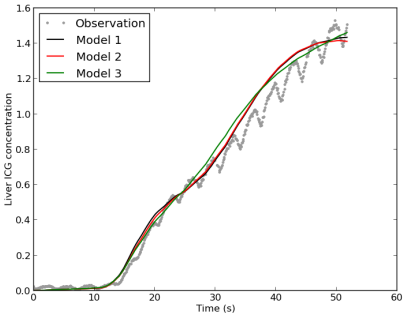

(c) iF13

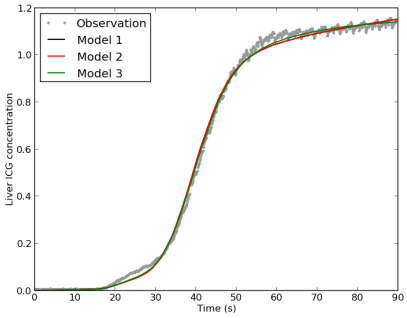

(d) iF14

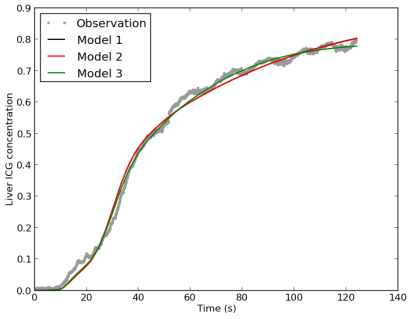

(e) iF1A

Figure 12.2: The three models and measurements liver ICG concentration over time, the parameters are set to individual estimates. The five animals are in the control group.

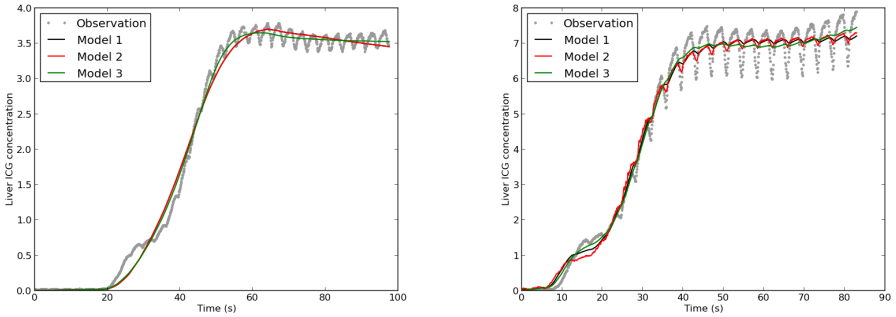

(a) iF16 (b) iFC6

Figure 12.3: The three models and measurements liver ICG concentration over time, the parameters are set to individual estimates. The two animals are in the 75% liver ablation group.

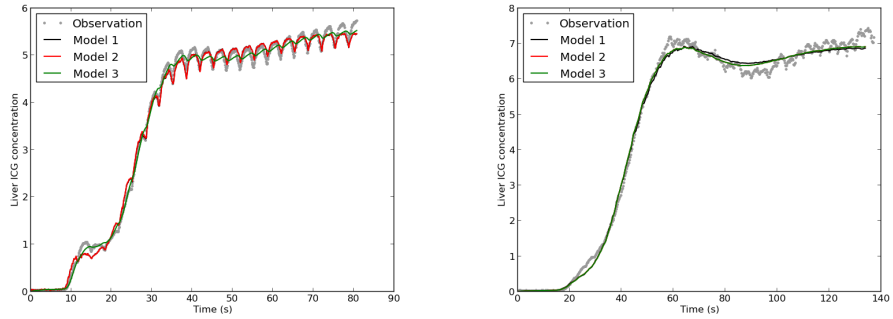

(a) iF1B (b) iF2B

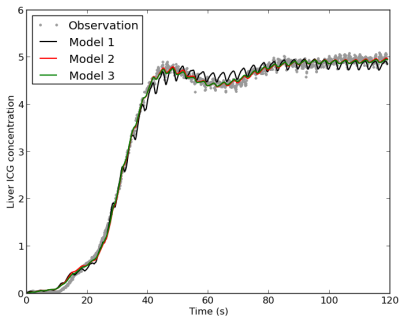

(c) iF3B

Figure 12.4: The three models and measurements liver ICG concentration over time, the parameters are set to individual estimates. The three animals are in the 90% liver ablation group.

Pop parameter	75%	90%
V_m	2.1	0.4
V_m/K_m	0.83	0.005
K_{sh}	0.14	0.06
F	0.6	0.48
r	0.26	0.7

Table 12.2: Population parameters over control population parameters for each group estimated by Monolix with the third model (Eq. 12.3).

between group parameters are difficult to analyze due to the small amount of animals per group. However the trends are the same. In comparison to the control group, V_m parameter increases in the 75% liver ablation group and it is decreased in the 90% liver ablation group. The ratio V_m/K_m is decreased after liver ablation, and the decrease is larger for a larger liver resection. K_{sh} parameter is decreased after liver resection. Therefore the exchange between sinusoids and hepatocytes seems impacted by the liver resection. The differences between groups obtained with this inverse problem are similar to the one obtained in chapter 11 (with the longer observations curve), specially for V_m.
The liver flow is decreased after partial hepatectomy, the estimated decrease after 75% liver ablation is 37.5% and 51.9 % after 90% liver ablation. The hemodynamics measurements recorded during the liver surgery on pigs (see Part I), enable to compute the liver inflow reduction after partial ablation in average (over all animals). A reduction of 24% after 75% liver ablation is observed and a decrease of 42% after 90% liver ablation is measured. In the measurement the ratio r is decreased after liver resection, in average before resection $r = 0.19$, after 75% liver ablation $r = 0.06$ and after 90% liver ablation $r = 0.09$. The estimated ratio with the ICG measurement follow the same behavior.

More measurements would be needed to conclude on the parameter estimation. However, the experimental measurements are explained with the proposed model. According to this framework, the hepatic uptake, which is part of the liver function, is impacted by the liver resection. The flow estimation, with ICG measurements, is a coarse approximation. However the flow decrease after liver resection is well captured.

12.2.2 Parameter estimation patient ICG measurements

The third model is used to explain the ICG concentration curve measured after liver transplantation on four patients. The model parameters are estimated, and the direct model is solved with the parameter estimates. Figure 12.5 displays the results. The observations curves are well matched with the model for all the patients. The model parameter estimates are presented in Table 12.3. The first patient is the only one with an initial poor graft function (meaning on the first post-operative day the blood analysis has shown that the graft function was poor). According to the model, compared with the other patients, this patient has a high exchange coefficient from hepatocytes to sinusoids and a very low ratio of hepatic artery flow over total inflow.
The proposed model is able to explain the measurements and with more data the framework

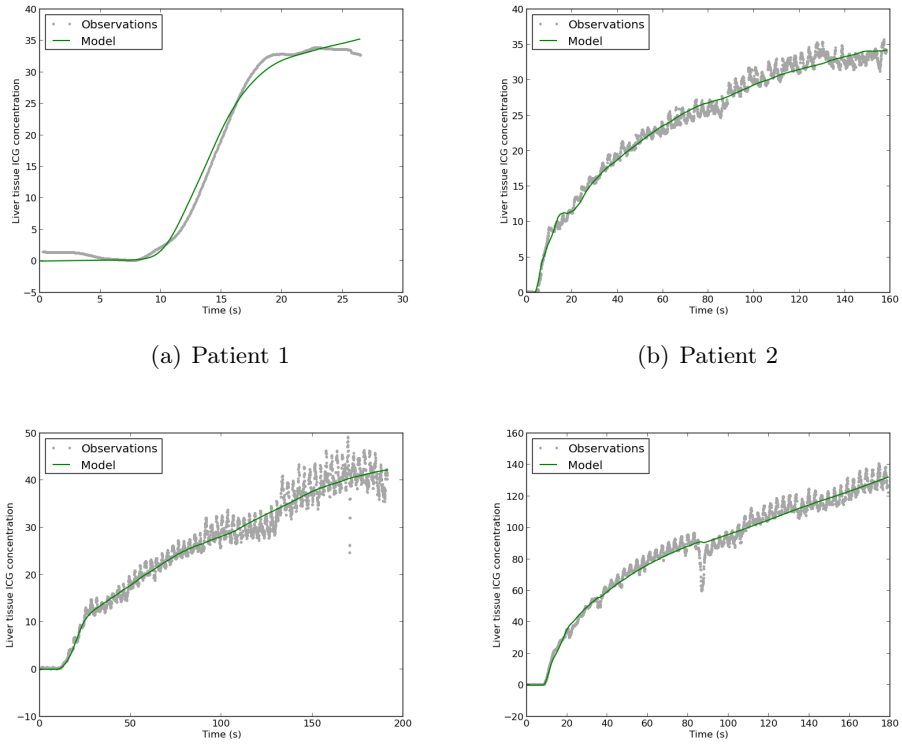

(a) Patient 1

(b) Patient 2

(c) Patient 3

(d) Patient 4

Figure 12.5: The models and measurements liver ICG concentration over time, the parameters are set to Monolix individual estimates.

described here can be used to link model parameters with the initial graft function.

12.3 Conclusions

In clinical application less measurements are available for parameter estimation and model testing than during animal experiments. For ICG measurements the recording time is reduced, and the flows are not measured. Several pharmacokinetics models are first tested with ICG measurements of pigs (taken in the same conditions as in the clinical peri-operative context). Three different processes are considered to model the exchange of ICG between sinusoids and hepatocytes. The three models are able to explain the measurements. However the best liver inflow estimation is obtained with the third process (active process with possible saturation between sinusoids and hepatocytes). This result may indicate that this process is more realistic than the two other processes studied.
The small amount of data makes it difficult to conclude on the link of the model parameters to the liver function. However, the first results show that the exchange between sinusoids and hepatocytes is impacted after liver resection, and that this can be detected with only 2-3 minutes of dynamic recording. Moreover as in the experiments, after liver resection the

Patient	K_l	V_m	K_m	K_{sh}	F	r
1	3.98	23409.01	0.035	796.59	25.80	0.0009
2	4.61	1212.11	0.016	30.86	44.65	0.2643
3	14.68	624.79	0.10	10.12	10.87	0.1541
4	9.52	1095.61	0.024	2.51	12.01	0.4899

Table 12.3: Model 3. parameter estimated with Monolix, using ICG concentration measured after liver transplantation.

estimated flow is reduced as well as the ratio of hepatic artery flow over liver inflow. Similarly the patient with poor initial graft function has an (estimated) reduced hepatic flow ratio. However, the length of time for this patient measurements is significantly smaller than the other patient measurements and this could impact the parameter estimation.
This work proposes a method to estimate liver perfusion and function quantitatively with ICG measurements. More measurements are required to confirm the first observations presented here.

Chapter 13

Conclusions and perspectives

The transport of a compound (indocyanine green) has been modeled in large arteries as well as through organs vascular trees. In this work, constant blood velocity was imposed, because non-physiological oscillations has appeared with time-varying velocity. In future work, more investigations on 1D model for transport with time-varying velocity is required to understand why these oscillations appears. One idea is to compare 3D model transport simulation results averaged on the vessel section with the 1D model simulation results. Moreover in this work, the transport through vascular tree of organs is modeled with simple series of two mixing compartments. In future, modeling investigations to obtain a mean transit time through organs that depends dynamically on the organ inflow, as well as on the organ size would increase the model realism. Ideally patient specific model (based on patient weight, size...) for transport through organs would improve the CT angiography acquisition with contrast techniques (arterial time and portal vein time acquisition). The impact of hepatic vein blockage and partial hepatectomy on the concentration in liver vessels has been studied. Improving the transport in vascular trees would also give more precise information on the impact of hemodynamics changes on the transport in blood of a compound (ICG, contrast agent, drug ...).

Next the ICG processing by the liver has been modeled. For the first time, the ICG fluorescence is measured simultaneously in the hepatic artery, the portal vein, the liver tissue and the common bile duct. A mathematical model including three compartments (sinusoids, hepatocytes and bile canaliculi) for the liver has been developed. The three compartments are required to match the ICG fluorescence measurements. Since the exchange processes between the different liver tissues are not precisely known, different processes are studied. The proposed model has been in agreement with measurements from literature on rabbits as well as with the measurements recorded on pigs. Patient ICG measurements has also been matched with a simplified model responding to the clinical requirements. The link between model parameters and liver function is explored, however more data are required to confirm the first results presented here. Longer measurements with a decrease in the ICG concentration of the liver tissue may give more information on the excretion function of the liver.

This work has proposed various investigations on ICG transport and processing. In the future, coupling the transport model of ICG in blood with the model of ICG processing may lead to new knowledge on the impact of hemodynamics changes on the ICG clearance or ICG concentration in the liver tissue. This may provide better understanding of ICG processing by the liver and may lead to a novel estimation of the liver function(s) peri-operatively, using ICG measurements.

Chapter 14

Thesis conclusions and perspectives

This thesis proposed mathematical modeling and numerical simulations of hemodynamics during liver surgery. Liver function was also investigated with pharmacokinetics models.
The measurements of hemodynamics during liver surgery on pigs enabled to build and validate the presented mathematical models. Our participation to the recording of measurements during pig surgeries was possible due to our collaboration with surgeons. Moreover, the discussions with surgeons were instrumental to adapt the experimental conditions of the recordings to the analysis requirements (stable signal with no intervention of the surgeons).
The two goals of this thesis were to better understand the liver hemodynamics during liver surgery and to explore the liver function quantification based on indocyanine green fluorescence measurements.
These two topics aim at improving the efficacy of the vascular ring MID-AVR^{TM}. Knowing the hemodynamics evolution during liver surgery enables to know how to modulate these hemodynamics with the ring. Moreover, the ring efficacy could be controlled based indocyanine green fluorescence measurements to quantify and thus evaluate the liver function intra-operatively. This thesis can be seen as a first step to reach the final goals.
Each part of this thesis was ended with a specific conclusion, therefore, here we establish a global conclusion and an outlook.

14.1 Liver hemodynamics

14.1.1 0D closed-loop model

The 0D closed-loop model was simple and numerically fast to solve. Since the model was closed-loop, the impact of blood losses was explored. Combining the analysis of the hemodynamics measurements and the numerical simulation results, the portal vein flow, after 75% liver resection, seemed to decrease due to the blood volume decrease (bleeding, body fluid evaporation and the removal of the blood contained in the liver part removed). However the simulations, without blood loss, showed that 75% liver resection accounted for a decrease of portal flow of around 5%.
Since the portal vein flow decrease seemed mainly due to the blood loss, it provided a possible explanation for the fact that no difference of portal flow reduction was observed between the liver resection with and without the vascular ring. Based on the measurements, the ring seemed to limit the increase of portal pressure during liver surgery. Then, during the first post-operative days (when blood volume increased back to baseline) the ring limited the portal vein flow and may have protected the liver during the early regeneration phase. Since the endothelial cells proliferation to restore the sinusoids network starts only after three days [Mic07], the ring may protect the liver and improve the regeneration. However, only one measurement of portal flow on third post-operative day was available in the ring group.

More data are required to confirm this finding and to integrate the vascular ring into the model.

14.1.2 Hepatic artery flow and pressure waveform

A robust scheme able to deal with arterial and venous tube laws has been investigated and implemented. The scheme was able to handle relatively small cross-section area, which was important for collapsible tubes. However, the collapsible tube law proposed in literature is not defined when the cross-section area tends to zero. In the future, further modeling is required to propose a modified pressure-area relationship that allows zero cross-section area. The developed 1D-0D model qualitatively reproduced the typical change of hepatic artery pressure and flow waveform after 75% liver resection. The limitation of this model was the large number of parameters. Specially, the parameter of arteries stiffness was difficult to estimate, even more for pigs (as few articles exist for pigs). Moreover, this parameter was important in our case, as the pressure and flow waveform are very sensitive to arterial stiffness. Simulating two different ways to remove the liver (removal of two liver lobes or of small piece in each lobe), we found that the typical change of waveform seemed linked to the architecture of the hepatic artery vascular tree. Therefore, during liver regeneration the hepatic artery flow waveform may inform on the architecture of the vascular tree regeneration. More measurements are required to confirm this assumption. Moreover the waveform should be correlated to the hepatic artery vascular tree during the regeneration process (using CT-scan to assess the hepatic artery tree).

14.1.3 What is next

Modeling the liver hemodynamics during liver regeneration is the natural future work of this thesis. Moreover adding a model of the vascular ring MID-AVR^{TM}, would enable to perform numerical simulation with and without the ring of the liver resection and regeneration.

A second important development is the clinical application of these models. A human model of the liver vascular tree should be developed. Besides, the patients undergoing surgery have diseased livers. Therefore including pathologies (fibrosis, cirrhosis) in the model is warranted.

Since the liver receives 25% of the cardiac output, it is important to consider the liver and the whole circulation in the models. Using CT-scan, the collateral circulation could be assessed and included in the model. In this work, a large number of pressure and flow were measured, that has enabled to estimate the models parameters. In clinical applications, less pressure and flow measurements would be available, however CT-scan are always done before liver surgery. The mathematical model should be built to take advantage of the available measurements.

14.2 Liver function

14.2.1 Transport of a compound in blood

The 1D model for hemodynamics was used to model transport of a compound in the main arteries. The transport of compound in blood has many applications in medicine (drug

targeting, CT-scan with contrast, ...) and the 1D model is a simple model to represent this transport. However, when blood velocity is time varying, it seems the one dimensional model does not take into account the mixing phenomenon happening in the vessel section (since the equation unknown is the concentration averaged over the vessel section area). To confirm this assumption, the differences between 3D model of transport simulation results averaged over the section area and the 1D model simulation results should be analyzed.
In this thesis, the transport in vascular trees of organs was modeled with a series of two mixing compartments. The transport through vascular trees requires more investigation to obtain more realistic models. With such transport model, the hemodynamics impact on the transport of a compound may be assessed, for several medical applications (indocyanine green clearance, drug targeting, CT-scan).

14.2.2 Indocyanine green processing by the liver

In this thesis, mathematical models for indocyanine green processing by the liver were built. These models were based on the measurements of indocyanine green fluorescence in the hepatic artery, the portal vein, the liver tissue and the common bile duct. Different processes for the exchange of indocyanine green between liver tissues were modeled and compared. Moreover, the link between fluorescence measurements and liver function was explored. The limitation for this work was the small amount of measurements.
Besides, this work was based on the assumption that indocyanine green concentration is linearly linked to the measured intensity. The link between concentration and intensity requires further analysis. To improve knowledge on that link a new experimental setup should be built.
Moreover, the fact that two injections of indocyanine green cannot be analyzed similarly was a major drawback. Indeed, after the first injection, the liver tissue is already fluorescent and the analysis of the second injection cannot be done similarly to the first one. Therefore, using indocyanine green intra-operatively is challenging. Indeed, if a first injection reveals a poor liver function, surgeons will act to improve it. The analysis of a second injection, to evaluate the new liver function, is then difficult because of this remaining fluorescence effect. Despite these limitations, pursuing researches to quantitatively estimate the liver function with indocyanine green measurements seems encouraging. To confirm the first findings of this thesis more data are required.

14.2.3 What is next

The investigation of the indocyanine green during liver regeneration is the next step of this work. Moreover, coupling the transport of a compound in the blood with the model of the compound processing by the liver seems natural. The coupling of both models may give more knowledge on the link between hemodynamics and liver function.

Appendix A

Unscented Kalman Filter

A.1 Parameter estimation: inverse problem

Parameter estimation problems can be defined as follows. With time as t, let $\mathbf{X}(t) \in \mathbb{R}^N$ be the state and $\mathbf{P} \in \mathbb{R}^p$ the model parameters, with $N, p \in \mathbb{N}$. The state is solution of $\dot{\mathbf{X}} = A(\mathbf{X}, \mathbf{P}), \quad \mathbf{X}(0) = \mathbf{X}_0$, where A is defined by the model equations and $\mathbf{X}_0$ is state initial condition at time $t = 0$. Let the observations operator be defined by $\mathcal{H}$, and let $\mathcal{Z}$ be the experimental measurements (observations), that are assumed to verify $\mathcal{Z}(t) = \mathcal{H}(\mathbf{X}(t)) + \xi$, where ξ refers to noise.

The inverse problem, consists in the minimization of a cost function, such as :

$$J(\mathbf{X}_0, \mathbf{P}) = \int_0^T \|\mathbf{Z} - H(\mathbf{X})\|^2_{W^{-1}} dt + \|\mathbf{P} - \hat{\mathbf{P}}_0\|^2_{P_{P_0}^{-1}} + \|\mathbf{X}_0 - \hat{\mathbf{X}}_0\|^2_{P_{X_0}^{-1}}, \tag{A.1}$$

where, $\hat{\mathbf{P}}_0$ and $\hat{\mathbf{X}}_0$ are given initial guesses for parameters and state. $\mathbf{X}$ is a solution of the model, $\mathbf{X}_0$ being the initial state and $\mathbf{P}$ the parameters. The discrete observations are $\mathbf{Z}_n = H_n(X_n) + \xi_n$, where ξ_n represents measurements noise and error due to discretization. $\mathbf{X}_n$ and $\mathbf{H}_n$ respectively denote for the approximation of $\mathbf{X}(n\Delta t)$ and $\mathcal{H}(\mathbf{X}(n\Delta t))$, where $n \in \mathbb{N}$ is the time iteration. Furthermore $\mathbf{X}_n$ and $\mathbf{H}_n$ are assumed available at each time step. The norms $\|.\|_{W^{-1}}, \quad \|.\|_{P_{P_0}^{-1}}$ and $\|.\|_{P_{X_0}^{-1}}$ are used to measure observations, parameters and state respectively. Different confidence in the observations and in the initial guesses are taken into account with weight, included into the norms. The confidence can be seen, from a statistical point of view, as the inverse of covariance matrices (W, P_{P_0} and P_{X_0}). For example, the norm $\|.\|_{C^{-1}}$ could be defined by $\|\mathbf{X}\|^2_{C^{-1}} = 0.5\mathbf{X}^T C^{-1}\mathbf{X}$, where the confidence matrix C^{-1} is associated to a guess state $\mathbf{X}$, and weighted by 0.5.

Different methods exist to minimize the cost function defined by equation (A.1). In this work, the sequential approach, based on Kalman filter [Kal60], is used. This approach consists in modifying the forward problem with a correction term that takes into account the actual difference between measurements and model outputs. The main benefit of this method is that, no tangent operator computation is required, which reduces the computational cost for non-linear operator.

A.2 Unscented Kalman Filter

Kalman filter initially is a state estimator for linear dynamic systems. For non-linear systems various modification of the Kalman filter have been proposed, e.g. the extended Kalman filter and the unscented Kalman filter [H+01, Sim10]. The Unscented Kalman Filter (UKF) algorithm [JUDW95, JUDW00] have been used for state and parameter estimation for different dimensional systems. A reduced order filtering, based on UKF, for the estimation of

parameters has been proposed in [MC11]. Parameter estimation for fluid-structure interaction problem using reduced-order UKF has been developed in [BMG12]. The unscented kalman filter has been used for patient specific lumped parameter estimation in [PFGVC14].

As UKF algorithm is designed for state estimation, it can be used to estimate parameters, by modifying the state. The parameters are added to the previous problem state, assuming they are constant in time or have a known dynamics. The initial problem reads: $\mathbf{x}_{n+1} = F(\mathbf{x}_n, \mathbf{P})$, where $\mathbf{x}_n$ and $\mathbf{x}_{n+1}$ are state vectors at time $t_n = n\Delta t$, t_{n+1}, where Δt is the time step. $\mathbf{P}$ are the parameters and F is the forward dynamic system of equations. The system of equations for the augmented state $\mathbf{x}^a$ is:

$$\mathbf{x}^a_{n+1} = \begin{bmatrix} \mathbf{x}_{n+1} \\ \mathbf{P}_{n+1} \end{bmatrix} = \begin{bmatrix} F(\mathbf{x}_n,\mathbf{P}) \\ \mathbf{P}_n \end{bmatrix}$$

UKF algorithm applied to the augmented problem gives an estimate of the parameters vector $\mathbf{P}$, using all the observations.

In order to ensure parameter and state positivity, when necessary, the augmented state can be re-scaled, defined by : $\theta = \log_2(x^a)$. The state and parameter estimates are based on prior confidence. Prior confidence is given by two covariance matrices; the initial covariance matrix of the augmented state vector and observations error matrix, which represents the confidence in the measurements.

Usually the two confidence matrices are assumed to be scaled identity matrices, with σ^2_{obs} scaling factor for the measurements confidence and σ^2_{init} for the initial augmented state confidence. The scaling are for the new parametrization (for the re-scale parameter and state variables).

More details on the unscented Kalman filter algorithm are given in [PFGVC14, BMG12, MC11, JUDW95].

Appendix B

Sensitivity Analysis

The sensitivity analysis aims at qualifying the sensitivity of the model outputs (observations) to the model parameters. This tool is used to identify parameters which are likely to be estimated from the observations available. Two sensitivity tools are used: traditional sensitivity and generalized sensitivity functions [TC99, MXPW11].

B.1 Traditional sensitivity

Traditional sensitivity quantifies the change in model output when a small perturbation in model parameter occurs. A low traditional sensitivity function value, in a time interval, means that the state value is insensitive to the parameter considered in this particular time interval [BBD+07]. The traditional sensitivity function are defined as follow [PFGVC14]. Consider the model for the state vector $\mathbf{x}= [x_1, x_2,...,x_L]$:

$$\dot{x_i}(t) = f_i(t, \mathbf{x}, \boldsymbol{\theta}) \quad i = 1,2,...,L \tag{B.1}$$

where $\boldsymbol{\theta} = [\theta_1, \theta_2,...,\theta_P]$ is the model parameters vector and the dynamic model is represented with functions f_i. The observations vector $\boldsymbol{z} = [z_1, ...,z_M]$, can be written as :

$$\boldsymbol{z}(t_n) = \mathbf{h}(t_n, \boldsymbol{\theta}) + \boldsymbol{\varepsilon}(t_n) \quad n = 1,2,..,N \quad \text{with } \mathbf{h}(t,\boldsymbol{\theta}) = H(\mathbf{x}(t,\boldsymbol{\theta})) \tag{B.2}$$

where H is the observations operator, $\mathbf{h}$ represents the noise-free observation vector and the vector $\boldsymbol{\varepsilon}(t_n)$ is the noise on measurements at time t_n. The noise vectors are assumed to be independent for all measurement times. Moreover, all components of the noise vector are assumed independent, with zero mean and variance $\sigma_i^2(t_n)$. Each noise component is associated with the measurement $z_i(t_n)$. The traditional sensitivity function $s_{i,j}(t, \boldsymbol{\theta_0})$ represents the changes of model output when small variations of parameter occur, it is defined by:

$$s_{i,j}(t, \boldsymbol{\theta_0}) = \frac{\partial h_i(t, \boldsymbol{\theta_0})}{\partial \theta_j} \tag{B.3}$$

The sensitivity is computed around a reference parameter vector $\boldsymbol{\theta_0}$. Parameters range of value and units are different, thus to compare the sensitivity between different parameters, relative sensitivity is introduced:

$$s_{i,j}(t, \boldsymbol{\theta_0}) = d_{i,j}\frac{\partial h_i(t, \boldsymbol{\theta_0})}{\partial \theta_j} \tag{B.4}$$

Where $d_{i,j}$ are scaling factors. In this work, the scaling factors are

$$d_{i,j} = \frac{1}{\left(\sum_k \left(\frac{\partial h_i(t_k, \boldsymbol{\theta_0})}{\partial \theta_j}\right)^2\right)^{1/2}} \tag{B.5}$$

with t_k the discrete times.

The traditional sensitivity functions are calculated using IDAS package from SUNDIALS [SPH15].

B.2 Generalized sensitivity

Traditional sensitivity fails to consider parameters correlation, hence generalized sensitivity functions are considered. Generalized sensitivity functions analysis allows to identify important correlation between parameters, and the distribution over time of information on a parameter contained into the observations. Time distribution of information on a parameter informs on the particular times where adding information in observations is likely to improve parameter estimation. Thus, measurements sampling can be adjusted depending on the obtained generalized sensitivity functions.

Generalized sensitivity functions start at value zero and end at one, the increase is not necessary monotonic and oscillations can occur if important correlations between parameters exist. The interval time where the sharpest increase appears in GSF is the time interval where most information on the parameter are contained into the observations [BBD+07]. The generalized sensitivity functions definition are recalled here [TC99, PFGVC14]. Considering the forward and the observation models described by equations (B.1) and (B.2), the generalized sensitivity function for the parameter θ_k is defined by:

$$g_k(t_n) = \sum_{i=1}^{n} \sum_{j=1}^{M} \left(\frac{1}{\sigma_j^2(t_j)} (\mathcal{M}^{-1} \nabla_\theta h_j(t_i, \boldsymbol{\theta_0}))_k (\nabla_\theta h_j(t_i, \boldsymbol{\theta_0}))_k \right) \tag{B.6}$$

The matrix $\mathcal{M}$ denotes the Fisher information matrix, defined as

$$\mathcal{M} = \sum_{i=1}^{N} \sum_{j=1}^{M} \frac{1}{\sigma_j^2(t_j)} \left(\nabla_\theta h_j(t_i, \boldsymbol{\theta_0})\right) \left(\nabla_\theta h_j(t_i, \boldsymbol{\theta_0})\right)^T \tag{B.7}$$

More details about sensitivity analysis can be found in [TC99, MXPW11, BBD+07, PFGVC14].

Appendix C

Kinetic scheme

C.1 Kinetic approach

The kinetic approach consists in obtaining a linear microscopic kinetic equation equivalent to the macroscopic model [Per02]. The macroscopic model considered here is the following:

$$\left\{ \begin{array}{rcl} \partial_t A + \partial_x(Au) & = & 0 \\ \partial_t(Au) + \partial_x(Au^2) + \partial_x \left(\displaystyle\int_{\varepsilon A_0}^{A(x,t)} c^2(a)da \right) & = & 0. \end{array} \right. \tag{C.1}$$

A real function χ defined on $\mathbb{R}$ and compactly supported is introduced. The χ function verifies the following properties:

$$\left\{ \begin{array}{l} \chi(-w) = \chi(w) \geq 0 \\ \displaystyle\int_{\mathbb{R}} \chi(w)dw = \int_{\mathbb{R}} w^2\chi(w)dw = 1 \end{array} \right. \tag{C.2}$$

In this work the function $\chi(w) = \dfrac{1}{2\sqrt{3}}\mathbf{1}_{|w|\leq\sqrt{3}}$ is chosen, but other possibilities exist. A distribution function $M(x,t,\xi)$ of friction particles with microscopic velocity ξ is introduced.

$$M(x,t,\xi) = \frac{A}{\gamma}\chi\left(\frac{\xi - u}{\gamma}\right) \tag{C.3}$$

with $\gamma^2 A = \int_{\varepsilon A_0}^{A(x,t)} c^2(a)da$. The relations between the microscopic density function M and the macroscopic variable solution of (C.1) read:

$$\begin{array}{rl} \displaystyle\int_{\mathbb{R}} M d\xi & = \dfrac{A}{\gamma}\int_{\mathbb{R}} \chi\left(\dfrac{\xi - u}{\gamma}\right) d\xi \\ & = A\displaystyle\int_{\mathbb{R}} \chi(w)dw \\ & = A \end{array} \tag{C.4}$$

with a change of variables $\xi = \gamma w + u$, and using the parity of χ:

$$\begin{array}{rl} \displaystyle\int_{\mathbb{R}} \xi M d\xi & = \dfrac{A}{\gamma}\int_{\mathbb{R}} \xi\chi\left(\dfrac{\xi - u}{\gamma}\right) d\xi \\ & = A\displaystyle\int_{\mathbb{R}} (\gamma w + u)\chi(w)dw \\ & = A\gamma\displaystyle\int_{\mathbb{R}} w\chi(w)dw + Au\int_{\mathbb{R}} \chi(w)dw \\ & = Au \end{array} \tag{C.5}$$

With these relations, the functions (A,u) are solutions of the Euler equations homogeneous system (C.1) if and only if $M(x,t,\xi)$ is solution of the linear kinetic equation [Per02]:

$$\partial_t M + \xi \partial_x M = Q(x,t,\xi) \tag{C.6}$$

where $Q(x,t,\xi)$ is a collision term that satisfies :

$$\int_{\mathbb{R}} Q d\xi = \int_{\mathbb{R}} \xi Q d\xi = 0$$

Indeed, using (C.6), (C.4) and (C.5) one can write:

$$\int_{\mathbb{R}} Q d\xi = \int_{\mathbb{R}} \partial_t M + \xi \partial_x M d\xi = \partial_t A + \partial_x (Au)$$

And

$$\int_{\mathbb{R}} \xi Q d\xi = \int_{\mathbb{R}} \xi(\partial_t M + \xi \partial_x M) d\xi = \partial_t(Au) + \partial_x(Au^2 + A\gamma^2) = \partial_t(Au) + \partial_x(Au^2) + \partial_x \left(\int_{\varepsilon A_0}^{A(x,t)} c^2(a) da \right)$$

Because

$$\int_{\mathbb{R}} \xi^2 M d\xi = A \int_{\mathbb{R}} (\gamma w + u)^2 \chi(w) dw = A\gamma^2 \int_{\mathbb{R}} w^2 \chi(w) dw + Au^2 \int_{\mathbb{R}} \chi(w) dw = A\gamma^2 + Au^2 \tag{C.7}$$

And $A\gamma^2 = \int_{\varepsilon A_0}^{A(x,t)} c^2(a) da$. The equivalence between the two systems of equations is then proven.

C.2 Kinetic numerical scheme

With the kinetic interpretation of the initial system of equation (C.1) a finite volume kinetic scheme is used to solve the equations. Time and space steps are respectively denoted by Δt and Δx. (A_i^n, u_i^n) denotes the approximation of $(A(x_i,t_n),u(x_i,t_n))$, with $t_n = n\Delta t$ and $x_i = i\Delta x$. M_i^n is the discrete particles density defined by:

$$M_i^n = M_i^n(\xi) = \frac{A_i^n}{\gamma_i^n} \chi \left(\frac{\xi - u_i^n}{\gamma_i^n} \right)$$

with $\gamma_i^n = \int_{\varepsilon A_0}^{A_i^n} (c_i^n(a))^2 da$.

Using an upwind scheme, (C.6) is approximated:

$$M_i^{n+1,-} = M_i^n - \frac{\Delta x}{\Delta t} \xi \left(M_{i+\frac{1}{2}}^n - M_{i-\frac{1}{2}}^n \right) \tag{C.8}$$

with $M_{i+\frac{1}{2}}^n = M_i^n \mathbf{1}_{\xi \geq 0} + M_{i+1}^n \mathbf{1}_{\xi \leq 0}$. The solution of the equation (C.6) can be approximated by:

$$M_i^{n+1} = M_i^{n+1,-} + \Delta t Q^n$$

The following relation is verified: $\int_{\mathbb{R}} M_i^{n+1} = \int_{\mathbb{R}} M_i^{n+1,-}$. Then, with (C.4) and (C.5), A_i^n and $(Au)_i^n = A_i^n u_i^n$ are computed:

$$X_i^{n+1} = \begin{pmatrix} A_i^{n+1} \\ A_i^{n+1} u_i^{n+1} \end{pmatrix} = \int_{\mathbb{R}} \begin{pmatrix} 1 \\ \xi \end{pmatrix} M_i^{n+1,-} d\xi \tag{C.9}$$

Thus $A_i^{n+1} = A_i^{n+1,-}$ and $(Au)_i^{n+1} = (Au)_i^{n+1,-}$. Notice that the collision term is not taken into account in the formula (C.8). A discontinuity is introduced for the microscopic variable: $M_i^{n+1} \neq M_i^{n+1,-}$. However, the macroscopic variables remain continuous. More details on the kinetic scheme can be found in [ABP00, ABBSM16]. To summarize the kinetic scheme reads:

$$X_i^{n+1} = X_i^n - \frac{\Delta x_i}{\Delta t^n} (\mathcal{F}_{i+\frac{1}{2}}^n - \mathcal{F}_{i-\frac{1}{2}}^n) \tag{C.10}$$

with $\mathcal{F}_{i+\frac{1}{2}}^n = \int_{\mathbb{R}} \xi \begin{pmatrix} 1 \\ \xi \end{pmatrix} M_{i+\frac{1}{2}}^n d\xi$. The fluxes $\mathcal{F}$ detailed calculation are given below.

$$\begin{aligned}
\mathcal{F}_{i+\frac{1}{2}}^n = & \int_{\mathbb{R}} \left[\xi \begin{pmatrix} 1 \\ \xi \end{pmatrix} M_{i+\frac{1}{2}}^n \right] d\xi \\
&= \int_{\mathbb{R}} \left[\xi \begin{pmatrix} 1 \\ \xi \end{pmatrix} M_i^n \mathbf{1}_{\xi \geq 0} + M_{i+1}^n \mathbf{1}_{\xi \leq 0} \right] d\xi \\
&= \int_{\xi \geq 0} \left[\xi \begin{pmatrix} 1 \\ \xi \end{pmatrix} M_i^n \right] d\xi + \int_{\xi \leq 0} \left[\xi \begin{pmatrix} 1 \\ \xi \end{pmatrix} M_{i+1}^n \right] d\xi \\
&= \int_{\xi \geq 0} \left[\xi \begin{pmatrix} 1 \\ \xi \end{pmatrix} \frac{A_i^n}{\gamma_i^n} \chi \left(\frac{\xi - u_i^n}{\gamma_i^n} \right) \right] d\xi + \int_{\xi \leq 0} \left[\xi \begin{pmatrix} 1 \\ \xi \end{pmatrix} \frac{A_{i+1}^n}{\gamma_{i+1}^n} \chi \left(\frac{\xi - u_{i+1}^n}{\gamma_{i+1}^n} \right) \right] d\xi \\
&= \mathcal{F}^+ \left(X_i^n \right) + \mathcal{F}^- \left(X_{i+1}^n \right)
\end{aligned} \tag{C.11}$$

To evaluate the fluxes, the following integrals are needed.

$$\int_{\xi \geq 0} \left[\xi^p \frac{A}{\gamma} \chi \left(\frac{\xi - u}{\gamma} \right) \right] d\xi \quad ; \quad \int_{\xi \leq 0} \left[\xi^p \frac{A}{\gamma} \chi \left(\frac{\xi - u}{\gamma} \right) \right] d\xi \, , \, p = 1, 2. \tag{C.12}$$

The integrals can be analytically computed with the χ function chosen.

$$\begin{aligned}
\int_{\xi \geq 0} \left[\xi^p \frac{A}{\gamma} \chi \left(\frac{\xi - u}{\gamma} \right) \right] d\xi &= A \int_{w\gamma + u \geq 0} (w\gamma + u)^p \chi(w) \, dw \\
&= A \int_{w \geq -\frac{u}{\gamma}} (w\gamma + u)^p \frac{1}{2\sqrt{3}} \mathbf{1}_{|w| \leq \sqrt{3}} dw \\
&= \frac{1}{2\sqrt{3}} \frac{A}{\gamma(p+1)} \left[(w\gamma + u)^{p+1} \right]_{\max(\frac{-u}{\gamma}; -\sqrt{3})}^{\max(\frac{-u}{\gamma}; \sqrt{3})}
\end{aligned} \tag{C.13}$$

And with the same calculation:

$$\int_{\xi \leq 0} \left[\xi^p \frac{A}{\gamma} \chi_1 \left(\frac{\xi - u}{\gamma} \right) \right] d\xi = \frac{1}{2\sqrt{3}} \frac{A}{\gamma(p+1)} \left[(w\gamma + u)^{p+1} \right]_{\min(\frac{-u}{\gamma}; -\sqrt{3})}^{\min(\frac{-u}{\gamma}; \sqrt{3})} \tag{C.14}$$

Second order extension in space. Second order kinetic scheme in space is obtained by a limited reconstruction of the variables at the left and right boundary of a cell. The second order scheme reads:

$$X_i^{n+1} = X_i^n - \frac{\Delta x}{\Delta t}(\mathcal{F}^n_{i+\frac{1}{2}} - \mathcal{F}^n_{i-\frac{1}{2}}) \tag{C.15}$$

With numerical fluxes given by

$$\mathcal{F}^n_{i+\frac{1}{2}} = \mathcal{F}^+\left(X^n_{i,l}\right) + \mathcal{F}^-\left(X^n_{i,r}\right) \tag{C.16}$$

Where

$$X^n_{i,l} = \begin{pmatrix} A^n_{i,l} \\ A^n_{i,l}u^n_{i,l} \end{pmatrix} \quad ; \quad X^n_{i,r} = \begin{pmatrix} A^n_{i,r} \\ A^n_{i,r}u^n_{i,r} \end{pmatrix} \tag{C.17}$$

And

$$A^n_{i,l} = A^n_i - 0.5\Delta x \,\text{minmod}\left(\frac{A^n_i - A^n_{i-1}}{\Delta x}, \frac{A^n_{i+1} - A^n_i}{\Delta x}\right) \tag{C.18}$$

$$A^n_{i,r} = A^n_i + 0.5\Delta x \,\text{minmod}\left(\frac{A^n_i - A^n_{i-1}}{\Delta x}, \frac{A^n_{i+1} - A^n_i}{\Delta x}\right) \tag{C.19}$$

with

$$\text{minmod}(a,b) = \begin{cases} a & \text{if } |a| < |b| \text{ and } ab > 0 \\ b & \text{if } |a| > |b| \text{ and } ab > 0 \\ 0 & \text{if } ab \leq 0 \end{cases} \tag{C.20}$$

And the same definitions for $u^n_{i,l}$ and $u^n_{i,r}$ are taken.

Appendix D

Monolix: parameter estimation by population approach

A population approach with stochastic approximation of expectation-maximization (SAEM) algorithm is used for parameter estimation. The SAEM algorithm details and convergence properties are largely described in [DLM99, KL04, KL05, GLV14]. The general principles are recalled in this appendix.

D.1 Population approach principle

Population approach principle main idea is to use the observations available for each individual to estimate parameters for the population instead of searching for individual parameters. Let y be the noisy measurements of a process. The process is described by the solution f of a system of ordinary differential equations. The equations read:

$$y_{i,j} = f(x_{i,j}, \psi_i) + \varepsilon_{i,j} \quad 1 \leq i \leq N; 1 \leq j \leq N_i$$

where N is the number of individual, N_i is the number of observations points for individual i, $y_{i,j}$ denotes the j^{th} observation on i^{th} subject, $x_{i,j}$ are known variables (time, state variables, ...) and ψ_i are the parameters for individual i. The noise is denoted by $\varepsilon_{i,j}$ (noise on measurements and simplification errors due to model approximations). Moreover, $\varepsilon_{i,j}$ are assumed to be independent and to follow a normal distribution law: $\varepsilon_{i,j} \sim_{i.i.d} \mathcal{N}(0,\sigma^2)$.
The individual parameters are decomposed in two parameters corresponding to fixed and random effects. In other words, the fixed effects correspond to the mean population parameters and the random effects account for inter-individual variability.

$$\psi_i = \mu + \eta_i, \quad \eta_i \sim_{i.i.d} \mathcal{N}(0,\Sigma)$$

Other law (non-normal laws) for ψ_i can also be treated in the same manner.
The purpose is to calculate a maximum likelihood estimator $\hat{\theta}$ for the unknown set of parameters $\theta = (\mu, \Sigma, \sigma^2)$, where μ is the mean population parameters, Σ is the population covariance matrix and σ^2 is the noise variance.
The estimator $\hat{\theta}$ maximizes $\theta \mapsto \log(p(y;\theta))$, with

$$p(y;\theta) = \prod_{i=1}^{N} p(y_i;\theta) = \prod_{i=1}^{N} \left(\int p(y_i, \psi_i; \theta) d\psi_i \right)$$

where $y_i = (y_{i,j}, 1 \leq j \leq N_i)$ is the vector of measurements of subject i.
Under the previous assumptions:

$$p(y_i, \psi_i; \theta) = p(y_i|\psi_i; \theta)p(\psi_i; \theta)$$

And,

$$p(\psi_i; \theta) = \frac{1}{\sqrt{2\pi}\,\Sigma} \exp\left(\frac{-(\psi_i - \mu)^2}{2\Sigma^2}\right) \tag{D.1}$$

$$p(y_i|\psi_i; \theta) = \frac{1}{(\sqrt{2\pi}\sigma)^{N_i}} \prod_{j=1}^{N_i} \exp\left(\frac{-(y_{i,j} - f(x_{i,j},\psi_i))^2}{2\sigma^2}\right) \tag{D.2}$$

Thus,

$$p(y; \theta) = \frac{1}{(\sqrt{2\pi}\Sigma)^N} \prod_{i=1}^{N} \int \left(\exp\left(\frac{-(\psi_i - \mu)^2}{2\Sigma^2}\right) \frac{1}{(\sqrt{2\pi}\sigma)^{N_i}} \prod_{j=1}^{N_i} \exp\left(\frac{-(y_{i,j} - f(x_{i,j},\psi_i))^2}{2\sigma^2}\right) \right) d\psi_i \tag{D.3}$$

Then, the individual parameters are estimated by maximizing the conditional probabilities $p(\psi_i|y_i; \hat{\theta})$, where $\hat{\theta}$ is the population parameters estimated at first.

D.2 Stochastic approximation of expectation-maximization (SAEM) algorithm

To calculate the maximum likelihood estimator $\hat{\theta}$, the expectation-maximization (EM) algorithm is performed. The iteration k of the E-step in the iterative EM algorithm consists in evaluate the following quantity:

$$Q_k(\theta) = \mathbb{E}\left[\log p(y,\psi; \theta) \,|y; \theta_{k-1}\right] \tag{D.4}$$

However, since ψ are unknown, to calculate the estimator $\hat{\theta}$ the quantity $\log(p(y,\psi; \theta))$ is not available. Due to the non-linear relation between y and ψ there is no explicit expression for (D.4). The SAEM algorithm uses a stochastic approximation to replace the E-step.
Iteration k of SAEM algorithm consists in:

- Simulation step: draw $\psi^{(k)}$ from conditional distribution $p(\psi_i|y_i; \theta_{k-1})$ with a Monte Carlo Markov Chain method. Using the following relation and the expression (D.2) :

$$p(\psi_i|y_i; \theta_{k-1}) \propto p(y_i|\psi_i; \theta_{k-1})p(\psi_i; \theta_{k-1}) \tag{D.5}$$

- Stochastic approximation step: the evaluation step is replace with an approximation:

$$Q_k(\theta) = Q_{k-1}(\theta) + \gamma_k \left[\log p(y,\psi^{(k)}; \theta) - Q_{k-1}(\theta)\right] \tag{D.6}$$

with (γ_k) a decreasing sequence such that : $\sum \gamma_k = +\infty, \quad \sum \gamma_k^2 < +\infty$

- Maximization step (unchanged): the estimator of θ is updated:

$$\theta_k = Argmax\, Q_k(\theta) \tag{D.7}$$

D.3 Parameter estimation with Monolix

In this work, the SAEM algorithm in Monolix software (developed by Lixoft [Mon]) is used for population and individual parameters estimation. The individual parameter distributions are assumed log-normal to avoid negative values. Moreover the parameters are re-scaled to vary between around 0 and 1.

Appendix E

Model of bile duct delay with a series of compartments

The delay between the apparition of fluorescence in the liver tissue and in the common bile duct is modeled with a series of transit compartments as proposed in [BDG76, SJKK07]. The exact solution of the system can be computed, showing that the series of N compartments is equivalent to the convolution of the input function with the function G_N (defined below). The system of equations for the series of transit compartments reads:

$$\begin{cases} \frac{d}{dt}(R_1) = input(t) - \frac{1}{\tau}R_1 \\ \frac{d}{dt}(R_i) = \frac{1}{\tau}R_{i-1} - \frac{1}{\tau}R_i \quad i \in \{2 \dots N\} \end{cases} \tag{E.1}$$

Assuming for all i that $R_i(0) = 0$, an analytic solution for R_N can be computed by induction:

$$R_N(t) = \int_0^t input(t-s)G_N(s)ds, \quad G_N(s) = \left(\frac{s}{\tau}\right)^{N-1} \frac{1}{N!} e^{-\frac{s}{\tau}}$$

The induction follows:

$$R_1(t) = \int_0^t input(s) \quad e^{-\frac{(t-s)}{\tau}} ds = \int_0^t input(t-u) \quad e^{-\frac{u}{\tau}} du$$

Thus,

$$R_1(t) = \int_0^t input(t-u) \quad G_1(u)du$$

Now, the following assumption is made:

$$\exists k \in \mathbb{N}^*, \quad R_k(t) = \int_0^t input(t-u) \quad G_k(u)du$$

Then,

$$\frac{d}{dt}(R_{k+1}) = \frac{1}{\tau}R_k - \frac{1}{\tau}R_{k+1}, \quad R_{k+1}(0) = 0$$

Thus,

$$
\begin{aligned}
R_{k+1}(t) = & \int_0^t \frac{1}{\tau} R_k(s) \quad e^{-\frac{t-s}{\tau}} ds \\
R_{k+1}(t) = & \int_0^t \frac{1}{\tau} \left(\int_0^s input(s-u) \quad G_k(u) du \right) \quad e^{-\frac{t-s}{\tau}} ds \\
R_{k+1}(t) = & \int_0^t \left(\int_0^s \frac{1}{\tau} input(z) \quad G_k(s-z) \quad e^{-\frac{t-s}{\tau}} dz \right) ds \\
R_{k+1}(t) = & \int_0^t \left(\int_z^t \frac{1}{\tau} input(z) \quad \left(\frac{s-z}{\tau} \right)^{k-1} \frac{1}{k!} e^{-\frac{(s-z)}{\tau}} \quad e^{-\frac{t-s}{\tau}} ds \right) dz \\
R_{k+1}(t) = & \int_0^t input(z) e^{-\frac{t-z}{\tau}} \left(\int_z^t \frac{1}{\tau} \quad \left(\frac{s-z}{\tau} \right)^{k-1} \frac{1}{k!} ds \right) dz \\
R_{k+1}(t) = & \int_0^t input(z) e^{-\frac{t-z}{\tau}} \frac{1}{\tau^k} \quad \left[(s-z)^k \right]_z^t \frac{1}{(k+1)!} dz \\
R_{k+1}(t) = & \int_0^t input(z) \quad G_{k+1}(t-z) dz \\
R_{k+1}(t) = & \int_0^t input(t-u) \quad G_{k+1}(u) du
\end{aligned}
\tag{E.2}
$$

Conclusion

$$
R_N(t) = \int_0^t input(t-s) G_N(s) ds, \quad G_N(s) = \left(\frac{s}{\tau} \right)^{N-1} \frac{1}{N!} e^{-\frac{s}{\tau}}
$$

Bibliography

[AAB+13] Marc-Antoine Allard, René Adam, Pétru-Octav Bucur, Salah Termos, Antonio Sa Cunha, Henri Bismuth, Denis Castaing, and Eric Vibert. Posthepatectomy portal vein pressure predicts liver failure and mortality after major liver resection on noncirrhotic liver. *Annals of surgery*, 258(5):822–830, 2013.

[ABB+04] Emmanuel Audusse, François Bouchut, Marie-Odile Bristeau, Rupert Klein, and Benoît Perthame. A fast and stable well-balanced scheme with hydrostatic reconstruction for shallow water flows. *SIAM Journal on Scientific Computing*, 25(6):2050–2065, 2004.

[ABBSM16] Emmanuel Audusse, François Bouchut, Marie-Odile Bristeau, and Jacques Sainte-Marie. Kinetic entropy inequality and hydrostatic reconstruction scheme for the saint-venant system. *Mathematics of Computation*, 2016.

[ABP00] Emmanuel Audusse, Marie-Odile Bristeau, and Benoît Perthame. Kinetic Schemes for Saint-Venant Equations with Source Terms on Unstructured Grids. Research Report RR-3989, INRIA, 2000. Projet M3N.

[AEV12] Kerstin Abshagen, Christian Eipel, and Brigitte Vollmar. A critical appraisal of the hemodynamic signal driving liver regeneration. *Langenbeck's Archives of Surgery*, 397(4):579–590, 2012.

[AKL+12] Jarmo T Alander, Ilkka Kaartinen, Aki Laakso, Tommi Pätilä, Thomas Spillmann, Valery V Tuchin, Maarit Venermo, and Petri Välisuo. A review of indocyanine green fluorescent imaging in surgery. *Int J Biomed Imaging*, 2012:940585, 2012.

[AKM+11] Jordi Alastruey, Ashraf W Khir, Koen S Matthys, Patrick Segers, Spencer J Sherwin, Pascal R Verdonck, Kim H Parker, and Joaquim Peiró. Pulse wave propagation in a model human arterial network: assessment of 1-D visco-elastic simulations against in vitro measurements. *Journal of biomechanics*, 44(12):2250–2258, 2011.

[Ana] Abdomene anatomy drawing. http://www.anatomy-diagram.info/anatomy-of-the-body-liver/anatomy-of-the-body-liver-human-anatomy-liver-anatomy-human-body-2/.

[ATR+16] Lydia Aslanidou, Bram Trachet, Philippe Reymond, Rodrigo A Fraga-Silva, Patrick Segers, and Nikolaos Stergiopulos. A 1D model of the arterial circulation in mice. *Altex*, 33(1):13, 2016.

[AVOS13] JM Asencio, J Vaquero, L Olmedilla, and JL García Sabrido. "small-for-flow" syndrome: shifting the "size" paradigm. *Medical hypotheses*, 80(5):573–577, 2013.

[AWB+11] Irwin Arias, Allan Wolkoff, James Boyer, David Shafritz, Nelson Fausto, Harvey Alter, and David Cohen. *The liver: biology and pathobiology*. John Wiley & Sons, 2011.

[AYIC06] Burak Alacam, Birsen Yazici, Xavier Intes, and Britton Chance. Extended kalman filtering for the modeling and analysis of icg pharmacokinetics in cancerous tumors using nir optical methods. *IEEE transactions on biomedical engineering*, 53(10):1861–1871, 2006.

[Bas10] Christopher Anthony Basciano. *Computational Particle-Hemodynamics Analysis Applied to an Abdominal Aortic Aneurysm with Thrombus and Microsphere-Targeting of Liver Tumors.* PhD thesis, 2010.

[BAW66] James B Bassingthwaighte, Francis H Ackerman, and Earl H Wood. Applications of the lagged normal density curve as a model for arterial dilution curves. *Circulation Research*, 18(4):398–415, 1966.

[BBA+16] Petru Bucur, Mohamed Bekheit, Chloe Audebert, Irene Vignon-Clementel, and Eric Vibert. Simplified technique for 75% and 90% hepatic resection with hemodynamic monitoring in a large white swine model. *Journal of Surgical Research*, 2016.

[BBD+07] P Bai, H T Banks, S Dediu, A Y Govan, M Last, A L Lloyd, H K Nguyen, M S Olufsen, G Rempala, and B D Slenning. Stochastic and deterministic models for agricultural production networks. *Math Biosci Eng*, 4(3):373–402, Jul 2007.

[BBV+16] Mohamed Bekheit, Petru Bucur, Eric Vibert, Christian Andres, et al. The reference values for hepatic oxygen consumption and net lactate production, blood gasses, hemogram, major electrolytes, and kidney and liver profiles in anesthetized large white swine model. *Translational Surgery*, 1(4):95, 2016.

[BBWV17] Mohamed Bekheit, Petru O Bucur, Mylene Wartenberg, and Eric Vibert. Computerized tomography–based anatomic description of the porcine liver. *Journal of Surgical Research*, 210:223–230, 2017.

[BDG76] Peter M Bungay, Robert L Dedrick, and Anthony M Guarino. Pharmacokinetic modeling of the dogfish shark (squalus acanthias): distribution and urinary and biliary excretion of phenol red and its glucuronide. *Journal of pharmacokinetics and biopharmaceutics*, 4(5):377–388, 1976.

[BDLB10] Emøke Bendixen, Marianne Danielsen, Knud Larsen, and Christian Bendixen. Advances in porcine genomics and proteomics—a toolbox for developing the

pig as a model organism for molecular biomedical research. *Briefings in functional genomics*, 9(3):208–219, 2010.

[BF13] P J Blanco and R A Feijóo. A dimensionally-heterogeneous closed-loop model for the cardiovascular system and its applications. *Med Eng Phys*, 35(5):652–67, May 2013.

[BFC01] S Bassez, P Flaud, and M Chauveau. Modeling of the deformation of flexible tubes using a single law: application to veins of the lower limb in man. *Journal of biomechanical engineering*, 123(1):58–65, 2001.

[BG84] JB Bassingthwaighte and CA Goresky. Modeling in the analysis of solute and water exchange in the microvasculature, chap. 13. *Handbook of Physiology-The Cardiovascular System IV*, 1984.

[BKK+10] Christopher A Basciano, Clement Kleinstreuer, Andrew S Kennedy, William A Dezarn, and Emily Childress. Computer modeling of controlled microsphere release and targeting in a representative hepatic artery system. *Annals of biomedical engineering*, 38(5):1862–1879, 2010.

[BLRS10] Andrea Bonfiglio, Kritsada Leungchavaphongse, Rodolfo Repetto, and Jennifer H Siggers. Mathematical modeling of the circulation in the liver lobule. *Journal of biomechanical engineering*, 132(11):111011, 2010.

[BMG12] Cristóbal Bertoglio, Philippe Moireau, and Jean-Frederic Gerbeau. Sequential parameter estimation for fluid–structure problems: Application to hemodynamics. *International Journal for Numerical Methods in Biomedical Engineering*, 28(4):434–455, 2012.

[BNB+15] Etienne Boileau, Perumal Nithiarasu, Pablo J Blanco, Lucas O Müller, Fredrik Eikeland Fossan, Leif Rune Hellevik, Wouter P Donders, Wouter Huberts, Marie Willemet, and Jordi Alastruey. A benchmark study of numerical schemes for one-dimensional arterial blood flow modelling. *Int J Numer Method Biomed Eng*, 31(10), Oct 2015.

[Boi17] Noemie Boissier. *Blood and bile flow mathematical modeling in healthy and damaged liver micro-architecture*. PhD thesis, Inria Paris & Laboratoire Jacques Louis Lions, Universite Pierre et Marie Curie, in preparation (2017).

[Box80] Harold Boxenbaum. Interspecies variation in liver weight, hepatic blood flow, and antipyrine intrinsic clearance: extrapolation of data to benzodiazepines and phenytoin. *Journal of pharmacokinetics and biopharmaceutics*, 8(2):165–176, 1980.

[BP02] B S Brook and T J Pedley. A model for time-dependent flow in (giraffe jugular) veins: uniform tube properties. *J Biomech*, 35(1):95–107, Jan 2002.

[BR81] Tom D Bennett and CARL F Rothe. Hepatic capacitance responses to changes in flow and hepatic venous pressure in dogs. *American Journal of Physiology-Heart and Circulatory Physiology*, 240(1):H18–H28, 1981.

[BTTB91] E Burns, DR Triger, GT Tucker, and NDS Bax. Indocyanine green elimination in patients with liver disease and in normal subjects. *Clinical Science*, 80(2):155–160, 1991.

[BVS+09] CC Botar, T Vasile, S Sfrangeu, S Clichici, PS Agachi, R Badea, P Mircea, MV Cristea, and R Moldovan. CFD simulation of the portal vein blood flow. In *International Conference on Advancements of Medicine and Health Care through Technology*, pages 359–362. Springer, 2009.

[BWKM+07] Johanne Bezy-Wendling, Marek Kretowski, Muriel Mescam, Krzysztof Jurczuk, and Pierre-Antoine Eliat. Simulation of hepatocellular carcinoma in mri by combined macrovascular and pharmacokinetic models. In *Biomedical Imaging: From Nano to Macro, 2007. ISBI 2007. 4th IEEE International Symposium on*, pages 1272–1275. IEEE, 2007.

[CGT13] Will Cousins, Pierre A Gremaud, and Daniel M Tartakovsky. A new physiological boundary condition for hemodynamics. *SIAM Journal on Applied Mathematics*, 73(3):1203–1223, 2013.

[CHS63] A R Cooke, D D Harrison, and A P Skyring. Use of indocyanine green as a test of liver function. *Am J Dig Dis*, 8:244–50, Mar 1963.

[CK14] Emily M Childress and Clement Kleinstreuer. Impact of fluid–structure interaction on direct tumor-targeting in a representative hepatic artery system. *Annals of biomedical engineering*, 42(3):461–474, 2014.

[CLM+04] Fiona G Court, Peter E Laws, Charles P Morrison, Benjamin D Teague, Matthew S Metcalfe, Simon A Wemyss-Holden, Ashley R Dennison, and Guy J Maddern. Subtotal hepatectomy: a porcine model for the study of liver regeneration. *Journal of Surgical Research*, 116(1):181–186, 2004.

[CPDG07] Pierre-Alain Clavien, Henrik Petrowsky, Michelle L DeOliveira, and Rolf Graf. Strategies for safer liver surgery and partial liver transplantation. *New England Journal of Medicine*, 356(15):1545–1559, 2007.

[CR92] Tai-Ming Chu and Narender P Reddy. A lumped parameter mathematical model of the splanchnic circulation. *Journal of biomechanical engineering*, 114(2):222–226, 1992.

[CWHM+03] FG Court, SA Wemyss-Holden, CP Morrison, BD Teague, PE Laws, J Kew, AR Dennison, and GJ Maddern. Segmental nature of the porcine liver and its potential as a model for experimental partial hepatectomy. *British journal of surgery*, 90(4):440–444, 2003.

[D'A07] Carlo D'ANGELO. *Multiscale modelling of metabolism and transport phenomena in living tissues.* PhD thesis, ÉCOLE POLYTECHNIQUE FÉDÉRALE DE LAUSANNE, 2007.

[DDWC+12] Charlotte Debbaut, David De Wilde, Christophe Casteleyn, Pieter Cornillie, Denis Van Loo, Luc Van Hoorebeke, Diethard Monbaliu, Ye-Dong Fan, and Patrick Segers. Modeling the impact of partial hepatectomy on the hepatic hemodynamics using a rat model. *Biomedical Engineering, IEEE Transactions on*, 59(12):3293–3303, 2012.

[Deb13] Charlotte Debbaut. *Multi-Level Modelling of Hepatic Perfusion in Support of Liver Transplantation Strategies.* PhD thesis, Ghent University, 2013.

[DGMP16] Andrea De Gasperi, Ernestina Mazza, and Manlio Prosperi. Indocyanine green kinetics to assess liver function: Ready for a clinical dynamic assessment in major liver surgery? *World journal of hepatology*, 8(7):355, 2016.

[DHM+01] K H Diehl, R Hull, D Morton, R Pfister, Y Rabemampianina, D Smith, J M Vidal, C van de Vorstenbosch, and European Federation of Pharmaceutical Industries Association and European Centre for the Validation of Alternative Methods. A good practice guide to the administration of substances and removal of blood, including routes and volumes. *J Appl Toxicol*, 21(1):15–23, 2001.

[DHM+06] U Dahmen, CA Hall, N Madrahimov, V Milekhin, and O Dirsch. Regulation of hepatic microcirculation in stepwise liver resection. *Acta gastro-enterologica Belgica*, 70(4):345–351, 2006.

[DL13] Olivier Delestre and P-Y Lagrée. A 'well-balanced' finite volume scheme for blood flow simulation. *International Journal for Numerical Methods in Fluids*, 72(2):177–205, 2013.

[DLM99] Bernard Delyon, Marc Lavielle, and Eric Moulines. Convergence of a stochastic approximation version of the em algorithm. *Annals of statistics*, pages 94–128, 1999.

[DMC+11] Charlotte Debbaut, Diethard Monbaliu, Christophe Casteleyn, Pieter Cornillie, Denis Van Loo, Bert Masschaele, Jacques Pirenne, Paul Simoens, Luc Van Hoorebeke, and Patrick Segers. From vascular corrosion cast to electrical analog model for the study of human liver hemodynamics and perfusion. *Biomedical Engineering, IEEE Transactions on*, 58(1):25–35, 2011.

[DMS14] Charlotte Debbaut, Diethard Monbaliu, and Patrick Segers. Validation and calibration of an electrical analog model of human liver perfusion based on hypothermic machine perfusion experiments. *International Journal of Artificial Organs*, 37(6):486–98, 2014.

[DQ08] Carlo D'ANGELO and Alfio Quarteroni. On the coupling of 1d and 3d diffusion-reaction equations: Application to tissue perfusion problems. *Mathematical Models and Methods in Applied Sciences*, 18(08):1481–1504, 2008.

[DVS+14] Charlotte Debbaut, Jan Vierendeels, Jennifer H Siggers, Rodolfo Repetto, Diethard Monbaliu, and Patrick Segers. A 3d porous media liver lobule model: the importance of vascular septa and anisotropic permeability for homogeneous perfusion. *Computer methods in biomechanics and biomedical engineering*, 17(12):1295–1310, 2014.

[EDSC+99] A El-Desoky, A M Seifalian, M Cope, D T Delpy, and B R Davidson. Experimental study of liver dysfunction evaluated by direct indocyanine green clearance using near infrared spectroscopy. *Br J Surg*, 86(8):1005–11, Aug 1999.

[FKR72] Joseph E Flaherty, Joseph B Keller, and SI Rubinow. Post buckling behavior of elastic tubes and rings with opposite sides in contact. *SIAM Journal on Applied Mathematics*, 23(4):446–455, 1972.

[FLQ03] Luca Formaggia, Daniele Lamponi, and Alfio Quarteroni. One-dimensional models for blood flow in arteries. *Journal of engineering mathematics*, 47(3-4):251–276, 2003.

[Flu] Fluoptics companie: Fluorescence imaging for surgery. http://www.fluoptics.com/.

[FQV09] Luca Formaggia, Alfio Quarteroni, and Alessandro Veneziani. *Cardiovascular Mathematics Modeling and simulation of the circulatory system*, volume 1. Springer, 2009.

[GEMG15] Stephanie M George, Lisa M Eckert, Diego R Martin, and Don P Giddens. Hemodynamics in normal and diseased livers: Application of image-based computational models. *Cardiovascular engineering and technology*, 6(1):80–91, 2015.

[GEN+06] M Glanemann, C Eipel, AK Nussler, B Vollmar, and P Neuhaus. Hyperperfusion syndrome in small-for-size livers. *European surgical research*, 37(6):335–341, 2006.

[GH06] A Guyton and J Hall. Textbook of medical physiology 11th edition elsevier inc. *Philadelphia PA*, 2006.

[GKB+83] SL Grainger, PW Keeling, IM Brown, JH Marigold, and RP Thompson. Clearance and non-invasive determination of the hepatic extraction of indocyanine green in baboons and man. *Clinical science (London, England: 1979)*, 64(2):207–212, 1983.

[GLV14] Emmanuel Grenier, Violaine Louvet, and Paul Vigneaux. Parameter estimation in non-linear mixed effects models with saem algorithm: extension from ode to pde. *ESAIM: Mathematical Modelling and Numerical Analysis*, 48(5):1303–1329, 2014.

[GM04] Simon Gelman and Phillip S Mushlin. Catecholamine-induced changes in the splanchnic circulation affecting systemic hemodynamics. *The Journal of the American Society of Anesthesiologists*, 100(2):434–439, 2004.

[GPCP90] C Guiot, PG Pianta, C Cancelli, and TJ Pedley. Prediction of coronary blood flow with a numerical model based on collapsible tube dynamics. *American Journal of Physiology-Heart and Circulatory Physiology*, 258(5):H1606–H1614, 1990.

[H+01] Simon S Haykin et al. *Kalman filtering and neural networks*. Wiley Online Library, 2001.

[HBB+10] Stefan Hoehme, Marc Brulport, Alexander Bauer, Essam Bedawy, Wiebke Schormann, Matthias Hermes, Verena Puppe, Rolf Gebhardt, Sebastian Zellmer, Michael Schwarz, et al. Prediction and validation of cell alignment along microvessels as order principle to restore tissue architecture in liver regeneration. *Proceedings of the National Academy of Sciences*, 107(23):10371–10376, 2010.

[HBH11] Harvey Ho, Adam Bartlett, and Peter Hunter. Hemodynamic simulation for an anatomically realistic portal system. In *International Conference on Medical Image Computing and Computer-Assisted Intervention*, pages 347–354. Springer, 2011.

[HdGN+13] Lisette T Hoekstra, Wilmar de Graaf, Geert A A Nibourg, Michal Heger, Roelof J Bennink, Bruno Stieger, and Thomas M van Gulik. Physiological and biochemical basis of clinical liver function tests: a review. *Ann Surg*, 257(1):27–36, Jan 2013.

[HHF+14] Seddik Hammad, Stefan Hoehme, Adrian Friebel, Iris Von Recklinghausen, Amnah Othman, Brigitte Begher-Tibbe, Raymond Reif, Patricio Godoy, Tim Johann, Amruta Vartak, et al. Protocols for staining of bile canalicular and sinusoidal networks of human, mouse and pig livers, three-dimensional reconstruction and quantification of tissue microarchitecture by image processing and analysis. *Archives of toxicology*, 88(5):1161–1183, 2014.

[HL73] Thomas JR Hughes and J Lubliner. On the one-dimensional theory of blood flow in the larger vessels. *Mathematical Biosciences*, 18(1):161–170, 1973.

[HLT+10] Cheng-Maw Ho, Reui-Kuo Lin, Shun-Feng Tsai, Rey-Hen Hu, Po-Chin Liang, Tony Wen-Hann Sheu, and Po-Huang Lee. Simulation of portal hemodynamic changes in a donor after right hepatectomy. *Journal of biomechanical engineering*, 132(4):041002, 2010.

[HSBH12] Harvey Ho, Keagan Sorrell, Adam Bartlett, and Peter Hunter. Blood flow simulation for the liver after a virtual right lobe hepatectomy. In *Medical Image Computing and Computer-Assisted Intervention–MICCAI 2012*, pages 525–532. Springer, 2012.

[HSBH13] Harvey Ho, Keagan Sorrell, Adam Bartlett, and Peter Hunter. Modeling the hepatic arterial buffer response in the liver. *Medical engineering & physics*, 35(8):1053–1058, 2013.

[HvLV+13] Lisette T Hoekstra, Krijn P van Lienden, Joanne Verheij, Chris M van der Loos, Michal Heger, and Thomas M van Gulik. Enhanced tumor growth after portal vein embolization in a rabbit tumor model. *Journal of Surgical Research*, 180(1):89–96, 2013.

[IHY+14] Kohta Iguchi, Etsuro Hatano, Kenya Yamanaka, Motohiko Sato, Gen Yamamoto, Yosuke Kasai, Tatsuya Okamoto, Masayuki Okuno, Kojiro Taura, Kyoko Fukumoto, et al. Hepatoprotective effect by pretreatment with olprinone in a swine partial hepatectomy model. *Liver transplantation*, 20(7):838–849, 2014.

[IYT+07] Taku Iida, Shintaro Yagi, Kentaro Taniguchi, Tomohide Hori, and Shinji Uemoto. Improvement of morphological changes after 70% hepatectomy with portocaval shunt: preclinical study in porcine model. *Journal of Surgical Research*, 143(2):238–246, 2007.

[JKE+14] Krzysztof Jurczuk, Marek Kretowski, Pierre-Antoine Eliat, Herve Saint-Jalmes, and Johanne Bezy-Wendling. In silico modeling of magnetic resonance flow imaging in complex vascular networks. *IEEE transactions on medical imaging*, 33(11):2191–2209, 2014.

[JRLB14] ALENA Jonášová, EDUARD Rohan, VLADIMÍR Lukeš, and O Bublık. Complex hierarchical modeling of the dynamic perfusion test: application to liver. In *Proceedings of the 11th World Congress on Computational Mechanics (WCCM2014), Barcelona*, page 3, 2014.

[JUDW95] Simon J Julier, Jeffrey K Uhlmann, and Hugh F Durrant-Whyte. A new approach for filtering nonlinear systems. In *American Control Conference, Proceedings of the 1995*, volume 3, pages 1628–1632. IEEE, 1995.

[JUDW00] Simon Julier, Jeffrey Uhlmann, and Hugh F Durrant-Whyte. Technical notes and correspondence : A new method for the nonlinear transformation of means and covariances in filters and estimators. *IEEE Transactions on automatic control*, 45(3):477, 2000.

[Kal60] Rudolph Emil Kalman. A new approach to linear filtering and prediction problems. *Journal of basic Engineering*, 82(1):35–45, 1960.

[KBWC07] Marek Kretowski, Johanne Bezy-Wendling, and Pierrick Coupé. Simulation of biphasic ct findings in hepatic cellular carcinoma by a two-level physiological model. *IEEE Transactions on Biomedical Engineering*, 54(3):538–542, 2007.

[KKBD10] Andrew S Kennedy, Clement Kleinstreuer, Christopher A Basciano, and William A Dezarn. Computer modeling of yttrium-90–microsphere transport in the hepatic arterial tree to improve clinical outcomes. *International Journal of Radiation Oncology* Biology* Physics*, 76(2):631–637, 2010.

[KL04] Estelle Kuhn and Marc Lavielle. Coupling a stochastic approximation version of em with an mcmc procedure. *ESAIM: Probability and Statistics*, 8:115–131, 2004.

[KL05] Estelle Kuhn and Marc Lavielle. Maximum likelihood estimation in nonlinear mixed effects models. *Computational Statistics & Data Analysis*, 49(4):1020–1038, 2005.

[KLH+15] JMT Keijsers, CAD Leguy, W Huberts, AJ Narracott, J Rittweger, and FN van de Vosse. A 1D pulse wave propagation model of the hemodynamics of calf muscle pump function. *International journal for numerical methods in biomedical engineering*, 31(7), 2015.

[Kri13] Murli Krishna. Role of special stains in diagnostic liver pathology. *Clinical Liver Disease*, 2(S1), 2013.

[KSI+13] Yoshikuni Kawaguchi, Yasuhiko Sugawara, Takeaki Ishizawa, Shouichi Satou, Junichi Kaneko, Sumihito Tamura, Taku Aoki, Yoshihiro Sakamoto, Kiyoshi Hasegawa, and Norihiro Kokudo. Identification of veno-occlusive regions in a right liver graft after reconstruction of vein segments 5 and 8: Application of indocyanine green fluorescence imaging. *Liver Transplantation*, 19(7):778–779, 2013.

[KWH13] Tobias Köppl, Barbara Wohlmuth, and R Helmig. Reduced one-dimensional modelling and numerical simulation for mass transport in fluids. *International Journal for Numerical Methods in Fluids*, 72(2):135–156, 2013.

[Lau07] W Wayne Lautt. Regulatory processes interacting to maintain hepatic blood flow constancy: vascular compliance, hepatic arterial buffer response, hepatorenal reflex, liver regeneration, escape from vasoconstriction. *Hepatology Research*, 37(11):891–903, 2007.

[LAVC+11] John F. LaDisa, C. Alberto Figueroa, Irene E. Vignon-Clementel, Hyun Jin Kim, Nan Xiao, Laura M. Ellwein, Frandics P. Chan, Jeffrey A. Feinstein, and Charles A. Taylor. Computational Simulations for Aortic Coarctation: Representative Results From a Sampling of Patients. *Journal of Biomechanical Engineering*, 133:091008, 2011.

[LC10] Rong-Ho Lin and Chun-Ling Chuang. A hybrid diagnosis model for determining the types of the liver disease. *Computers in Biology and Medicine*, 40(7):665–670, 2010.

[LeV02] Randall J LeVeque. *Finite volume methods for hyperbolic problems*, volume 31. Cambridge university press, 2002.

[LFLH81] BM Lantz, JM Foerster, DP Link, and JW Holcroft. Regional distribution of cardiac output: normal values in man determined by video dilution technique. *American Journal of Roentgenology*, 137(5):903–907, 1981.

[Liv] https://upload.wikimedia.org/wikipedia/commons/e/ec/Liver_Cirrhosis.png.

[LJJ+14] Vladimír Lukeš, Miroslav Jiřík, Alena Jonášová, Eduard Rohan, Ondřej Bublík, and Robert Cimrman. Numerical simulation of liver perfusion: from ct scans to fe model. *arXiv preprint arXiv:1412.6412*, 2014.

[LL05] Fuyou Liang and Hao Liu. A closed-loop lumped parameter computational model for human cardiovascular system. *JSME International Journal*, 48(4):484–493, 2005.

[Lom14] D Lombardi. Inverse problems in 1d hemodynamics on systemic networks: a sequential approach. *Int J Numer Method Biomed Eng*, 30(2):160–79, Feb 2014.

[LTHL09] Fuyou Liang, Shu Takagi, Ryutaro Himeno, and Hao Liu. Multi-scale modeling of the human cardiovascular system with applications to aortic valvular and arterial stenoses. *Medical & biological engineering & computing*, 47(7):743–755, 2009.

[LWC+15] X Li, XK Wang, B Chen, YS Pu, ZF Li, P Nie, and K Su. Computational hemodynamics of portal vein hypertension in hepatic cirrhosis patients. *Bio-Medical Materials and Engineering*, 26(s1):S233–S243, 2015.

[LXT+13] J Leng, H Xing, J Tan, K Chen, and J Dong. The safe minimally ischemic liver remnant for small-for-size syndrome in porcine hepatectomy. In *Transplantation proceedings*, volume 45, pages 2419–2424. Elsevier, 2013.

[MAP+07] Koen S Matthys, Jordi Alastruey, Joaquim Peiró, Ashraf W Khir, Patrick Segers, Pascal R Verdonck, Kim H Parker, and Spencer J Sherwin. Pulse wave propagation in a model human arterial network: assessment of 1-D numerical simulations against in vitro measurements. *Journal of biomechanics*, 40(15):3476–3486, 2007.

[MC11] Philippe Moireau and Dominique Chapelle. Reduced-order unscented kalman filtering with application to parameter identification in large-dimensional systems. *ESAIM: Control, Optimisation and Calculus of Variations*, 17(2):380–405, 2011.

[MD05] George K Michalopoulos and Marie DeFrances. Liver regeneration. In *Regenerative Medicine I*, pages 101–134. Springer, 2005.

[MF10] Emilie Marchandise and Patrice Flaud. Accurate modelling of unsteady flows in collapsible tubes. *Computer Methods in Biomechanics and Biomedical Engineering*, 13(2):279–290, 2010.

[MGN15] J Murillo and P Garcia-Navarro. A roe type energy balanced solver for 1d arterial blood flow and transport. *Computers & Fluids*, 117:149–167, 2015.

[Mic07] George K Michalopoulos. Liver regeneration. *Journal of cellular physiology*, 213(2):286–300, 2007.

[Mic10] George K Michalopoulos. Liver regeneration after partial hepatectomy: critical analysis of mechanistic dilemmas. *The American journal of pathology*, 176(1):2–13, 2010.

[MID] Mid company. http://www.mid-med.com/.

[MKBW10] Muriel Mescam, Marek Kretowski, and Johanne Bezy-Wendling. Multiscale model of liver dce-mri towards a better understanding of tumor complexity. *IEEE transactions on medical imaging*, 29(3):699–707, 2010.

[MMT12] Lucas O Müller, Gino I Montecinos, and Eleuterio F Toro. Some issues in modelling venous haemodynamics. *Numerical Methods for Hyperbolic Equations: Theory and Applications. An international conference to honour Professor EF Toro*, pages 347–354, 2012.

[MMT14] Gino I Montecinos, Lucas O Müller, and Eleuterio F Toro. Hyperbolic reformulation of a 1d viscoelastic blood flow model and ader finite volume schemes. *Journal of Computational Physics*, 266:101–123, 2014.

[Mon] Monolix documentation. http://monolix.lixoft.com/.

[MRA74] F G Moody, L F Rikkers, and J S Aldrete. Estimation of the functional reserve of human liver. *Ann Surg*, 180(4):592–8, Oct 1974.

[MS15] Jonathan P Mynard and Joseph J Smolich. One-dimensional haemodynamic modeling and wave dynamics in the entire adult circulation. *Annals of biomedical engineering*, 43(6):1443–1460, 2015.

[MT14] Lucas O Müller and Eleuterio F Toro. A global multiscale mathematical model for the human circulation with emphasis on the venous system. *International journal for numerical methods in biomedical engineering*, 30(7):681–725, 2014.

[Mur26] Cecil D Murray. The physiological principle of minimum work applied to the angle of branching of arteries. *The Journal of general physiology*, 9(6):835–841, 1926.

[MXPW11] Hongyu Miao, Xiaohua Xia, Alan S Perelson, and Hulin Wu. On identifiability of nonlinear ode models and applications in viral dynamics. *SIAM Rev Soc Ind Appl Math*, 53(1):3–39, Jan 2011.

[NMA+99] Takashi Niiya, Masahiko Murakami, Takeshi Aoki, Noriyuki Murai, Yoshinori Shimizu, and Mitsuo Kusano. Immediate increase of portal pressure, reflecting sinusoidal shear stress, induced liver regeneration after partial hepatectomy. *Journal of hepato-biliary-pancreatic surgery*, 6(3):275–280, 1999.

[OKJB94] P Ott, S Keiding, A H Johnsen, and L Bass. Hepatic removal of two fractions of indocyanine green after bolus injection in anesthetized pigs. *Am J Physiol*, 266(6 Pt 1):G1108–22, Jun 1994.

[Olu99] M S Olufsen. Structured tree outflow condition for blood flow in larger systemic arteries. *Am J Physiol*, 276(1 Pt 2):H257–68, Jan 1999.

[Ott98] Peter Ott. Hepatic elimination of indocyanine green with special reference to distribution kinetics and the influence of plasma protein binding. *Pharmacology & toxicology*, 83(s2):1–48, 1998.

[PBS96] T J Pedley, B S Brook, and R S Seymour. Blood pressure and flow rate in the giraffe jugular vein. *Philos Trans R Soc Lond B Biol Sci*, 351(1342):855–66, Jul 1996.

[PCB+15] Sanjay Pant, Chiara Corsini, Catriona Baker, Tain-Yen Hsia, Giancarlo Pennati, and Irene Vignon-Clementel. Data assimilation and modelling of patient-specific single-ventricle physiology with and without valve regurgitation. *Journal of Biomechanics* , November 2015.

[PDC+15] Geert Peeters, Charlotte Debbaut, Pieter Cornillie, Thomas De Schryver, Diethard Monbaliu, Wim Laleman, and Patrick Segers. A multilevel modeling framework to study hepatic perfusion characteristics in case of liver cirrhosis. *Journal of biomechanical engineering*, 137(5):051007, 2015.

[Per02] Benoît Perthame. *Kinetic formulation of conservation laws*, volume 21. Oxford University Press, 2002.

[PFGVC14] S Pant, B Fabrèges, J-F Gerbeau, and I E Vignon-Clementel. A methodological paradigm for patient-specific multi-scale CFD simulations: from clinical measurements to parameter estimates for individual analysis. *Int J Numer Method Biomed Eng*, 30(12):1614–48, Dec 2014.

[PHNP03] Svetla Petkova, Alamgir Hossain, Jamal Naser, and Enzo Palombo. CFD modelling of blood flow in portal vein hypertension with and without thrombosis. In *Third International Conference on CFD in the minerals and Process Industries*, pages 527–530, 2003.

[PLG+09] V Pamecha, A Levene, F Grillo, N Woodward, A Dhillon, and BR Davidson. Effect of portal vein embolisation on the growth rate of colorectal liver metastases. *British journal of cancer*, 100(4):617–622, 2009.

[PMD+97] Giancarlo Pennati, Francesco Migliavacca, Gabriele Dubini, Riccardo Pietrabissa, and Marc R de Leval. A mathematical model of circulation in the presence of the bidirectional cavopulmonary anastomosis in children with a univentricular heart. *Medical Engineering & Physics*, 19(3):223–234, 1997.

[PMPS07] Michel Pouyet, Isabelle Méchet, Christian Paquet, and Jean-Yves Scoazec. Liver regeneration and hemodynamics in pigs with mesocaval shunt. *Journal of Surgical Research*, 138(1):128–134, 2007.

[Pol92] MS Pollanen. Dimensional optimization at different levels of the arterial hierarchy. *Journal of theoretical biology*, 159(2):267–270, 1992.

[PRM+06] Geoff JM Parker, Caleb Roberts, Andrew Macdonald, Giovanni A Buonaccorsi, Sue Cheung, David L Buckley, Alan Jackson, Yvonne Watson, Karen Davies, and Gordon C Jayson. Experimentally-derived functional form for a population-averaged high-temporal-resolution arterial input function for dynamic contrast-enhanced mri. *Magnetic resonance in medicine*, 56(5):993–1000, 2006.

[PV05] Massimo Pinzani and Francesco Vizzutti. Anatomy and vascular biology of the cells in the portal circulation. In *Portal hypertension*, chapter 2, pages 15–35. Springer, 2005.

[R D08] R Development Core Team. *R: A Language and Environment for Statistical Computing*. R Foundation for Statistical Computing, Vienna, Austria, 2008. ISBN 3-900051-07-0.

[Rab77] Hartmut M Rabes. Kinetics of hepatocellular proliferation as a function of the microvascular structure and functional state of the liver. In *Ciba Foundation Symposium 55-Hepatotrophic Factors*, pages 31–59. Wiley Online Library, 1977.

[RDD10] Tim Ricken, Uta Dahmen, and Olaf Dirsch. A biphasic model for sinusoidal liver perfusion remodeling after outflow obstruction. *Biomechanics and modeling in mechanobiology*, 9(4):435–450, 2010.

[RDM05] Andrew P Robinson, Remko A Duursma, and John D Marshall. A regression-based equivalence test for model validation: shifting the burden of proof. *Tree physiology*, 25(7):903–913, 2005.

[RF04] Andrew P Robinson and Robert E Froese. Model validation using equivalence tests. *Ecological Modelling*, 176(3):349–358, 2004.

[RJS74] Jeffrey K Raines, Michel Y Jaffrin, and Ascher H Shapiro. A computer simulation of arterial dynamics in the human leg. *Journal of biomechanics*, 7(1):77–91, 1974.

[Rob16] Andrew Robinson. Package 'equivalence'. Technical report, https://cran.r-project.org/web/packages/equivalence/equivalence.pdf, 2016.

[RRS+87] Eric B Rypins, Kevin M Rosenberg, I James Sarfeh, James Houck, Robert M Conroy, and Norah Milne. Computer analysis of portal hemodynamics after small-diameter portacaval h-grafts: the theoretical basis for partial shunting. *Journal of surgical research*, 42(4):354–361, 1987.

[RWH+15] T Ricken, D Werner, HG Holzhütter, M König, U Dahmen, and O Dirsch. Modeling function–perfusion behavior in liver lobules including tissue, blood, glucose, lactate and glycogen by use of a coupled two-scale pde–ode approach. *Biomechanics and modeling in mechanobiology*, 14(3):515–536, 2015.

[SBSC+11] Mauricio Sainz-Barriga, Luigia Scudeller, Maria Gabriella Costa, Bernard de Hemptinne, and Roberto Ivan Troisi. Lack of a correlation between portal vein flow and pressure: toward a shared interpretation of hemodynamic stress governing inflow modulation in liver transplantation. *Liver Transplantation*, 17(7):836–848, 2011.

[SD12] V. Springel and C.P. Dullemond. Lecture, chapter 4. http://www.ita.uni-heidelberg.de/∼dullemond/lectures/num_fluid_2012/, 2012.

[Sec36] H Seckei. Blood volume and circulation time in children. *Archives of disease in childhood*, 11(61):21, 1936.

[SFPF03] SJ Sherwin, L Formaggia, J Peiro, and V Franke. Computational modelling of 1D blood flow with variable mechanical properties and its application to the simulation of wave propagation in the human arterial system. *International Journal for Numerical Methods in Fluids*, 43(6-7):673–700, 2003.

[Sha77] Ascher H Shapiro. Steady flow in collapsible tubes. *Journal of Biomechanical Engineering*, 99(3):126–147, 1977.

[Sim10] Dan Simon. Kalman filtering with state constraints: a survey of linear and nonlinear algorithms. *IET Control Theory & Applications*, 4(8):1303–1318, 2010.

[SJKK07] Radojka M Savic, Daniël M Jonker, Thomas Kerbusch, and Mats O Karlsson. Implementation of a transit compartment model for describing drug absorption in pharmacokinetic studies. *Journal of pharmacokinetics and pharmacodynamics*, 34(5):711–726, 2007.

[SKN+14] Lars Ole Schwen, Markus Krauss, Christoph Niederalt, Felix Gremse, Fabian Kiessling, Andrea Schenk, Tobias Preusser, and Lars Kuepfer. Spatio-temporal simulation of first pass drug perfusion in the liver. *PLoS Comput Biol*, 10(3):e1003499, 2014.

[SLH11] Yubing Shi, Patricia Lawford, and Rodney Hose. Review of zero-d and 1-d models of blood flow in the cardiovascular system. *Biomedical engineering online*, 10(1):1, 2011.

[SMH+12] MM Swindle, A Makin, AJ Herron, FJ Clubb, and KS Frazier. Swine as models in biomedical research and toxicology testing. *Veterinary Pathology Online*, 49(2):344–356, 2012.

[SNFS63] N SUWA, T NIWA, H FUKASAWA, and Y SASAKI. Estimation of intravascular blood pressure gradient by mathematical analysis of arterial casts. *The Tohoku journal of experimental medicine*, 79:168–198, 1963.

[SOT07] Brooke N Steele, Mette S Olufsen, and Charles A Taylor. Fractal network model for simulating abdominal and lower extremity blood flow during resting and exercise conditions. *Computer Methods in Biomechanics and Biomedical Engineering*, 10(1):39–51, 2007.

[SPH15] R Serban, C Petra, and A.C Hindmarsh. User documentation of ida v2.7.0. 2015.

[Spl] Splanchnic circulation drawing. http://schoolbag.info/biology/concepts/165.html.

[SS74] Hiroyuki Suga and Kiichi Sagawa. Instantaneous pressure-volume relationships and their ratio in the excised, supported canine left ventricle. *Circulation research*, 35(1):117–126, 1974.

[SSK+15] Lars Ole Schwen, Arne Schenk, Clemens Kreutz, Jens Timmer, María Matilde Bartolomé Rodríguez, Lars Kuepfer, and Tobias Preusser. Representative sinusoids for hepatic four-scale pharmacokinetics simulations. *PloS one*, 10(7):e0133653, 2015.

[SSS+00] Patrick Segers, Nikos Stergiopulos, Jan J Schreuder, Berend E Westerhof, and Nico Westerhof. Left ventricular wall stress normalization in chronic pressure-overloaded heart: a mathematical model study. *American Journal of Physiology-Heart and Circulatory Physiology*, 279(3):H1120–H1127, 2000.

[SSW+03] P Segers, N Stergiopulos, N Westerhof, P Wouters, P Kolh, and P Verdonck. Systemic and pulmonary hemodynamics assessed with a lumped-parameter heart-arterial interaction model. *Journal of Engineering Mathematics*, 47:185–199, Dec 2003.

[STC99] Romil Saxena, Neil D Theise, and James M Crawford. Microanatomy of the human liver—exploring the hidden interfaces. *Hepatology*, 30(6):1339–1346, 1999.

[STK+96] H Shinohara, A Tanaka, T Kitai, N Yanabu, T Inomoto, S Satoh, E Hatano, Y Yamaoka, and K Hirao. Direct measurement of hepatic indocyanine green clearance with near-infrared spectroscopy: separate evaluation of uptake and removal. *Hepatology*, 23(1):137–44, Jan 1996.

[Sys] Systemic circulation schematic representation. http://pocketdentistry.com/4-the-circulatory-system/.

[TC99] Karl Thomaseth and Claudio Cobelli. Generalized sensitivity functions in physiological system identification. *Annals of biomedical engineering*, 27(5):607–616, 1999.

[TD08] Gerard J Tortora and Bryan H Derrickson. *Principles of anatomy and physiology*. John Wiley & Sons, 2008.

[TOS+07] Stéphanie Truant, Olivier Oberlin, Géraldine Sergent, Gilles Lebuffe, Luc Gambiez, Olivier Ernst, and François-René Pruvot. Remnant liver volume to body weight ratio $\geq 0.5\%$: a new cut-off to estimate postoperative risks after extended resection in noncirrhotic liver. *Journal of the American College of Surgeons*, 204(1):22–33, 2007.

[TWM16] Simona Turco, Hessel Wijkstra, and Massimo Mischi. Mathematical models of contrast transport kinetics for cancer diagnostic imaging: A review. *IEEE Reviews in Biomedical Engineering*, 9:121–147, 2016.

[VCFJT06] Irene E Vignon-Clementel, C Alberto Figueroa, Kenneth E Jansen, and Charles A Taylor. Outflow boundary conditions for three-dimensional finite element modeling of blood flow and pressure in arteries. *Computer methods in applied mechanics and engineering*, 195(29):3776–3796, 2006.

[VCFJT10] I. E. Vignon-Clementel, C. A. Figueroa, K. E. Jansen, and C. A. Taylor. Outflow boundary conditions for 3D simulations of non-periodic blood flow and pressure fields in deformable arteries. *Computer Methods in Biomechanics and Biomedical Engineering*, 13:625–640, 2010.

[VCZ14] Bhavin B Vasavada, Chao Long Chen, and Muhammad Zakaria. Portal flow is the main predictor of early graft dysfunction regardless of the grwr status in living donor liver transplantation–a retrospective analysis of 134 patients. *International Journal of Surgery*, 12(2):177–180, 2014.

[VDPtHV+04] A Van Der Plaats, NA t Hart, GJ Verkerke, HG Leuvenink, Pascal Verdonck, RJ Ploeg, and G Rakhorst. Numerical simulation of the hepatic circulation. *The International journal of artificial organs*, 27(3):222–230, 2004.

[VL77] Bram Van Leer. Towards the ultimate conservative difference scheme. iv. a new approach to numerical convection. *Journal of computational physics*, 23(3):276–299, 1977.

[VSTC+10] Christophe Van Steenkiste, Bram Trachet, Christophe Casteleyn, Denis Van Loo, Luc Van Hoorebeke, Patrick Segers, Anja Geerts, Hans Van Vlierberghe, and Isabelle Colle. Vascular corrosion casting: analyzing wall shear stress in the portal vein and vascular abnormalities in portal hypertensive and cirrhotic rodents. *Laboratory investigation*, 90(11):1558–1572, 2010.

[VT04] Irene E Vignon and Charles A Taylor. Outflow boundary conditions for one-dimensional finite element modeling of blood flow and pressure waves in arteries. *Wave Motion*, 39(4):361–374, 2004.

[WDF+12] X Wang, O Delestre, J-M Fullana, M Saito, Y Ikenaga, M Matsukawa, and P-Y Lagrée. Comparing different numerical methods for solving arterial 1D flows in networks. *Computer Methods in Biomechanics and Biomedical Engineering*, 15(sup1):61–62, 2012.

[WES71] Nicolaas Westerhof, GIJS Elzinga, and P Sipkema. An artificial arterial system for pumping hearts. *Journal of applied physiology*, 31(5):776–781, 1971.

[WKA11] Michael Weiss, Tom C Krejcie, and Michael J Avram. A physiologically based model of hepatic icg clearance: Interplay between sinusoidal uptake and biliary excretion. *European Journal of Pharmaceutical Sciences*, 44(3):359–365, 2011.

[WLZ47] S H Webster, E J Liljegren, and D J Zimmer. Organ; body weight ratios for liver, kidneys and spleen of laboratory animals; albino rat. *Am J Anat*, 81(3):477–513, Nov 1947.

[XHW+16] L Xiang, L Huang, X Wang, Y Zhao, Y Liu, and J Tan. How much portal vein flow is too much for liver remnant in a stable porcine model? In *Transplantation proceedings*, volume 48, pages 234–241. Elsevier, 2016.

[Zam99] M Zamir. On fractal properties of arterial trees. *Journal of theoretical biology*, 197(4):517–526, 1999.

[ZLCK09] Jean-David Zeitoun, Jérémie Lefèvre, and Ariane Chryssostalis-Kulundzic. *Hépato-gastro-entérologie, chirurgie viscérale*. Vernazobres-Grego, 2009.